

Numerical Investigation of Lateral–Torsional Buckling of T-shaped Steel Beams

by

Michael Manarin

A thesis submitted in partial fulfillment of the requirements for the degree of

Master of Science

in

STRUCTURAL ENGINEERING

Department of Civil and Environmental Engineering
University of Alberta

© Michael Manarin, 2019

ABSTRACT

Lateral–torsional buckling (LTB) is a failure mode that is associated with simultaneous vertical displacement and twisting of a beam when subjected to flexural loading. LTB behaviour is generally well understood for I-shaped steel beams; however, the LTB behaviour of T-shaped steel beams is not as well understood. The aim of this study is to better understand the behaviour of T-shaped steel beams in single-curvature with the flange in compression through numerical finite element analysis, with a special focus on the moment gradient factor to consider the effect of varying moments along the beam axis.

Eighteen T-shaped beams were selected to represent the entire population cut from standard rolled wide-flange shapes in terms of various geometric properties (e.g., flange width and thickness, stem depth and thickness, second moment of area about the major and minor axes, and minimum slenderness ratio for elastic LTB to occur). Once validated, the finite element model was used to determine the elastic LTB behaviour, and consequently the moment gradient factor, for three loading scenarios with simply-supported end conditions: constant moment, point load, and uniformly distributed load. It was proposed that the CSA S16-14 moment gradient factor for doubly- and singly-symmetric I-shaped beams in single-curvature be utilized also for T-shaped beams when in single-curvature with the flange in compression for the aforementioned loading cases.

The finite element model was also used to investigate inelastic LTB behaviour. It was determined that class 1 and class 2 T-shaped beams were able to achieve the plastic moment when they reached the cross-sectional capacity. The class 3 T-shaped beam also reached the plastic moment capacity when they reached the cross-sectional capacity; however, it may not be

the case for all class 3 sections as they are susceptible to local buckling. Finally, the results were compared to CSA Standard S16 and changes were proposed to improve the estimation of the inelastic LTB critical moment.

ACKNOWLEDGEMENTS

I would like to begin by thanking my co-supervisors, Dr. Robert Driver and Dr. Yong Li, for their guidance throughout this project. Their technical expertise coupled with their ability to articulate complex ideas in laymen's terms proved invaluable. This project would not have been possible without them.

This research project was funded by the Natural Sciences and Engineering Research Council and the CISC Centre for Steel Structures Education and Research. Financial support, in the form of scholarships, were provided by the Faculty of Graduate Studies and Research and the Canadian Institute of Steel Construction.

To my fellow Steel Centre colleagues, thank you for your valuable discussions throughout my research project. To the current and past Steel Centre lateral-torsional buckling researchers, thank you for sharing your knowledge.

Finally, to my friends and family. Thank you for being there when you were called upon, providing support throughout the entirety of my project. And to everyone that asked, "When will you be done so you can move back home?" and endured my answer of "I'm not sure yet.", I can now tell you "I'm done and on my way home".

TABLE OF CONTENTS

CHAPTER 1: INTRODUCTION	1
1.1 Background.....	1
1.2 Statement of Problem	3
1.3 Objectives and Scope.....	3
1.4 Organization of Thesis.....	4
CHAPTER 2: LITERATURE REVIEW	5
2.1 Introduction.....	5
2.2 Review of Design Standards.....	5
2.2.1 CSA S16-14	5
2.2.2 AISC 360-16	8
2.2.3 Eurocode 1993-1-1.....	10
2.3 Review of Numerical and Experimental Studies.....	12
2.3.1 Lateral–Torsional Buckling of Doubly-Symmetric I-shaped Beams	13
2.3.2 Lateral–Torsional Buckling of Singly-Symmetric I-shaped Beams	15
2.3.3 Lateral–Torsional Buckling of T-shaped Beams	18
2.3.4 Residual Stress Patterns	19
2.4 Summary.....	21
CHAPTER 3: FINITE ELEMENT MODEL	22
3.1 Introduction.....	22
3.2 Finite Element Modelling	22
3.2.1 Material Model.....	22
3.2.2 Elements and Mesh.....	23
3.2.3 Load Application	24
3.2.4 Boundary Conditions and Constraints	25

3.2.5	Methods of Analysis	35
3.2.6	Initial Geometrical Imperfections	36
3.2.7	Residual Stresses.....	37
3.3	Validation	38
3.3.1	Original Constraints	40
3.3.2	Updated Constraints.....	41
3.3.3	Validation Discussion	43
3.4	Conclusions.....	43
CHAPTER 4: NUMERICAL TEST SECTIONS		44
4.1	Introduction.....	44
4.2	Test Matrix.....	44
4.3	Conclusions.....	49
CHAPTER 5: ELASTIC LATERAL–TORSIONAL BUCKLING.....		51
5.1	Introduction.....	51
5.2	LTBeam	51
5.2.1	LTBeam Results.....	51
5.2.2	Comparison to Design Standards.....	53
5.2.3	Additional Model Validation	54
5.3	Finite Element Modelling.....	55
5.3.1	Load–Deflection Curves	56
5.3.2	Analyses and Results	58
5.3.3	Comparison to Design Standards.....	59
5.4	Discussion.....	61
5.5	Design Recommendations	62
5.6	Summary.....	63

CHAPTER 6: INELASTIC LATERAL–TORSIONAL BUCKLING	64
6.1 Introduction.....	64
6.2 Finite Element Modelling.....	64
6.2.1 Effect of Residual Stresses.....	64
6.2.2 Analyses and Results	69
6.2.3 Comparison to Design Standards.....	71
6.3 Discussion and Design Recommendations.....	80
6.4 Summary.....	83
CHAPTER 7: CONCLUSIONS AND RECOMMENDATIONS	84
7.1 Summary.....	84
7.2 Conclusions.....	85
7.3 Recommendations for Future Work	85
REFERENCES	87
APPENDIX A: ELASTIC LATERAL–TORSIONAL BUCKLING RESULTS	90
A.1: Tabular Results	90
A.2: Graphical Results	93
APPENDIX B: INELASTIC LATERAL–TORSIONAL BUCKLING RESULTS	111
B.1: Tabular Results.....	111
B.2: Graphical Results	115

LIST OF FIGURES

Figure 1-1: Lateral–Torsional Buckling Deflected Shape for the Midspan of a Beam: (a) Initial Position; (b) Position Before Buckling; (c) Position After Buckling	1
Figure 1-2: LTB Moment Resistance vs Unbraced Length of Beams (after Kabir 2016).....	2
Figure 2-1: Cross-section Shapes for Beams (a) Doubly-Symmetric I-Shape; (b) Singly-Symmetric I-Shape; (c) T-Shape.....	13
Figure 2-2: Singly-symmetric I-sections with Geometric Dimensions (Koch et al. 2019)	16
Figure 2-3: Residual Stress in the Flange (left) and Stem (right) (Nagaraja Rao et al. 1964).....	19
Figure 2-4: Assumed Residual Stress Distribution for Tee Struts (Kitipornchai and Lee 1986a) 21	
Figure 3-1: Steel Stress–Strain Curve under Uniaxial Tension	23
Figure 3-2: Element Selection based on Thickness-to-Length Ratio (Akin 2010).....	23
Figure 3-3: Mesh Sensitivity Analysis.....	24
Figure 3-4: Boundary Conditions	26
Figure 3-5: Original Constraints	27
Figure 3-6: Overall Beam (Forces in N).....	28
Figure 3-7: Forces Along the Flange and Stem	29
Figure 3-8: Nodal Forces of the Centre Flange Node.....	30
Figure 3-9: Nodal Forces of the Top Stem Node.....	30
Figure 3-10: Distribution of the Stem Nodal Forces	31
Figure 3-11: Updated Constraints	32
Figure 3-12: Overall Beam Subjected to a Mid-span Point Load with Updated End Constraints	32
Figure 3-13: Resultant Forces for the Flange and Stem of the Beam with Updated Constraints .	33
Figure 3-14: Nodal Forces of the Centre Flange Node of the Beam with Updated Constraints ..	34
Figure 3-15: Nodal Forces of the Top Stem Node of the Beam with Updated Constraints	34
Figure 3-16: Stem Nodal Forces with Updated Constraints	35
Figure 3-17: Original Residual Stress Distribution and ABAQUS Residual Stress Pattern	37
Figure 3-18: Reported Residual Stress Distribution (Fukumoto et al. 1980)	39
Figure 3-19: Comparison of the Load–Deflection Curves from Experiments and Finite Element Models with Original Constraints—Point Load	40
Figure 3-20: Comparison of the Load-Deflection Curves from Experiments and Finite Element Models with Updated Constraints—Point Load	42

Figure 4-1: Section Candidates vs Sections Selected: Top Flange.....	47
Figure 4-2: Section Candidates vs Sections Selected: Stem.....	47
Figure 4-3: Section Candidates vs Sections Selected: Second Moment of Area.....	48
Figure 4-4: Section Candidates vs Sections Selected: Minimum Slenderness Ratio for Global Elastic LTB.....	48
Figure 5-1: Comparison of LTBeam Moments to S16-14 Moments Including Proposed Moment Gradient Factors.....	54
Figure 5-2: Load–Deflection Curves for Beams with a WT420×236 Section: (a) Constant Moment; (b) Point Load; (c) UDL; and (d) Moment–Deflection Curves for all Three Loading Scenarios.....	57
Figure 5-3: Comparison of Abaqus Results to S16-14 Moments Including Proposed Moment Gradient Factors (* denotes snap-back behaviour).....	60
Figure 5-4: Ratio of Abaqus Results to S16-14 Moments Including Proposed Moment Gradient Factors Compared to the Slenderness Ratio	61
Figure 6-1: Residual Stress Patterns: (a) Kitipornchai and Lee (1986a); (b) Nagarajao Rao et al. (1964).....	65
Figure 6-2: Finite Element Analysis Results for IPE 220 Section with and without Residual Stresses Compared to Eurocode LTB Design Curve (Vila Real et al. 2004)	66
Figure 6-3: Strains at the midspan of a WT500×124 Beam with a Slenderness of 20 in the Stem and Flange at Maximum Moment.....	69
Figure 6-4: Load–Deflection Curves of a Beam with WT500×124 and Slenderness Ratio = 30: (a) Constant Moment; (b) Point Load; (c) UDL; and (d) Moment Deflection Curves for all Three Loading Scenarios.	70
Figure 6-5: Ratio of the ABAQUS Moment to the CSA S16 Moment	71
Figure 6-6: Lateral–Torsional Buckling Curve for Beams with a WT500×124 Section Subjected to a Constant Moment.....	72
Figure 6-7: Lateral–Torsional Buckling Curve for Beams with a WT500×124 Section Subjected to a Point Load.....	73
Figure 6-8: Lateral–Torsional Buckling Curve for Beams with a WT500×124 Section Subjected to a UDL	74

Figure 6-9: Magnified Midpoint of a WT500×124 Beam with a Slenderness Ratio of 5 Subjected to a Point Load at the Instant of LTB Depicting Element Distortion	75
Figure 6-10: Lateral–Torsional Buckling Curve for Beams with a WT265×36 Section Subjected to a Constant Moment.....	76
Figure 6-11: WT265×36 Lateral–Torsional Buckling Curve for Beams with a WT265×36 Section Subjected to a Point Load	77
Figure 6-12: WT265×36 Lateral–Torsional Buckling Curve for Beams with a WT265×36 Section Subjected to a UDL.....	78
Figure 6-13: Pictorial Representation of My' and Sx'	81
Figure 6-14: Ratio of ABAQUS Moments to Proposed Equation Moments.....	82

LIST OF TABLES

Table 2-1: EN 1993-1-1 LTB Curves	12
Table 2-2: LTB Imperfection Factor.....	12
Table 3-1: Comparison of the Buckling Loads from Experiments and Finite Element Models with Original Constraints: Point Load Condition	41
Table 3-2: Comparison of the Buckling Loads from Experiments and Numerical Models with Updated Constraints: Point Load Condition	42
Table 4-1: Test Matrix Including Relevant Geometric Properties.....	46
Table 4-2: Test Section Beam Slenderness Ratios	49
Table 5-1: Moment Gradient Factors Based on Eigenvalue Analysis in LTBeam.....	52
Table 5-2: LTBeam vs ABAQUS Buckling Analysis Moment Capacities (Point Load).....	55
Table 5-3: Moment Gradient Factors Based on an ABAQUS Riks Analysis	59
Table 5-4: Moment Gradient Factor Recommendations	63
Table 6-1: Inelastic LTB Moment Comparison for Beams with Various Residual Stress Patterns and Subjected to Three Loading Scenarios.....	67

LIST OF ABBREVIATIONS AND SYMBOLS

b_c	: Width of the compression flange
b_f, b	: Width of the flange
C_w	: Warping torsional constant
d	: Section depth
d_t	: Depth of the tee in tension
E	: Modulus of elasticity
F_{cr}	: Critical stress
F_y, F_Y, f_y	: Specified minimum yield stress
G	: Shear modulus
h	: Stem depth
h_c	: Depth of the web (or stem) in compression
I_x	: Moment of inertia about the strong axis
I_y	: Moment of inertia about the weak axis
I_{yc}	: Moment of inertia of the compression flange about the weak axis
I_{yt}	: Moment of inertia of the tension flange about the weak axis
I_{yTop}	: Moment of inertia of the top flange about the weak axis
J	: St. Venant torsional constant
L, L_b	: Unbraced length of the beam
L_p	: Laterally unbraced length for the limit state of yielding
L_r	: Laterally unbraced length for the limit state of inelastic LTB

L_u	: Longest unbraced length where a beam reaches the cross-sectional capacity
L_{yr}	: Length of beam where $M_u = M_{yr}$
M_1	: Smaller end moment
M_2	: Larger end moment
M_a	: Moment at the one-quarter point
M_b	: Moment at the midspan
$M_{b,rd}$: Factored buckling resistance of a laterally unrestrained beam
M_c	: Moment at the three-quarter point
M_{cr1}	: Elastic critical moment based on uniform bending
M_{max}	: Maximum moment along the unbraced segment
M_n	: Nominal moment capacity
$M_{n,FLB}$: Moment associated with flange local buckling
$M_{n,LTB}$: Inelastic LTB moment
$M_{n,SLB}$: Moment associated with stem local buckling
M_p	: Plastic moment resistance of a beam
M_r	: Resisting moment of a beam against LTB failure
M_u, M_{cr}	: Critical elastic LTB buckling moment
M_y	: Yield section moment
M'_y	: Cross-sectional moment corresponding to yielding in the top flange
M_{yr}	: Yielding moment resistance of a singly-symmetric beam including the effects of residual stresses
r_t	: Radius of gyration of the compression flange plus one-third of the web (or stem) area in

compression due to major axis bending

- r_y : Radius of gyration about the y-axis
- S_x : Elastic section modulus about the x-axis
- S_{xc} : Elastic section modulus of the compression flange about the x-axis
- t_c : Thickness of the compression flange
- t_f : Thickness of the flange
- w, t_w : Web (or stem) thickness
- W_y : Plastic section modulus for Class 1 or 2 sections and elastic section modulus for Class 3 sections
- Z_x : Plastic section modulus about the x-axis
- α_{LT} : Imperfection factor
- β_x : Asymmetry parameter
- ϕ_s : Factor of safety for steel
- γ_{M1} : Resistance factor for member instability checks
- λ_{pf} : Limiting slenderness for a compact flange
- λ_{rf} : Limiting slenderness for a non-compact flange
- χ_{LT} : LTB reduction factor
- ω_2, C_b : Moment gradient factor for doubly-symmetric sections
- ω_3 : Moment gradient factor for singly-symmetric sections
- ρ : Degree of monosymmetry

CHAPTER 1: INTRODUCTION

1.1 Background

Several limit states need to be taken into account to ensure the overall serviceability and safety of steel beams. Serviceability considerations include deflections and vibrations of the beam. Safety of steel beams is determined using limit state checks including cross-sectional yielding, local buckling, failure in shear, fatigue limit states, and lateral–torsional buckling. Lateral–torsional buckling (LTB) is a failure mode in which the beam, with a section at midspan of the beam initially positioned as in Figure 1-1 (a), deflects vertically to the position shown in Figure 1-1 (b) and then deflects laterally and twists simultaneously, as seen in Figure 1-1 (c).

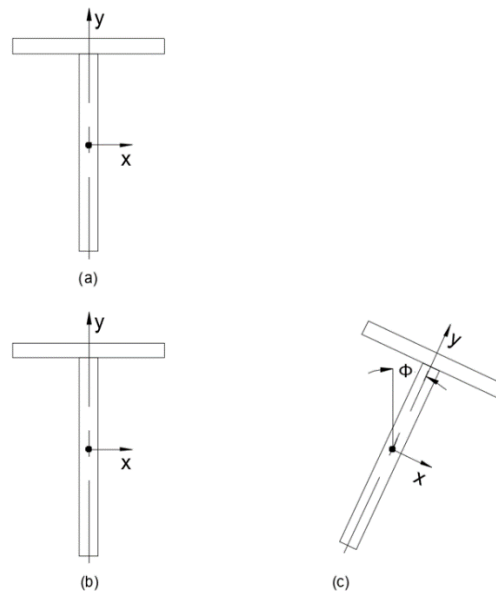


Figure 1-1: Lateral–Torsional Buckling Deflected Shape for the Midspan of a Beam: (a) Initial Position; (b) Position Before Buckling; (c) Position After Buckling

A beam or girder is susceptible to LTB failure when the major-axis stiffness is larger than the minor-axis stiffness. When this structural property holds true, laterally unsupported beams and girders may not achieve their flexural cross-sectional capacity and instead fail in LTB. LTB failures of beams can occur when the top flange is not adequately braced from lateral movement. Once the top flange has been securely attached to an adjacent component (e.g., concrete floor, road deck, steel struts, etc.) the beam is less susceptible to LTB.

LTB failures can be categorized into one of three categories depending on the slenderness of the beam: (1) no LTB with the cross-sectional capacity attainable, (2) inelastic LTB, or (3) elastic LTB, as shown in Figure 1-2.

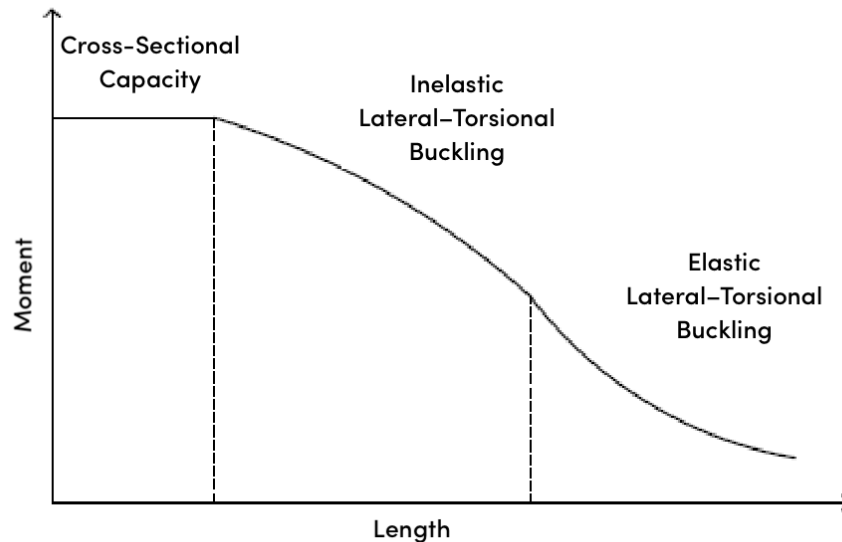


Figure 1-2: LTB Moment Resistance vs Unbraced Length of Beams (after Kabir 2016)

As implied in Figure 1-2, stocky beams fail one the maximum moment in the beam reaches the cross-sectional capacity, beams of intermediate lengths fail in inelastic LTB, and slender beams fail in elastic LTB.

To design beams against LTB failure, various steel standards (e.g., CSA S16, AISC 360, Eurocode 3, etc.) follow similar design equations to determine the LTB resistance of steel beams. The elastic LTB moment capacity is derived from governing equations (Galambos 1968) and adjusted for the specific loading scenario using a moment gradient factor. The inelastic LTB moment capacity is approximated using an empirical solution. The cross-sectional capacity is determined based on the yield stress of the material and either the cross-sectional plastic modulus or elastic modulus, depending on the section classification.

1.2 Statement of Problem

The LTB moment capacity of a beam depends on the moment distribution along the beam caused by different loading scenarios. The constant moment loading scenario allows a closed-form solution to the governing equations (e.g., the system of differential equations) to determine the LTB moment capacity of a beam. In contrast, under other loading scenarios (e.g., point loading, uniformly distributed loading), a moment gradient factor is typically used to adjust the elastic LTB moment derived under the constant moment condition. The current steel standards specify similar moment gradient factors for doubly- and singly-symmetric I-shaped beams; however, they are inconsistent when determining the moment gradient factor for T-shaped beams. The Canadian and American steel standards (i.e., CSA S16-14 and AISC 360-16) currently specify no moment gradient factor, while the European steel code (i.e., Eurocode 1993-1-1) does not explicitly specify the moment gradient factor as the elastic LTB moment may be determined using structural engineering software or hand calculations. There is currently a lack of research on lateral-torsional buckling of T-shaped beams in the elastic and inelastic LTB regions.

1.3 Objectives and Scope

The goal of this research is to investigate the LTB behaviour of simply supported (i.e., pin on one end and roller on the other end) T-shaped beams and assess the current Canadian steel standard considering three loading scenarios: constant moment, point load, and uniformly distributed load (UDL) with the flange in compression and no intermediate bracing. The analysis is completed using finite element modelling. The following objectives are used to achieve the ultimate goal:

- Investigate the elastic LTB behaviour of T-shaped beams and determine the moment gradient factor.
- Investigate the effect of residual stresses on T-shaped beams susceptible to inelastic LTB.
- Investigate the inelastic LTB behaviour of T-shaped beams and determine the inelastic LTB moments.
- Assess the current CSA S16's elastic and inelastic LTB provisions and provide potential changes accordingly if needed.

1.4 Organization of Thesis

This thesis is organized into seven chapters. Chapter 2 contains a literature review of three design standards—the Canadian, American and European standards—and previous LTB research of beams with doubly-symmetric and singly-symmetric cross sections. A detailed explanation and validation of the finite element modelling strategies used for this study can be found in Chapter 3. Chapter 4 includes the numerical test matrix and subsequent chosen sections for numerical investigation purposes to ensure they well represent the majority of T-shaped beams. Chapter 5 contains the elastic LTB analysis results, along with an additional validation of the model and proposed design recommendations based on the results. The inelastic LTB results and design recommendations can be found in Chapter 6. Finally, a summary of the research, along with conclusions and recommendations for future work are presented in Chapter 7. The elastic and inelastic LTB finite element analysis results, respectively, in tabular and graphical forms can be found in Appendices A and B.

CHAPTER 2: LITERATURE REVIEW

2.1 Introduction

Lateral-torsional buckling has been studied extensively for doubly- and singly-symmetric I-shaped beams under single and double curvature bending. However, there is a lack of research surrounding the LTB of T-shaped beams, which are typically used as secondary structural members (e.g. to support façades). First, a review of the Canadian steel design standard (CSA S16-14), American steel design specification (AISC 360-16), and Eurocode (1993-1-1 (2005)) are presented. Next, a review of LTB research is conducted to explore prior research on LTB of I- and T-shaped beams. Finally, residual stress patterns, which in general tend to be influential for inelastic LTB analysis, are discussed in the context of T-shaped beams.

2.2 Review of Design Standards

Among the many steel design standards around the world, three are reviewed regarding LTB. Although the standards look different at first glance, they produce similar results when disregarding the load and resistance factors. This section focuses primarily on LTB of T-shaped beams, with references to singly-and doubly-symmetric I-shaped beams or other beams where necessary for context.

Due to the inherent geometry of T-shaped beams (i.e., the presence of only one flange), they are expected to act differently depending on whether the flange is in compression or tension. When the flange is in compression, the beam should act similarly to I-shaped beams because the majority of the stem is in tension and not susceptible to local buckling. The same cannot be said when the flange is in tension, since the stem would be in compression and is susceptible to local buckling.

2.2.1 CSA S16-14

The Canadian standard (CSA S16-14) for the design of steel structures defines the LTB moment for doubly-symmetric and singly-symmetric beams (CSA 2014) in §13.6 a) - b) and §13.6 e), respectively. This review focuses specifically on the LTB design of beams with T-shaped cross-sections.

In CSA S16-14, the factored resisting moment, M_r , of a beam for the limit state of LTB failure is determined based on the relative magnitudes of the critical elastic LTB buckling moment, M_u , the yield moment resistance of a singly-symmetric beam including the effects of residual stresses, M_{yr} , and the plastic moment resistance of the beam, M_p . When $M_u > M_{yr}$:

$$M_r = \phi \left[M_p - (M_p - M_{yr}) \left(\frac{L - L_u}{L_{yr} - L_u} \right) \right] \leq \phi M_p \quad (2-1)$$

S16 specifies that M_p shall be replaced with M_y (the yield section moment) for class 3 beams and all T-shaped beams with the tip of the stem in compression. $M_{yr} = 0.7S_xF_y$, where S_x is the smaller of the two elastic section moduli, F_y is the specified minimum yield stress, and L_{yr} is the length that leads to $M_u = M_{yr}$. L_u is the longest unbraced length with which a beam will reach the cross-sectional capacity and utilizes r_t , which is the radius of gyration of the compression flange plus one-third of the stem area in compression due to major-axis bending. These two values can be determined using Equation 2-2 and Equation 2-3.

$$L_u = 1.1r_t \sqrt{\frac{E}{F_y}} \quad (2-2)$$

$$r_t = \frac{b_c}{\sqrt{12 \left(1 + \frac{h_c w}{3b_c t_c} \right)}} \quad (2-3)$$

in which E is the elastic modulus of steel, b_c is the width of the compression flange, h_c is the depth of the stem in compression, w is the stem thickness, and t_c is the thickness of the compression flange.

When $M_u \leq M_{yr}$, $M_r = \phi M_u$ where:

$$M_u = \frac{\omega_3 \pi^2 E I_y}{2L^2} \left[\beta_x + \sqrt{\beta_x^2 + 4 \left(\frac{GJL^2}{\pi^2 E I_y} + \frac{C_w}{I_y} \right)} \right] \quad (2-4)$$

where β_x is the asymmetry parameter, G is the shear modulus, J is St. Venant torsional constant, L is the unbraced length, I_y is the moment of inertia about the weak axis, and C_w is the warping torsional constant. The moment gradient factor for singly-symmetric sections, ω_3 , is based on the moment gradient factor for doubly-symmetric sections, ω_2 , and changes based on the following criteria:

- If the beam is under single-curvature bending:

$$\omega_3 = \omega_2 \text{ for beams with two flanges}$$

$$\omega_3 = 1.0 \text{ for beams with T-sections}$$

- For all other cases:

$$\omega_3 = \omega_2 \left(0.5 + 2 \left(\frac{I_{yc}}{I_y} \right)^2 \right) \text{ but } \leq 1.0 \text{ for beams with T-sections}$$

The moment gradient factor is used to account for moments that vary over the length of the beam, as the shape of the moment diagram affects the LTB moment. The worst-case scenario for beams with two flanges is a constant moment. The best-case scenario for beams with two flanges is the maximum moment at the support locations and the minimum moment at the midpoint of the beam. The moment gradient factor is determined using the quarter-point equation presented in Equation 2-5.

$$\omega_2 = \frac{4M_{max}}{\sqrt{M_{max}^2 + 4M_a^2 + 7M_b^2 + 4M_c^2}} \leq 2.5 \quad (2-5)$$

in which the maximum moment in the unbraced segment is M_{max} , the moment at the one-quarter point is M_a , the moment at midspan is M_b , and the moment at the three-quarter point is M_c .

CSA S16-14 contains a provision that the section shall not yield under service loads. This thesis neglects this provision for comparisons to the standards since the ultimate limit state is being investigated; however, this provision can govern the design in many practical cases. CSA S16-14 also states that when the beam is loaded above or below the cross-section mid-height, a rational method of accounting for the destabilizing or stabilizing effect must be used. Additionally, no differentiation is made for rolled and welded cross-sections.

The moment gradient factor for T-shaped beams in single curvature bending is given as a single value. This is unexpected since it implies that T-shaped beams do not act the same way as doubly- and singly-symmetric I-shaped beams.

2.2.2 AISC 360-16

LTB of beams is covered in section F in the AISC 360-16 (2016). Section F4 includes I-shaped members with compact, non-compact or slender flanges and compact or non-compact webs bent about their major axis of the cross section, section F5 covers doubly- and singly-symmetric I-shaped members with slender webs bent about their major axis, and section F9 discusses tees and double-angle beams loaded in the plane of symmetry. Compact sections are expected to attain the full plastic moment capacity, non-compact sections may buckle locally prior to attaining the plastic moment capacity, and slender sections are expected to experience local buckling prior to reaching the yield moment. This review focuses on the determination of the nominal moment capacity using section F9—tees and double-angles loaded in the plane of symmetry—with an emphasis on T-shaped beams with the stem in tension.

The nominal moment capacity, M_n , of T-shaped beams is the minimum of the plastic moment, M_p , the elastic LTB moment, M_{cr} , the inelastic LTB moment $M_{n,LTB}$, the moment associated with flange local buckling, $M_{n,FLB}$, and the moment associated with stem local buckling, $M_{n,SLB}$, as shown in Equation 2-6.

$$M_n = \min \left\{ \begin{array}{l} M_p \\ M_{cr} \text{ or } M_{n,LTB} \\ M_{n,FLB} \text{ or } M_{n,SLB} \end{array} \right. \quad (2-6)$$

The LTB moment is determined based on the unbraced length, L_b , the maximum laterally unbraced length that would permit the beam to achieve the limit state of yielding, L_p , and the maximum laterally unbraced length that would permit the beam to achieve the limit state of inelastic LTB, L_r . L_p and L_r are defined in Equations 2-7 and 2-8.

$$L_p = 1.76r_y \sqrt{\frac{E}{F_y}} \quad (2-7)$$

$$L_r = 1.95 \left(\frac{E}{F_y} \right) \frac{\sqrt{I_y J}}{S_x} \sqrt{2.36 \left(\frac{F_y}{E} \right) \frac{d_t S_x}{J} + 1} \quad (2-8)$$

in which r_y is the radius of gyration about the y-axis, S_x is the elastic section modulus, and d_t is the depth of the tee in tension.

When $L_b \leq L_p$, as long as local buckling is precluded, the beam fails in yielding and the limiting moment is determined differently depending on whether the tee stem is in tension or compression. If the tee stem is in tension, $M_n = M_p$, determined as follows:

$$M_p = F_y Z_x \leq 1.6 M_y \quad (2-9)$$

in which Z_x is the plastic section modulus about the x-axis, and M_y is the yield section moment. M_p is taken as the lesser of the plastic section moment and $1.6 M_y$. The limit of $1.6 M_y$ prevents early yielding under service loads as per the Commentary (AISC 2016). Many beams are limited by $1.6 M_y$ due to the large shape factor arising from the T-shaped cross-section and thus will not achieve the ultimate limit state of M_p , but rather fail due to the serviceability limit state.

When $L_p < L_b \leq L_r$, the beam fails in inelastic LTB with the inelastic LTB moment, $M_{n,LTB}$, determined using Equation 2-10.

$$M_{n,LTB} = M_p - (M_p - M_y) \left(\frac{L_b - L_p}{L_r - L_p} \right) \quad (2-10)$$

When $L_b > L_r$ the beam fails in elastic LTB, with the elastic LTB moment, M_{cr} , determined using Equations 2-11 and Equation 2-12.

$$M_{cr} = \frac{1.95 E}{L_b} \sqrt{I_y J} \left(B + \sqrt{1 + B^2} \right) \quad (2-11)$$

$$B = 2.3 \left(\frac{d}{L_b} \right) \sqrt{\frac{I_y}{J}} \quad (2-12)$$

It should be noted that AISC 360 does not include the moment gradient factor, C_b , as it is implicitly given a value of 1.0; however, if the moment gradient factor were included, C_b would appear as a multiplicative coefficient to the M_{cr} equation. The exclusion of the moment gradient factor implies that, unlike I-shaped beams, T-shaped and double-angle beams are not affected by moments that vary over the length of the unbraced beam segment.

Even if the flange is in compression, if the flange is classified as compact the limit state of flange local buckling does not apply. If the flange is classified as noncompact the moment associated with flange local buckling is determined using Equation 2-13 and if the flange is classified as slender the moment associated with flange local buckling is determined using Equation 2-14.

$$M_{n,FLB} = \left[M_p - (M_p - 0.7F_y S_{xc}) \left(\frac{\lambda - \lambda_{pf}}{\lambda_{rf} - \lambda_{pf}} \right) \right] \leq 1.6M_y \quad (2-13)$$

$$M_{n,FLB} = \frac{0.7ES_{xc}}{\left(\frac{b_f}{2t_f} \right)^2} \quad (2-14)$$

in which $\lambda = \frac{b_f}{2t_f}$, b_f is the width of the flange, t_f is the thickness of the flange, λ_{pf} is the limiting slenderness for a compact flange ($\lambda_{pf} = 0.38\sqrt{E/F_y}$), λ_{rf} is the limiting slenderness for a noncompact flange ($\lambda_{rf} = 1.0\sqrt{E/F_y}$), and S_{xc} is the elastic section modulus referred to the (compression) flange. It should be noted that $0.7S_{xc}$ is larger than Z_x in many T-shaped beams.

$M_{n,SLB}$ is not applicable when the stem is in tension.

2.2.3 Eurocode 1993-1-1

Reductions in cross-sectional capacity arising specifically from the influence of LTB are discussed in two sections of the Eurocode (CEN 2005): a general case for members of constant

cross-section (Section 6.3.2.2) and a case for rolled I-sections or equivalently sized welded sections (Section 6.3.2.3), with the overall LTB design equation in Section 6.3.2.1. Since the focus is singly-symmetric T-shaped beams, the general case is discussed. The factored buckling resistance of a laterally unrestrained beam, $M_{b,Rd}$, is determined using Equation 2-15.

$$M_{b,Rd} = \chi_{LT} W_y \frac{f_y}{\gamma_{M1}} \quad (2-15)$$

in which W_y is the section modulus, which takes the value of the plastic section modulus, i.e., $W_y = W_{pl,y}$, for Class 1 or 2 cross sections, or the elastic section modulus, i.e., $W_y = W_{el,y}$, for Class 3 cross sections, f_y is the yield strength of steel, γ_{M1} is a resistance factor for member instability checks and prescribed a value of 1.0, and χ_{LT} is the LTB reduction factor defined in Equation 2-16.

$$\chi_{LT} = \frac{1}{\Phi_{LT} + \sqrt{\Phi_{LT}^2 - \bar{\lambda}_{LT}^2}} \leq 1.0 \quad (2-16)$$

$$\Phi_{LT} = 0.5[1 + \alpha_{LT}(\bar{\lambda}_{LT} - 0.2) + \bar{\lambda}_{LT}^2] \quad (2-17)$$

$$\bar{\lambda}_{LT} = \sqrt{\frac{W_y f_y}{M_{cr}}} \quad (2-18)$$

where α_{LT} is an imperfection factor based on the ratio of cross section depth, d/\bar{h} , to cross section width, b , the shape of the cross-section, and whether the section is rolled or welded (see Table 2-1 and Table 2-2), and M_{cr} is the elastic critical moment for lateral-torsional buckling and includes the effect of moment variation along the beam axis.

Table 2-1: EN 1993-1-1 LTB Curves

Cross-section	Limits	Buckling curve
Rolled I-sections	$d/b \leq 2$	a
	$d/b > 2$	b
Welded I-sections	$d/b \leq 2$	c
	$d/b > 2$	d
Other cross-sections	–	d

Table 2-2: LTB Imperfection Factor

Buckling curve	a	b	c	d
Imperfection Factor, α_{LT}	0.21	0.34	0.49	0.76

Note that M_{cr} is not explicitly defined in the code and the supplementary material (also known as the Non-contradictory, Complementary Information, or NCCI) only includes an equation for doubly-symmetric sections. Since the NCCI allows designers to calculate M_{cr} using any method they deem appropriate (i.e., equations and computer programs), the moment gradient factor is determined depending on what method is chosen, as it may or may not be included in the calculation. For example, if the designer chooses to calculate M_{cr} using a similar equation to that presented in Equation 2-4 or Equation 2-11 there would be no moment gradient factor included in the critical moment calculation. Conversely, if the designer chooses to use LTBeam (a software endorsed by the NCCI for the calculation of elastic critical moments) the moment gradient factor would be within the reported value since the program calculates the critical moment by solving the classic eigenvalues.

2.3 Review of Numerical and Experimental Studies

As previously discussed, the design standards differentiate the members' LTB capacity based on the cross-sectional shape. The following studies are also categorized in the same manner: doubly-symmetric I shapes, singly-symmetric I shapes, and T shapes, as shown in Figure 2-1.

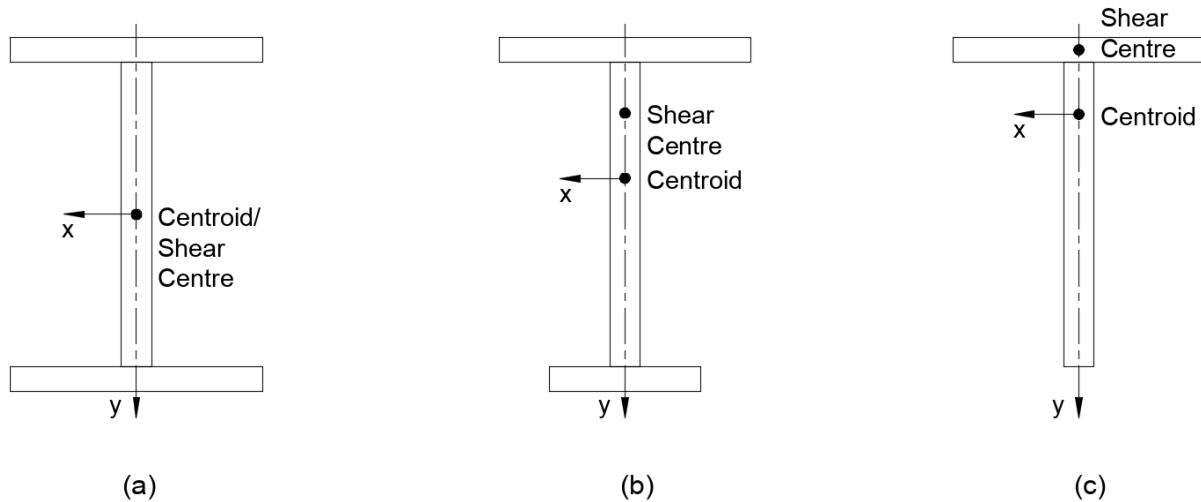


Figure 2-1: Cross-section Shapes for Beams (a) Doubly-Symmetric I-Shape; (b) Singly-Symmetric I-Shape; (c) T-Shape

Figure 2-1 (a) depicts I-shapes that are symmetric about the x- and y-axes, Figure 2-1 (b) depicts I-shapes that are symmetric about the y-axis only, and Figure 2-1 (c) depicts T-shapes symmetric about the y-axis.

2.3.1 Lateral–Torsional Buckling of Doubly-Symmetric I-shaped Beams

LTB of doubly-symmetric beams has been extensively studied beginning in the mid-1900s. It was determined that the LTB behaviour could be described using a set of differential equations. The differential equations could then be simplified, and solved, for the case of doubly-symmetric beams under constant moment. Although this was a large advancement for LTB research, the differential equations could not be readily solved for other loading scenarios. This led to the introduction of a moment gradient factor to account for moments that varied over the length of the beam.

2.3.1.1 *Salvadori (1955)*

The effect of the moment gradient was investigated by Salvadori (1955), who observed that beams with a linear, non-zero-slope moment are less susceptible to LTB than beams with a constant moment. Based on this work, Equation 2-19 was proposed for the moment gradient factor due to linearly varying moment along the beam:

$$\omega_2 = 1.75 + 1.05 \left(\frac{M_1}{M_2} \right) + 0.3 \left(\frac{M_1}{M_2} \right)^2 \leq 2.3 \quad (2-19)$$

where M_1 is the smaller end moment and M_2 is the larger end moment. The ratio between M_1 and M_2 is negative for beams in single curvature and positive for beams in double curvature. This equation is allowed in AISC 360-16 as is and in CSA S16-14 with 2.5 as the upper limit, as long as the moment variation within the unbraced segment is linear.

2.3.1.2 Kirby and Nethercot (1979)

Due to the limitation of Equation 2-19—a requirement that the moment diagram must be linear—Kirby and Nethercot (1979) proposed Equation 2-20, which is purported to be valid for an arbitrary bending moment diagram, as one of the earliest quarter-point methods that was used for calculating the moment gradient factor. Equation 2-20 was slightly modified by AISC as shown in Equation 2-21.

$$\omega_2 = \frac{12M_{max}}{2M_{max} + 3M_a + 4M_b + 3M_c} \quad (2-20)$$

$$\omega_2 = \frac{12.5M_{max}}{2.5M_{max} + 3M_a + 4M_b + 3M_c} \quad (2-21)$$

in which M_a is the moment at the one-quarter point of the unbraced length, M_b is the moment at the midpoint of the unbraced length, M_c is the moment at the three-quarter point of the unbraced length, and M_{max} is the maximum moment anywhere along the unbraced length. The use of Equation 2-21 is still permitted by AISC 360-16.

2.3.1.3 Wong and Driver (2010)

Wong and Driver (2010) determined that the equation specified in AISC 360 (Equation 2-21) yielded unconservative results for some common loading cases (e.g., point load at midspan of the unbraced segment and concentrated moments at the adjacent braced points). They also stated that designers should be aware that quarter-point methods may yield unconservative results when there are abrupt changes in the moment diagram. In an attempt to make the predictions more

accurate, they proposed a new quarter-point method with a square root function in the denominator:

$$\omega_2 = \frac{4M_{max}}{\sqrt{M_{max}^2 + 4M_a^2 + 7M_b^2 + 4M_c^2}} \leq 2.5 \quad (2-22)$$

Wong and Driver (2010) stated that the upper limit could be increased or removed, as the square root method produces good results without the limit; however, the limit was retained due to the increased influence of imperfections as the value of ω_2 increases. They concluded that the proposed equation produced “reasonable and conservative equivalent moment factors, even in cases where other methods do not”. They admitted that there were some situations, namely concentrated applied moments, which rarely occur in practice, where the quarter point methods would not produce suitable results. This equation is currently the only accepted method for non-linear moment gradients in CSA S16-14 and is permitted by AISC 360-16 according to the commentary to the specifications.

2.3.2 Lateral–Torsional Buckling of Singly-Symmetric I-shaped Beams

Although singly-symmetric I-shaped beams seem similar to doubly-symmetric I-shaped beams, they have different behaviours due to the difference in the flange widths or thicknesses. Similarly to doubly-symmetric I-shaped beams, the differential equation for singly-symmetric I-shaped beams cannot be solved directly for varying moments (without the involvement of approximate solutions) and a moment gradient factor is therefore used to account for varying moments. Unless otherwise specified, the following researchers exclude T-shaped beams from their respective research programs.

2.3.2.1 *Kitipornchai and Trahair (1980)*

Kitipornchai and Trahair (1980) studied sectional properties specific to singly-symmetric sections, including the degree of monosymmetry, ρ , an approximation of the degree of monosymmetry, and the asymmetry parameter, β_x , defined in Equation 2-23, Equation 2-24, and Equation 2-25, respectively.

$$\rho = \frac{I_{yC}}{I_{yC} + I_{yT}} \quad (2-23)$$

$$\rho \approx \frac{I_{yC}}{I_y} \quad (2-24)$$

$$\beta_x = \frac{1}{I_x} \left\{ (h - \bar{y}) \left[\frac{b_t^3 t_t}{12} + b_t t_t (h - \bar{y})^2 + (h - \bar{y})^3 \frac{w}{4} \right] - \bar{y} \left(\frac{b_c^3 t_c}{12} + b_c t_c \bar{y}^2 + \bar{y}^3 \frac{w}{4} \right) \right\} - 2y_o \quad (2-25)$$

I_{yC} and I_{yT} are the moments of inertia of the compression and tension flanges, respectively, about the y -axis (axis of symmetry), and the symbols used in the asymmetry parameter can be seen in Figure 2-2. Specifically, for a T-section with the flange in tension (see Figure 2-2 (a)), $\rho = 0$, and when the flange is in compression, $\rho = 1$. The value of ρ falls in the range between 0 and 1 for singly-symmetric sections except for $\rho = 0.5$, which is for a doubly-symmetric section.

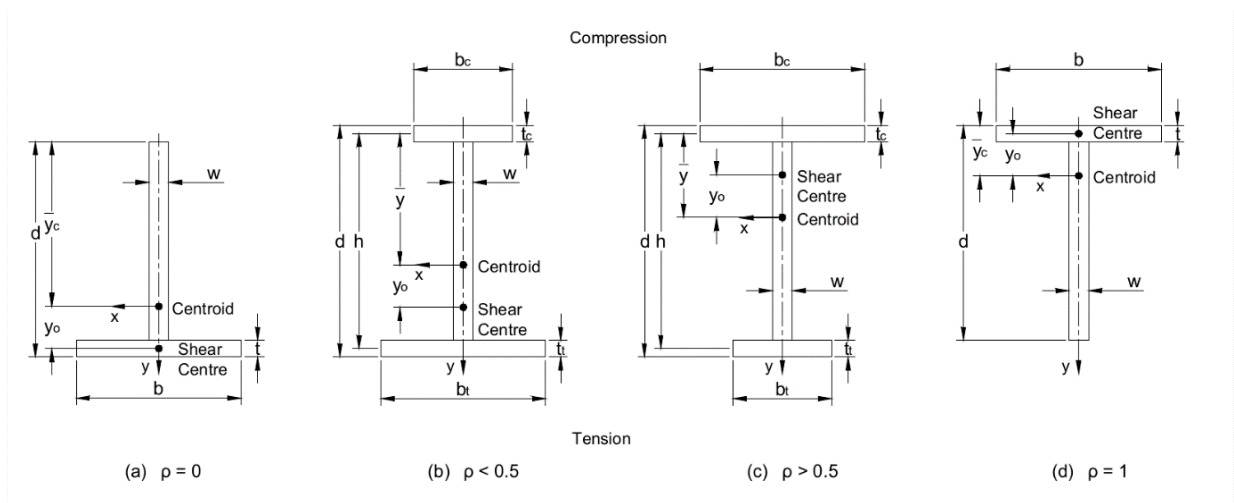


Figure 2-2: Singly-symmetric I-sections with Geometric Dimensions (Koch et al. 2019)

Kitipornchai and Trahair determined that the asymmetry parameter, β_x , in Equation 2-25 can be approximated using Equation 2-26.

$$\beta_x \approx 0.9h(2\rho - 1) \left[1 - \left(\frac{I_y}{I_x} \right)^2 \right] \quad (2-26)$$

The authors limited Equation 2-26 to $\frac{I_y}{I_x} \leq 0.5$, since the equation tends to overestimate the asymmetry parameter outside of the limits.

2.3.2.2 Helwig, Frank and Yura (1997)

This paper focused on LTB of singly-symmetric I-shaped beams subjected to loading at the mid-height of the beam. It was determined that Equation 2-21 accurately captured the effect of the moment gradient on the critical buckling moment for singly-symmetric beams in single curvature with the load applied at mid-height of the web. A slight modification to the equation in AISC 360 accurately predicted the buckling moment when the beam is in double curvature:

$$\omega_2 = \left[\frac{12.5M_{max}}{2.5M_{max} + 3M_a + 4M_b + 3M_c} \right] \left\{ 0.5 + 2 \left(\frac{I_{y\ top}}{I_y} \right)^2 \right\} \leq 3.0 \quad (2-27)$$

in which $I_{y\ top}$ is the weak-axis moment of inertia of the top flange. The second term, in curly brackets, accounts for the effects of reverse-curvature. This research was also limited to $0.1 \leq \rho \leq 0.9$, thus excluding T-shaped beams.

2.3.2.3 Slein, Jeong and White (2018)

The aim of this paper was to improve the reliability of the moment gradient factor for singly-symmetric beams. Slein et al. (2018) compared AISC 360-16, the American Association of State Highway and Transportation Officials (AASHTO) LRFD Bridge Design Specifications, and the equation proposed by Wong and Driver (2010) for doubly-symmetric beams. The equation proposed by Wong and Driver (2010) is recommended for doubly-symmetric beams in single and double curvature and singly-symmetric beams in single curvature. The original equation is modified for singly-symmetric beams in double curvature as shown in Equation 2-28.

$$\omega_2 = \frac{4 \left(\frac{M_{max}}{M_{cr1}} \right)}{\sqrt{\left(\left(\frac{M_{max}}{M_{cr1}} \right)^2 + 4 \left(\frac{M_A}{M_{cr1}} \right)^2 + 7 \left(\frac{M_B}{M_{cr1}} \right)^2 + 4 \left(\frac{M_C}{M_{cr1}} \right)^2 \right)}} \quad (2-28)$$

M_{cr1} is defined as the elastic critical moment based on uniform bending. Since the beams are singly-symmetric it is imperative to ensure the critical moment being calculated is for the flange under compression at the point being analyzed. The authors concluded that the equation proposed by Wong and Driver (2010) was significantly more accurate for singly-symmetric beams in single curvature than the other two methods under consideration. It was also reported that the updated equation performed well for singly-symmetric beams in reverse curvature. The authors noted that the current equation in the AISC 360-16 (Equation 2-21) produced grossly conservative and unconservative results. Equation 2-35 has been proposed for adoption into the next AISC 360 code revisions.

2.3.2.4 Koch, Driver, Li and Manarin (2019)

Koch et al. (2019) completed an in-depth analysis of the asymmetry parameter for singly-symmetric I-sections and T-sections. Specifically, they focused on the simplified equations initially proposed by Kitipornchai and Trahair (Kitipornchai and Trahair 1980). The authors determined that the limits initially proposed could be expanded to $0.1 \leq \rho \leq 0.9$ with a maximum error of 9% in the asymmetry parameter. They also reported that the original asymmetry parameter equation (Equation 2-25) should be used for T-sections, as the simplified equation (Equation 2-26) leads to inaccuracies.

2.3.3 Lateral–Torsional Buckling of T-shaped Beams

There is limited research on LTB of T-shaped beams. The only study located was completed in the 1980s and since then there have been significant advancements in the calculation of moment gradient factors for doubly- and singly-symmetric I-shaped beams.

2.3.3.1 Kitipornchai and Wang (1986)

The energy method was used to investigate the capacities of singly-symmetric T-shaped beams undergoing elastic lateral–torsional buckling. Research was focused on the moment gradient factor for linear moment distributions. It was determined that results for T-shaped beams with the flange in compression provide good correlation with Equation 2-19. In contrast, when the stem is in compression, there is poor correlation with Equation 2-19. It is worth noting that the

energy method produces solutions that are based on an upper-bound solution, and thus a large number of terms are required correctly estimate the results.

2.3.4 Residual Stress Patterns

It has been demonstrated in many studies that in general residual stresses play a significant role in the inelastic LTB range. There has been significant research completed on doubly- and singly-symmetric I-shaped beams; however, there have been few studies regarding T-shaped beams. T-shaped beams are commonly fabricated by cutting a rolled doubly-symmetric I-shaped beam longitudinally or by welding two plates together. Researchers have proposed two residual stress patterns for T-shaped beams: one for welded T-shaped beams and one for I-shaped beams cut to form a T-shaped beam.

2.3.4.1 Nagaraja Rao, Estuar and Tall (1964)

Nagaraja Rao et al. (1964) studied residual stresses in welded shapes made up of flame-cut plates using the method of sectioning. The test specimens included individual plates, L-, T-, H-, and box-shapes; however, the T-shape is of particular interest here. The plates used for fabricating the T-shapes varied from 150mm to 250mm wide and 6mm to 13mm thick. All the T-shapes used the same plate width and thickness for both the flange and the stem elements. An idealized residual stress pattern for flame-cut plates welded into a T-shape is shown in Figure 2-3.

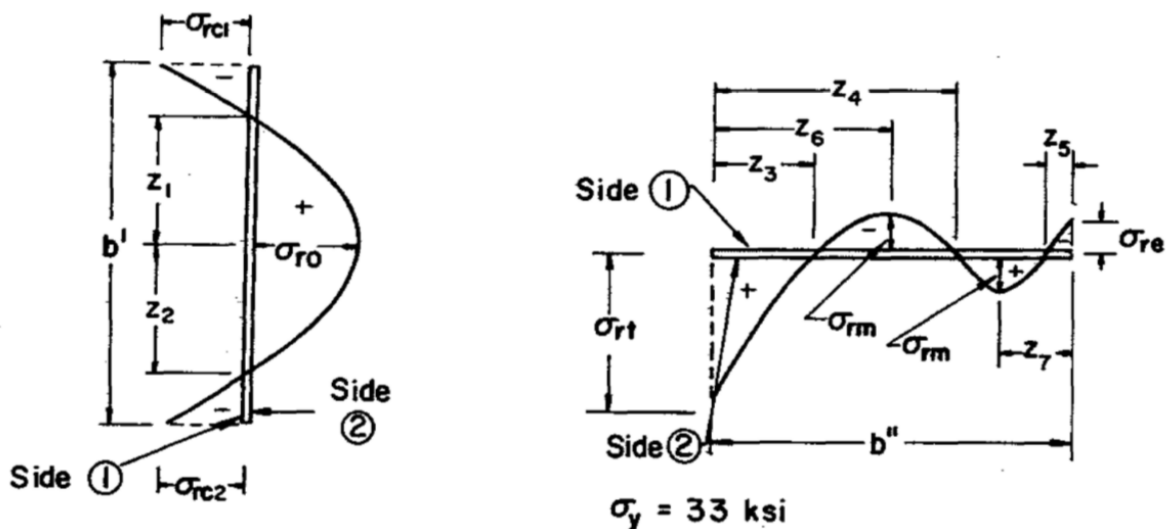


Figure 2-3: Residual Stress in the Flange (left) and Stem (right) (Nagaraja Rao et al. 1964)

The sign convention in Figure 2-3 is tension is positive and compression is negative. The reported stress ranges below are the mean of the two sides of the plate and assume that a positive value is the same direction as the figure and a negative value is the opposite direction of the figure. The study found that the free end of the stem (see σ_{re} in Figure 2-3) has residual stresses that range from -3% to +37% of the yield stress of the base material, σ_{rm} varied from +25% to +31% the yield stress of the base material, σ_{rn} varied from -2% to +33% of the yield stress of the base material, where σ_{rn} is at the location specified by the dimension Z_7 as there is a typographical error in the original figure, and the portion of the stem that was welded to the flange (see σ_{rt} in Figure 2-3) contains residual stresses that can approach +190% of the yield stress of the base material. It was reported that the residual stresses varied from +55% to +121% of the yield stress in the flange tips (see σ_{rc1} and σ_{rc2} in Figure 2-3) and +60% to +160% at the middle of the flange (see σ_{ro} in Figure 2-3).

2.3.4.2 *Kitipornchai and Lee (1986a)*

The authors experimentally studied inelastic column buckling of angle and tee struts. The results were compared to theoretical predictions and the Structural Stability Research Council (SSRC) column curves. The researchers assumed a residual stress pattern for tee struts, as they did not complete any residual stress measurements. These assumptions were then utilized for the theoretical predictions. The assumed residual stress distribution is shown in Figure 2-4 where C and T represent the compression and tension regions, respectively, and $F_Y \overline{F_Y}$ is the material yield stress. The assumed residual stress distribution is half of an idealized residual stress distribution for doubly-symmetric I-shaped beams and does not allow for the effect of heat-cutting the web.

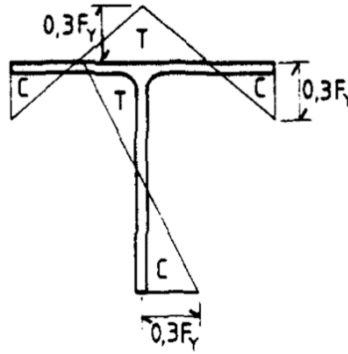


Figure 2-4: Assumed Residual Stress Distribution for Tee Struts (Kitipornchai and Lee 1986a)

The experimental load capacities of the struts ranged from 90% to 103% of the theoretical load, with a mean of 95%, and a standard deviation for the test-to-predicted ratio of 0.05. This leads to a theoretical load that is in reasonable agreement with the experimental load. The same researchers also published a related paper more focused on the theoretical buckling load comparisons with the column buckling curves (Kitipornchai and Lee 1986b). The assumed residual stress distribution was the same for both papers. It is interesting to note that they found the experimental loads “are all lower than the inelastic buckling curve, which could be due to the interaction between local and overall buckling, or that the residual stresses in the test struts are more severe than the assumed values.”

2.4 Summary

Extensive research has been conducted on moment gradient factors for doubly- and singly-symmetric I-shaped beams; however, there is a lack of experimental test data and finite element analysis on T-shaped beams. Additional research is required to determine moment gradient factors for T-shaped beams.

There is a need to investigate whether critical inelastic buckling moments are correctly estimated by CSA S16 and AISC 360, as there has been no research that discusses T-shaped beams exhibiting inelastic LTB.

CHAPTER 3: FINITE ELEMENT MODEL

3.1 Introduction

This study investigates the moment gradient distribution factors for the LTB capacity of singly-symmetric beams through numerical analysis using the general-purpose finite element software ABAQUS. Nonlinear static structural analysis with the arc-length method (i.e., Riks analysis) is conducted to determine the buckling loads. Both experimental results available from the literature and a specialized elastic buckling analysis tool are used to co-validate the FEA model.

3.2 Finite Element Modelling

Finite element models require several different aspects to be defined, including material models, element type, mesh size, load application, boundary conditions, kinematic constraints, analysis options, geometric imperfections, and residual stresses. The following section includes a brief discussion of the aforementioned inputs.

3.2.1 Material Model

The steel material was assumed as elastic–plastic with a yield stress, F_y , of 345 MPa, a modulus of elasticity, E , of 200 GPa and Poisson’s ratio, ν , of 0.3. Since design standards typically neglect the strain-hardening behaviour, no strain hardening was included in the model; however, the inclusion of strain hardening may result in increased member capacities. The stress–strain relationship contained a slight slope in the yield plateau, increasing to a stress of 350 MPa at a strain of 0.2, to ensure no convergence issues arose out of the numerical analysis. The true stress–strain curve can be seen in Figure 3-1. The material model differs slightly for the validation model since it is based on an actual test, where the flange yield stress is 252 MPa and the stem yield stress is 287 MPa. In both cases, the yield plateau was given a slight positive slope to ensure numerical stability in the inelastic range.

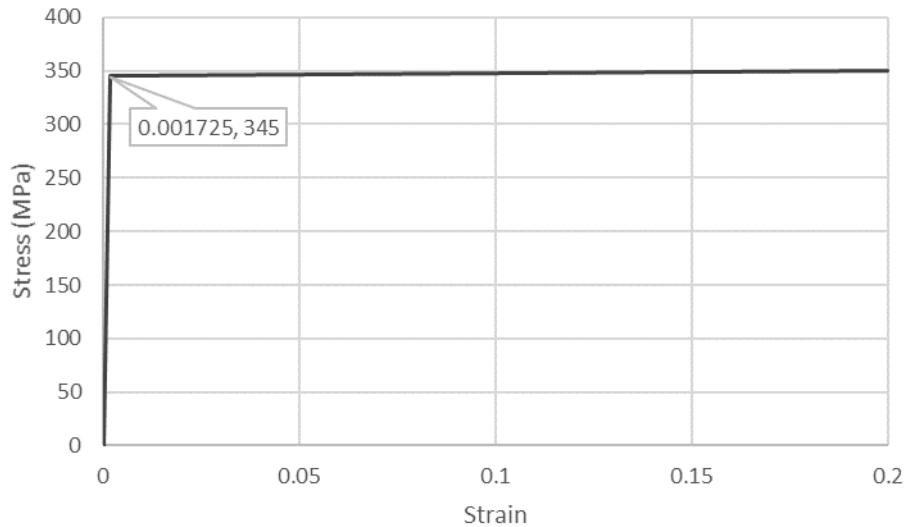


Figure 3-1: Steel Stress–Strain Curve under Uniaxial Tension

3.2.2 Elements and Mesh

The LTB analysis of steel beams can be performed in ABAQUS by modeling the beam using solid elements or shell elements. Solid elements were avoided as they are particularly computationally expensive and not well suited for elements with a thickness-to-length ratio (h/L) below 0.5, as shown in Figure 3-2. The largest thickness-to-length ratio considered in this study is less than 0.05 and thus a thin shell element is the preferred element.

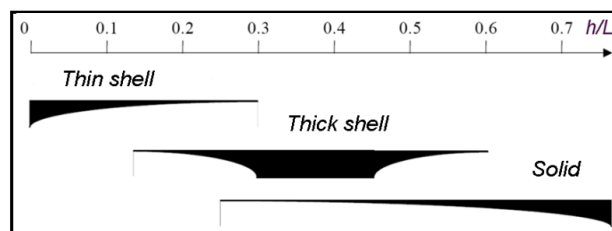


Figure 3-2: Element Selection based on Thickness-to-Length Ratio (Akin 2010)

Considering square, general-purpose shell elements that are suitable for finite strains, there are two shell elements: S4 and S4R. Both S4 and S4R elements have six degrees of freedom at each node; however, S4 uses full integration, while S4R uses reduced integration. Since the

computational requirements are less for S4R, and little accuracy is lost when reduced integration is employed, S4R elements were chosen for the model.

Quad-dominated mesh elements were used, as the flange and stem are rectangular in shape. A mesh sensitivity analysis was completed to determine the optimized mesh density for the study of T-shaped beams undergoing LTB. The comparison between the critical moment and the number of elements along the cross-section of the beam can be seen in Figure 3-3.

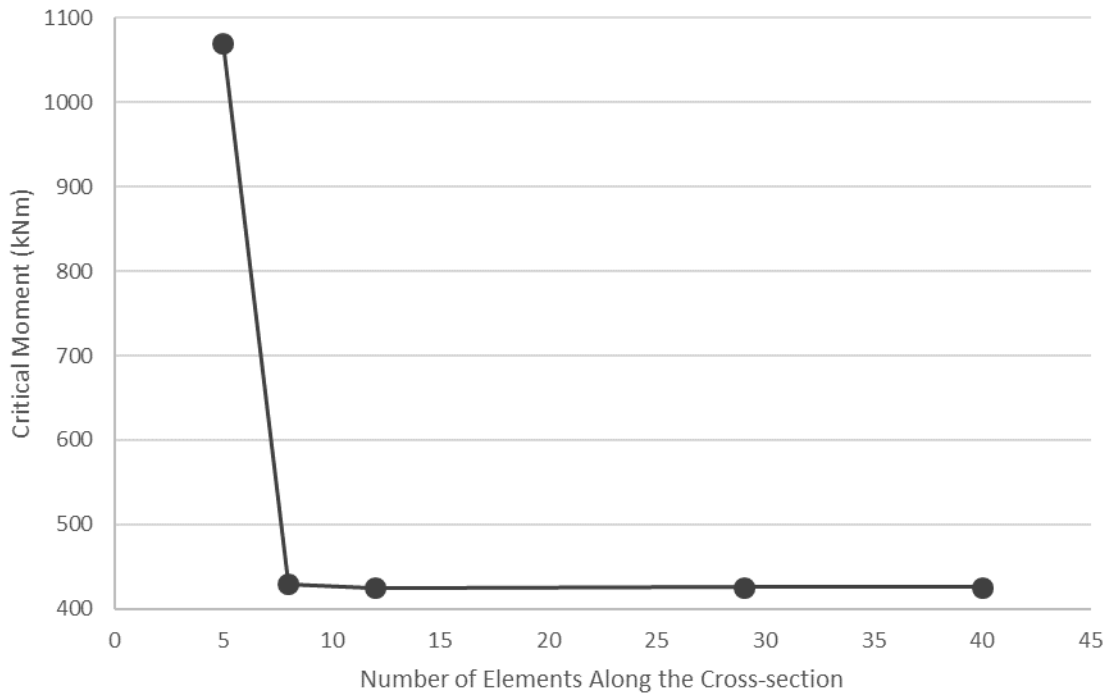


Figure 3-3: Mesh Sensitivity Analysis

The adequate mesh density that led to the converged critical moment, shown in Figure 3-3, utilized six elements over the width of the flange and six elements over the depth of the stem for a total of 12 elements in the cross-section.

3.2.3 Load Application

Three different types of load conditions are considered in this research. They include constant moment (i.e., applying two concentrated moments in the opposite directions at the ends of the

beam), point load at midspan, and UDL conditions. The loads are implemented in the finite element simulation as follows:

- constant moment: the moment can be applied in terms of a force couple. However, for the T-shaped beams, a concentrated point load is applied horizontally at each of the flange tips and another concentrated point load twice as large is applied horizontally at the tip of the stem in the opposite direction. A concentrated moment cannot be applied at the end of the beam, as it is applied to a single node and creates localized stresses and occasionally local buckling at the point of application.
- point load: instead of applying a single point load at the mid-height and mid-span of the beam, 3 x 3 concentrated point loads are applied over a localized square area to avoid local buckling or distortion.
- UDL: equal concentrated point loads are applied at all nodes at the mid-height of the stem along the full length of the beam.

These loading cases were used for both the validation (Section 3.3) and the elastic and inelastic LTB analyses (Chapters 5 and 6).

3.2.4 Boundary Conditions and Constraints

The boundary conditions for lateral–torsional buckling of simply-supported beams are applied in two steps. The first step consists of applying two single-point constraints (i.e., boundary conditions), creating a simply-supported, torsionally pinned beam by fixing the centroid of the section in the horizontal (U1) and vertical (U2) directions along with the torsional degree of freedom (UR3)—the torsional degree of freedom must be constrained so that the beam does not rotate about the longitudinal axis at the supports—at both ends of the beam and the longitudinal direction (U3) is additionally constrained at the right support. This boundary condition is depicted in Figure 3-4 for both I- and T-shaped beams. For I-shaped beams the centroid of the section is coincident with the mid-height of the web, while the centroid is significantly closer to the flange in T-shaped beams.

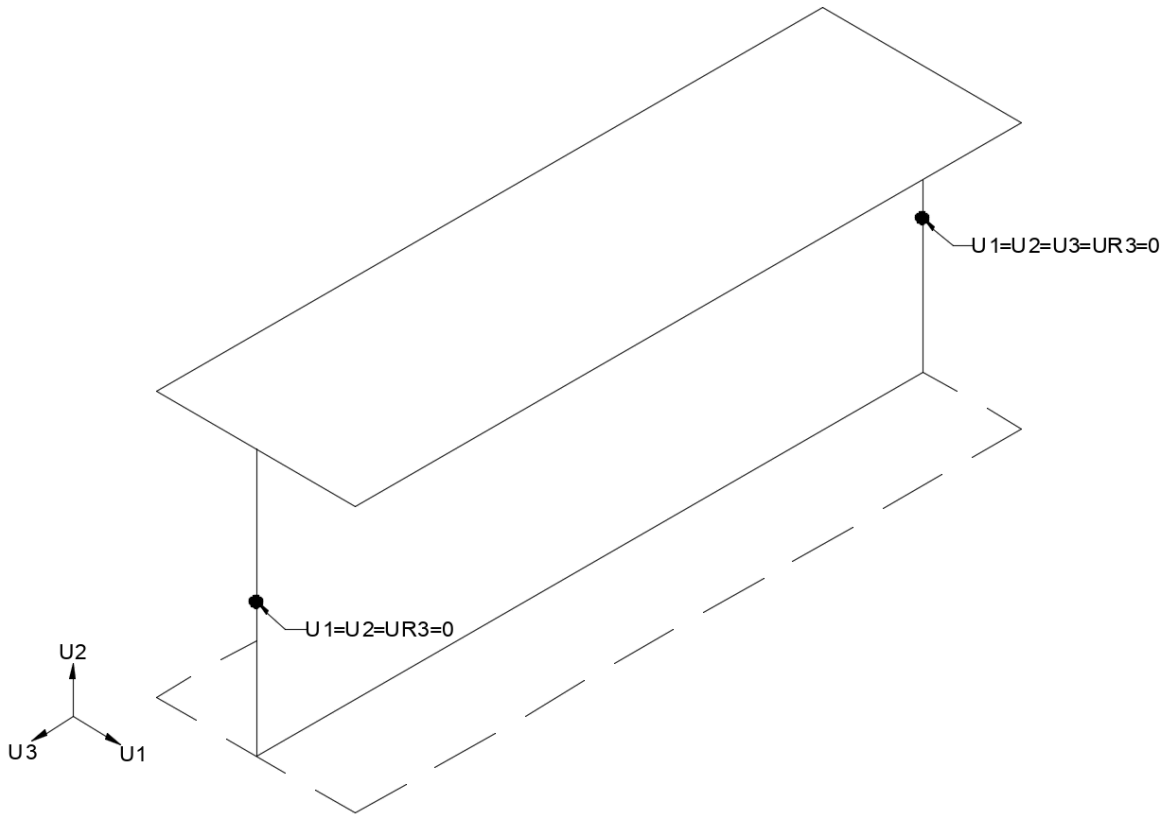


Figure 3-4: Boundary Conditions

The second step consists of applying multiple-point constraints through the application of kinematic constraints in ABAQUS at each beam end. Kinematic constraints limit the motion of groups of nodes to rigid body motion defined by the master node (i.e., the centroid in this case). The constraint is applied to specific user-defined degrees of freedom as shown in Figure 3-5 and Figure 3-11.

3.2.4.1 Original Constraints

Initially the constraints were aimed to guarantee the flange nodes move the same amount in the U1 and U2 directions and rotate the same amount in all three rotational directions, and the stem was tied together so that those elements act in unison as seen in Figure 3-5. The constraint in the

longitudinal direction was released so the nodes along the flange could vary differentially as the beam deflects laterally during LTB. This additionally ensures that the beam was free to warp.

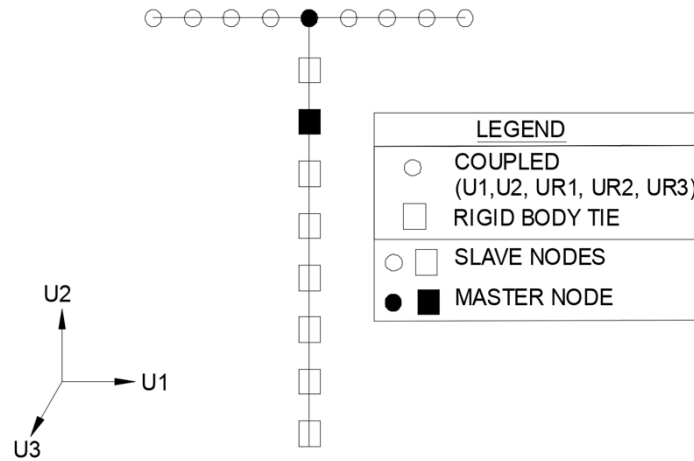


Figure 3-5: Original Constraints

Constraints similar to those shown in Figure 3-5 have been used in prior LTB research (Ji 2019; Kabir 2016) and were further investigated here for its validity. The constraints were applied to a 2.5m long steel beam with a WT500×247 section. A very short beam was used to ensure that it would develop the fully plastic cross-sectional capacity and not enter the elastic or inelastic LTB regions. A 900 kN point load was applied as described in Section 3.2.3.

The expected vertical force at the supports can be calculated as shown in Equation 3-1.

$$V = \frac{P}{2} = \frac{9(100 \text{ kN})}{2} = 450 \times 10^3 \text{ N} = 450 \text{ kN} \quad (3-1)$$

Using the original constraints, Figure 3-6 depicts the resultant vertical forces at the support locations.

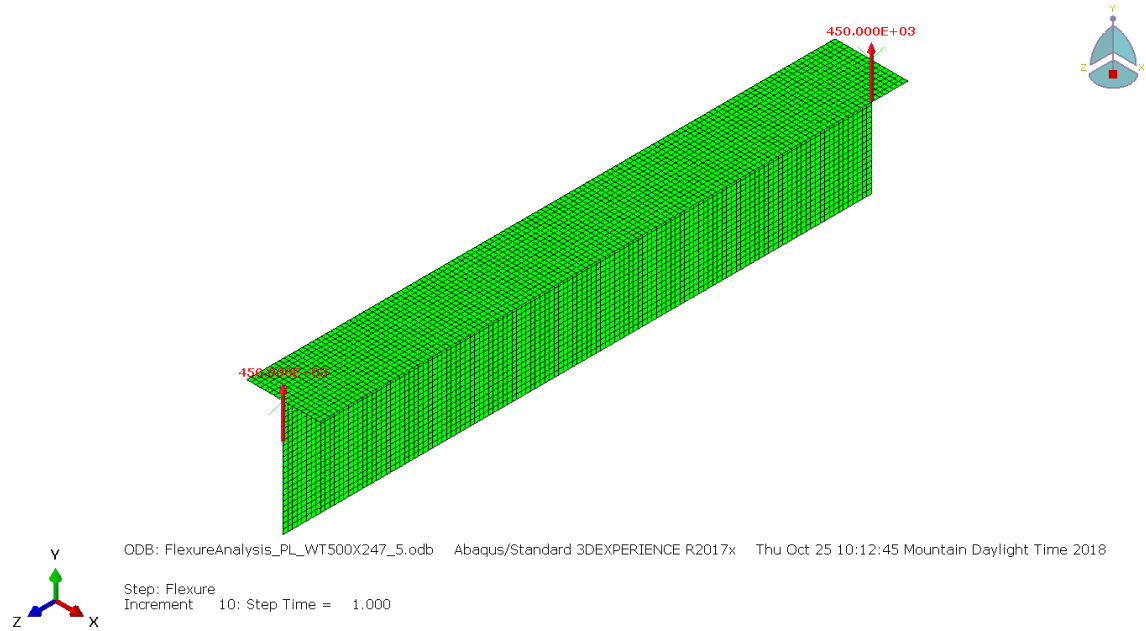


Figure 3-6: Overall Beam (Forces in N)

As seen in Figure 3-6, the shear force is correctly calculated as 450 kN at both ends of the beam. Next, the resultant nodal forces (i.e., the summation of all nodal forces) along the flange and stem at the ends of the beam were determined as shown in Figure 3-7. The resultant horizontal and vertical nodal forces along the flange were calculated by summing the horizontal or vertical force components at each of the nodes along the edge in the same vertical plane as the beam support location. The nodal forces along the stem were similarly determined for the stem nodes along the same vertical plane.

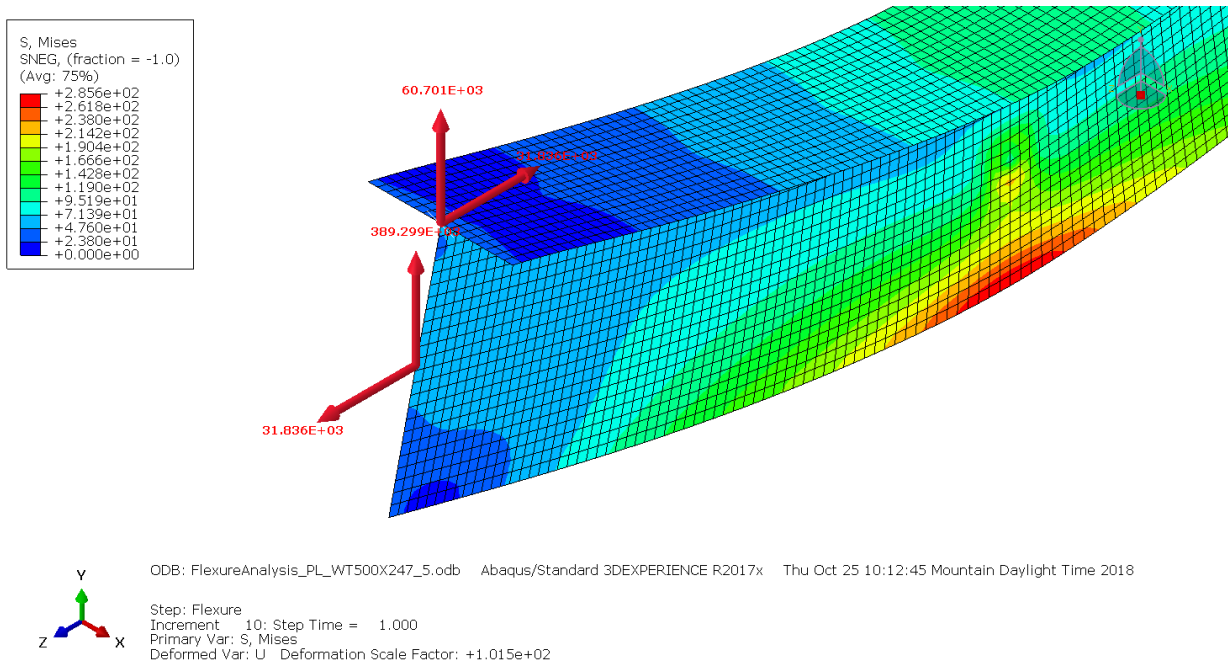


Figure 3-7: Forces Along the Flange and Stem

It was determined that the sum of the two vertical nodal forces (see Equation 3-2) was equal to the resultant vertical force at the support, as evaluated in Equation 3-1.

$$389.3kN + 60.7kN = 450kN \quad (3-2)$$

Note that horizontal resultant forces exist in the flange and stem, but the two forces are equal (31.8 kN) and opposite. To look into this further, the nodal forces were then separately extracted at the centre flange node and the top stem node as seen in Figure 3-8 and Figure 3-9, respectively.

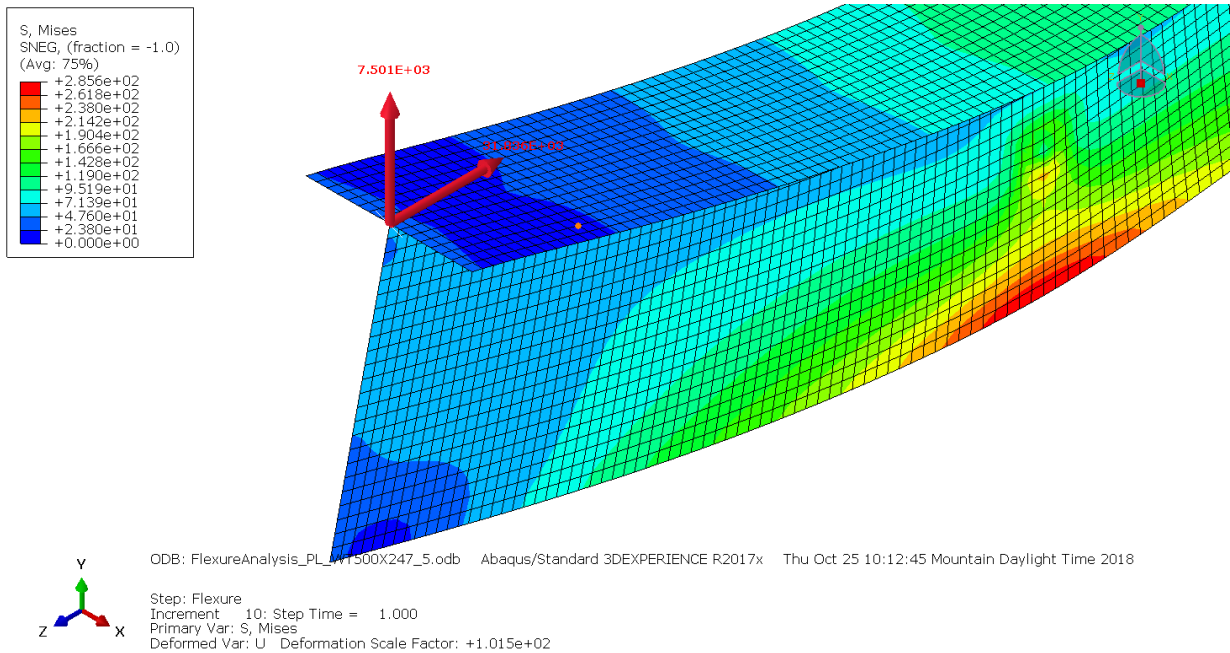


Figure 3-8: Nodal Forces of the Centre Flange Node

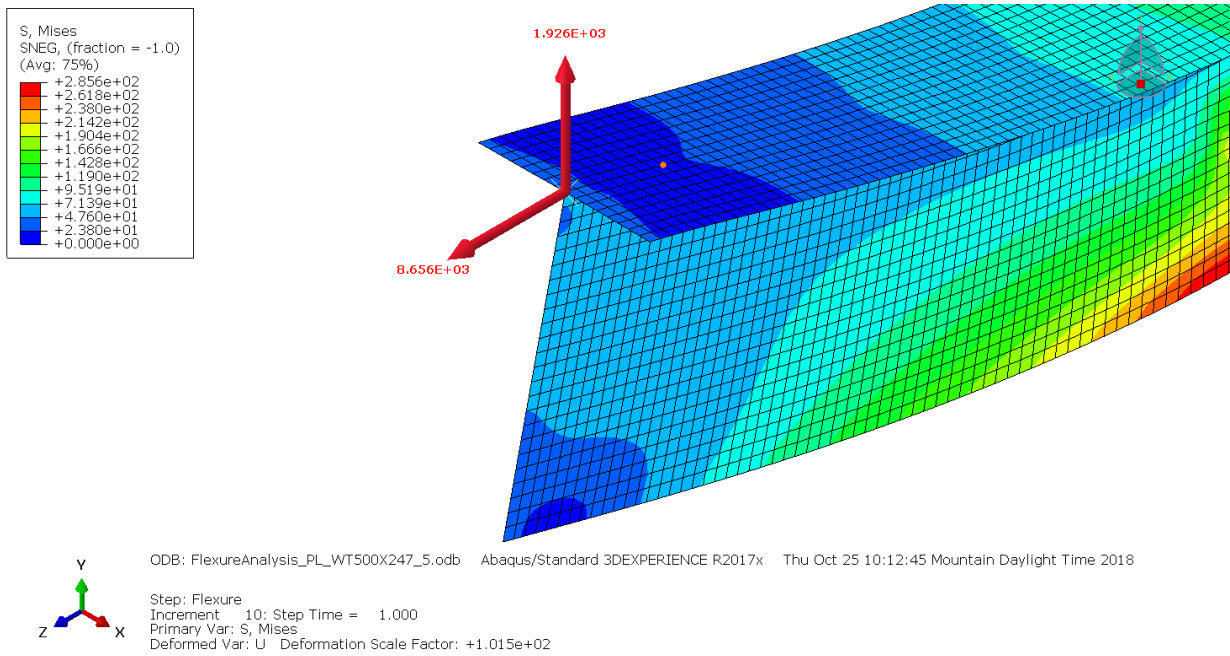


Figure 3-9: Nodal Forces of the Top Stem Node

The horizontal nodal force extracted at the centre node of the flange is again 31.8 kN, confirming that all other flange nodes at the beam ends developed no longitudinal stress as expected, while

the horizontal force from the node at the top of the stem is only 8.7 kN, a net difference of 23.1 kN. The nodal forces were then extracted along the entire stem leading to Figure 3-10

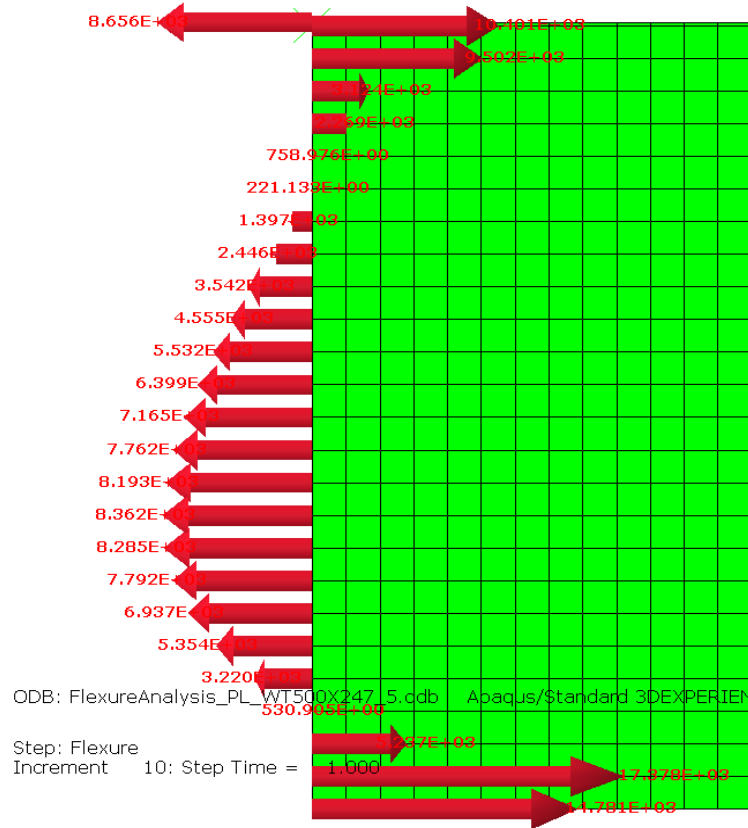


Figure 3-10: Distribution of the Stem Nodal Forces

The values sum to 31.8 kN to the left, which is the same as the overall force shown in Figure 3-7. The left figure depicts the force distribution along the stem. A simply-supported, torsionally pinned beam should not experience tensile forces at the free ends. This led to a modification of the constraints.

3.2.4.2 Updated Constraints

To eliminate the tensile nodal forces along the stem, the longitudinal constraint (U3) was released by changing the rigid tie constraint to a kinematic coupling constraint. This led to the same constraints along the flange and stem (i.e., U1, U2, UR1, UR2, and UR3 coupled); see

Figure 3-11. These updated boundary conditions were applied to the same beam as described in Section 3.2.4.1, and the same analysis was completed.

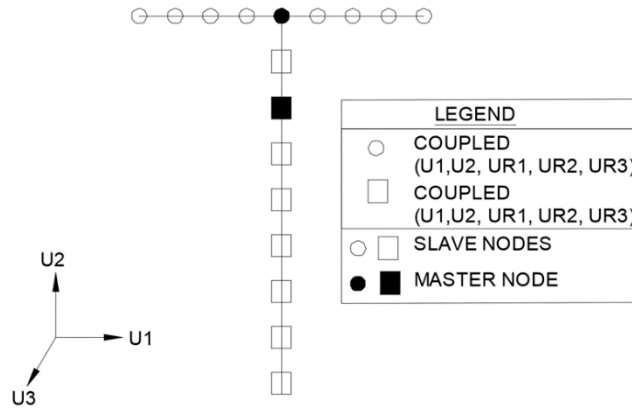


Figure 3-11: Updated Constraints

The vertical reactions at the supports are correctly determined as 450 kN, as seen in Figure 3-12, due to a 900 kN point load applied at the mid-span of the beam.

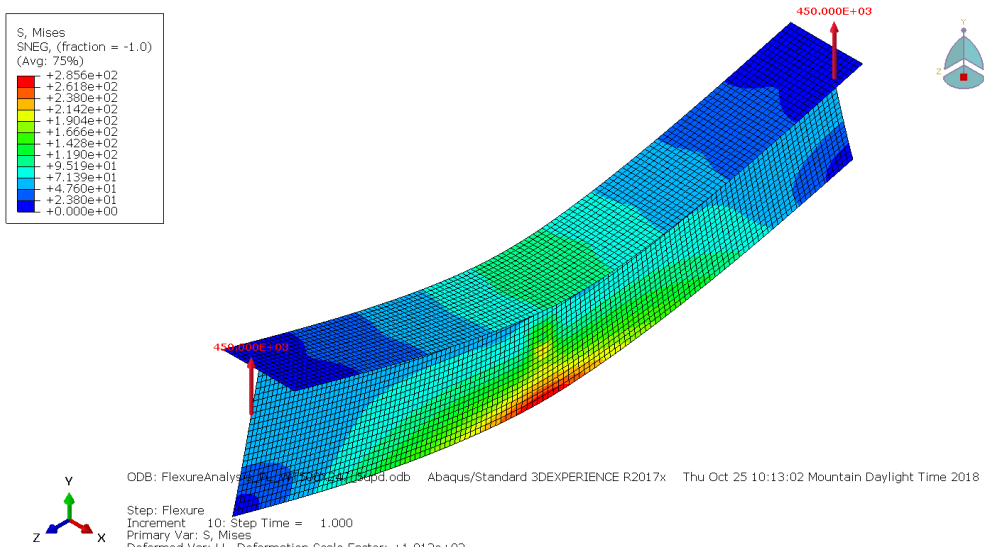


Figure 3-12: Overall Beam Subjected to a Mid-span Point Load with Updated End Constraints

The resultant nodal forces were again determined for the flange and stem. Figure 3-13 confirms the vertical force is correctly determined as 450 kN, as shown in Equation 3-3, but there are still equal and opposite horizontal forces for the flange and stem nodes.

$$444 \text{ kN} + 6 \text{ kN} = 450 \text{ kN} \tag{3-3}$$

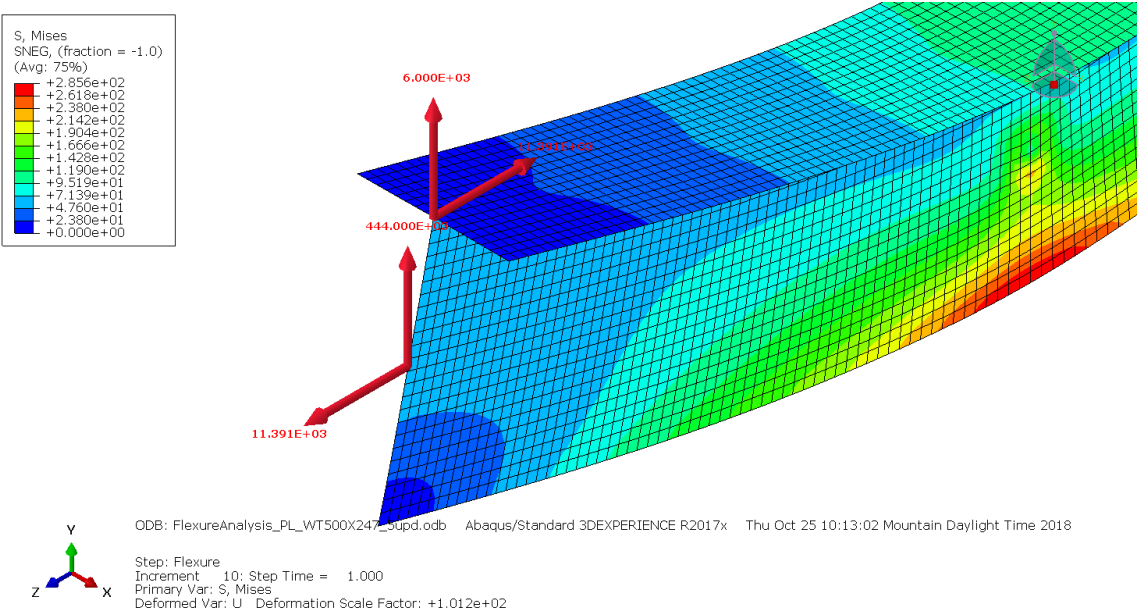


Figure 3-13: Resultant Forces for the Flange and Stem of the Beam with Updated Constraints

To better understand where the forces originated from, the forces were extracted at only the centre flange node (Figure 3-14) and top stem node (Figure 3-15).

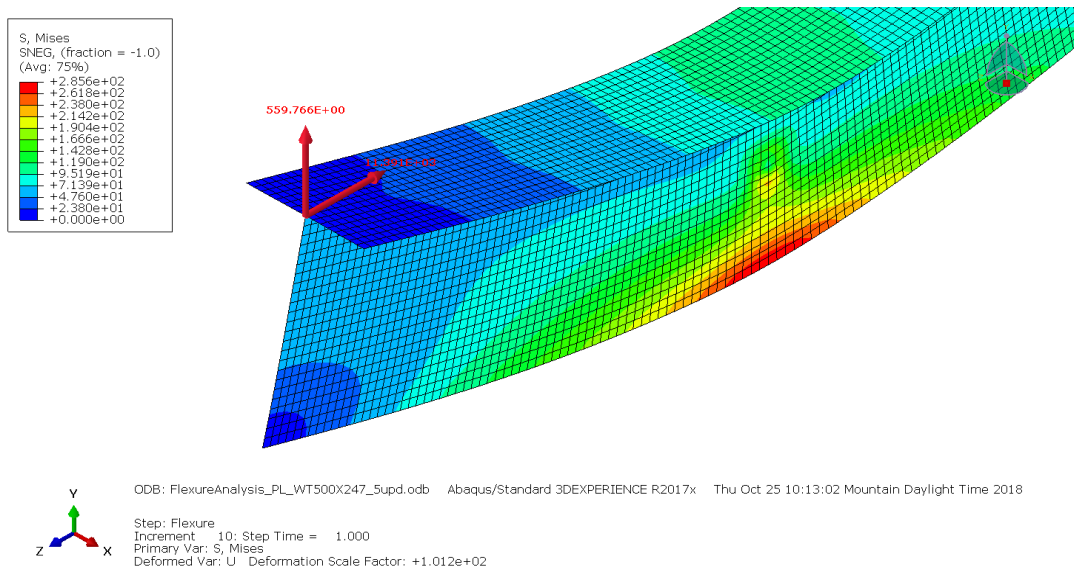


Figure 3-14: Nodal Forces of the Centre Flange Node of the Beam with Updated Constraints

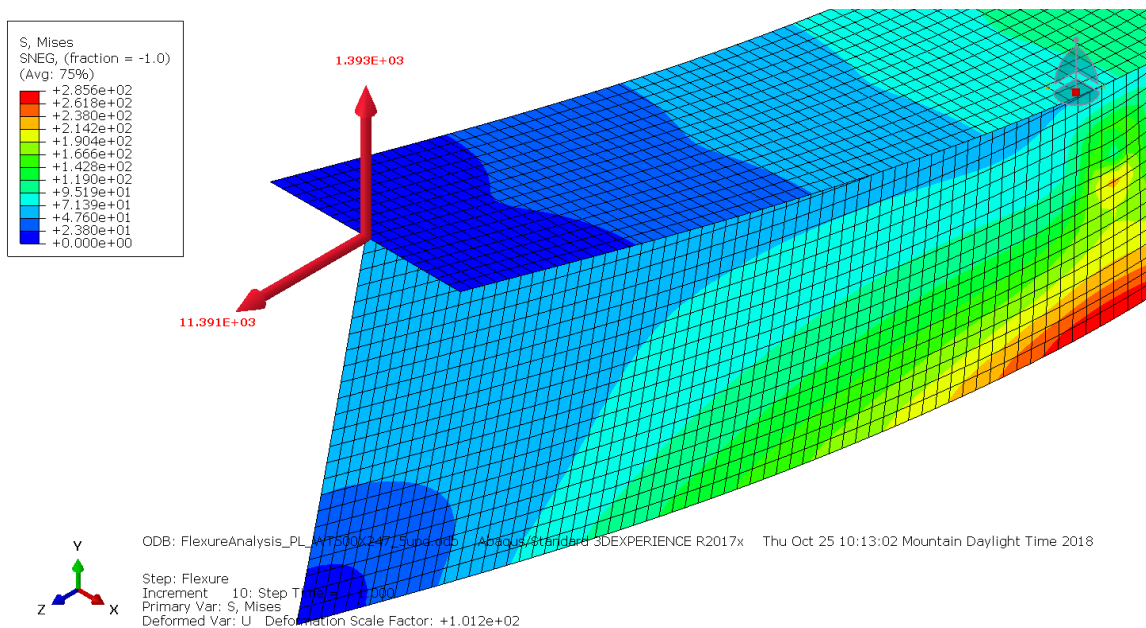


Figure 3-15: Nodal Forces of the Top Stem Node of the Beam with Updated Constraints

Similar to the original constraints, the only horizontal nodal force for the flange acted at the centre flange node, but the exclusion of the kinematic coupling constraint of the stem nodes in

the longitudinal direction revealed a nodal force at the top stem node that was equal to the nodal force at the centre flange node.

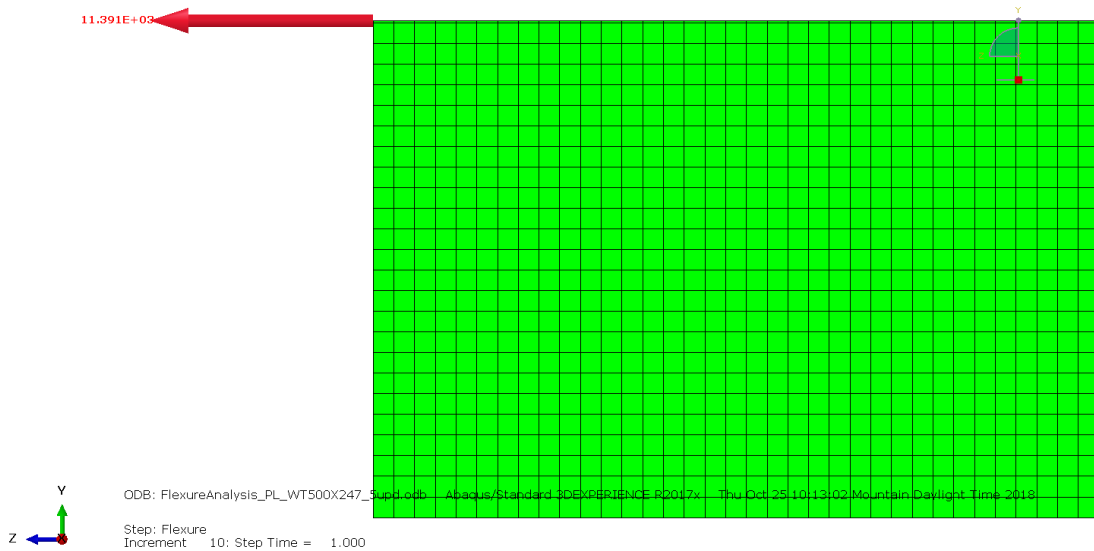


Figure 3-16: Stem Nodal Forces with Updated Constraints

For added confidence, the nodal forces were again extracted at all the nodes. Figure 3-16 confirms that the only stem nodal force originates from the flange–stem interaction. This is acceptable because when all the elements surrounding the flange–stem interaction node are selected, there are no horizontal forces produced at the ends of the beam.

The comparison between the original and updated constraints led to the preferred use of the updated constraints, which are further validated later using experimental results.

3.2.5 Methods of Analysis

Two types of analysis are available in ABAQUS to determine the elastic critical lateral–torsional buckling moment: buckling analysis and Riks analysis. Both are used in this research to determine the buckling load.

3.2.5.1 Buckling Analysis

Buckling analysis, otherwise known as eigenvalue analysis, was performed to determine the buckling shape as well as the buckling load. This is completed using a linear perturbation

procedure. These results are used for two purposes: (1) compare the buckling load results to the classical solutions (e.g., LTBeam results) for cross-validation, which can be used to validate the computational model (presented in Section 5.2.3), and (2) define initial imperfections based on buckling shapes when running a static Riks analysis.

3.2.5.2 *Riks Analysis*

Riks analysis is a nonlinear solver based on displacement control with an arc-length algorithm and the capability to simulate the post-buckling response. The load–deflection curve derived from structural analysis can be used to determine the buckling load for the beam with the inclusion of initial geometrical imperfection and residual stresses. The definition of initial geometrical imperfection and residual stresses in ABAQUS are elaborated in the following sections.

3.2.6 Initial Geometrical Imperfections

In order to introduce an initial geometrical imperfection to the Riks analysis, a buckling analysis was run to determine the beam’s buckled shape and the first positive buckling mode was used to apply the imperfection shape. In this study an imperfection of $L/1500$ was applied, where L is the length of the beam. The decision to use $L/1500$ was based on the competing arguments that were made during the creation of the SSRC column buckling curves: (1) The maximum imperfection of $L/1000$ is a reasonable yet conservative value to develop the column buckling curves, (2) the geometric imperfection is small enough to be accounted for within the resistance factor, and (3) an intermediate position that falls between the two extremes. The SSRC recommended that a geometric imperfection of $L/1500$ be used in the creation of steel column buckling curves since the average imperfection of many laboratory columns was approximately $L/1500$ (Ziemian 2010). Since the maximum imperfection allowed in the S16-14 is $L/1000$, the same reasoning can be applied to lateral–torsional buckling research and an initial imperfection equal to $L/1500$ was applied to the beams analyzed.

The imperfection shape is scaled according to the scaling factor as follows. The buckling analysis normalizes the maximum displacement component to a unit displacement (Ellobody et

al. 2014) and the scaling factor determines the numerical value of the displacement and is applied to every node in the model prior to performing the Riks analysis. It is imperative to ensure the model for buckling analysis and the model for Riks analysis are identical, since the initial geometrical imperfection is applied at the specific node.

3.2.7 Residual Stresses

Residual stresses can be included by defining predefined stress fields in ABAQUS; however, they first have to be modified from their original form. Figure 3-17 shows a possible residual stress pattern for a T-shaped beam in the dotted line. The residual stress pattern had to be modified to be entered into ABAQUS since the stress is applied over the width of an element. If a beam is divided into 10 elements over the width and 10 elements over the height of the beam, the residual stress can be averaged over the width of each element to obtain the ABAQUS residual stress pattern.

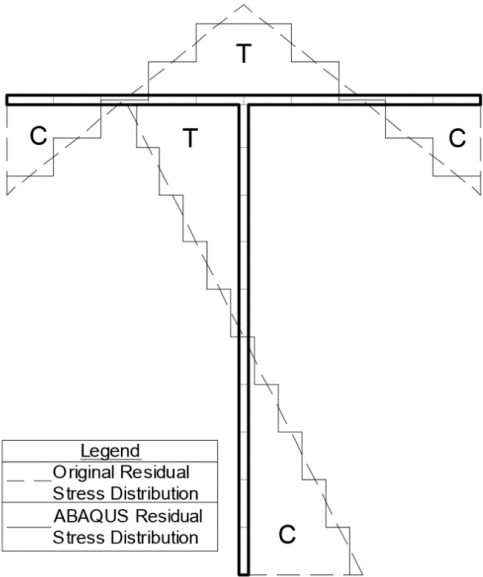


Figure 3-17: Original Residual Stress Distribution and ABAQUS Residual Stress Pattern

Linear residual stress patterns can be averaged over the element width with relative ease. With non-linear residual stress patterns, special care has to be taken to ensure the residual stress pattern entered into ABAQUS is in equilibrium to ensure no additional unexpected forces are

applied to the beam. The influence of residual stresses on inelastic LTB behaviour is discussed in Section 6.2.1.

3.3 Validation

The model was validated against LTB tests from Nagoya University (Fukumoto et al. 1980). This test programme was selected, as sufficient information was published to develop a detailed model. Twenty-five beams were tested for each length—2.6m, 2.0m and 1.5m—for a total of 75 tests and one load–displacement curve was reported for each length. The beams were tested with a vertical point load applied at the midspan of the compression flange. The test beams are doubly-symmetric I-shaped beams with dimensions of 200mm (section depth) x 100mm (flange width) x 5.5mm (web thickness) x 8mm (flange thickness). The material properties were obtained from coupon tests: the modulus of elasticity is 201.7 GPa, the yield stress of the flange plates is 252 MPa, and the yield stress of the web plate is 287 MPa. Geometrical imperfections corresponding to the 95th percentile of the measured value were applied, as $L/5000$, where L is the beam length. The geometrical imperfection is only one-fifth of the permissible initial imperfections. Residual stress measurements were also reported as part of the experimental programme, as shown in Figure 3-18.

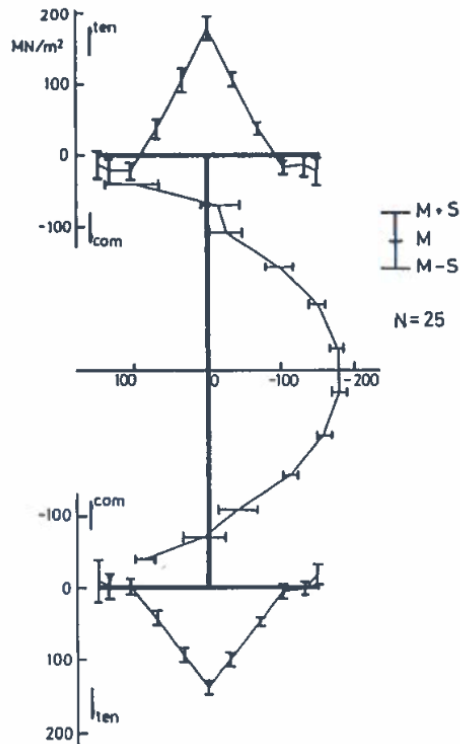


Figure 3-18: Reported Residual Stress Distribution (Fukumoto et al. 1980)

The mean residual stress pattern was used to convert the reported residual stresses to constant stresses over the width of the elements for use in the validation models.

Numerical results from models using the original and updated constraints were compared to the test results. This was necessary, as during the preliminary elastic LTB analysis it was determined that the updated constraints did not perform well for constant moments due to the way constant moment is applied and they were subsequently revised to the original constraints. As discussed in Section 3.2.3, a constant moment is equally applied by use of force couples at the beam ends and not by end moments. When end moments are applied, the longitudinal DOF of the stem node needs to be rigidly tied. Otherwise, when the force couples are applied at the beam ends, a concentrated tensile force applied at the bottom of the stem can cause significant element distortion. Thus, the original constraints were implemented for the constant moment condition to avoid extreme distortion of the stem locally, without affecting the global behaviour, and the updated constraints were implemented for the point load and UDL conditions.

3.3.1 Original Constraints

The numerical model with the original constraints was validated using the three reported load–deflection curves of Fukumoto et al. (1980). The comparison of the load–deflection curves obtained from the experimental tests and the finite element models is shown in Figure 3-5, where δ_H is the horizontal deflection of the extreme fibre of the top flange, and δ_V is the vertical deflection of the centre of the bottom flange at the mid-span of the beam.

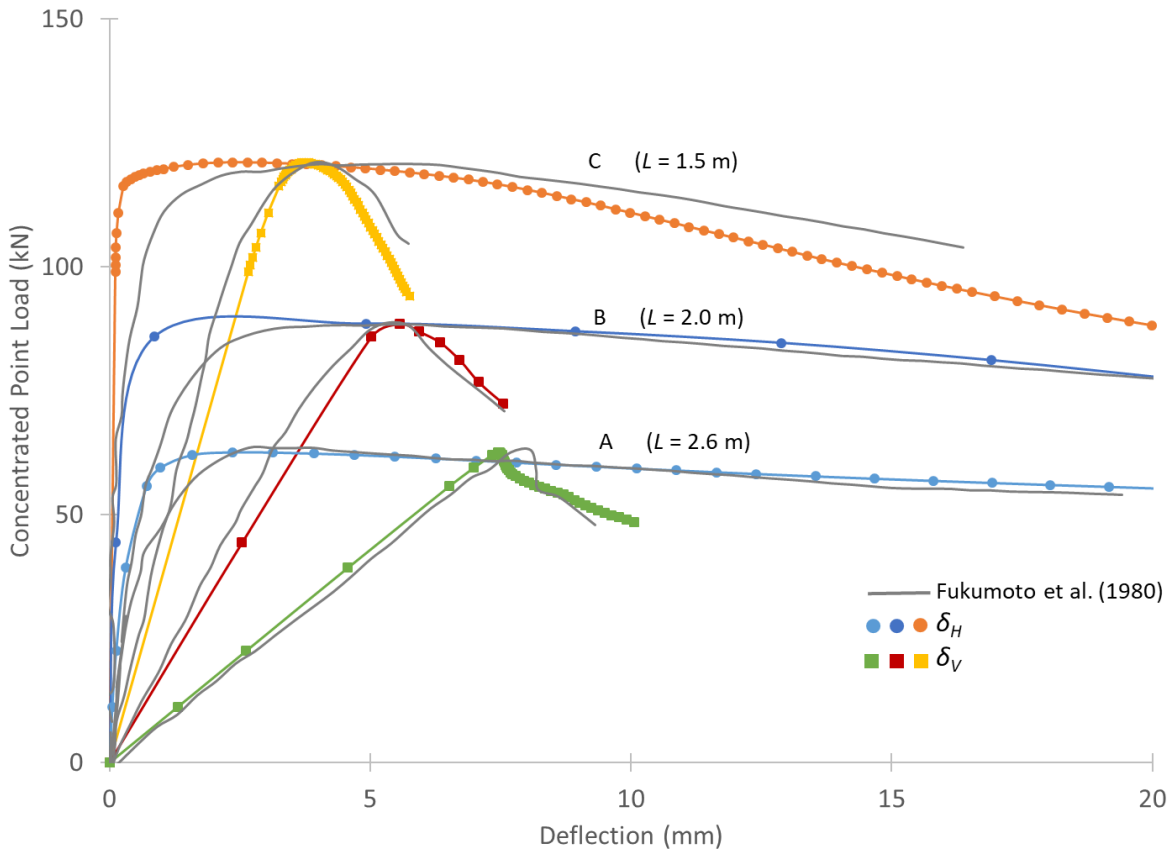


Figure 3-19: Comparison of the Load–Deflection Curves from Experiments and Finite Element Models with Original Constraints—Point Load

Table 3-1 shows the comparison of the buckling loads from experiments and finite element models with original constraints.

Table 3-1: Comparison of the Buckling Loads from Experiments and Finite Element Models with Original Constraints: Point Load Condition

Beam Length	Test Result (kN)	FEA Result (kN)	Difference (%)
1560 mm	120	121.1	0.89
2060 mm	87.5	88.48	1.12
2660 mm	68.5	62.56	-8.66
		Mean	-2.22
		Standard Deviation	0.056

3.3.2 Updated Constraints

The numerical model with the updated constraints was validated using the three reported load–deflection curves of Fukumoto et al. (1980). The comparison of the load–deflection curves obtained from the experimental tests and the finite element models is shown in Figure 3-11, where δ_H and δ_V are the horizontal and vertical displacements as defined in Section 3.3.1.

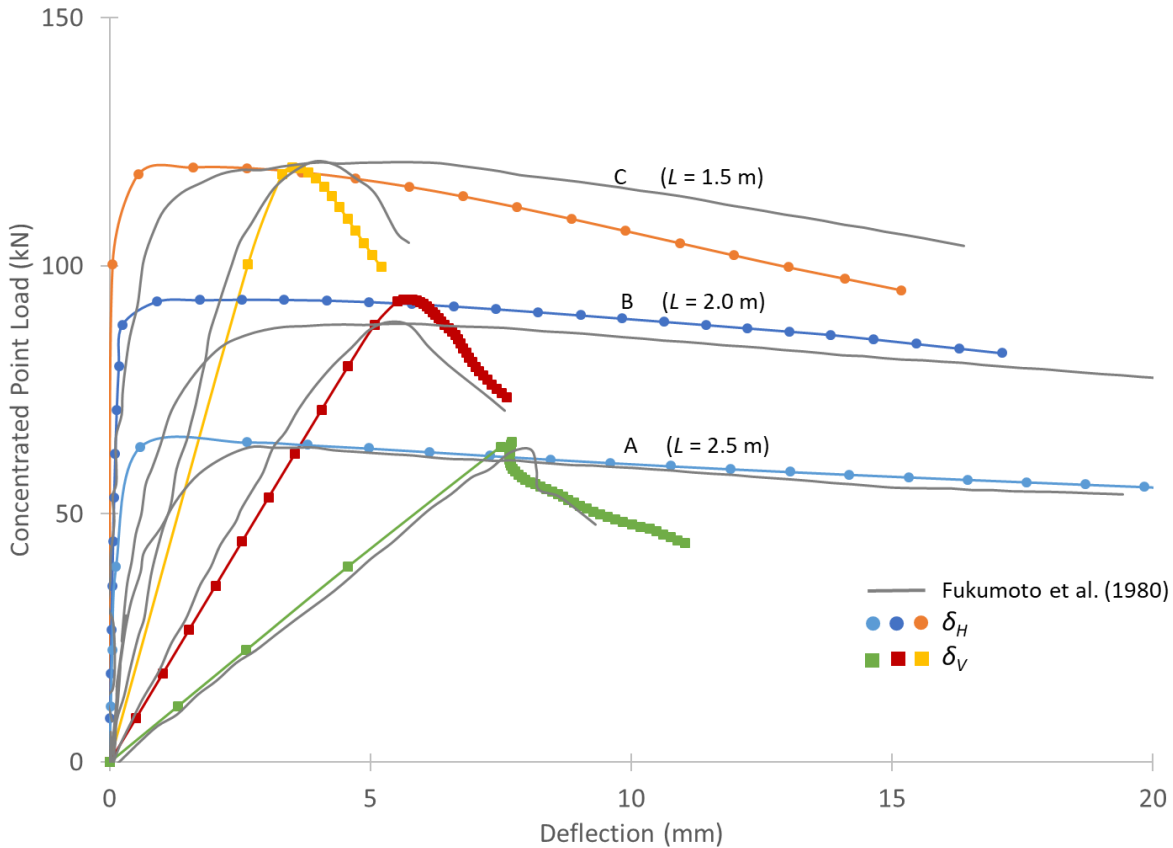


Figure 3-20: Comparison of the Load-Deflection Curves from Experiments and Finite Element Models with Updated Constraints—Point Load

Table 3-2 shows the comparison of the buckling loads from experiments and finite element models with updated constraints.

Table 3-2: Comparison of the Buckling Loads from Experiments and Numerical Models with Updated Constraints: Point Load Condition

Beam Length	Test Result (kN)	FEA Result (kN)	Difference (%)
1560 mm	120	119.9	-0.11
2060 mm	87.5	93.20	6.51
2660 mm	68.5	64.46	-5.89
		Mean	0.17
		Standard Deviation	0.062

3.3.3 Validation Discussion

Figure 3-19 and Figure 3-20 show the comparison of the load–deflection curves obtained from the experimental tests and the finite element model. The comparison displays a reasonably good correlation between the numerical prediction and experiment measurements. Although the validation proved that both constraints provide reasonably good correlation for doubly-symmetric I-shaped beams, the constraints are extended to T-shaped beams due to the lack of experimental data. To ensure accuracy due to the extension, the constraints were thoroughly investigated to ensure that the global results correlated well with experimental results, while maintaining internal stresses consistent with the defined boundary conditions as explained in Section 3.2.4.1 and Section 3.2.4.2. The initial stiffness is either slightly over-estimated or under-estimated, which may be due to the initial geometric imperfection assumed. The initial imperfection corresponding to the 95th percentile was reported as $L/5000$ without information on the imperfection distribution along the beam. In the numerical analysis, an initial imperfection is thus assumed to take the same shape as the first eigen-buckling mode with a maximum lateral displacement of $L/5000$. Overall, both constraint configurations can reasonably predict the LTB behaviour of doubly symmetric I-shaped beams, and thus the original constraints can be used to predict the LTB behaviour of T-shaped beams under a constant moment and the updated constraints can be used to predict the LTB behaviour of T-shaped beams under a point load and UDL as studied in this work.

3.4 Conclusions

Various aspects of the finite element model for numerical analysis to determine the elastic critical moment against LTB are addressed in this chapter. The model validation was completed using experimental results for doubly-symmetric I-shaped beam tested by Fukumoto et al. (1980). The boundary conditions in the validation model are then applied to T-shaped beams due to a lack of corresponding experimental data. To bridge the gap between doubly-symmetric I-shaped beams and T-shaped beams, the elastic LTB analysis was completed using both the finite element model and a freely available software to further validate the model as discussed in Chapter 5.

CHAPTER 4: NUMERICAL TEST SECTIONS

4.1 Introduction

A comprehensive numerical investigation is performed to study the elastic critical moment of T-shaped beams subject to three different load conditions (i.e., point load at midspan, UDL, and constant moment). A representative test matrix was determined using a subset of all T-shaped beams cut from standard wide-flange shapes (WT-sections) by eliminating sections that had similar sectional properties. The chosen sections were then used throughout the entirety of the numerical simulations—both in the elastic and inelastic LTB regions.

4.2 Test Matrix

The WT-sections are selected from the 283 WT-sections available in the AISC online Shapes Database (AISC 2017). The AISC online shapes database was chosen because the CISC does not have a shapes database that can be downloaded with the necessary sectional properties and there are more shapes in the AISC online database than in the CISC Handbook of Steel Construction (CISC 2017). This allows for a wider range of sections to be analyzed. Additionally, the AISC database provides the metric equivalent shape dimensions and section properties. Of the 283 WT-sections, 178 are considered potentially susceptible to the failure mode of LTB considering the second moment of area about the strong axis (I_x) must be greater than the second moment of area about the weak axis (I_y).

The section candidates susceptible to LTB are first grouped into class 1, 2, and 3 sections based on the classification criteria in S16 for elements in flexural compression using a yield stress of 345 MPa (CSA 2014). Since the flange is the element in compression, only the flange is classified. There are 162 class 1 sections, 13 class 2 sections, and three class 3 sections. To obtain good coverage, 6% of the class 1 sections, 15% of the class 2 sections and 33% of the class 3 sections were chosen for analysis.

The chosen sections vary in depth from 150 to 550mm and 100 to 470mm in width. The stem thickness varies from 6 to 77mm and the flange thickness varies from 8 to 115mm. WT-sections are selected based on section classes, top flange thickness and width, stem thickness and depth,

area moment of inertia, and minimum slenderness ratio for global elastic LTB. There are many different slenderness ratios that can be considered using parameters that influence LTB (e.g., torsional stiffness, lateral stiffness, etc.); however, in this study the minimum slenderness ratio is defined as the minimum ratio between the beam length (L) and the section depth (d), commonly referred to as the span-to-depth ratio, for the beam to be susceptible to elastic LTB assuming the beam is subjected to a constant moment and including the effect of residual stresses by limiting the maximum elastic LTB to 0.7 times the yield moment as per CSA S16 §13.6 e) (2014).

A subset of the sections is selected to cover the range of section properties and minimum slenderness ratios for global elastic LTB (referred to as min L/d in Table 4-1). This resulted in a total of 18 sections. The selected sections, and their geometric properties, are shown in Table 4-1.

Table 4-1: Test Matrix Including Relevant Geometric Properties

Section	min L/d	b_f (mm)	t_f (mm)	d (mm)	w (mm)	I_x $\times 10^6$ (mm ⁴)	Z_x $\times 10^3$ (mm ³)	S_x $\times 10^3$ (mm ³)	I_y $\times 10^6$ (mm ⁴)	J $\times 10^3$ (mm ⁴)	C_w $\times 10^9$ (mm ⁶)	I_y/I_x
<u>Class 1 Sections</u>												
WT100×11	127	102	8	103	6.22	1.37	31.3	17.5	0.708	28.3	0.0103	0.52
WT265×109	244	318	29.2	279	18.3	84.9	695	388	78.3	3200	8.73	0.92
WT265×184	392	325	50.5	302	27.9	153	1240	661	145	16700	43.8	0.95
WT305×70	83	230	22.2	310	13.1	77.4	592	333	22.7	1090	2.57	0.29
WT305×186	292	335	48	335	26.4	199	1420	773	151	13800	44.3	0.76
WT345×274	312	373	63	386	35.1	391	2470	1340	273	35200	143	0.70
WT345×401	407	389	89.9	414	50	637	3970	2100	441	103000	467	0.69
WT380×194	193	386	41.9	401	23.6	318	1840	1020	200	11200	49.4	0.63
WT420×236	181	406	48	447	26.4	483	2520	1410	268	17500	90	0.55
WT460×393	229	437	73.9	505	40.9	1020	4880	2690	516	67800	430	0.51
WT460×688	300	472	115	549	76.7	2140	10100	5520	1030	294000	2600	0.48
WT500×124	46	300	26.2	490	16.5	374	1880	1040	58.7	2910	16.9	0.16
WT500×247	83	310	54.1	518	31	783	3790	2100	134	21900	130	0.17
WT500×488	209	429	89.9	554	50	1550	6980	3840	599	122000	857	0.39
WT550×171	68	401	31	546	18	599	2570	1450	166	5160	37.3	0.28
<u>Class 2 Sections</u>												
WT155×19	135	165	9.65	155	5.84	4.87	68.8	39.3	3.6	62.4	0.0467	0.74
WT380×73	48	267	17	376	13.2	134	891	492	26.6	783	3.84	0.20
<u>Class 3 Sections</u>												
WT265×36	53	207	10.9	262	8.89	31.2	292	162	8.07	166	0.408	0.26

Figure 4-1 to Figure 4-4 show all the section candidates (denoted as open markers) and the sections selected (denoted as closed markers) with section classes differentiated by shapes. These plots indicate the selected sections have good coverage of top flange width and thickness, stem depth and thickness, second moments of area I_x and I_y , minimum slenderness ratio for global elastic LTB and section depth.

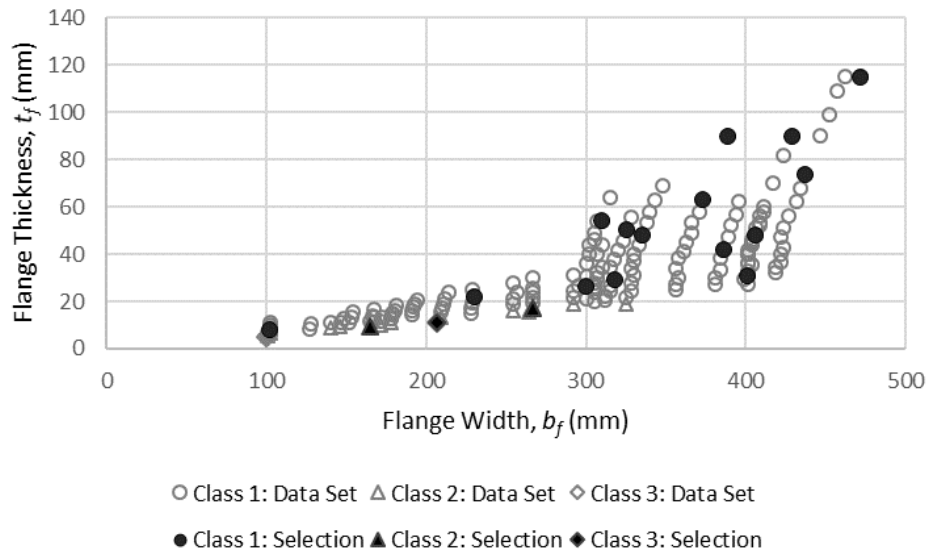


Figure 4-1: Section Candidates vs Sections Selected: Top Flange

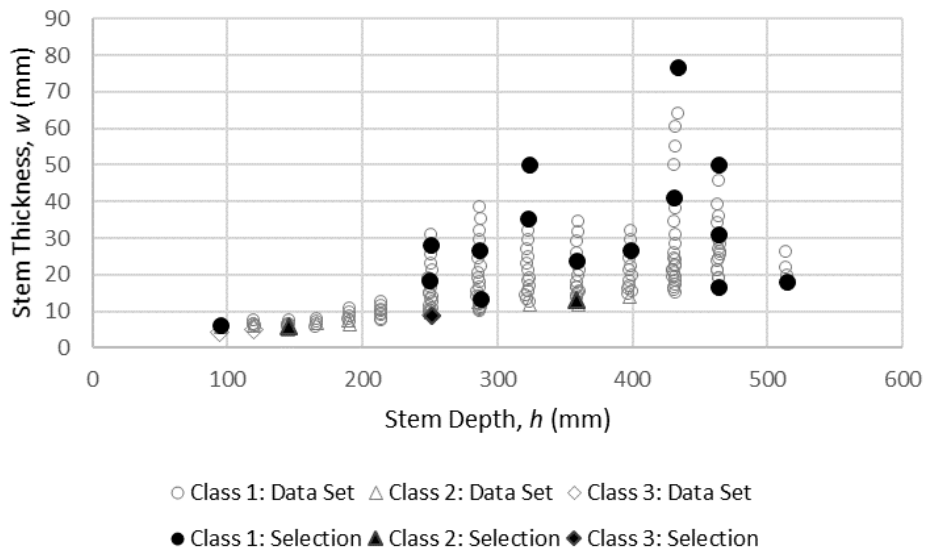


Figure 4-2: Section Candidates vs Sections Selected: Stem

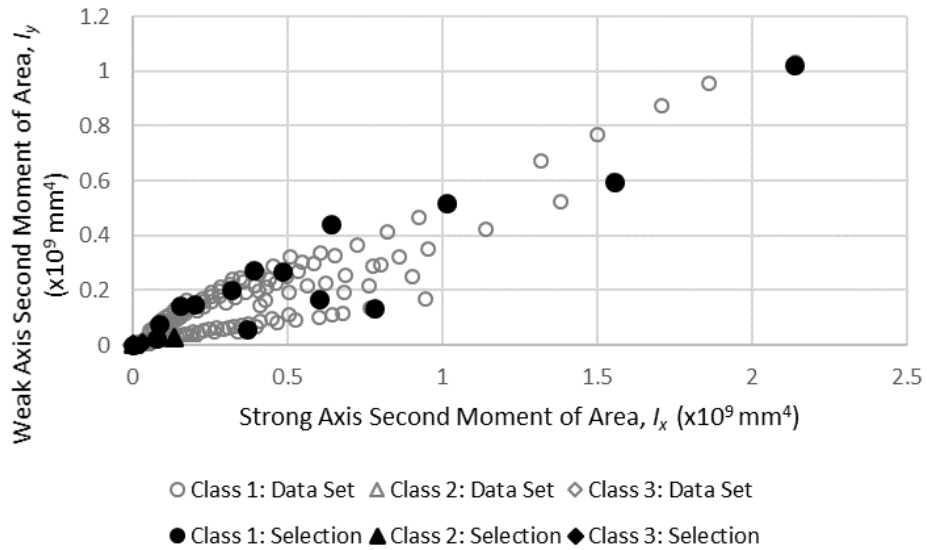


Figure 4-3: Section Candidates vs Sections Selected: Second Moment of Area

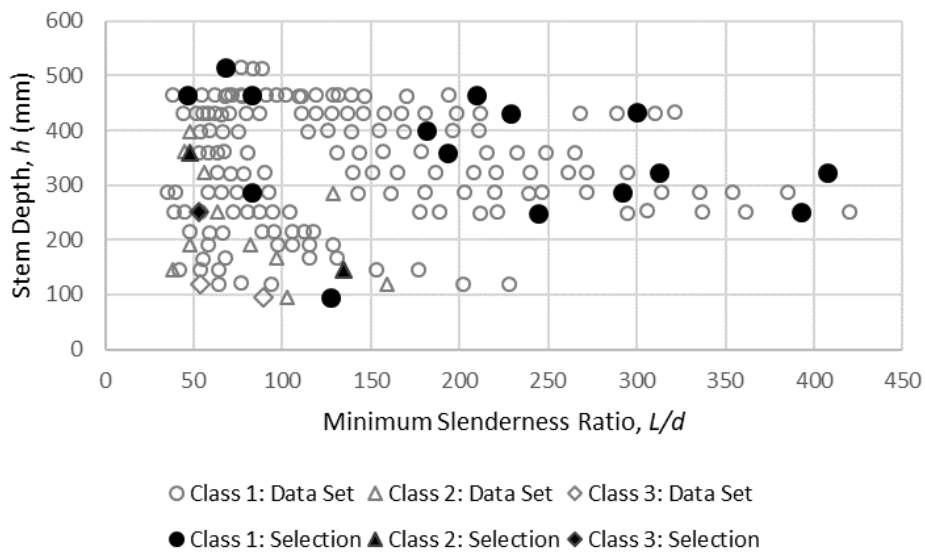


Figure 4-4: Section Candidates vs Sections Selected: Minimum Slenderness Ratio for Global Elastic LTB

Figure 4-4 depicts the minimum slenderness ratio for elastic LTB to occur. The minimum slenderness ratios—ranging from 35 to 420—are extremely large and would not normally be used in design. The slenderness ratio was included in the selection of the test matrix to capture a wide variety of sections in the elastic range. The slenderness ratios used for the elastic LTB

analysis were calculated by applying a hypothetical moment gradient factor of 1.7 (and rounded up to the nearest integer divisible by 5) to ensure all the beams were in the elastic LTB region. It was hypothesized that the moment gradient factors would be close to those proposed by Wong and Driver (2010); however, the factor was increased beyond the values hypothesized to account for values greater than expected. This led to the slenderness ratios shown in Table 4-2.

Table 4-2: Test Section Beam Slenderness Ratios

Section	L/d
WT100×11	225
WT155×19	230
WT265×36	90
WT265×109	410
WT265×184	685
WT305×70	140
WT305×186	490
WT345×274	525
WT345×401	680
WT380×73	80
WT380×194	325
WT420×236	305
WT460×393	385
WT460×688	505
WT500×124	80
WT500×247	145
WT500×488	355
WT550×171	115

Slenderness ratios of 5, 10, 20 and 30 were chosen for the analysis of inelastic sections. These slenderness ratios are chosen to represent cases that would most likely be used in the design of structures and façades.

4.3 Conclusions

T-sections were selected by section class, then were selected based on the flange width, flange thickness, stem depth, stem thickness, major axis moment of inertia, and minor axis moment of inertia. Ultimately, eighteen sections were selected to represent the T-sections listed in the AISC

shapes database. The sections are used for the elastic and inelastic LTB analyses to achieve a balance between the computational costs associated with modelling and analyzing as well as good coverage of the section properties of all possible sections.

CHAPTER 5: ELASTIC LATERAL–TORSIONAL BUCKLING

5.1 Introduction

The LTB design equations in both CSA S16 and AISC 360 neglect the moment gradient effect by using a moment gradient factor $\omega_3 = 1$ when determining the critical moment for T-shaped beams in single curvature. This inherently conveys that WT-sections do not abide by the same LTB principles as W-sections and singly symmetric I-shaped sections because these moment gradient factors use a quarter point method, as shown in Equation 5-1.

$$\omega_2 = \omega_3 = \frac{4M_{max}}{\sqrt{M_{max}^2 + 4M_a^2 + 7M_b^2 + 4M_c^2}} \quad (5-1)$$

where M_a , M_b and M_c are the moments at one-quarter, half and three-quarter points of the beam segment, respectively, and M_{max} is the maximum moment along the beam segment. Therefore, this chapter addresses the current strength predictions by CSA S16-14 and AISC 360-16 of T-shaped beams subject to constant moment, point load, and UDL loading scenarios. The numerical test sections discussed in Chapter 4 and slenderness ratios provided in Table 4-2 are analyzed in the elastic LTB region using two different software—LTBeam and ABAQUS.

5.2 LTBeam

LTBeam is a freely available software (CTICM 2001) that is used to calculate the elastic critical moment by solving the classic eigenvalue problem using an iterative dichotomic process without considering initial imperfections. This tool has been validated by other analysis tools (e.g., ANSYS). With a maximum difference of only 1.48% between LTBeam and ANSYS in predicting the elastic critical moments for six T-shaped beams (CTICM 2002). As such, LTBeam can be used to predict the elastic critical moment, as stated in the NCCI, which provides guidance not given in the Eurocode (Bureau 2008).

5.2.1 LTBeam Results

The moment gradient factor, ω_3 , is determined as the ratio of the elastic critical moment of a beam subject to a specific loading condition (e.g., point load or UDL) to that of a beam with a constant moment. Using, Equation 5-1 proposed by Wong and Driver (2010), the moment

gradient factor is 1.26 for a point load condition, as shown in Equation 5-2, and 1.13 for a UDL condition, as shown in Equation 5-3.

$$\omega_{3,\text{point load}} = \frac{4M}{\sqrt{M^2 + 4\left(\frac{M}{2}\right)^2 + 7M^2 + 4\left(\frac{M}{2}\right)^2}} = 1.26 \quad (5-2)$$

$$\omega_{3,\text{UDL}} = \frac{4\left(\frac{wL^2}{8}\right)}{\sqrt{\left(\frac{wL^2}{8}\right)^2 + 4\left(\frac{3wL^2}{32}\right)^2 + 7\left(\frac{wL^2}{8}\right)^2 + 4\left(\frac{3wL^2}{32}\right)^2}} = 1.13 \quad (5-3)$$

where M is the maximum moment in a beam subject to a point load and w is the UDL density along the length of the beam, denoted as L . The elastic critical moments determined using LTBeam are utilized to calculate the moment gradient factors, as reported in Table 5-1.

Table 5-1: Moment Gradient Factors Based on Eigenvalue Analysis in LTBeam

Section	ω_3 Constant Moment	ω_3 Point Load	ω_3 UDL
WT100×11	1.00	1.35	1.13
WT155×19	1.00	1.36	1.13
WT265×36	1.00	1.33	1.11
WT265×109	1.00	1.35	1.13
WT265×184	1.00	1.35	1.13
WT305×70	1.00	1.35	1.12
WT305×186	1.00	1.35	1.13
WT345×274	1.00	1.35	1.13
WT345×401	1.00	1.35	1.13
WT380×73	1.00	1.32	1.11
WT380×194	1.00	1.35	1.13
WT420×236	1.00	1.35	1.13
WT460×393	1.00	1.35	1.13
WT460×688	1.00	1.35	1.13
WT500×124	1.00	1.33	1.11
WT500×247	1.00	1.35	1.12
WT500×488	1.00	1.35	1.13
WT550×171	1.00	1.34	1.12
Mean		1.35	1.12
Standard Dev.		0.01	0.01

From Table 5-1, it is observed that eigenvalue analysis gives ω_3 for the point load scenario as 1.35 and for the UDL scenario as 1.12. Both the point load and UDL scenarios results are tightly grouped with very small standard deviations (less than 0.01).

5.2.2 Comparison to Design Standards

The ω_3 value for a point load ($\omega_3 = 1.35$) is 6.3% larger than the value obtained using Equation 5-1. It should be noted that the ω_3 value was initially reported as 1.35 for a point load at the midspan of the beam with simply supported boundary conditions and calculated using a program written in Fortran (Nethercot and Rockey 1971). With the introduction of Equation 5-1 by Wong and Driver (2010), the conservatism was deemed an acceptable compromise for the improvement of other loading scenarios that previously produced erroneous results. Additionally, $\omega_3 = 1.12$ for a UDL, which is 0.6% smaller than the value obtained using Equation 5-1.

The ratio of moments determined using LTBeam to the corresponding S16-14 elastic LTB moments, including the moment gradient factor for the point load scenario (presented in Equation 5-2) and the UDL scenario (presented in Equation 5-3) for each beam are shown in Figure 5-1. When the ratio is greater than 1.0, the S16-14 elastic LTB moment is smaller than the LTBeam elastic LTB moment and thus deemed conservative for use in design, and when the ratio is less than 1.0, the S16-14 elastic LTB moment is larger than the LTBeam elastic LTB moment and thus deemed unconservative. The same scale is used for Figure 5-1, Figure 5-3, and Figure 5-4 for consistency.

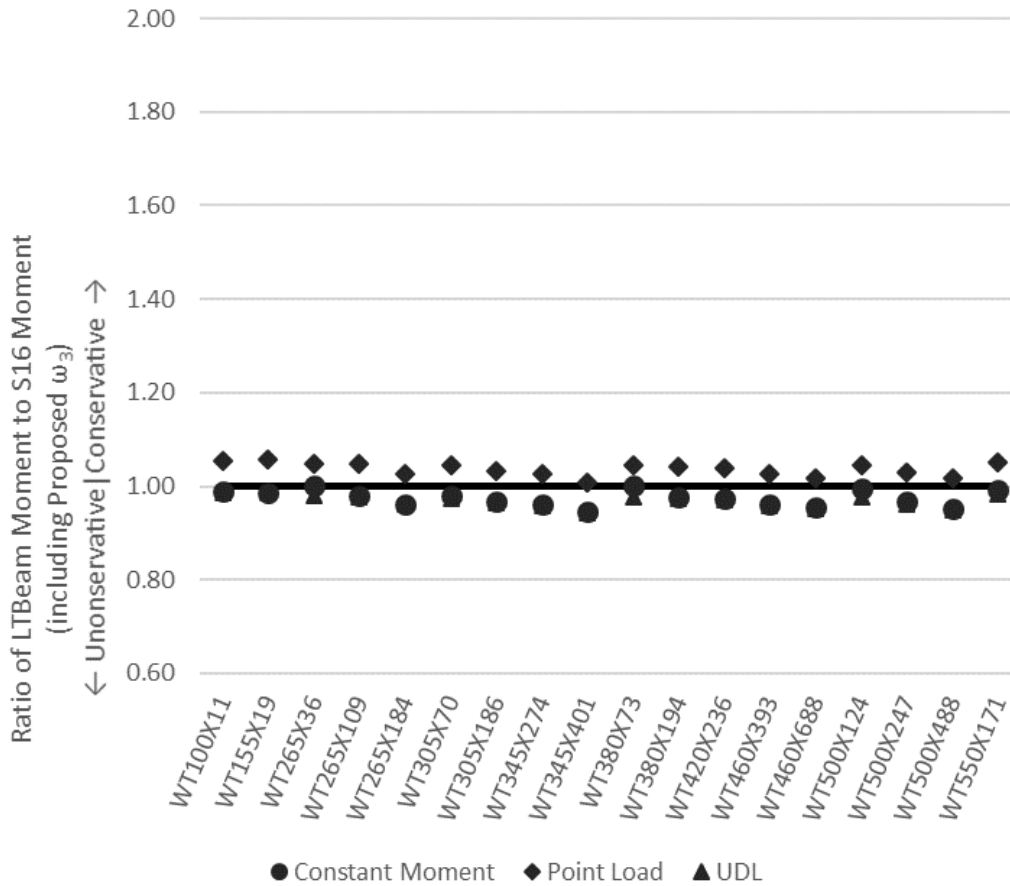


Figure 5-1: Comparison of LTBeam Moments to S16-14 Moments Including Proposed Moment Gradient Factors

As seen in Figure 5-1, the S16-14 elastic LTB moments vary from about 0.94 to 1.06 times the LTBeam elastic LTB moments with a standard deviation of 0.03. With the inclusion of ω_3 , S16-14 adequately predicts the elastic LTB moment when compared to LTBeam.

5.2.3 Additional Model Validation

The initial validation was completed using doubly-symmetric tests (see Section 3.2) and then the finite element model was utilized for T-sections, leaving an apparent gap in the validation protocol. To bridge this gap, the results from LTBeam were compared to the eigenvalue buckling analyses from ABAQUS. The LTBeam and ABAQUS analyses were completed for each section with a point load applied at the midspan, mid-height of the beam.

Table 5-2: LTBeam vs ABAQUS Buckling Analysis Moment Capacities (Point Load)

Section	Slenderness Ratio (L/d)	LTBeam (kNm)	ABAQUS Buckling (kNm)	ABAQUS <u>Buckling</u> LTBeam
WT100×11	225	3.1	3.1	1.01
WT155×19	230	7.1	7.2	1.01
WT265×36	90	27.7	29.2	1.06
WT265×109	410	72.3	72.5	1.00
WT265×184	685	117.9	117.5	1.00
WT305×70	140	61.1	62.5	1.02
WT305×186	490	144.4	144.2	1.00
WT345×274	525	248.7	247.9	1.00
WT345×401	680	388.1	385.6	0.99
WT380×73	80	86.0	91.0	1.06
WT380×194	325	189.8	190.6	1.00
WT420×236	305	262.3	263.4	1.00
WT460×393	385	495.2	494.7	1.00
WT460×688	505	1016.1	1005.6	0.99
WT500×124	80	177.1	185.1	1.05
WT500×247	145	370.6	373.6	1.01
WT500×488	355	697.6	695.6	1.00
WT550×171	115	259.0	267.3	1.03
	Mean			1.01
	Standard Dev.			0.02

It can be seen that the critical moments from LTBeam and ABAQUS—using eigenvalue buckling—have good correlation, as shown in Table 5-2. ABAQUS produced results that are, on average, 1.3% larger than the results of LTBeam, with a standard deviation of 0.02. The analysis showed that the ABAQUS buckling critical moments are similar to those from LTBeam and provided additional confidence that the ABAQUS model estimates the elastic critical moments of T-shaped beams accurately.

5.3 Finite Element Modelling

The Riks analysis in ABAQUS provided the load–deflection curve, i.e., the load versus the lateral deflection at the mid-height of the stem at the midspan of the beam. To calculate the maximum moment, the lateral displacement at the maximum load from the load–deflection curve

is used to determine the corresponding moment at that lateral displacement using the moment–deflection curve.

5.3.1 Load–Deflection Curves

The load–deflection curve, which is usually employed to determine the LTB critical moment, behaves nonlinearly due to the initial geometric imperfection and the nonlinear geometric stiffness. The slope of the load–deflection curve is an equivalent (generalized) stiffness to resist LTB. For example, if the load–deflection curve starts to soften, the capability to resist LTB starts to degrade. A common practice is to define the critical load corresponding to zero slope, and the maximum associated moment in the vertical plane is regarded as the critical moment. The moment gradient factor, ω_3 , is determined for the point load and UDL scenarios using the moments obtained from Riks analysis in ABAQUS.

The load–deflection curves for a WT420×236 section and a slenderness ratio (length/height) of 305 are plotted in Figure 5-2 (a), (b) and (c) for the load scenarios of a constant moment, a point load, and a UDL, respectively. The moment–deflection curves for these three load scenarios are shown in Figure 5-2 (d). Note that the vertical axis in Figure 5-2 (a) is the constant moment, while in Figure 5-2 (b) and (c) the vertical axes are the total load applied. The moment plotted in Figure 5-2 (d) is at the midspan of the beam, which, due to symmetry, is the maximum moment on the span. The three loading scenarios are included in Figure 5-2 (d) to identify their relative effects.

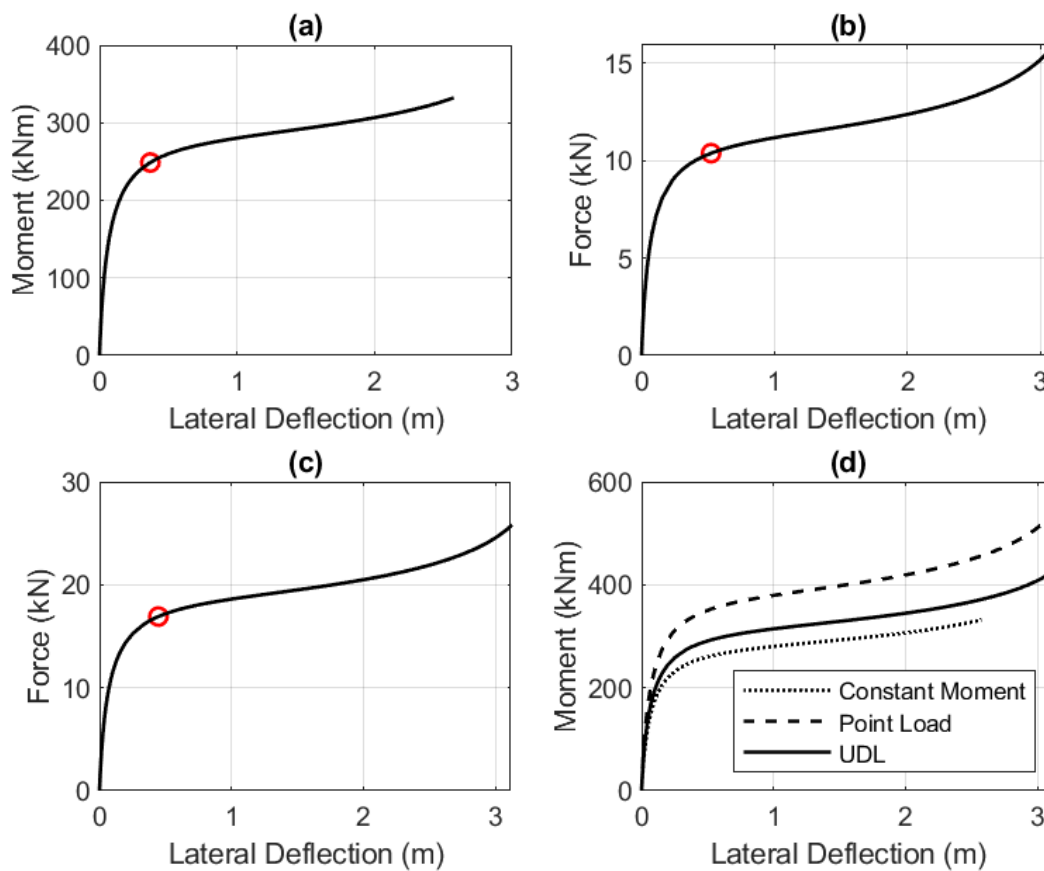


Figure 5-2: Load–Deflection Curves for Beams with a WT420×236 Section: (a) Constant Moment; (b) Point Load; (c) UDL; and (d) Moment–Deflection Curves for all Three Loading Scenarios.

Figure 5-2 does not include the initial imperfections in the lateral displacement. The initial lateral deflection for this beam is 91mm (or 0.091m). The initial geometric imperfection accounts for 17% to 25% of the lateral displacement at the critical state for this section. The initial geometric imperfection can account for up to 50% of the lateral displacement in some of the sections studied (excluding the beams with a snap-back behaviour, which is discussed below). When the load–displacement curves for the beams considered were analyzed, it was found that the slopes rarely approached zero (i.e., 100% stiffness loss), even with a large vertical deflection (e.g., 25% of the length). In this study, a stiffness loss of 97.5% of the initial stiffness is considered the critical state. This point is denoted by the red circles in Figure 5-2 (a), (b) and (c). To determine the critical moment, the lateral deflection at the critical load is recorded and the corresponding moment at the recorded lateral deflection is the associated critical moment.

Two beams (i.e., WT265×109 and WT265×184) exhibited a so-called “snap-back” behaviour in the load–deflection curves, i.e., the deflection starts to decrease with the increase of load after a certain deflection. These two beams have the largest ratios of I_y to I_x of the sections tested. The ratios of I_y to I_x are 0.92 and 0.95 for a WT265×109 and WT265×184 section, respectively and the third largest was 0.76. It was observed that the beams exhibited small lateral deflections as the ratio of I_y to I_x approached 1.0. At the snap-back point, the beam rotates in a swing like motion around the axis formed by a straight line through the two support locations. Along with the ratio of I_y to I_x , this swing like motion is due to the internal tension force developed in the member because of the vertical deflections which leads to a new equilibrium path and therefore the beam no longer experiences LTB. Although many different parameters were varied in an effort to remain on the original equilibrium path, the analysis continued to exhibit this snap-back behaviour. The results were omitted for the two beams that exhibited this behaviour because although the beam has experienced some lateral deflections, LTB has not occurred. Except the two beams discussed above, the critical points are determined following the above algorithm (i.e., 97.5% stiffness loss).

5.3.2 Analyses and Results

The maximum stress was below the yield stress at the point of elastic LTB for all the beams that experienced LTB. The moment gradient factors based on the Riks analysis in ABAQUS are presented in Table 5-3. The mean moment gradient factors are 1.36 and 1.15 for a point load and a UDL, respectively. As previously stated, the reference values from Equation 5-1 are 1.26 and 1.13 (see Equation 5-2 and Equation 5-3 for the specific calculations). Thus, ω_3 for a point load scenario is 5.4% larger, and ω_3 for a UDL scenario is 0.9% larger than the values from Equation 5-1.

Table 5-3: Moment Gradient Factors Based on an ABAQUS Riks Analysis

Section	ω_3 for Constant Moment	ω_3 for Point Load	ω_3 for UDL
WT100×11	1.00	1.21	1.39
WT155×19	1.00	1.23	1.17
WT265×36	1.00	1.59	1.23
WT265×109*	-	-	-
WT265×184*	-	-	-
WT305×70	1.00	1.34	1.12
WT305×186	1.00	1.29	1.07
WT345×274	1.00	1.29	1.08
WT345×401	1.00	1.27	1.06
WT380×73	1.00	1.42	1.14
WT380×194	1.00	1.39	1.13
WT420×236	1.00	1.42	1.15
WT460×393	1.00	1.37	1.15
WT460×688	1.00	1.33	1.26
WT500×124	1.00	1.42	1.16
WT500×247	1.00	1.37	1.13
WT500×488	1.00	1.34	1.09
WT550×171	1.00	1.43	1.14
Mean		1.36	1.15
Standard Dev.		0.09	0.08

* denotes snap-back behaviour

5.3.3 Comparison to Design Standards

The ratio of the ABAQUS moments including geometrical imperfections to S16-14 elastic LTB moments, including the proposed moment gradient factor for the point load scenario (presented in Equation 5-2) and the UDL scenario (presented in Equation 5-3), for each beam are shown in Figure 5-3. When the ratio is greater than 1.0, the S16-14 elastic LTB moment is smaller than the ABAQUS elastic LTB moment and thus deemed conservative and when the ratio is less than 1.0, the S16-14 elastic LTB moment is larger than the ABAQUS elastic LTB moment and thus deemed unconservative. The two beams that experienced the snap-back behaviour are labelled with an asterisk and thus have no associated values.

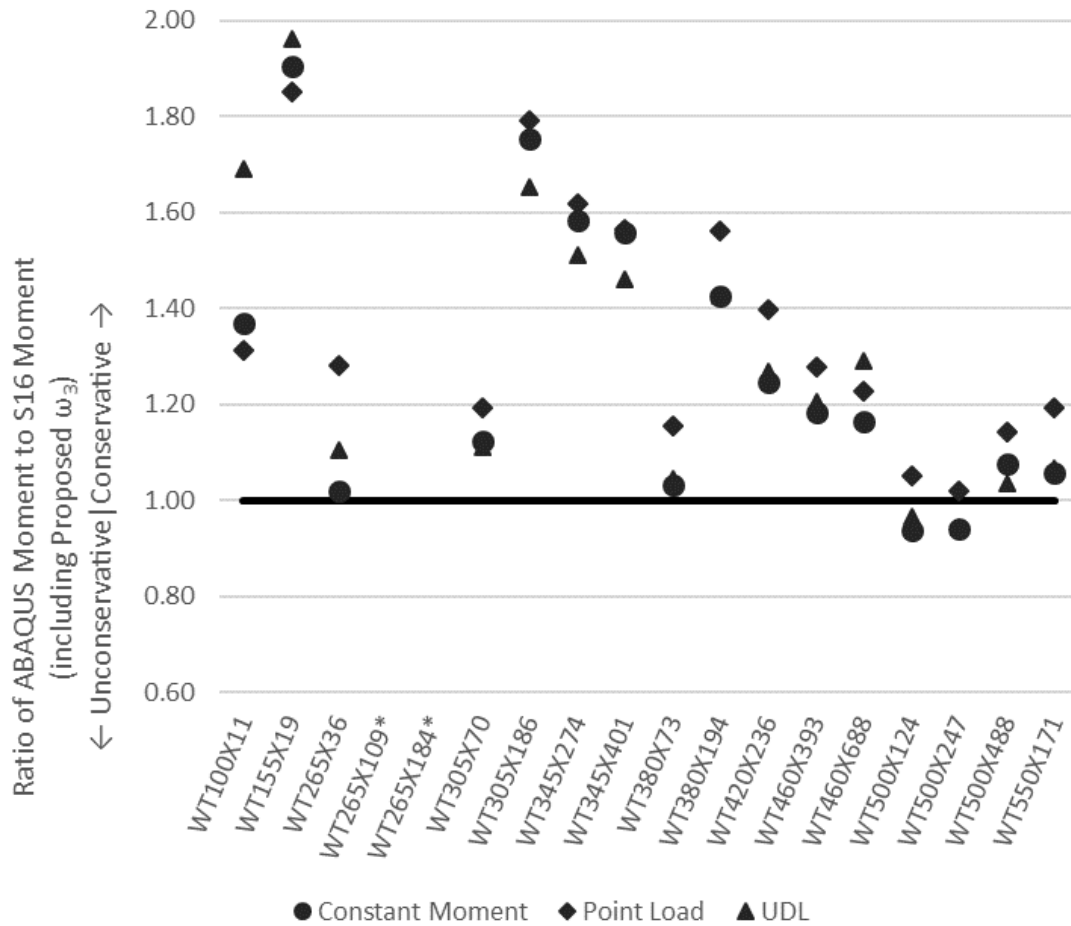


Figure 5-3: Comparison of Abaqus Results to S16-14 Moments Including Proposed Moment Gradient Factors (* denotes snap-back behaviour)

As seen in Figure 5-3, the ABAQUS elastic LTB moments vary from 0.94 to 1.96 times the S16-14 elastic LTB moments. Due to the nature of the load–deflection curves, shown in Section 5.3.1, the value that signified a significant stiffness loss (in this study 97.5% stiffness loss) indicates the level of conservatism in the elastic LTB moment prediction. The ABAQUS analysis shows that the CSA S16-14, including the proposed ω_3 factor, underestimates the elastic LTB moment. Figure 5-4 depicts the same ratio (ABAQUS moment to S16 moment including the proposed ω_3) as shown in Figure 5-3, but compares the ratio to the slenderness ratio.

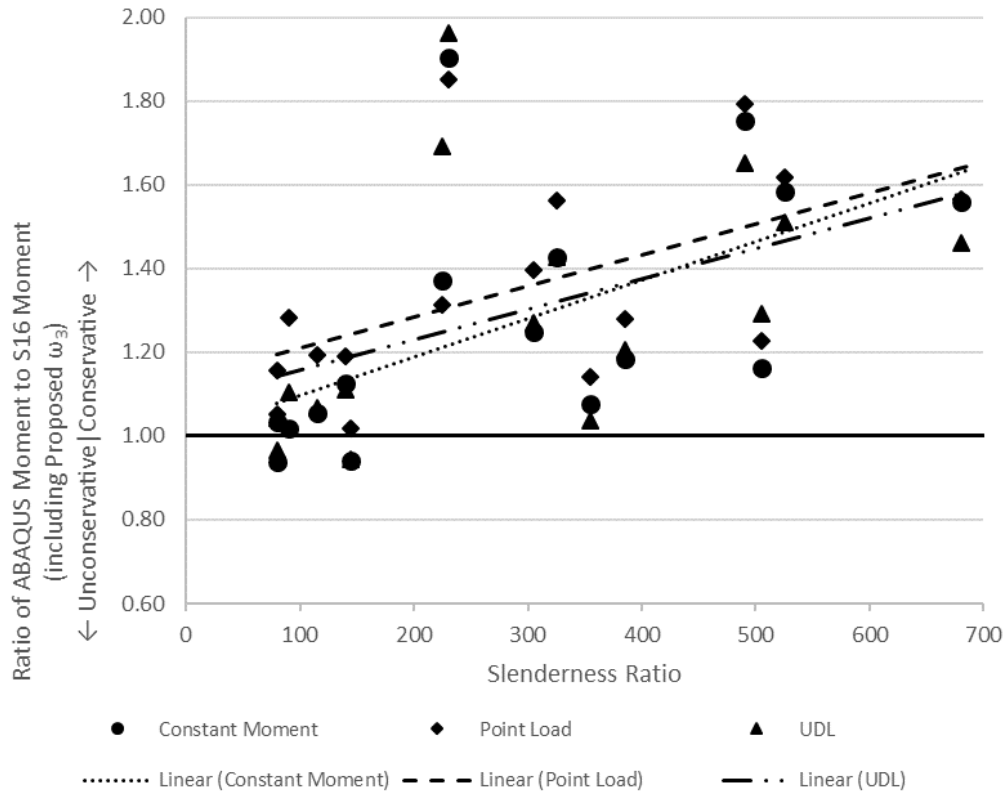


Figure 5-4: Ratio of Abaqus Results to S16-14 Moments Including Proposed Moment Gradient Factors Compared to the Slenderness Ratio

Figure 5-4 shows that as the slenderness ratio increases, the moment ratio becomes increasingly conservative. Beams of these slenderness ratios are impractical and thus the large conservatism is not a concern. By addressing the conservatism, there would be minimal to no change in the inelastic LTB range because the slenderness ratios for practical beams would appear in the uppermost range of inelastic LTB resulting in a minimal contribution from the elastic LTB moment. For beams of practical length refer to Chapter 6.

5.4 Discussion

There is a larger dispersion in ω_3 obtained from the Riks analysis in ABAQUS when compared to ω_3 from eigenvalue analysis in LTBeam. This is partly due to the initial geometric imperfection considered and the algorithm used to determine the critical point and thus the elastic critical moment. Eigenvalue analysis in LTBeam determines the elastic critical moment

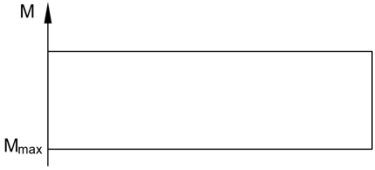
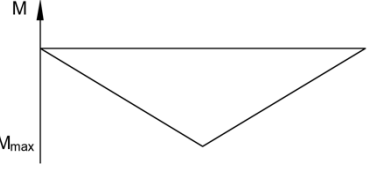
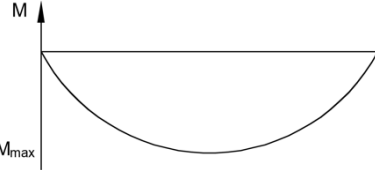
using the system of equations from the first principles of buckling. Due to the mathematical nature, the results are not influenced by other factors. The Riks analysis in ABAQUS uses an equilibrium path to determine the elastic critical moment of the beam, in which the effect of initial geometric imperfection and non-linear geometry is considered.

The results from eigenvalue analysis and Riks analysis both confirm that the moment gradient for T-shaped beams has similar effects to doubly- and singly-symmetric I-shaped beams. The beams analyzed would be uneconomical in practice as they are overly slender; however, the elastic critical moment is required to calculate the inelastic LTB moment in the design process. Further analysis needs to be performed to evaluate the adequacy of Equation 5-1 for inelastic LTB, since the elastic LTB moment is used to calculate the inelastic LTB moment.

5.5 Design Recommendations

S16-14 and AISC 360-16 steel design standards recommend a moment gradient factor of 1.0 for T-shaped beams. Both LTBeam and ABAQUS resulted in values that correlate well with the equation of Wong and Driver (2010). It is recommended that the Wong and Driver (2010) moment gradient values be adopted for T-shaped beams with the flange in compression. The updated recommendations can be seen in Table 5-4.

Table 5-4: Moment Gradient Factor Recommendations

Moment Distribution	LTBeam	ABAQUS	$\omega_3 = \frac{4M_{max}}{\sqrt{M_{max}^2 + 4M_a^2 + 7M_b^2 + 4M_c^2}}$
	1.00	1.00	1.00
	1.35	1.36	1.27
	1.12	1.15	1.13

The increase in the moment gradient factors from the value of 1.0 currently used in design, is related to a proportional increase in the critical moment for elastic LTB. This allows designers to design more efficient T-shaped beams. Although the moment gradient factor captures the effect of the moment distribution in the elastic LTB range, the elastic LTB moment is also used to calculate the inelastic LTB moment. To ensure that the recommended moment gradient factor does not lead to unconservative results in the inelastic LTB range, the inelastic LTB moment is determined in the following chapter.

5.6 Summary

The current moment gradient factor, $\omega_3 = 1$, tends to be overly conservative for T-shaped beams susceptible to elastic LTB in the CSA S16 and AISC 360 when the top flange is in compression. It was observed that the moment gradient factors for T-shaped beams depend on the moment distribution and are comparable to the moment gradient factors used for doubly-symmetric and singly-symmetric I-shaped beams. The results presented here show that the moment gradient factor is 1.36 for a point load at the midspan and 1.15 for UDL.

CHAPTER 6: INELASTIC LATERAL–TORSIONAL BUCKLING

6.1 Introduction

The majority of T-shaped beams used in practice are not susceptible to elastic LTB and instead need to be checked for either inelastic LTB or cross-sectional moment capacity. CSA S16 and AISC 360 use similar equations to determine the inelastic LTB moment capacity; however, the standards have different cross-sectional capacities for T-shaped beams. This chapter aims to study the inelastic LTB behaviour of T-shaped beams.

Prior to analyzing T-shaped beams in the inelastic LTB region, a study was completed to determine the effect of residual stresses in the inelastic LTB region for T-shaped beams. Residual stresses are introduced into beams during the fabrication phase through cutting and/or welding of the beam. In the aforementioned I-shaped beams, residual stresses are expected to affect the LTB moment significantly in the inelastic range, particularly for the beams with LTB moments between 0.6 and 0.85 times the cross-sectional capacity. Residual stresses are not as influential below the ratio of 0.6, as the beam is expected to fail in elastic LTB and above the ratio of 0.85 the beam approaches the cross-sectional capacity and is minimally affected by residual stresses. However, the effect of residual stresses on the inelastic LTB capacity of T-shaped beams remains unclear and thus are clarified in this chapter.

6.2 Finite Element Modelling

6.2.1 Effect of Residual Stresses

A study was undertaken to determine the effect of residual stresses on the LTB critical moment considering the following three cases:

1. Without residual stresses
2. With residual stresses, assuming the residual stress model proposed by Kitipornchai and Lee (1986a) (see Section 2.3.4.2)
3. With residual stresses, assuming the residual stress model proposed by Nagarajao Rao et al. (1964) (see Section 2.3.4.1)

The two residual stress patterns studied have similar residual stress distributions in the flange, although the peak residual stress values are significantly different. The distributions are vastly different in the stem. Figure 6-1 (a) shows the residual stress pattern proposed by Kitipornchai and Lee (1986a), where the tip of the stem is in compression then reverses into tension as it approaches the flange. On the other hand, the residual stress pattern shown in Figure 6-1(b), proposed by Nagarajao Rao et al. (1964), begins in compression, then oscillates between tension and compression. Nagarajao Rao et al. (1964) presented measured residual stress distributions for varying sized T-shaped beams. The residual stress pattern of the beam that was closest in size to the mean size of the selected sections was utilized for this analysis.

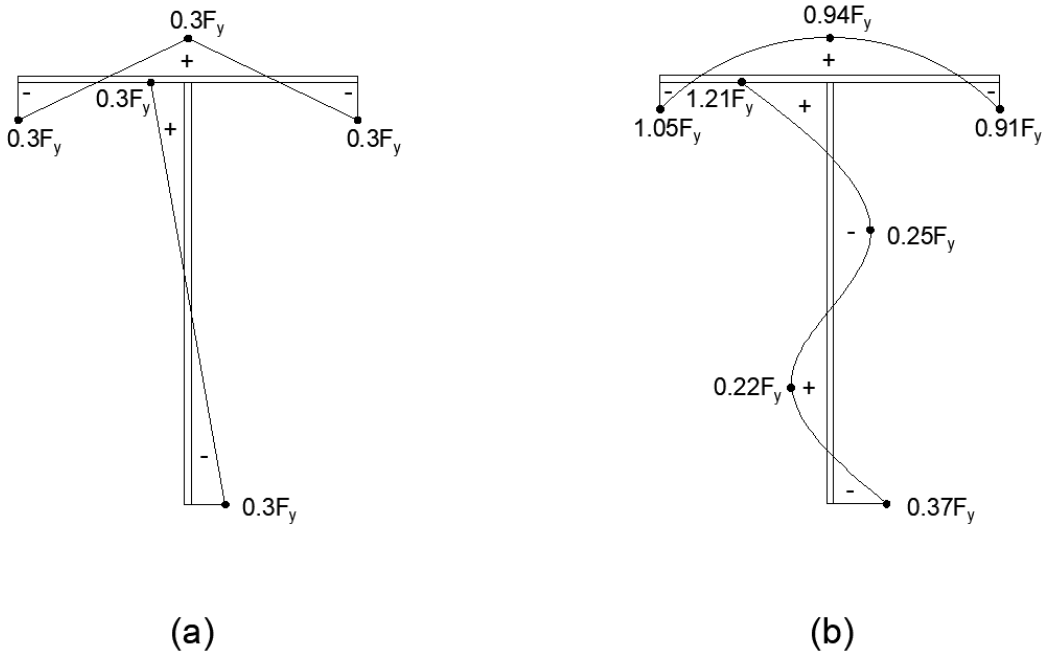


Figure 6-1: Residual Stress Patterns: (a) Kitipornchai and Lee (1986a); (b) Nagarajao Rao et al. (1964)

Based on doubly- and singly-symmetric I-shaped beams, residual stresses are expected to play a significant role when the ratio of the LTB moment to the cross-sectional moment ranges from 0.6 to 0.85. This range is supported by the data presented for an IPE 200 section in Figure 6-2.

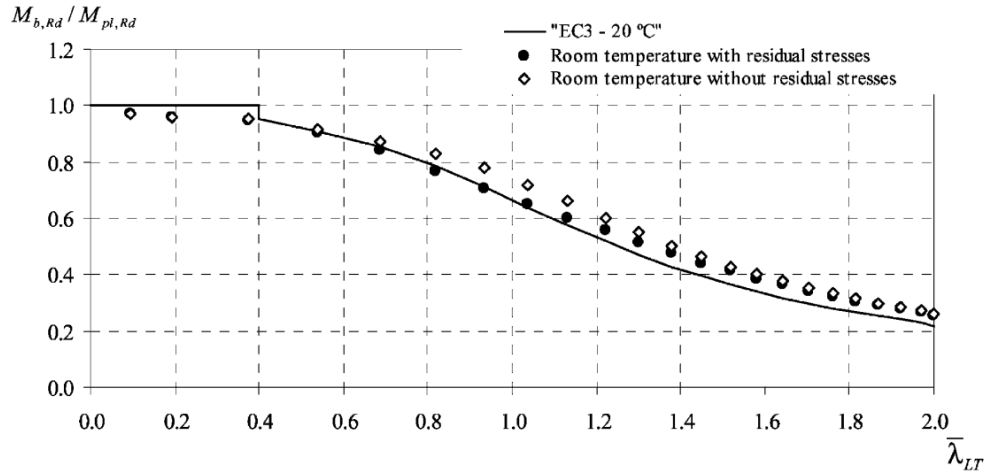


Figure 6-2: Finite Element Analysis Results for IPE 220 Section with and without Residual Stresses Compared to Eurocode LTB Design Curve (Vila Real et al. 2004)

As shown in Figure 6-2, the addition of residual stresses decreases the ratio of the LTB moment to the cross-sectional capacity ($M_{b,Rd}/M_{pl,Rd}$) most significantly between the ratios of about 0.6 to 0.85 for the IPE 220 section with varying non-dimensional slenderness ($\bar{\lambda}_{LT}$) studied by Vila Real et al. (2004). To determine the effect of residual stresses in T-shaped beams, it is assumed that the same range applies. Thus, the selected T-shaped beams of different slenderness ratios, where the ratio of the LTB moment to the cross-sectional capacity ranges from 0.6 to 0.85, were studied. The sections analyzed along with the slenderness ratio, defined as the ratio of length to section depth, the section classification and the LTB moment are summarized in Table 6-1.

Table 6-1: Inelastic LTB Moment Comparison for Beams with Various Residual Stress Patterns and Subjected to Three Loading Scenarios

Section (Slenderness Ratio) [Section Class]	Loading	$\frac{M_r}{M_p}$	No Residual Stress (kNm)	Kitipornchai & Lee (kNm)	Nagaraja Rao et al. (kNm)
WT305×70 (30) [Class 1]	Constant Moment	0.81	201.6	196.7	200.0
	Point Load	0.85	206.0	208.2	203.4
	UDL	0.84	202.1	211.2	200.9
WT380×73 (20) [Class 2]	Constant Moment	0.80	287.1	290.0	292.9
	Point Load	0.84	309.6	313.7	306.5
	UDL	0.82	302.5	318.7	302.5
WT380×73 (30) [Class 2]	Constant Moment	0.65	236.2	237.1	243.0
	Point Load	0.72	302.5	310.9	312.1
	UDL	0.68	284.0	262.1	286.0
WT500×124 (20) [Class 1]	Constant Moment	0.79	617.2	627.1	625.9
	Point Load	0.83	654.2	662.6	647.7
	UDL	0.81	639.2	670.2	636.8
WT500×124 (30) [Class 1]	Constant Moment	0.65	456.5	454.4	466.1
	Point Load	0.72	618.9	628.4	630.6
	UDL	0.68	535.0	529.1	543.5
WT500×247 (30) [Class 1]	Constant Moment	0.80	1264.3	1186.7	1220.9
	Point Load	0.85	1310.9	1361.9	1326.5
	UDL	0.83	1286.7	1317.2	1286.6
WT550×171 (30) [Class 1]	Constant Moment	0.77	855.5	856.2	860.8
	Point Load	0.81	887.5	900.4	881.3
	UDL	0.79	870.7	916.1	871.2

Comparing the results from the models with the residual stress patterns provided by Kitipornchai and Lee (1986a) and Nagaraja Rao et al. (1964) to the results from the models neglecting residual stresses, it was found that inclusion of residual stresses produced, on average, equal inelastic LTB moments (see Table 6-1). Specifically, the inelastic LTB moments after considering the residual stress patterns provided by Kitipornchai and Lee (1986a) varied from 0.92 to 1.05 times (mean value of 1.01) the inelastic LTB moments when neglecting residual stresses; the inelastic LTB moments after considering the residual stress patterns provided by

Nagaraja Rao et al. (1964) varied from 0.97 to 1.03 times (mean value of 1.00) the inelastic LTB moment when neglecting residual stresses. This outcome is different than the effect of residual stresses on singly- and doubly-symmetric I-shaped beams. The apparently negligible effect of residual stresses on the inelastic LTB capacity of T-shaped beams with the flange in compression is rationalized in the following discussion.

When a T-shaped beam is loaded in single curvature with the flange in compression, the stem is in tension due to flexural loading. Additionally, the centroid of the cross-section is located much closer to the flange than the bottom of the stem. This leads to significantly larger strains at the bottom of the stem than in the flange. Referring to Figure 6-1, there are compressive residual stresses at the bottom of the stem for both residual stress patterns. Since the bottom of the stem is the farthest point from the centroid, this is where the largest applied tensile strain is located due to the effects of loading. Since the bottom of the stem is initially in compression due to the presence of residual stresses, yielding of the stem tip is initially delayed. Additionally, due to the close proximity of the flange to the centroidal axis, only small strains develop in the flanges under the applied moment. Whereas doubly-symmetric sections tend to lose stiffness rapidly through early yielding of the compression flange in regions where compressive residual stresses were present, yielding generally does not occur in the flange of a T-section until the moment is very large.

Since the location of the neutral axis is different for each section, not all sections behave the same. Even identical beams subjected to different residual stress patterns experience stiffness loss at different rates in the flange and stem. Consequently, no single residual stress pattern always leads to the lowest LTB moment. It should also be noted that when residual stresses are introduced into ABAQUS, the analysis attempts to resolve the stresses and thus the results may vary slightly from the expected results. Considering the beam of a slenderness ratio of 20 with a WT500×124 section and subjected to a UDL, at the maximum LTB moment the strain along the stem and flange at the middle of the beam can be seen in Figure 6-3.

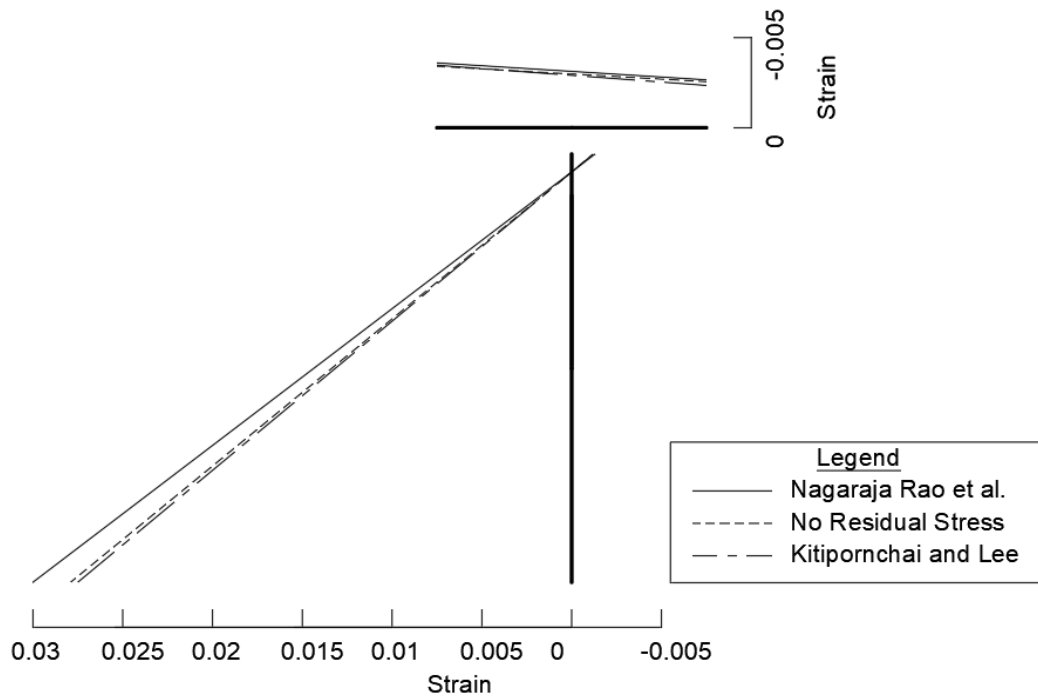


Figure 6-3: Strains at the midspan of a WT500×124 Beam with a Slenderness of 20 in the Stem and Flange at Maximum Moment

The WT500×124 section with a slenderness of 20 experienced the largest to smallest strains at the tip of the stem, and consequently the smallest to largest LTB moment, under the Nagaraja Rao et al. residual stress pattern, no residual stress, and Kitipornchai and Lee residual stress pattern, respectively.

Since the LTB moments obtained using models that neglect residual stresses are, on average, equal to the inelastic LTB moments obtained using models that include residual stresses, the following analysis is completed neglecting residual stresses.

6.2.2 Analyses and Results

The beams were analyzed for four slenderness ratios—5, 10, 20 and 30—and three loading configurations—constant moment, point load and UDL. An example of the load–deflection curves for a WT500×124 beam and a slenderness ratio of 30 can be seen in Figure 6-4. In Figure 6-4 (a) the vertical axis is the applied moment, the vertical axis in Figure 6-4 (b) and (c) is the

total applied load, and the vertical axis in Figure 6-4 (d) is the moment at the midspan of the beam.

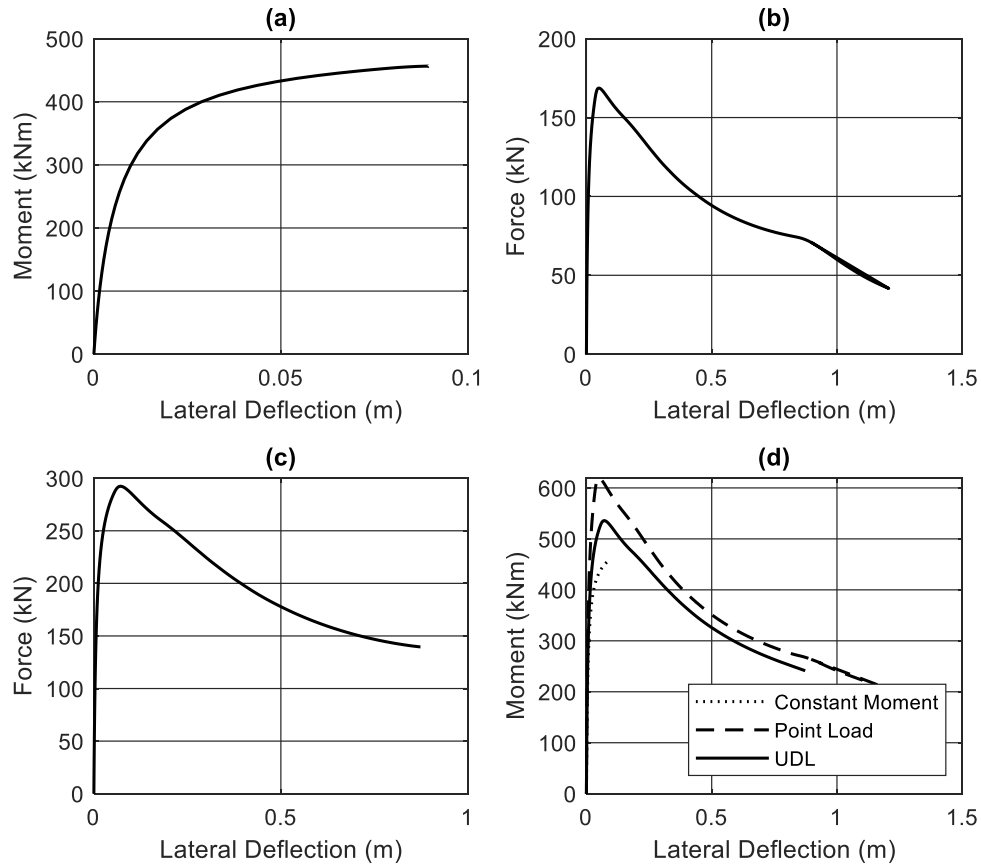


Figure 6-4: Load–Deflection Curves of a Beam with WT500×124 and Slenderness Ratio = 30: (a) Constant Moment; (b) Point Load; (c) UDL; and (d) Moment Deflection Curves for all Three Loading Scenarios.

It can be seen that the beam under constant moment loading does not experience a decrease in the moment capacity, while the beams under point load and UDL configurations do. As the constant moment load–deflection curve reached the peak, the analysis’ step size becomes increasingly smaller and the numerical analysis terminates once the pre-defined increment is exceeded (i.e., an increment less than one-hundred-thousandth). Although the constant moment loading scenario does not experience a decrease in the moment capacity, the beam experiences greater than 99% stiffness loss, which can be attributed to the critical LTB load.

6.2.3 Comparison to Design Standards

The critical moment was determined through finite element analysis for each of the beams with various sections and slenderness ratios considered. The ratio between the ABAQUS results and the corresponding moments as specified by CSA S16-14 are summarized in Figure 6-5. The vertical axis does not include the proposed moment gradient factors from Chapter 5 in CSA S16-14 results. The horizontal axis is the T-sections tested, where all loading scenarios and slenderness ratios for each T-section are grouped together. The average of ABAQUS numerical test results to the proposed equation is 1.09 with a standard deviation of 0.22.

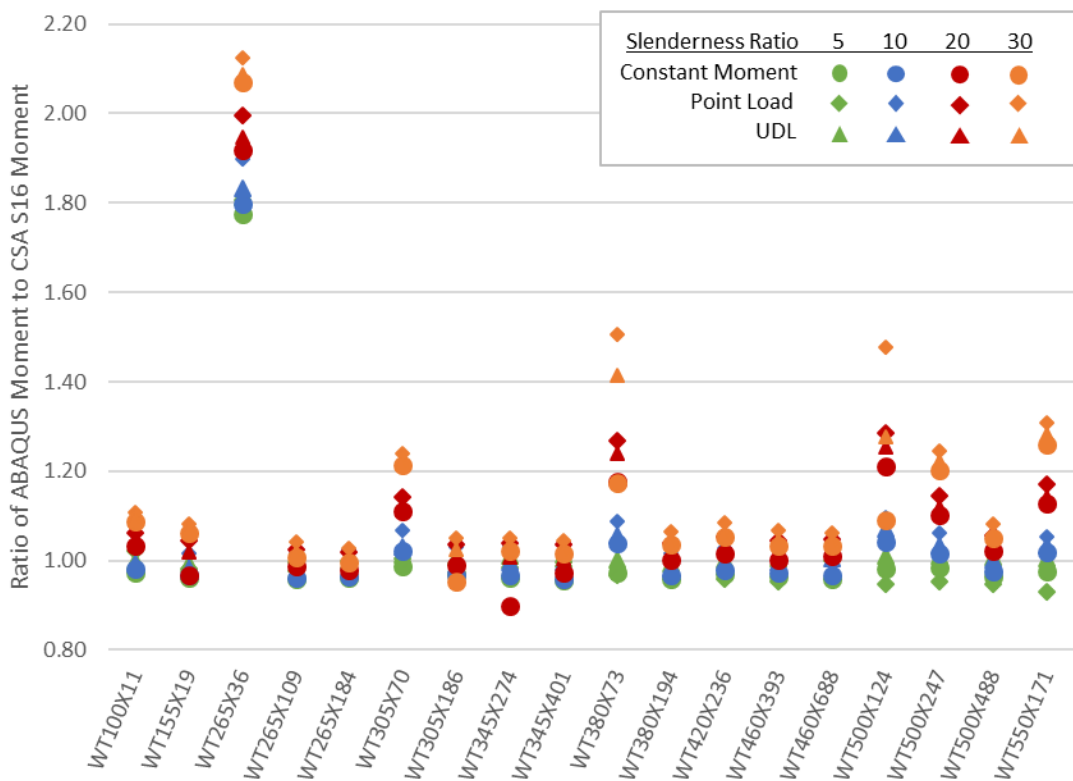


Figure 6-5: Ratio of the ABAQUS Moment to the CSA S16 Moment

As seen in Figure 6-5 the CSA S16 standard reasonably estimates the critical moment of T-shaped beams. The one section that is considerably underestimated is the class 3 section, as it reaches the plastic moment capacity prior to local buckling occurring.

Figure 6-6 to Figure 6-8 and Figure 6-10 to Figure 6-12 depict the LTB curves for WT500×124 and WT265×36 sections in comparison with the CSA S16 standard and AISC 360 specification including the limitation of $1.6M_y$ and without the limitation (labelled “AISC 360 (M_p)” in the following graphs) along with the CSA S16 equation including the proposed changes described in Section 6.3 (labelled “Proposed” in the following graphs). The square boxes represent the ABAQUS results with the four leftmost boxes representing the inelastic LTB results and the rightmost point representing elastic LTB (see Chapter 5). The left kink is the transition point from the cross-sectional capacity to inelastic LTB and the right kink in the curve is the transition point from inelastic LTB to elastic LTB. Similar curves for the remaining sections can be seen in Appendix B.2.

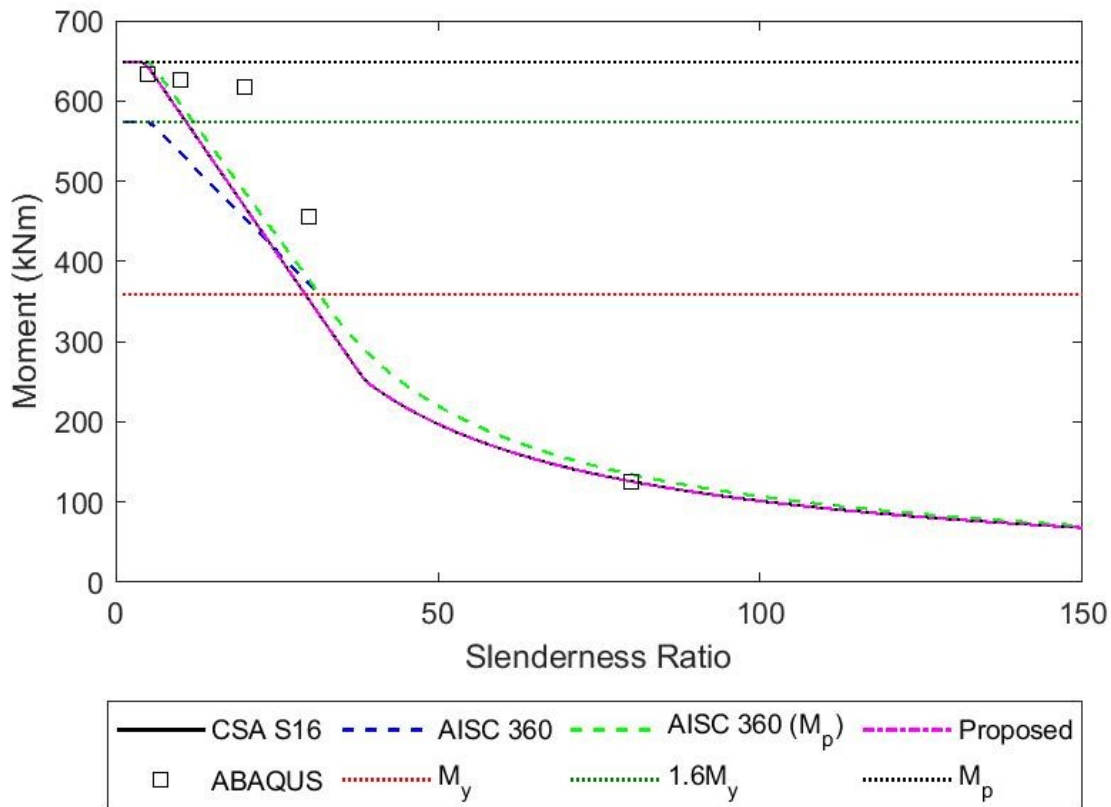


Figure 6-6: Lateral-Torsional Buckling Curve for Beams with a WT500×124 Section Subjected to a Constant Moment

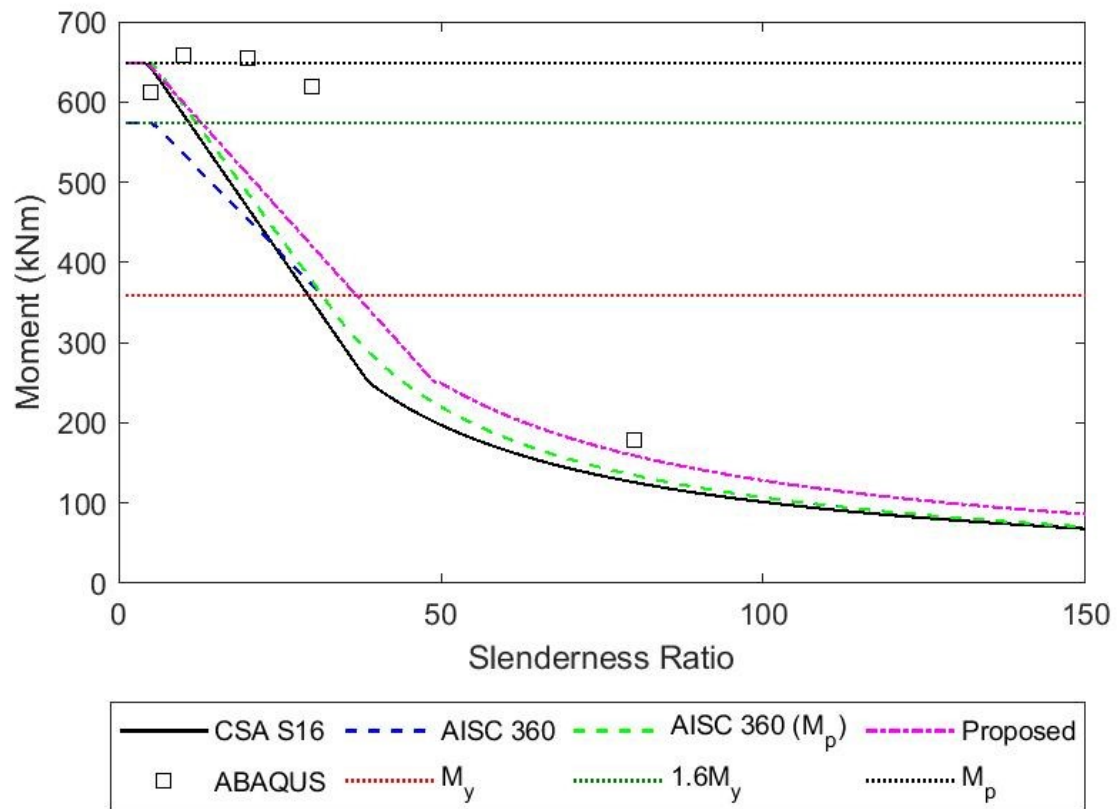


Figure 6-7: Lateral-Torsional Buckling Curve for Beams with a WT500x124 Section Subjected to a Point Load

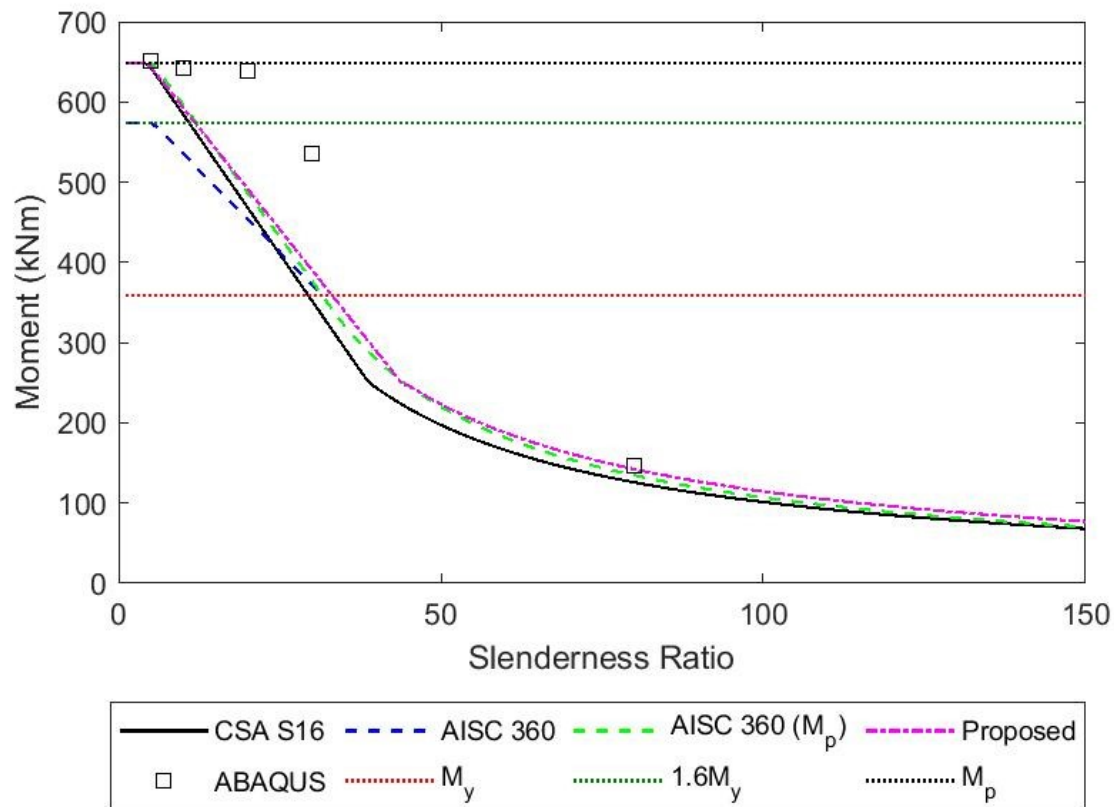


Figure 6-8: Lateral-Torsional Buckling Curve for Beams with a WT500x124 Section Subjected to a UDL

It can be seen that the beam is able to achieve the plastic moment capacity and, in some cases, slightly surpasses the plastic moment capacity when LTB does not occur (i.e., very stocky sections). The plastic moment capacity is slightly surpassed in the finite element models because the model's material property included a yield plateau to a final stress of 350 MPa, and due to the model definition, there is a small material overlap at the flange-stem junction.

Figure 6-7 shows that when subjected to a point load, the beam with the second smallest slenderness ratio, a slenderness ratio of 10, reached the expected cross-sectional capacity of the beam, while the beam with the smallest slenderness ratio, a slenderness ratio of 5, was not able to reach the cross-sectional capacity. This is due to the beam experiencing distortion through the elements at the midpoint of the beam. As seen in Figure 6-9, the elements are distorted in the

region of high stress (represented in red) at the bottom of the stem. In order to identify the distortion, the deformations in Figure 6-9 have been amplified five times.

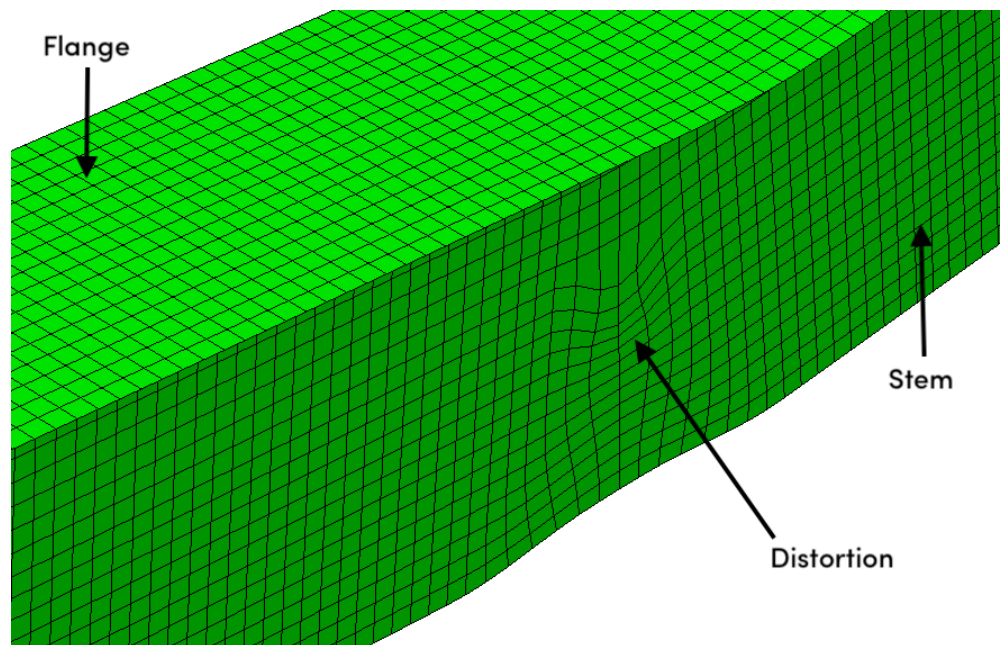


Figure 6-9: Magnified Midpoint of a WT500×124 Beam with a Slenderness Ratio of 5 Subjected to a Point Load at the Instant of LTB Depicting Element Distortion

In an attempt to mitigate the distortion, the beams were analyzed with a finer mesh; however, the distortion was still present, and the moment was unchanged. Stem buckling can be ruled out because the majority of the stem is in tension due to the location of the neutral axis. The stem shear strength was checked to determine that the stem had sufficient capacity. There is little guidance in S16 for stems of flexural T-shaped beams so the AISC equation was used to calculate the shear strength of the stem (AISC 2016; CSA 2014). The shear force from the ABAQUS models that experienced this phenomenon ranged from 0.3 to 0.4 times the stem capacity calculated by the AISC method. Since the distortion only occurred in the point load models at the location of the applied load and within the tension region, it was concluded that the distortion was predominantly a localized effect—due to the large applied load. Although it was expected that the beam with a slenderness ratio of 5 have more capacity than a beam with a slenderness ratio of 10 when both beams are subjected to a point load, the moments were deemed within an acceptable range for the analysis.

The LTB curves for a WT265×36 section (Class 3 flange) can be seen in Figure 6-10 to Figure 6-12.

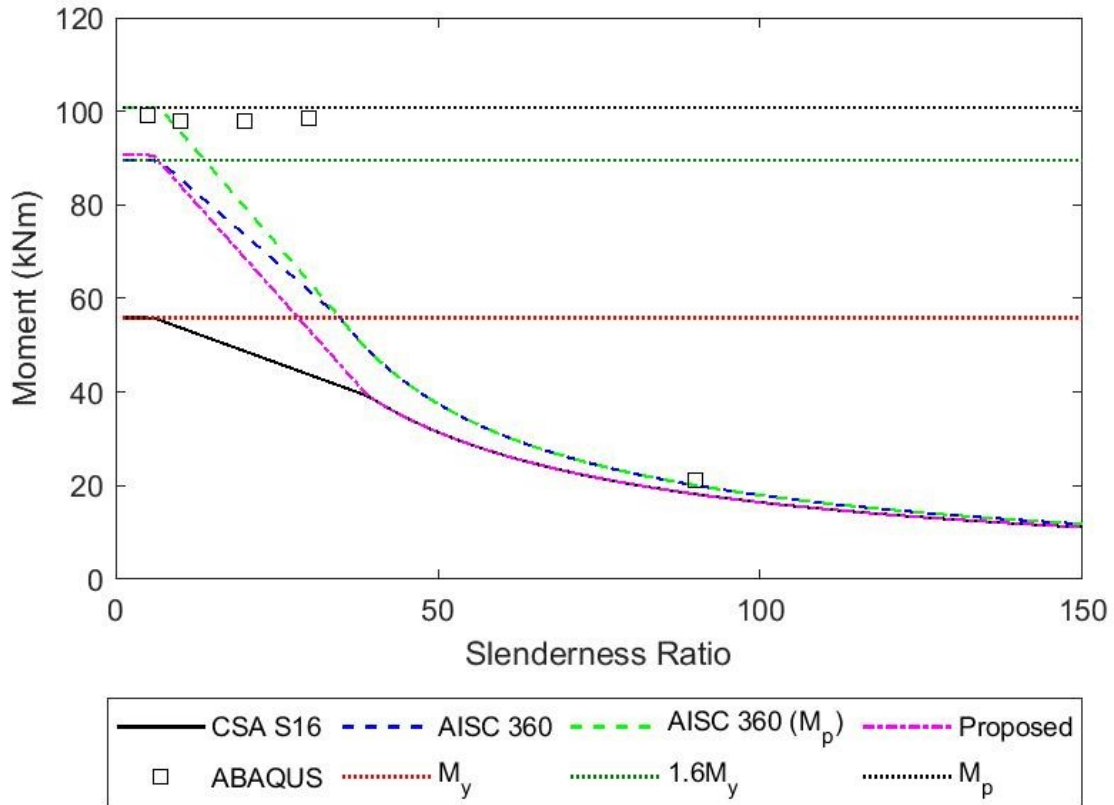


Figure 6-10: Lateral-Torsional Buckling Curve for Beams with a WT265×36 Section Subjected to a Constant Moment

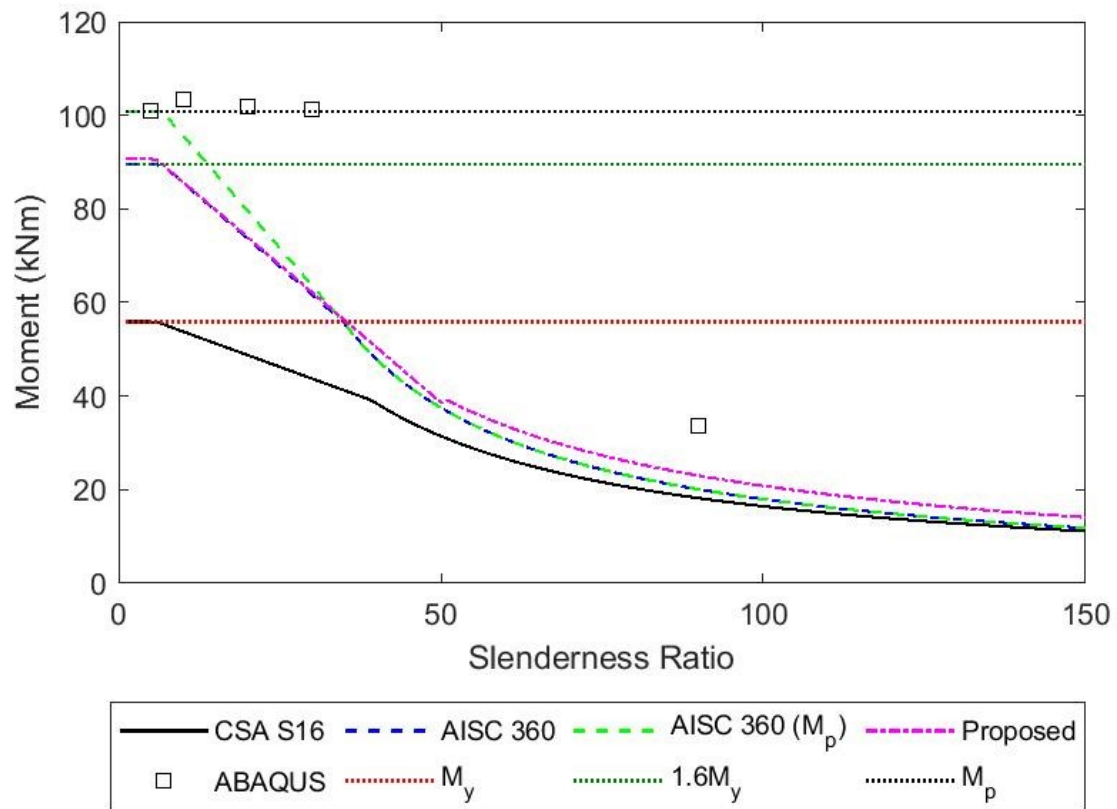


Figure 6-11: WT265×36 Lateral–Torsional Buckling Curve for Beams with a WT265×36 Section Subjected to a Point Load

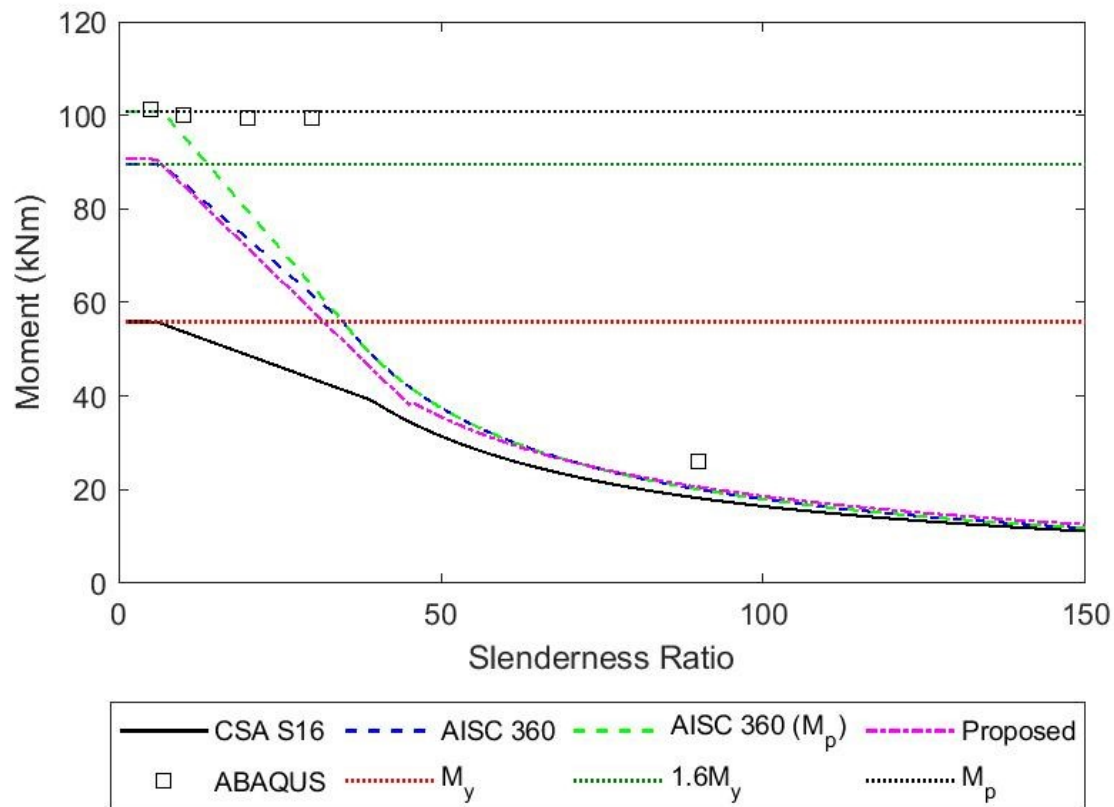


Figure 6-12: WT265×36 Lateral–Torsional Buckling Curve for Beams with a WT265×36 Section Subjected to a UDL

The WT265×36 section (a class 3 section) subjected to a point load experienced a similar effect where the smallest slenderness ratio considered, a slenderness ratio of 5, resulted in a slightly smaller maximum moment than beam with the second smallest slenderness ratio (i.e., 10) considered. This is once again due to the distortion as shown in Figure 6-9. It was unexpected that a class 3 section was able to reach the plastic moment capacity, and thus discussed further in relation to the CSA S16 and AISC 360 codes in Section 6.2.3.1 and Section 6.2.3.2, respectively.

6.2.3.1 CSA S16

The WT500×124 beam is classified as a class 1 section in the CSA S16. A class 1 section is expected to achieve the plastic moment capacity (shown as a dotted line in Figure 6-6 to Figure

6-8) if the beam fails by cross-sectional capacity and not LTB. Figure 6-6 to Figure 6-8 also show that the CSA S16 reasonably estimates the capacity of the beam in the inelastic range.

It can also be seen that the WT265×36 section is able to reach the plastic moment even though it is classified as a class 3 section. Rearranging the equations slightly, class 3 section limits as defined in the CSA S16 for flange elements are shown in Equation 6-1, where b_f is the width of the flange, t_f is the thickness of the flange and f_y is the minimum specified yield stress. If the resulting value is above the upper bound of 200, it is classified as a class 4 section. Conversely, if the value is below the lower bound of 170 it falls into a classification of a class 1 or 2 with further limits delineating the bounds between class 1 and class 2 sections.

$$170 \leq \frac{b_f}{2t_f} * \sqrt{f_y} \leq 200 \quad (6-1)$$

For a WT265×36 section, the middle term in Equation 6-1 is 176. This leads to the beam being classified as a class 3 section. In CSA S16, the maximum moment for class 3 sections is limited to the yield moment because even though class 3 sections may reach the plastic moment capacity, they are susceptible to local buckling. Although the section classifications have defined limits to classify the sections, it is an estimation used to provide guidance on the behaviour of the beam section and this beam specifically did not experience local buckling.

6.2.3.2 AISC 360

As seen in Figure 6-6 to Figure 6-8 the AISC 360 underestimates the WT500×124 beam's inelastic LTB moment capacity. The underestimation is due to limiting the maximum moment to the minimum of the plastic moment or 1.6 times the yield moment, a limit used to represent the serviceability limit state. The ultimate limit state is accurately represented when the limit is neglected. By limiting the maximum moment, the capacity in the inelastic range is also underestimated since the inelastic range is determined based on a relationship between the elastic LTB moment and the cross-sectional moment capacity.

Conversely, the WT265×36 section is classified as a noncompact section. Rearranging the AISC 360 equations for flanges of unstiffened T-sections, the noncompact section limits as defined in the AISC 360 are shown in Equation 6-2.

$$0.38 \leq \frac{b_f}{2t_f} \sqrt{\frac{f_y}{E}} \leq 1.0 \quad (6-2)$$

For a WT265×36 section, the middle term in Equation 6-2 is 0.39. This places the section on the boundary of compact and noncompact. In the AISC 360, the flange local buckling limit state is determined through a relationship of the plastic and yield moment as shown in Equation 2-13. This allows for a reasonable estimate of the LTB moment for class 3 sections.

6.3 Discussion and Design Recommendations

CSA S16 underestimates the inelastic LTB moment and AISC 360 underestimates both the cross-sectional capacity—when the limit of $1.6M_y$ is included, since this factor is meant to address the serviceability of the beam and not the ultimate limit state—and the inelastic LTB moment. The underestimation of the inelastic LTB moment in both standards is due to a combination of the moment gradient factor being neglected and the assumption that the inelastic LTB curve is linear. All sections that reached the cross-sectional capacity of the beam were limited by the plastic moment capacity; however, this may not be the case for all class 3 sections, as they are susceptible to local buckling.

The moment capacity of class 3 sections is limited by the onset of yielding in the extreme fibre at the tip of the stem; however, local buckling will not occur until the top of the flange reaches the yield strain. This is not accurately represented for T-shaped beams by the use of S_x to determine the cross-sectional moment capacity. To more accurately represent that local buckling can occur when yielding occurs in the top flange, a modified section modulus, denoted by S'_x , can be calculated for the case where the extreme fibre of the flange reaches the yield strain in compression, and the coexistent partial yielding of the stem in tension is accounted for. The cross-sectional moment capacity corresponding to the onset of yielding in the top flange, M'_y , along with a pictorial representation of the stresses and strains at M'_y can be seen in Figure 6-13.

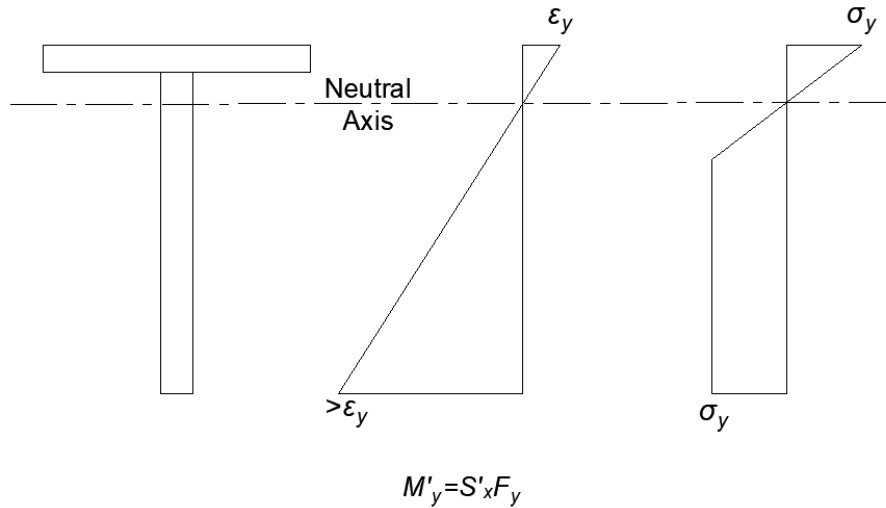


Figure 6-13: Pictorial Representation of M'_y and S'_x

Special care should be taken to determine if the neutral axis is located in the flange or stem, as either is possible with standard T-shaped beams. It was determined that the ratio of S'_x to Z_x ranged from 0.90 to 0.98, with a mean value of 0.95 and a standard deviation of 0.023 for the beams considered.

The following changes are proposed to more accurately calculate the LTB moment when T-shaped beams are in single curvature with the flange in compression:

- $\omega_3 = \frac{4M_{max}}{\sqrt{M_{max}^2 + 4M_a^2 + 7M_b^2 + 4M_c^2}}$;
- for class 3 sections, M'_y is taken as $0.9Z_x F_y$ to account for the possibility of local buckling occurring in the flange when it reaches the yield stress.

Figure 6-14 depicts the ratio of ABAQUS moments to the inelastic LTB moment and cross-sectional capacity. With the inclusion of the proposed changes, the average of ABAQUS numerical test results to the proposed equation is 1.05 with a standard deviation of 0.10.

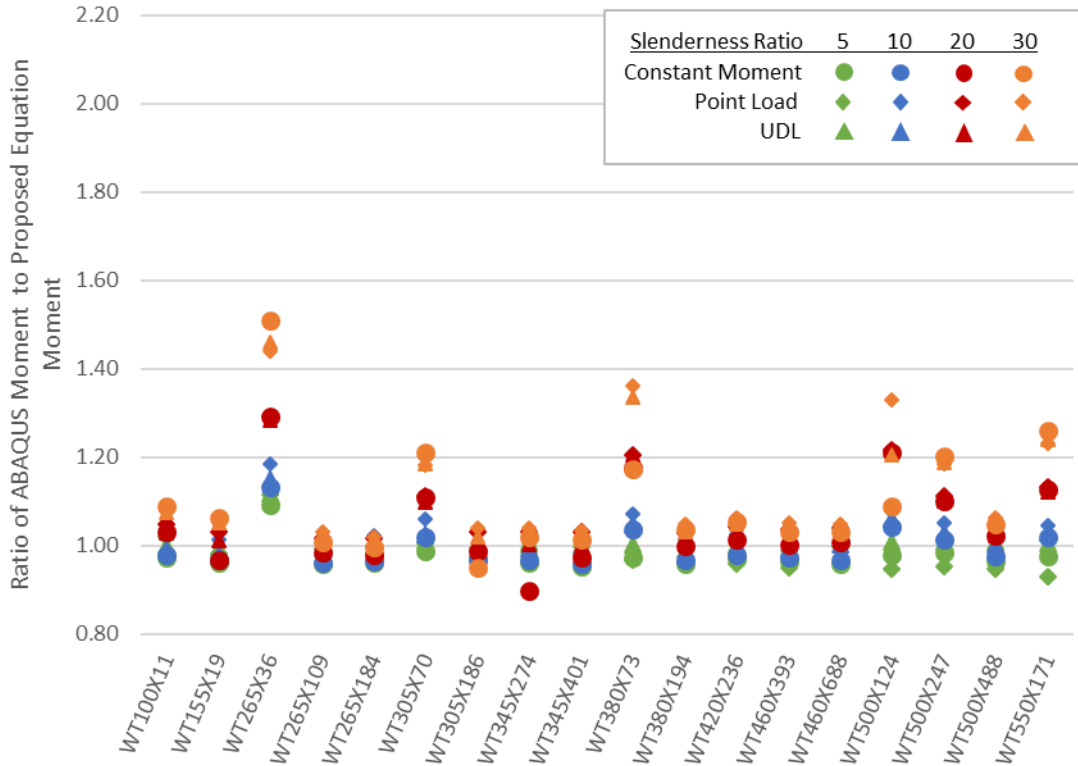


Figure 6-14: Ratio of ABAQUS Moments to Proposed Equation Moments

The points above a value of 1.0 indicate that the capacities are underestimated (conservative) and those below a value of 1.0 are overestimated (unconservative) using the proposed equation. It can be seen that the capacity of the class 3 section is still underestimated; however, in lieu of an additional study focused on the yield moment for class 3 T-shaped beams M'_y was conservatively estimated at $0.9Z_xF_y$. There are other values that are underestimated that can be attributed to a non-linear relationship (the inelastic LTB curve) being approximated as a linear one between the elastic LTB curve and development of the full cross-sectional moment capacity.

Considering the 12 scenarios analyzed for each beam section, the proposed changes involving the cross-sectional capacity and the moment gradient factor improved the inelastic LTB estimation from a mean underestimation of 9% to a mean underestimation of 5% with a maximum improvement of 11% for class 1 and 2 sections and a maximum improvement of 62% for the class 3 section.

6.4 Summary

CSA S16 slightly underestimates the inelastic LTB capacity for T-shaped beams when the top flange is in compression. It was observed that class 1 and class 2 sections were able to reach the plastic moment capacity and the class 3 section was also able to reach the plastic moment capacity prior to local buckling occurring in the flange. It was shown that by introducing the proposed moment gradient factor shown in Equation 5-1, there is a mean underestimation of 5% with a standard deviation of 0.11 for beams that fail due to inelastic LTB or cross-sectional moment.

CHAPTER 7: CONCLUSIONS AND RECOMMENDATIONS

7.1 Summary

The primary objective of this research was to investigate the LTB behaviour of T-shaped beams in single curvature with the flange in compression and compare the numerical analysis results to the CSA S16 design standard. The numerical study was completed using ABAQUS, a commercially available finite element program. Both the elastic and inelastic LTB behaviours were investigated through the research program.

A finite element model was created in ABAQUS and the model was validated using doubly-symmetric LTB tests by Fukumoto et al. (1980). Due to the lack of experimental tests, the model was modified for the LTB analysis of T-shaped beams. A numerical test matrix was created to determine the test sections for T-shaped beams. The test sections consisted of fifteen class 1 sections, two class 2 sections and one class 3 sections for a total of eighteen T-shaped sections. The numerical studies included elastic and inelastic LTB analyses of beams subjected to three loading scenarios: constant moment, point load and UDL.

The T-shaped beams were initially analyzed in the elastic LTB region using LTBeam and ABAQUS. The LTBeam results were used to co-validate the ABAQUS results as LTBeam had been validated by the program authors. This additionally allowed further validation of the ABAQUS results. Both LTBeam and ABAQUS results were used to determine the moment gradient factor for T-shaped beams.

A study was undertaken to determine the effect of residual stresses on T-shaped beams in single curvature with the flange in compression. It is widely accepted that residual stresses affect the critical buckling load in the inelastic region for I-shaped beams; however, the effect is unknown for T-shaped beams. Following the study, T-shaped beams were analyzed in the inelastic LTB region to determine the critical buckling moment.

Finally, the results of the numerical analyses were used to propose modifications to the current S16 design provisions for T-shaped beams.

7.2 Conclusions

The following conclusions can be made for T-shaped beams in single-curvature with the flange in compression and the load applied at the mid-height of the stem:

- T-shaped beams susceptible to elastic LTB are extremely slender and unlikely to occur in practical applications.
- The elastic LTB moment was affected by the loading scenario. Therefore, the moment gradient factor is applicable to T-shaped beams in single-curvature with the flange in compression, when calculating the elastic LTB moment.
- Modifications were proposed for the current CSA S16 standard to include the moment gradient factor to calculate the elastic LTB moment.
- It was determined that based on the two residual stress patterns studied for T-shaped beams, the inclusion or exclusion of residual stresses did not significantly impact the LTB critical moments.
- All the sections tested were able to achieve the plastic moment capacity without exhibiting local buckling, and followed the inelastic LTB trend decreasing to the elastic LTB moment.
- Modifications were proposed for the CSA S16 provisions to include the moment gradient factor proposed by Wong and Driver (2010).
- Modifications were proposed to increase the cross-sectional moment capacity for class 3 sections to $0.9Z_x F_y$.

7.3 Recommendations for Future Work

Although this study contained a comprehensive analysis of T-shaped beams in single-curvature with the flange in compression in the elastic and inelastic lateral–torsional buckling regions, future investigations can further improve the understanding of T-shaped beams. The following investigations are recommended:

- Perform large-scale experimental tests to confirm the results of the numerical analysis.
- Further investigate possible loading scenarios (i.e., maximum moment at one beam end and no moment on the other beam end which corresponds to $\omega_3 = 1.75$) to ensure the

moment gradient factor proposed by Wong and Driver (2010) is applicable for common single-curvature loading scenarios with the flange in compression.

- Further investigate class 3 sections in single curvature with the flange in compression to determine the cross-sectional capacity.
- Investigate the lateral–torsional buckling behaviour of T-shaped beams in single curvature with the stem in compression.
- Investigate the lateral–torsional buckling behaviour of T-shaped beams in double curvature.
- Investigate the influence of the load-height for T-shaped beams in single and double curvature.

REFERENCES

- AISC. (2016). *Specification for Structural Steel Buildings, ANSI / AISC 360-16*. AISC, Chicago.
- AISC. (2017). “AISC Shapes Database v15.0.” <<https://www.aisc.org/globalassets/aisc/manual/v15.0-shapes-database/aisc-shapes-database-v15.0.xlsx>>.
- Akin, J. E. (2010). *Finite Element Analysis Concepts: via SolidWorks*. World Scientific, Hackensack, NJ.
- Bureau, A. (2008). *NCCI: Elastic Critical Moment for Lateral Torsional Buckling*.
- CEN. (2005). *Eurocode 3: Design of steel structures -Part 1-1: General rules and rules for buildings*. CEN, Brussels.
- CISC. (2017). *Handbook of Steel Construction*. Canadian Institute of Steel Construction, Toronto, ON.
- CSA. (2014). *CSA S16: Design of Steel Structures*. Canadian Standards Association, Toronto, ON.
- CTICM. (2001). “LTBeam.” Saint-Aubin, France.
- CTICM. (2002). “LTBeam Report on validation tests.” (July), 1–21.
- Ellobody, E., Young, B., and Feng, R. (2014). *Finite Element Analysis and Design of Metal Structures*. Butterworth-Heinemann, Waltham, MA.
- Fukumoto, Y., Itoh, Y., and Kubo, M. (1980). “Strength Variation of Laterally Unsupported Beams.” *Journal of the Structural Division, ASCE*, 106(ST1), 165–181.
- Galambos, T. V. (1968). *Structural Members and Frames*. Prentice-Hall Inc., Englewood Cliffs, N.J.
- Helwig, T. A., Frank, K. H., and Yura, J. A. (1997). “Lateral-Torsional Buckling of Singly

- Symmetric I-Beams.” *Journal of Structural Engineering*, 123(9), 1172–1179.
- Ji, D. (2019). “Large-scale lateral-torsional buckling tests of welded girders.” Civil and Environmental Engineering, University of Alberta, AB.
- Kabir, M. I. (2016). “Lateral Torsional Buckling of Welded Wide Flange Beams.” Building, Civil and Environmental Engineering, Concordia University, Montreal, QC.
- Kirby, P. A., and Nethercot, D. A. (1979). *Design for Structural Stability*. Halsted Press, New York, NY, USA.
- Kitipornchai, S., and Lee, H. W. (1986a). “Inelastic experiments on angle and tee struts.” *Journal of Constructional Steel Research*, 6(3), 219–236.
- Kitipornchai, S., and Lee, H. W. (1986b). “Inelastic buckling of single-angle, tee and double-angle struts.” *Journal of Constructional Steel Research*, 6(1), 3–20.
- Kitipornchai, S., and Trahair, N. S. (1980). “Buckling Properties of Monosymmetric I-Beams.” *Journal of the Structural Division*, ST5(5), 941–957.
- Kitipornchai, S., and Wang, C. M. (1986). “Lateral Buckling of Tee Beams Under Moment Gradient.” *Computers and Structures*, 23(1), 69–76.
- Koch, J. C., Driver, R. G., Li, Y., and Manarin, M. (2019). “Evaluation of CSA S16-14 Asymmetry Parameter for Singly-symmetric Beams.” *Canadian Journal of Civil Engineering*, 46(3), 230–235.
- Nagaraja Rao, N., Estuar, F. R., and Tall, L. (1964). “Residual stresses in welded shapes.” *The Welding Journal*, 43(7), 295–s.
- Nethercot, D. A., and Rockey, K. C. (1971). “A unified approach to the elastic lateral buckling of beams.” *The Structural Engineer*, 49(7), 321–330.
- Salvadori, M. G. (1955). “Lateral Buckling of I-Beams.” *ASCE Transactions*, 120, 1165–1177.

- Slein, R., Jeong, W. Y., and White, D. W. (2018). *A Critical Evaluation of Moment Gradient (Cb) Factor Calculation Procedures for Singly Symmetric I-Section Members*. School of Civil and Environmental Engineering, Georgia Institute of Technology, Atlanta, GA.
- Vila Real, P. M. M., Cazeli, R., Simões da Silva, L., Santiago, A., and Piloto, P. (2004). “The effect of residual stresses in the lateral-torsional buckling of steel I-beams at elevated temperature.” *Journal of Constructional Steel Research*, 60, 783–793.
- Wong, E., and Driver, R. G. (2010). “Critical Evaluation of Equivalent Moment Factor Procedures for Laterally Unsupported Beams.” *Engineering Journal*, 47(1), 1–20.
- Ziemian, R. D. (2010). *Guide to Stability Design Criteria for Metal Structures*. John Wiley & Sons, Inc, New Jersey.

APPENDIX A: ELASTIC LATERAL-TORSIONAL BUCKLING RESULTS

A.1: Tabular Results

Table A-1: Comparison of LTB Moment: Constant Moment

Section	L/d	S16 including ω_3 (kNm)	LTBeam (kNm)	ABAQUS (kNm)
WT100×11	225	2.3	2.3	3.2
WT155×19	230	5.3	5.3	10.2
WT265×36	90	20.8	20.9	21.2
WT265×109	410	54.6	53.5	-
WT265×184	685	90.7	87.3	-
WT305×70	140	46.3	45.3	52.0
WT305×186	490	110.7	106.9	194.1
WT345×274	525	191.8	184.2	303.4
WT345×401	680	304.2	287.6	474.1
WT380×73	80	65.0	65.1	67.1
WT380×194	325	143.9	140.4	205.2
WT420×236	305	199.5	194.2	248.7
WT460×393	385	381.6	366.9	451.8
WT460×688	505	789.3	753.3	918.2
WT500×124	80	134.0	133.3	125.7
WT500×247	145	284.6	275.4	268.0
WT500×488	355	542.4	517.0	583.4
WT550×171	115	194.6	192.9	205.5

Table A-2: Comparison of LTB Moment: Point Load

Section	L/d	S16 including ω_3 (kNm)	LTBeam (kNm)	ABAQUS (kNm)
WT100×11	225	3.0	3.1	3.7
WT155×19	230	6.8	7.1	12.5
WT265×36	90	26.4	27.7	33.8
WT265×109	410	69.0	72.3	-
WT265×184	685	114.7	117.9	-
WT305×70	140	58.5	61.1	69.7
WT305×186	490	140.0	144.4	251.0
WT345×274	525	242.6	248.7	392.3
WT345×401	680	384.9	388.1	602.5
WT380×73	80	82.3	86.0	95.1
WT380×194	325	182.1	189.8	284.3
WT420×236	305	252.3	262.3	352.6
WT460×393	385	482.7	495.2	617.2
WT460×688	505	998.5	1016.1	1225.7
WT500×124	80	169.5	177.1	178.3
WT500×247	145	360.0	370.6	366.6
WT500×488	355	686.1	697.6	783.8
WT550×171	115	246.2	259.0	294.0

Table A-3: Comparison of LTB Moment: UDL

Section	L/d	S16 including ω_3 (kNm)	LTBeam (kNm)	ABAQUS (kNm)
WT100×11	225	2.6	2.6	4.5
WT155×19	230	6.0	6.0	11.9
WT265×36	90	23.6	23.1	26.0
WT265×109	410	61.7	60.4	-
WT265×184	685	102.56	98.5	-
WT305×70	140	52.3	51.0	58.1
WT305×186	490	125.2	120.6	206.8
WT345×274	525	216.9	207.7	327.5
WT345×401	680	344.1	324.3	502.8
WT380×73	80	73.6	72.0	76.8
WT380×194	325	162.8	158.4	232.4
WT420×236	305	225.6	219.0	286.4
WT460×393	385	431.5	413.7	519.6
WT460×688	505	892.7	849.1	1152.8
WT500×124	80	151.6	148.1	146.5
WT500×247	145	321.9	309.6	304.1
WT500×488	355	613.4	582.8	636.0
WT550×171	115	220.1	216.2	234.7

A.2: Graphical Results

The ABAQUS load–deflection curves for all the beam sections can be found in Figure A-1 to Figure A-18.

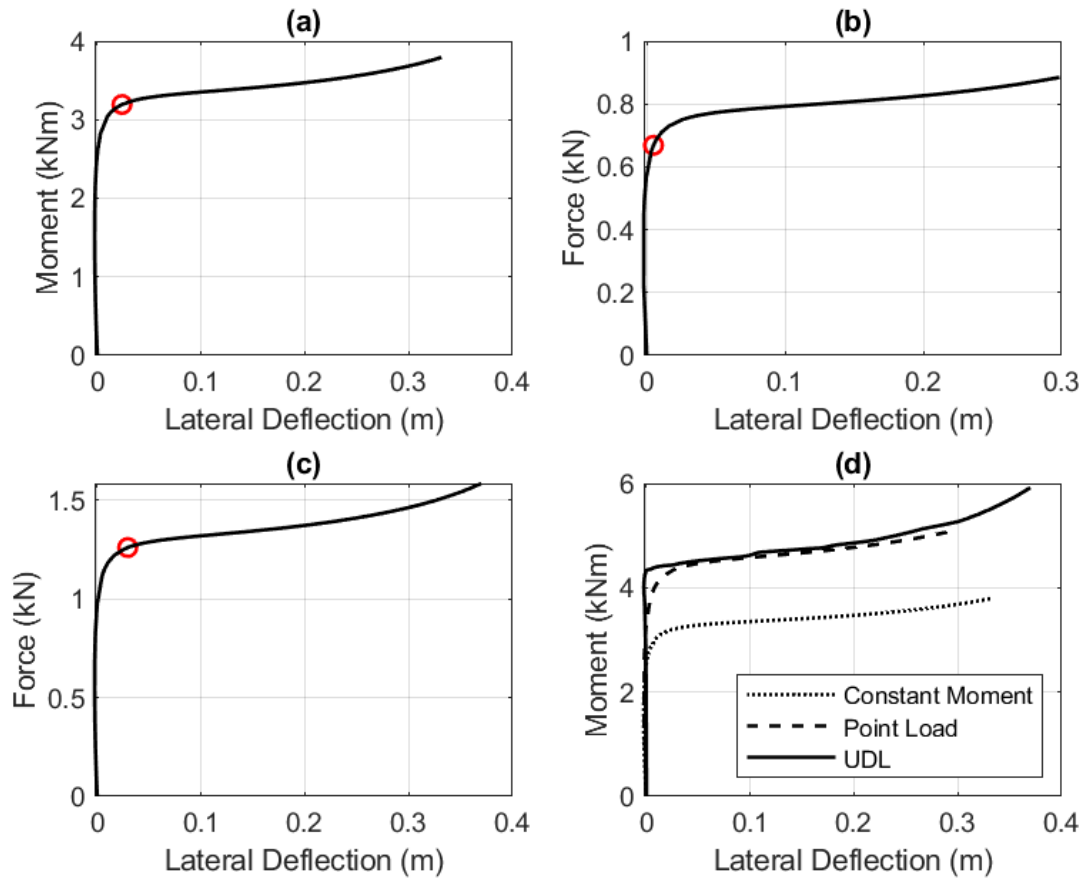


Figure A-1: Load Deflection Curves for Beams with a WT110×11 Section: (a) Constant Moment; (b) Point Load; (c) UDL; and (d) Moment Deflection Curves for all Three Loading Scenarios.

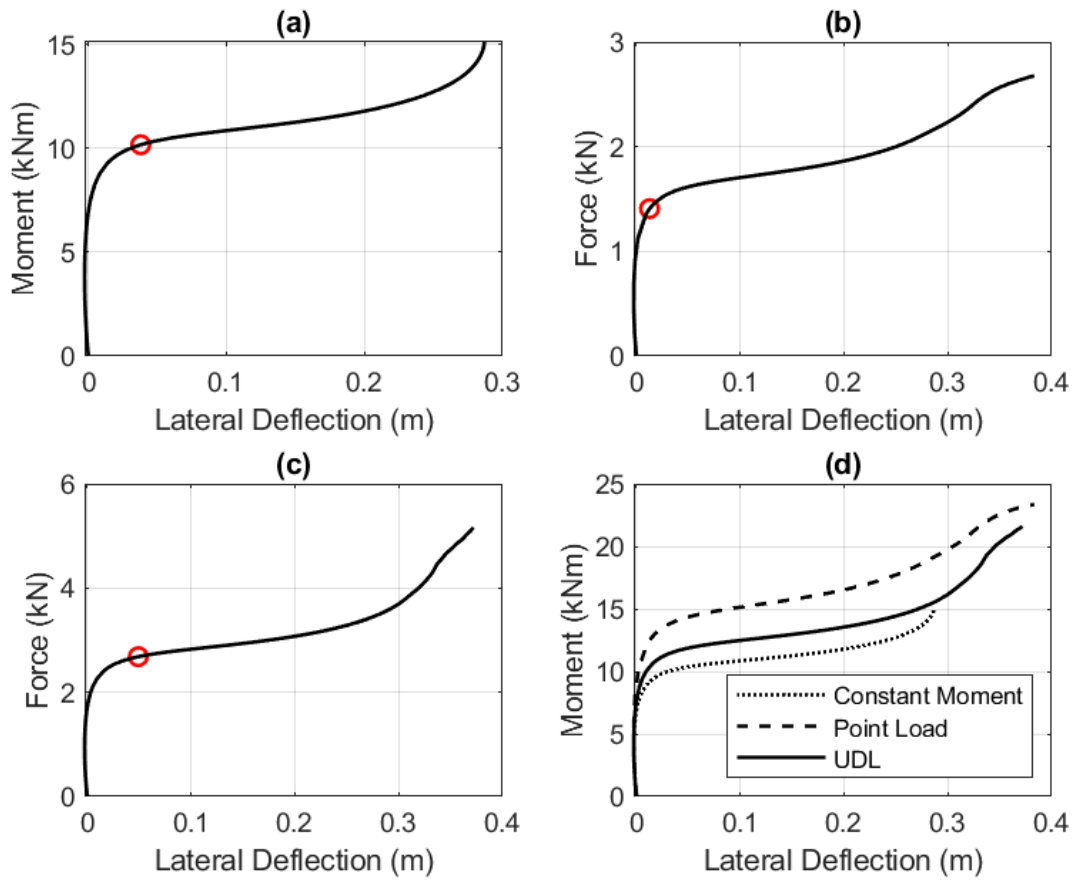


Figure A-2: Load Deflection Curves for Beams with a WT155×19 Section: (a) Constant Moment; (b) Point Load; (c) UDL; and (d) Moment Deflection Curves for all Three Loading Scenarios.

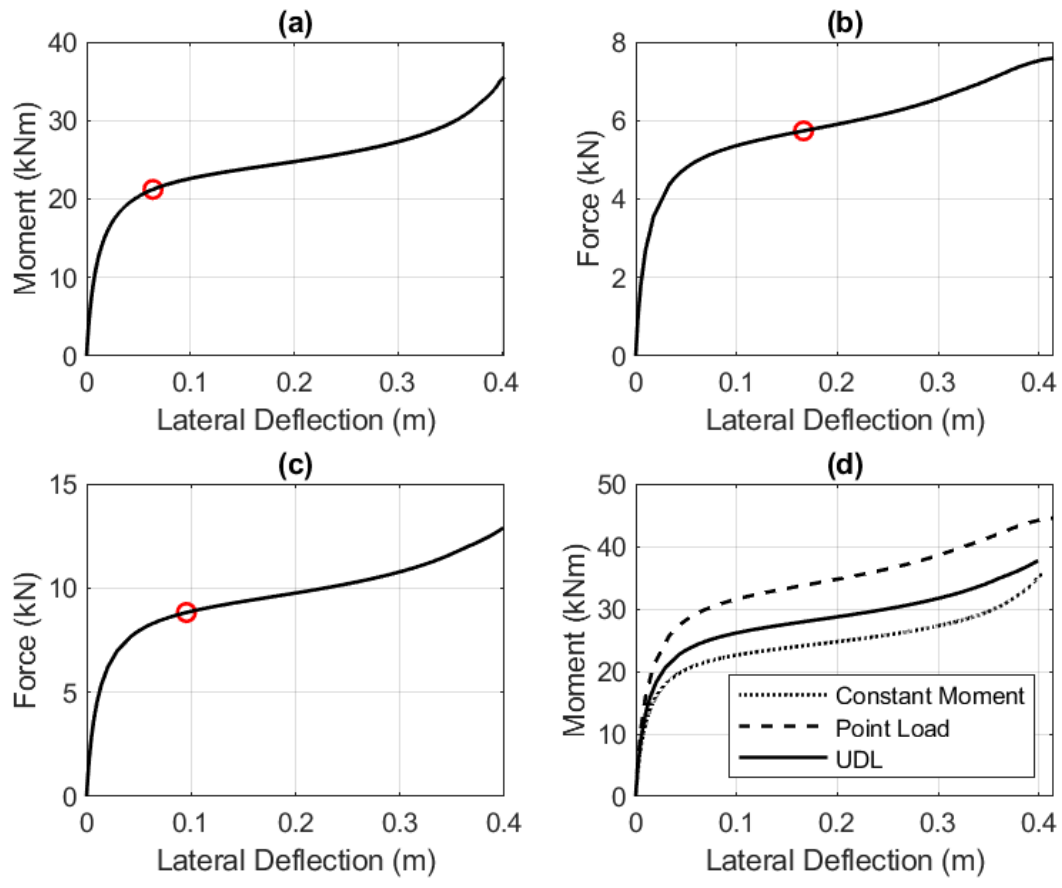


Figure A-3: Load Deflection Curves for Beams with a WT265x36 Section: (a) Constant Moment; (b) Point Load; (c) UDL; and (d) Moment Deflection Curves for all Three Loading Scenarios.

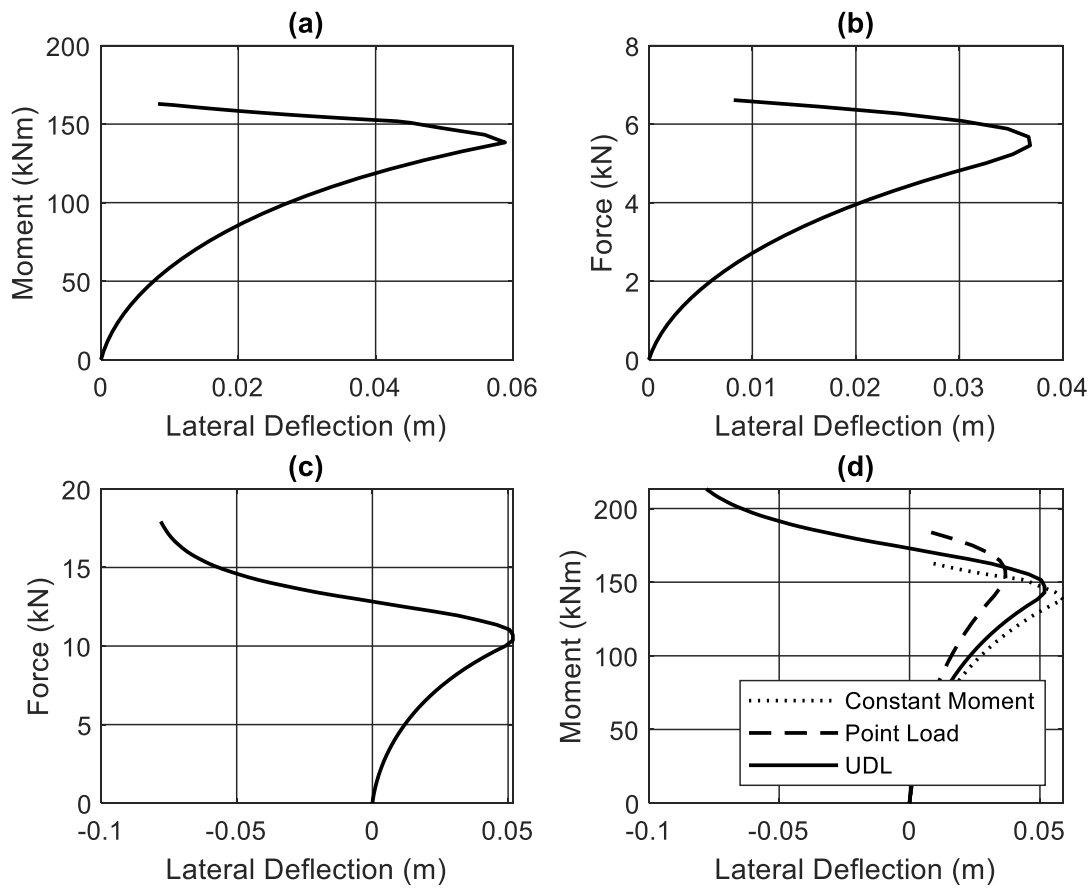


Figure A-4: Load Deflection Curves for Beams with a WT265x109 Section: (a) Constant Moment; (b) Point Load; (c) UDL; and (d) Moment Deflection Curves for all Three Loading Scenarios.

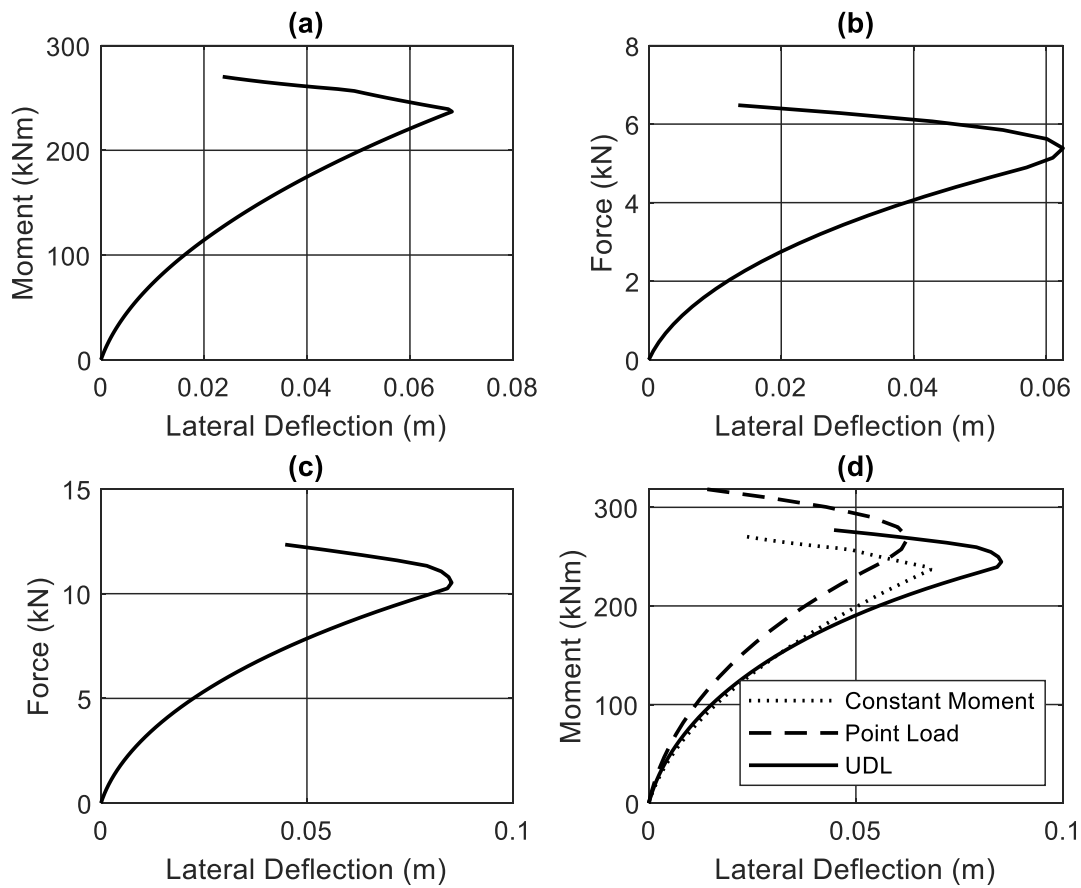


Figure A-5: Load Deflection Curves for Beams with a WT265x184 Section: (a) Constant Moment; (b) Point Load; (c) UDL; and (d) Moment Deflection Curves for all Three Loading Scenarios.

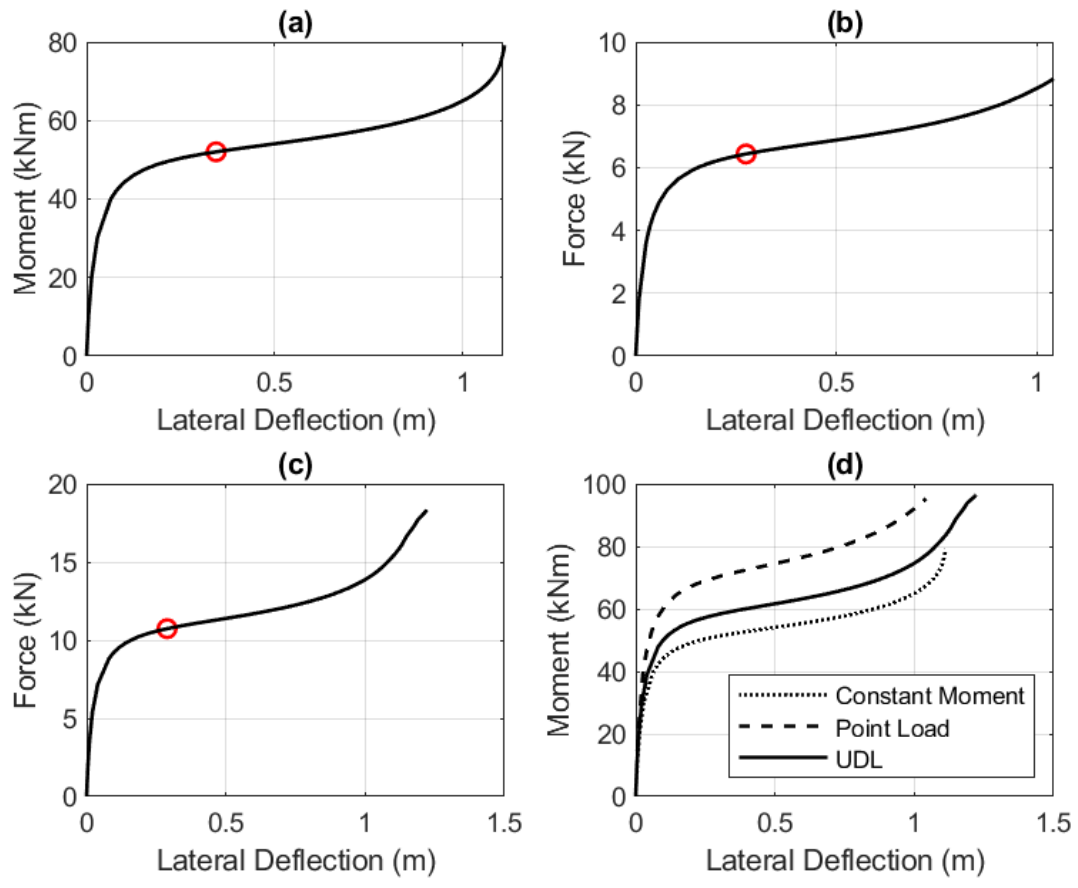


Figure A-6: Load Deflection Curves for Beams with a WT305×70 Section: (a) Constant Moment; (b) Point Load; (c) UDL; and (d) Moment Deflection Curves for all Three Loading Scenarios.

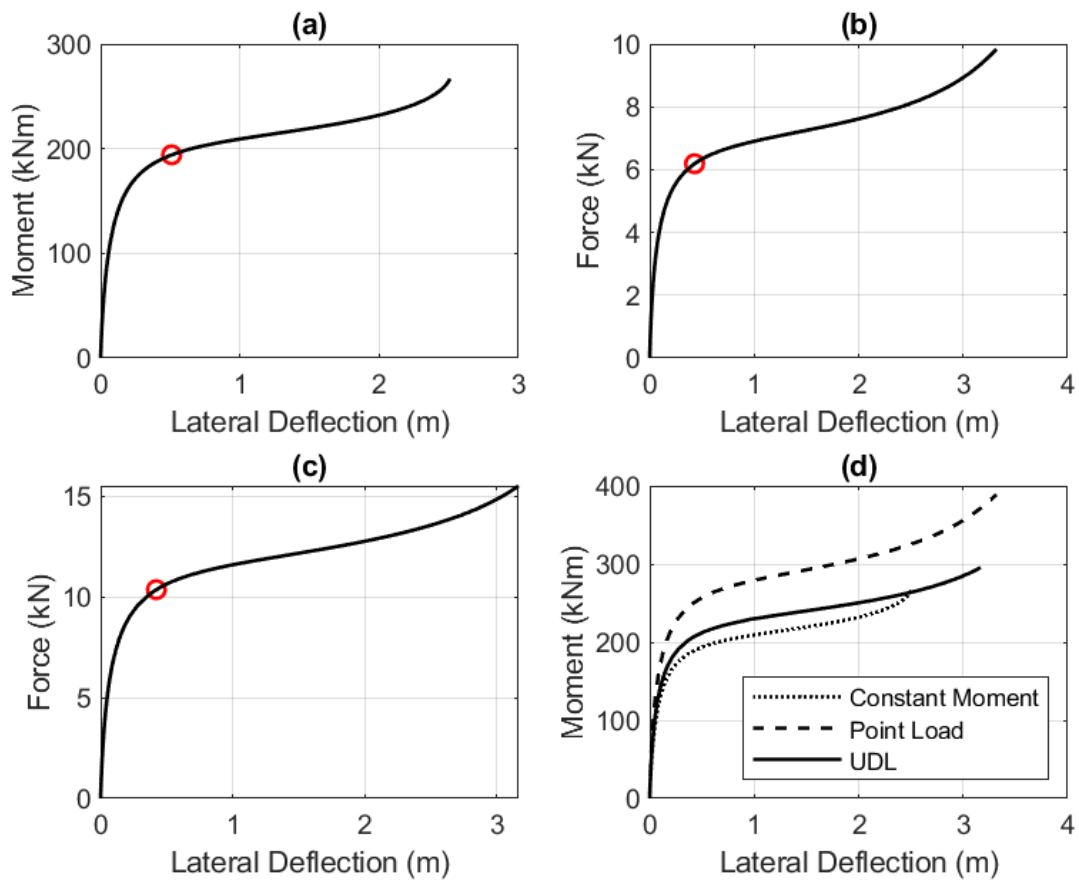


Figure A-7: Load Deflection Curves for Beams with a WT305x186 Section: (a) Constant Moment; (b) Point Load; (c) UDL; and (d) Moment Deflection Curves for all Three Loading Scenarios.

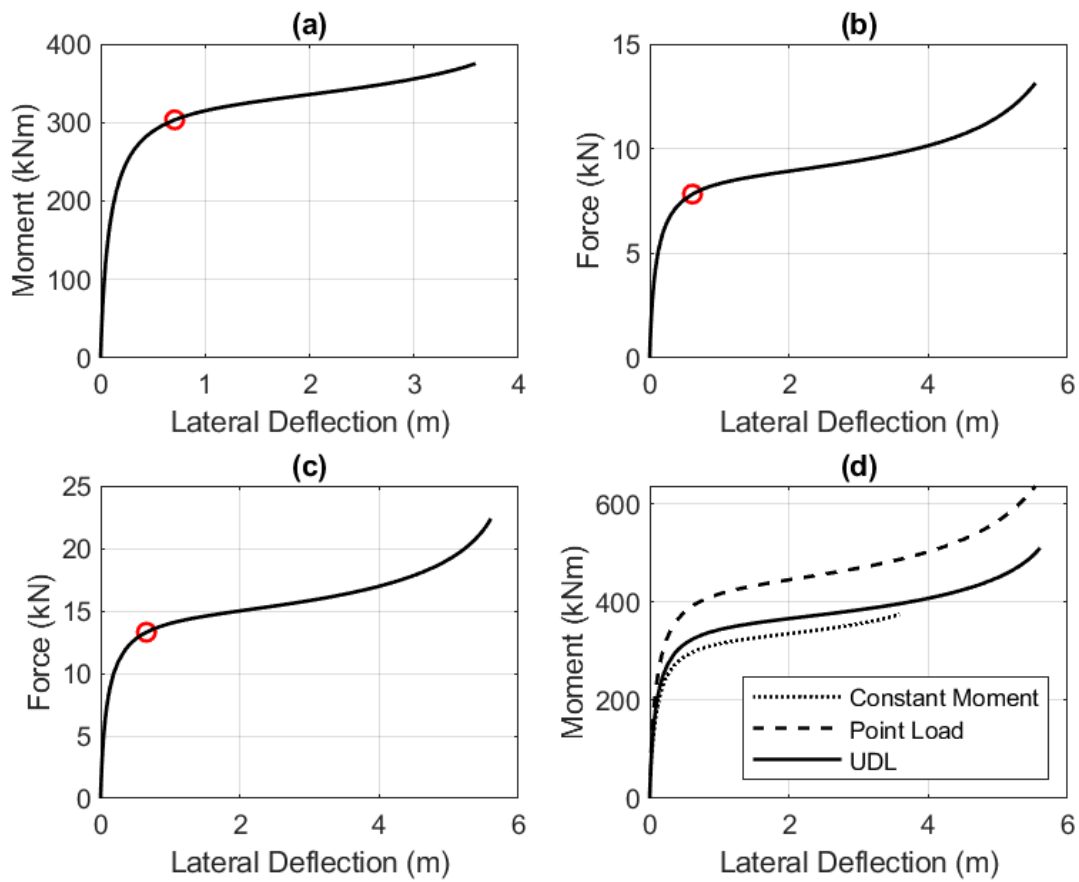


Figure A-8: Load Deflection Curves for Beams with a WT345x274 Section: (a) Constant Moment; (b) Point Load; (c) UDL; and (d) Moment Deflection Curves for all Three Loading Scenarios.

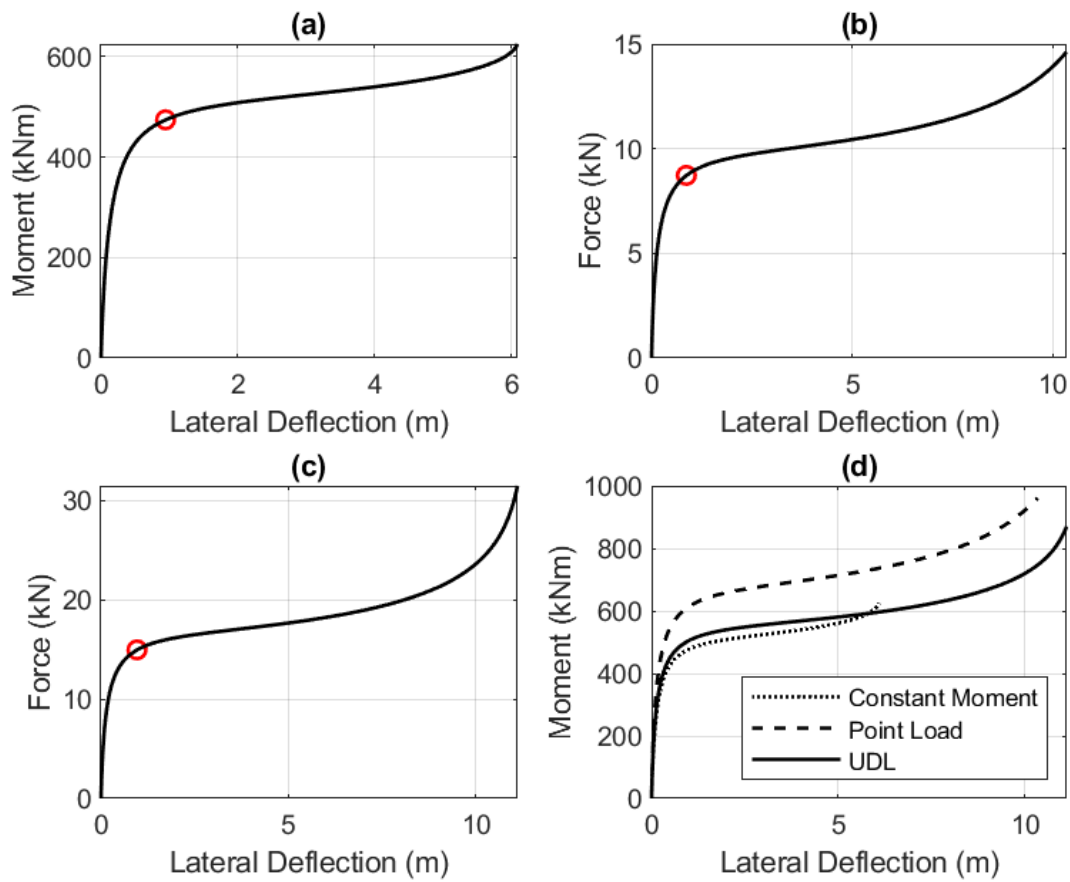


Figure A-9: Load Deflection Curves for Beams with a WT345×401 Section: (a) Constant Moment; (b) Point Load; (c) UDL; and (d) Moment Deflection Curves for all Three Loading Scenarios.

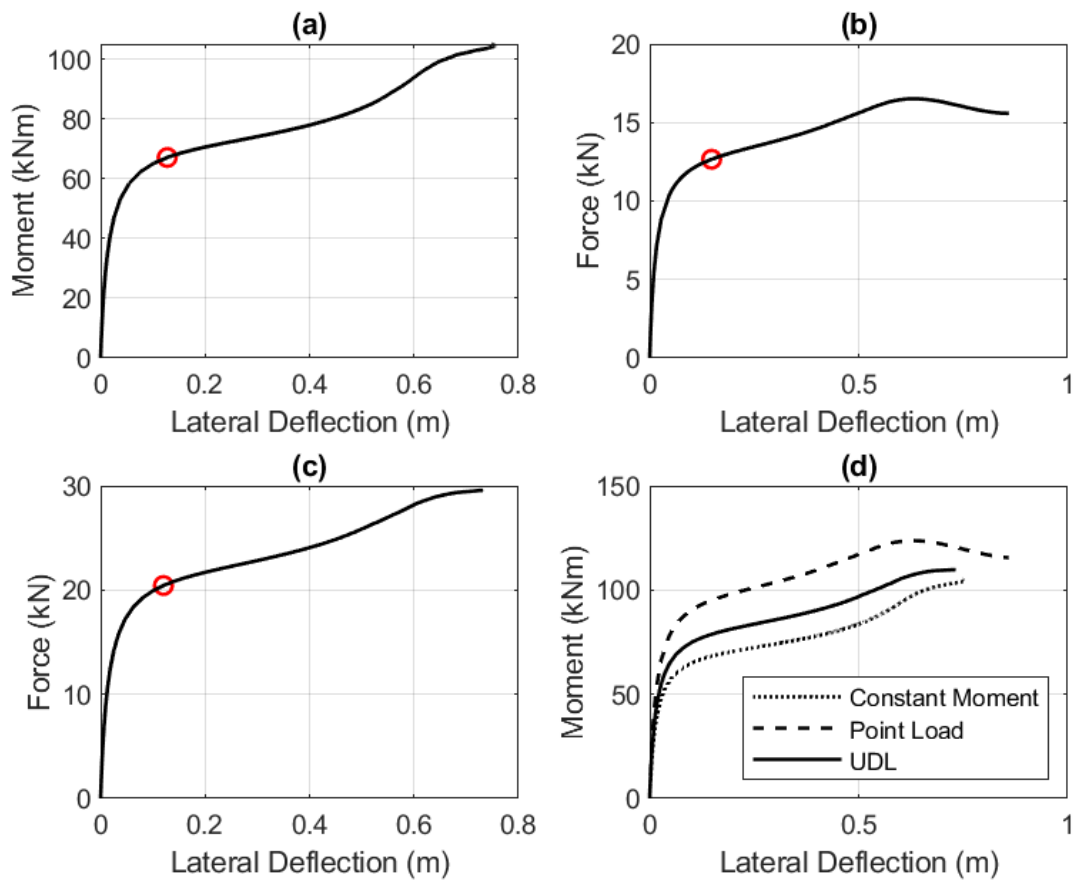


Figure A-10: Load Deflection Curves for Beams with a WT380×73 Section: (a) Constant Moment; (b) Point Load; (c) UDL; and (d) Moment Deflection Curves for all Three Loading Scenarios.

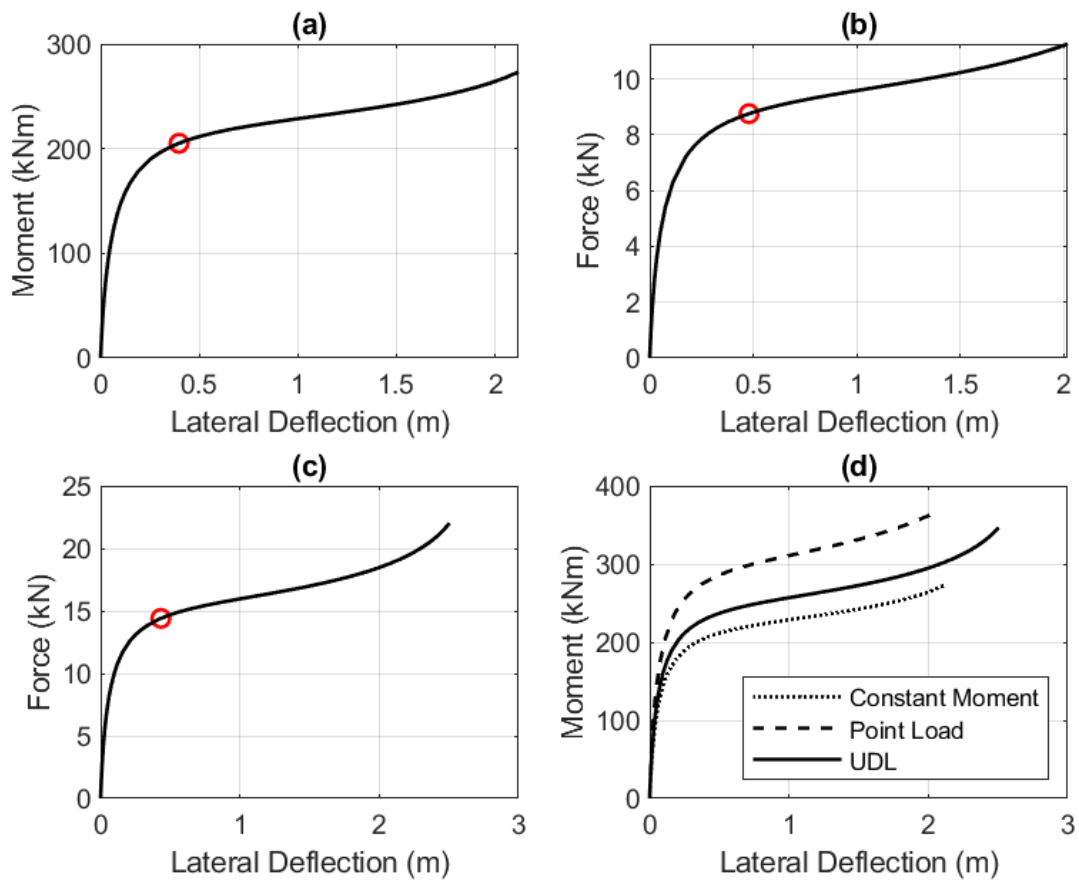


Figure A-11: Load Deflection Curves for Beams with a WT380×194 Section: (a) Constant Moment; (b) Point Load; (c) UDL; and (d) Moment Deflection Curves for all Three Loading Scenarios.

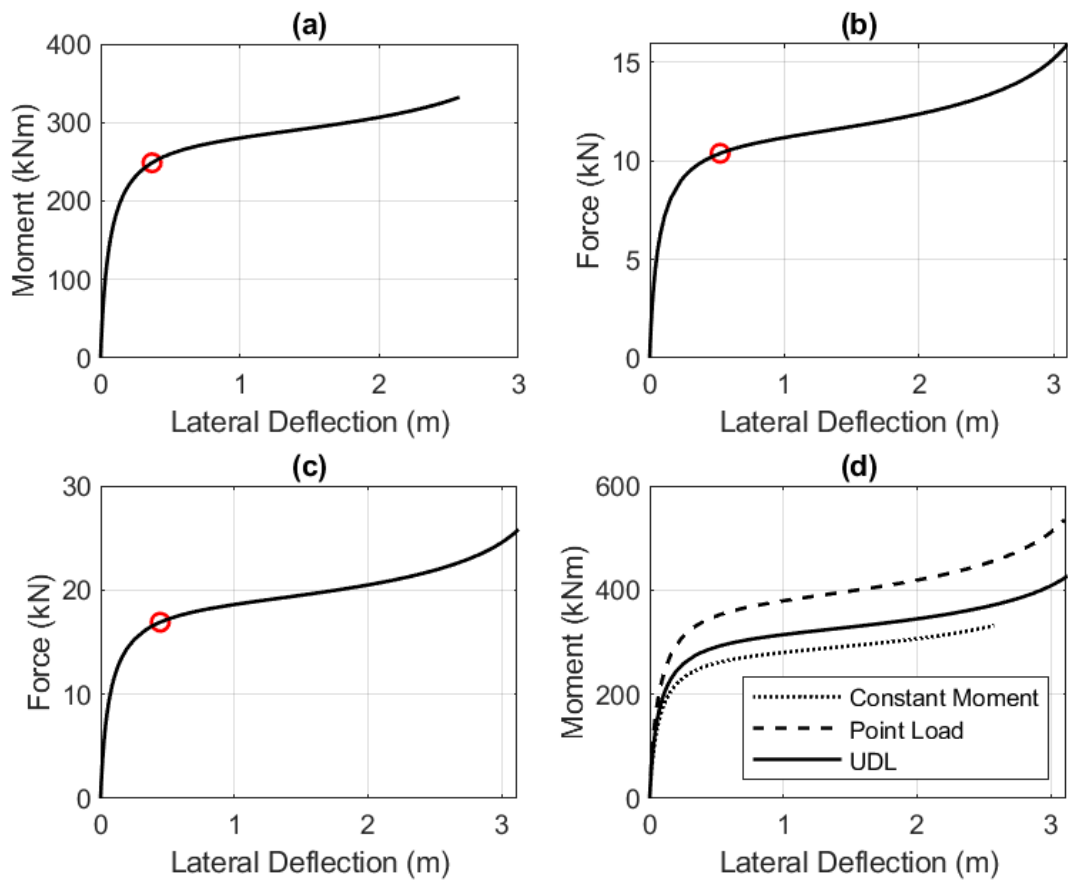


Figure A-12: Load Deflection Curves for Beams with a WT420x236 Section: (a) Constant Moment; (b) Point Load; (c) UDL; and (d) Moment Deflection Curves for all Three Loading Scenarios.

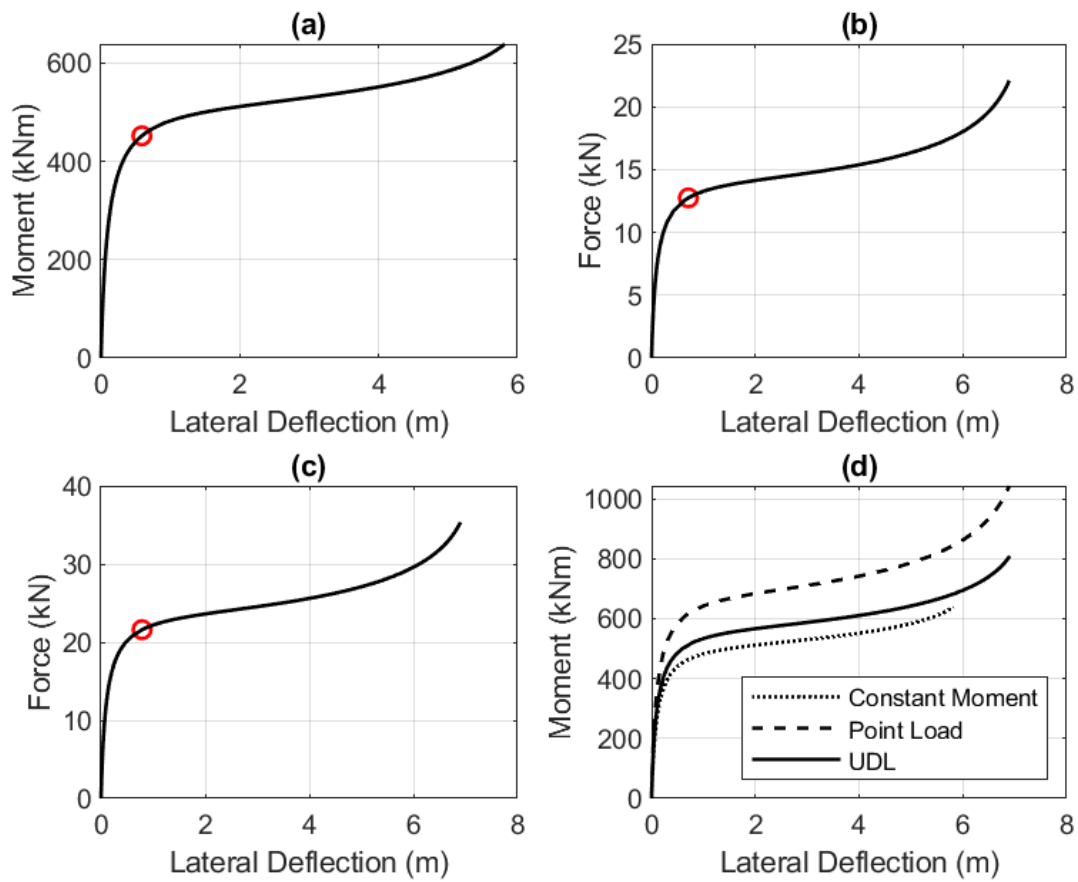


Figure A-13: Load Deflection Curves for Beams with a WT460x393 Section: (a) Constant Moment; (b) Point Load; (c) UDL; and (d) Moment Deflection Curves for all Three Loading Scenarios.

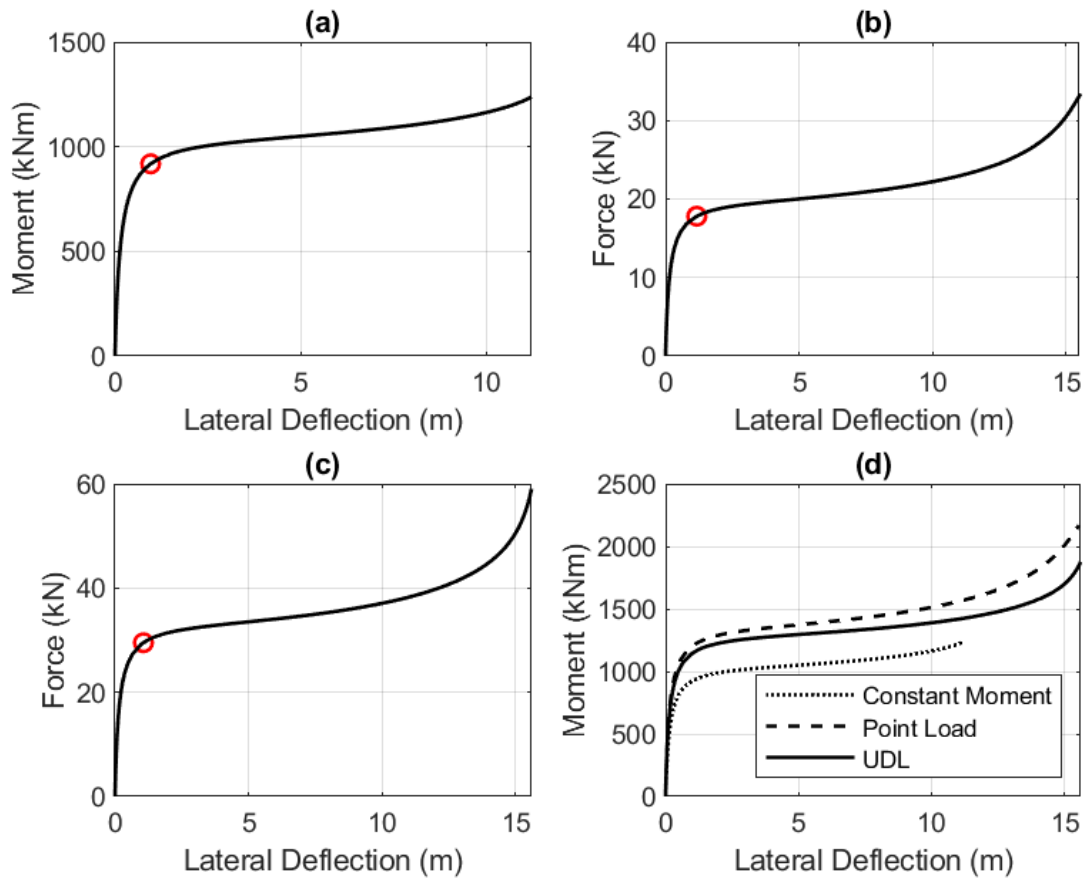


Figure A-14: Load Deflection Curves for Beams with a WT460×688 Section: (a) Constant Moment; (b) Point Load; (c) UDL; and (d) Moment Deflection Curves for all Three Loading Scenarios.

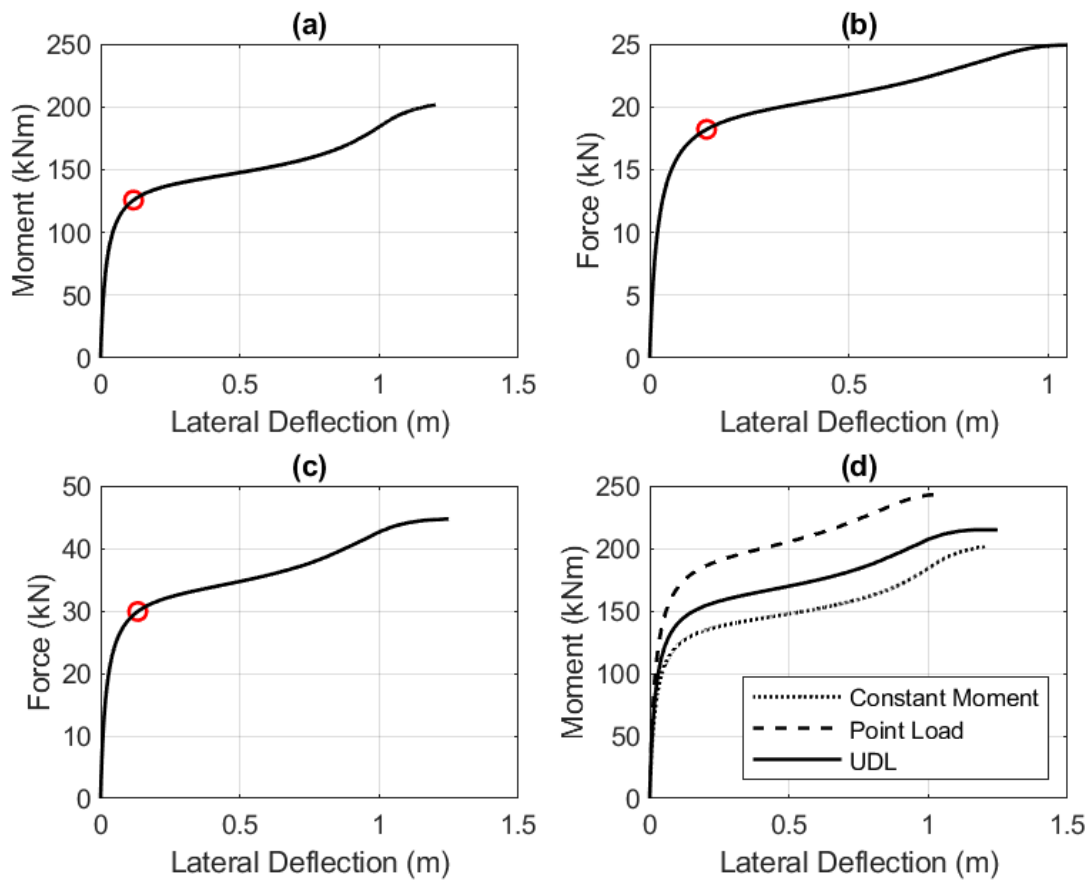


Figure A-15: Load Deflection Curves for Beams with a WT500×124 Section: (a) Constant Moment; (b) Point Load; (c) UDL; and (d) Moment Deflection Curves for all Three Loading Scenarios.

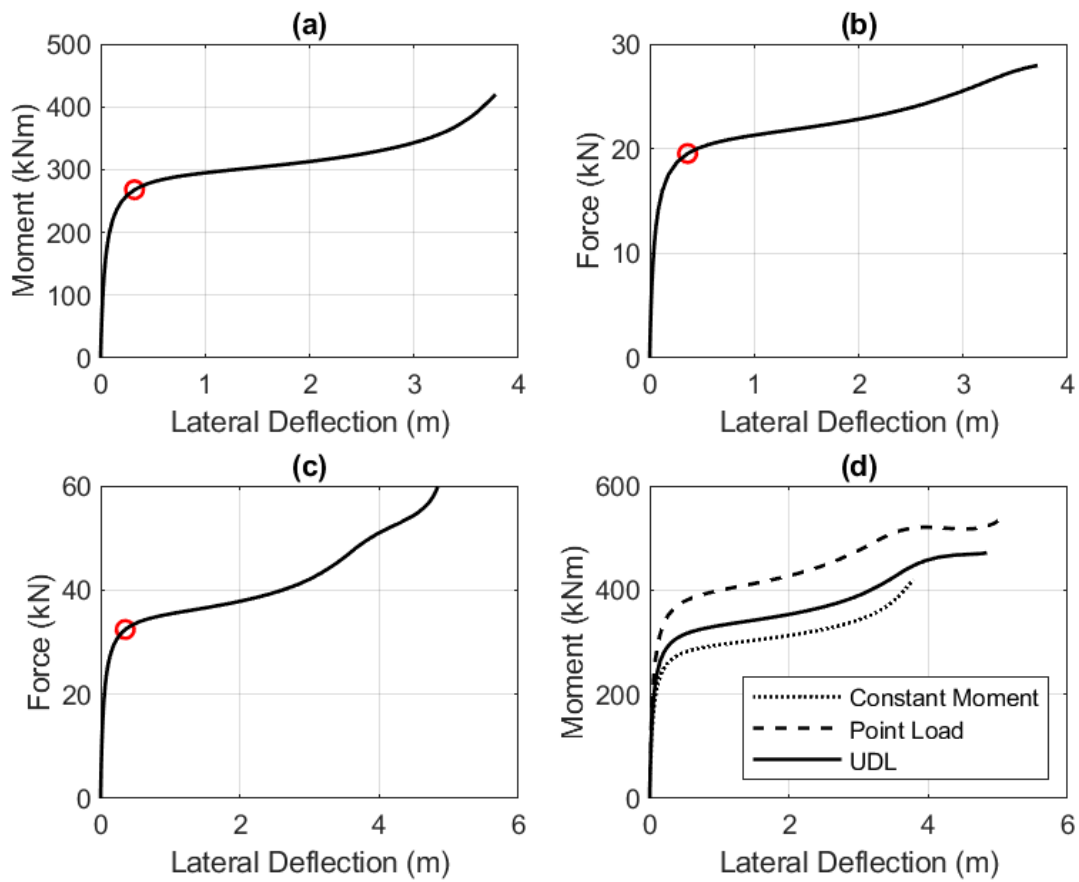


Figure A-16: Load Deflection Curves for Beams with a WT500x247 Section: (a) Constant Moment; (b) Point Load; (c) UDL; and (d) Moment Deflection Curves for all Three Loading Scenarios.

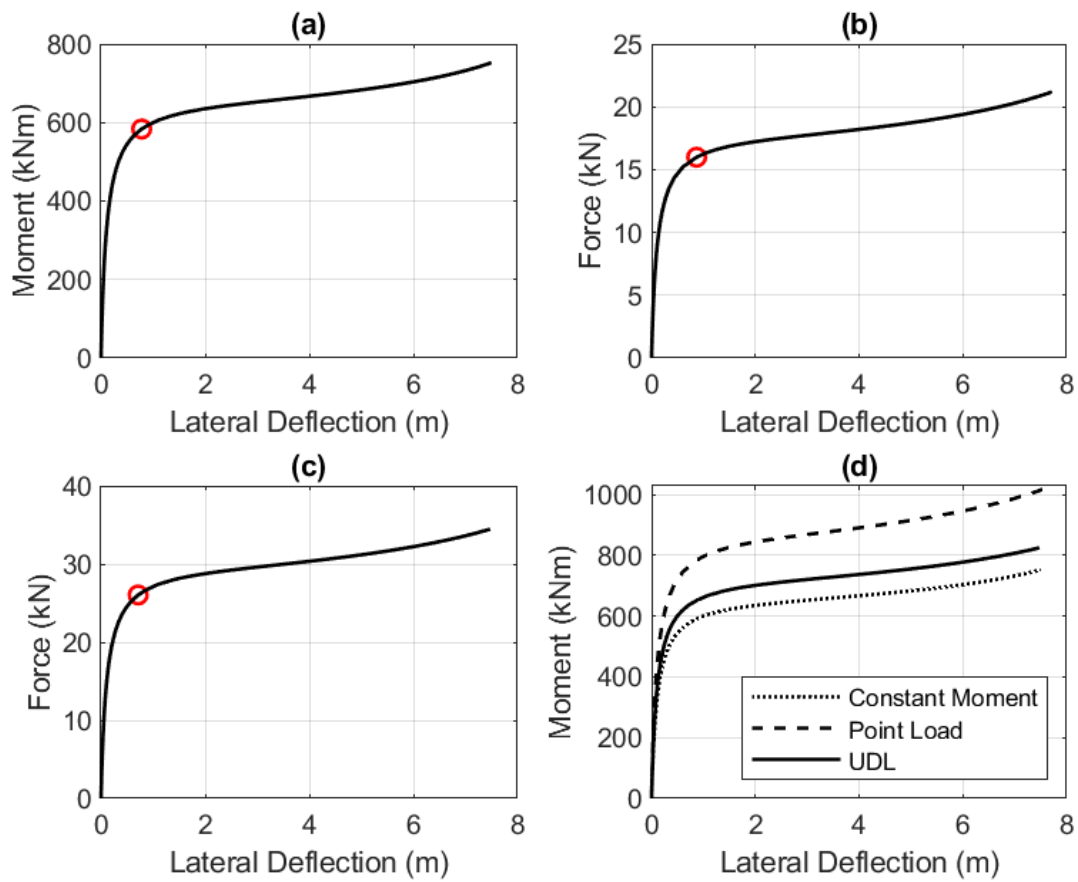


Figure A-17: Load Deflection Curves for Beams with a WT500x488 Section: (a) Constant Moment; (b) Point Load; (c) UDL; and (d) Moment Deflection Curves for all Three Loading Scenarios.

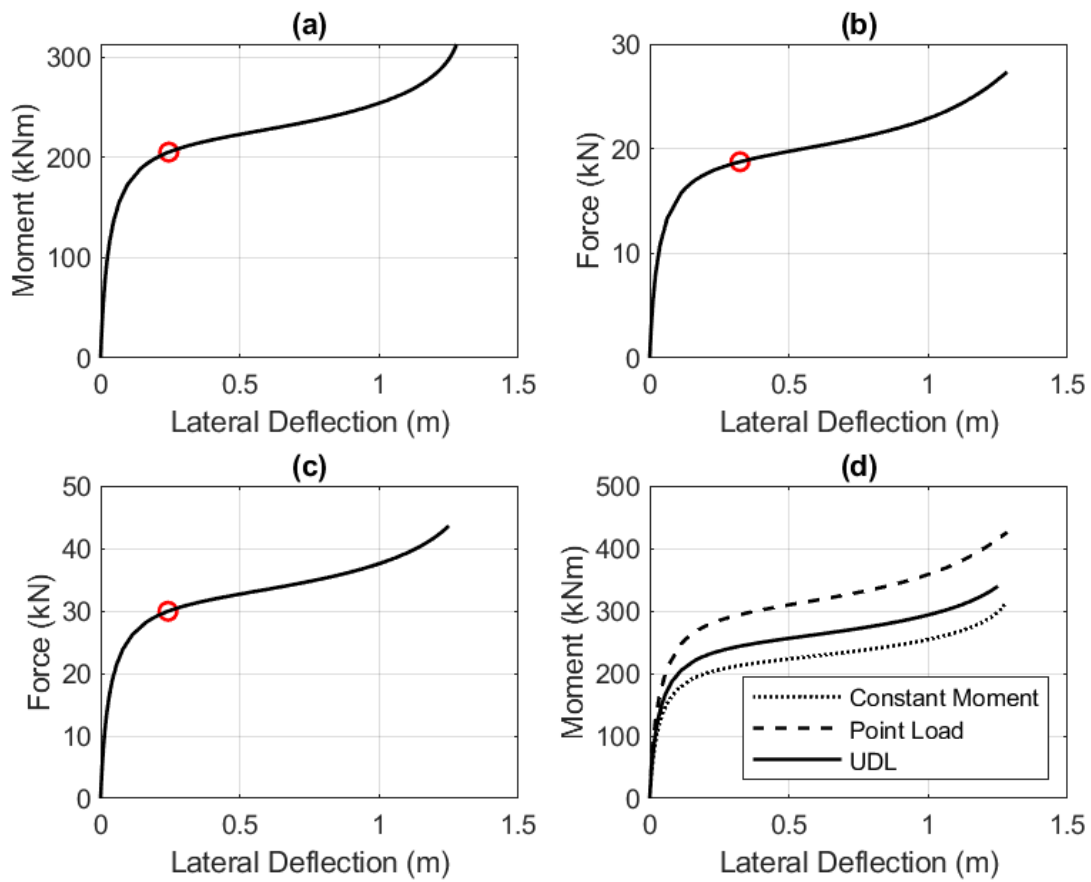


Figure A-18: Load Deflection Curves for Beams with a WT550×171 Section: (a) Constant Moment; (b) Point Load; (c) UDL; and (d) Moment Deflection Curves for all Three Loading Scenarios.

APPENDIX B: INELASTIC LATERAL-TORSIONAL BUCKLING RESULTS

B.1: Tabular Results

The following are tables outlining the entirety of the test data:

Table B-1: ABAQUS Moments: Slenderness Ratio = 5

Section	M_p (kNm)	Constant Moment (kNm)	Point Load (kNm)	UDL (kNm)
WT100×11	10.8	10.5	11.0	10.8
WT155×19	23.7	22.8	23.3	23.6
WT265×36	100.7	99.1	101.0	101.3
WT265×109	239.8	229.8	238.7	238.0
WT265×184	427.8	411.7	427.8	427.7
WT305×70	204.2	201.7	205.4	206.8
WT305×186	489.9	475.6	487.2	493.0
WT345×274	852.2	820.3	838.6	860.2
WT345×401	1369.7	1307.7	1350.7	1388.7
WT380×73	307.4	299.3	297.2	308.2
WT380×194	634.8	609.4	608.4	629.9
WT420×236	869.4	842.8	834.2	872.0
WT460×393	1683.6	1622.6	1602.6	1691.8
WT460×688	3484.5	3344.0	3344.4	3535.9
WT500×124	648.6	633.2	611.6	651.7
WT500×247	1307.6	1283.0	1241.6	1316.1
WT500×488	2408.1	2324.0	2278.7	2429.1
WT550×171	886.7	866.2	823.5	890.9

Table B-2: ABAQUS Moments: Slenderness Ratio = 10

Section	M_p (kNm)	Constant Moment (kNm)	Point Load (kNm)	UDL (kNm)
WT100×11	10.8	10.5	11.0	10.6
WT155×19	23.7	22.8	23.9	23.1
WT265×36	100.7	98.0	103.4	99.9
WT265×109	239.8	229.6	243.1	233.3
WT265×184	427.8	411.2	436.8	418.8
WT305×70	204.2	201.6	210.9	203.5
WT305×186	489.9	471.8	502.8	483.2
WT345×274	852.2	820.2	875.6	843.3
WT345×401	1369.7	1307.2	1412.8	1359.2
WT380×73	307.4	298.3	312.9	304.1
WT380×194	634.8	609.1	640.0	617.8
WT420×236	869.4	842.5	883.6	855.5
WT460×393	1683.6	1622.1	1710.0	1660.1
WT460×688	3484.5	3343.4	3573.8	3471.4
WT500×124	648.6	626.0	657.4	642.5
WT500×247	1307.6	1272.0	1329.1	1296.4
WT500×488	2408.1	2323.5	2450.0	2385.3
WT550×171	886.7	866.4	895.6	877.2

Table B-3: ABAQUS Moments: Slenderness Ratio = 20

Section	M_p (kNm)	Constant Moment (kNm)	Point Load (kNm)	UDL (kNm)
WT100×11	10.8	10.5	10.8	10.5
WT155×19	23.7	21.7	23.4	22.8
WT265×36	100.7	98.0	101.9	99.5
WT265×109	239.8	229.6	238.6	231.1
WT265×184	427.8	411.2	428.3	414.8
WT305×70	204.2	201.7	207.6	202.4
WT305×186	489.9	471.6	494.0	478.9
WT345×274	852.2	746.2	861.9	836.1
WT345×401	1369.7	1306.9	1390.5	1347.6
WT380×73	307.4	287.1	309.6	302.5
WT380×194	634.8	609.0	631.3	612.6
WT420×236	869.4	842.5	873.9	848.2
WT460×393	1683.6	1623.7	1694.9	1646.7
WT460×688	3484.5	3417.7	3543.0	3444.5
WT500×124	648.6	617.2	654.2	639.2
WT500×247	1307.6	1269.4	1320.3	1288.7
WT500×488	2408.1	2354.7	2434.0	2367.1
WT550×171	886.7	862.2	893.5	872.0

Table B-4: ABAQUS Moments: Slenderness Ratio = 30

Section	M_p (kNm)	Constant Moment (kNm)	Point Load (kNm)	UDL (kNm)
WT100×11	10.8	10.5	10.7	10.5
WT155×19	23.7	22.7	23.1	22.7
WT265×36	100.7	98.6	101.2	99.4
WT265×109	239.8	228.2	236.3	230.5
WT265×184	427.8	411.2	424.1	413.6
WT305×70	204.2	201.6	206.0	202.1
WT305×186	489.9	443.4	489.4	477.6
WT345×274	852.2	829.9	854.2	833.9
WT345×401	1369.7	1339.6	1377.6	1344.2
WT380×73	307.4	236.2	302.5	284.0
WT380×194	634.8	609.1	625.9	611.1
WT420×236	869.4	842.7	866.6	846.1
WT460×393	1683.6	1624.1	1681.1	1642.8
WT460×688	3484.5	3418.8	3514.8	3436.9
WT500×124	648.6	456.5	618.9	535.0
WT500×247	1307.6	1264.3	1310.9	1286.7
WT500×488	2408.1	2342.4	2415.0	2361.9
WT550×171	886.7	855.5	887.5	870.7

B.2: Graphical Results

B.2a: Constant Moment Loading Scenario

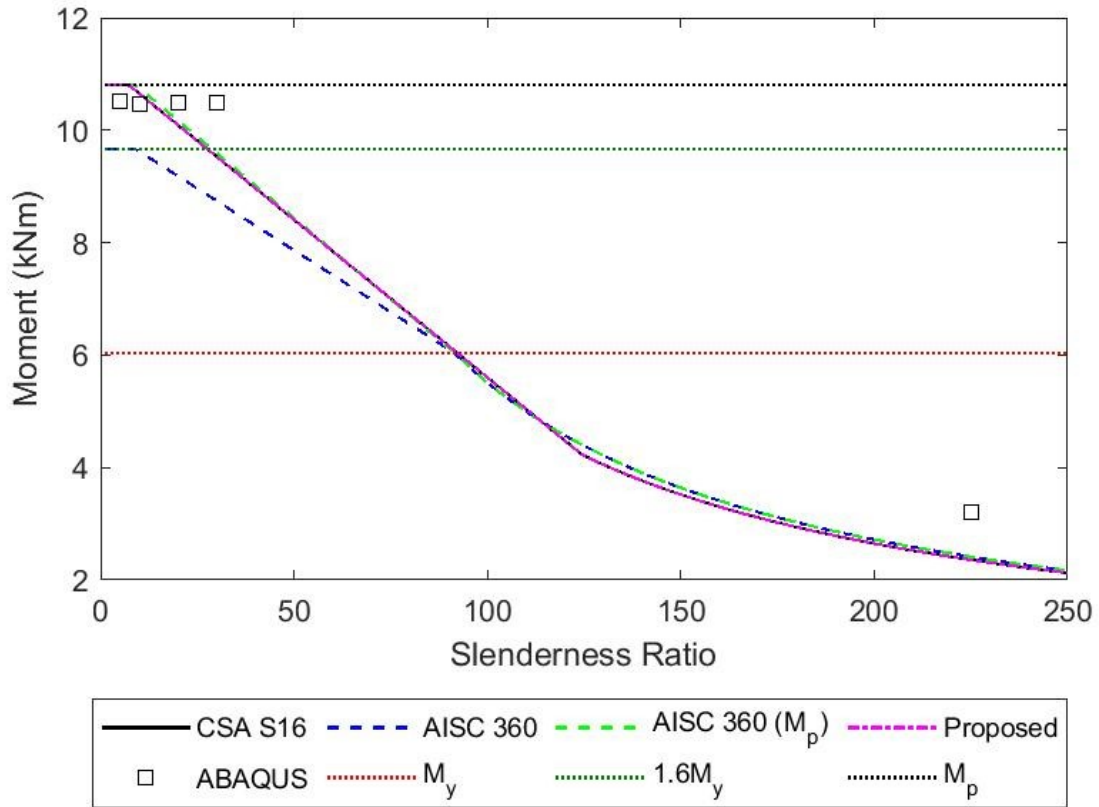


Figure B- 1: Lateral-Torsional Buckling Curve for Beams with a WT100×11 Section Subjected to a Constant Moment

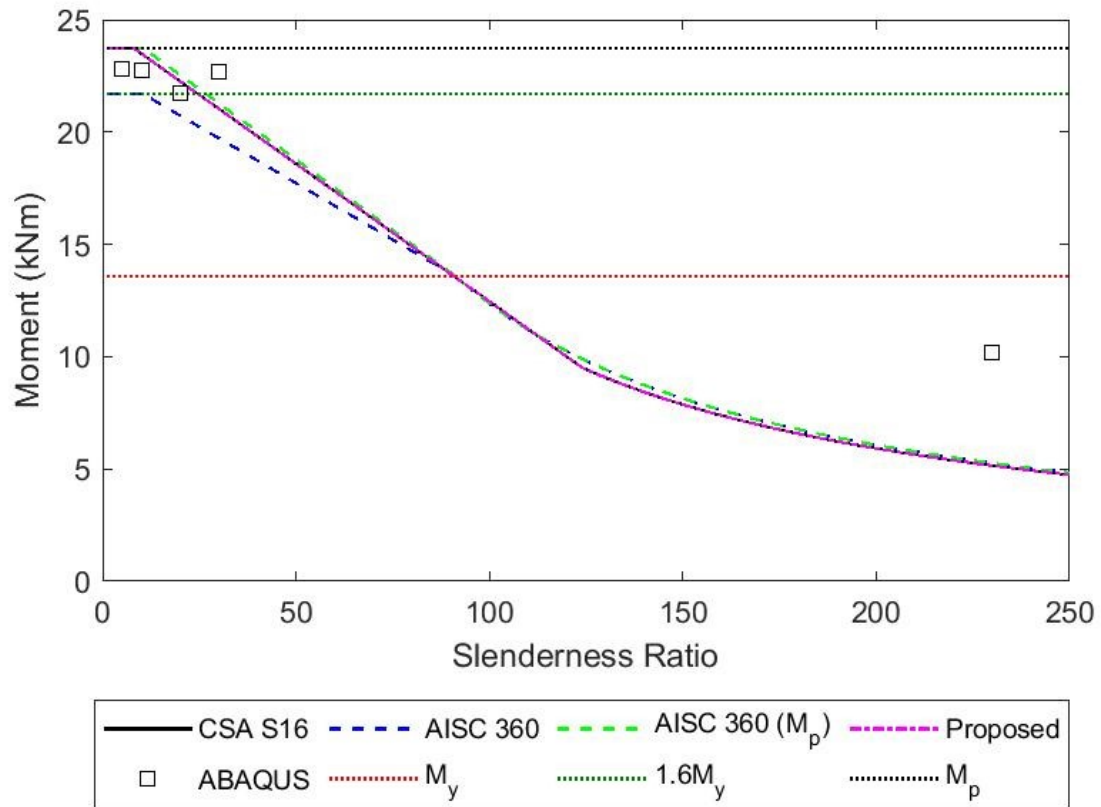


Figure B- 2: Lateral-Torsional Buckling Curve for Beams with a WT155x19 Section Subjected to a Constant Moment

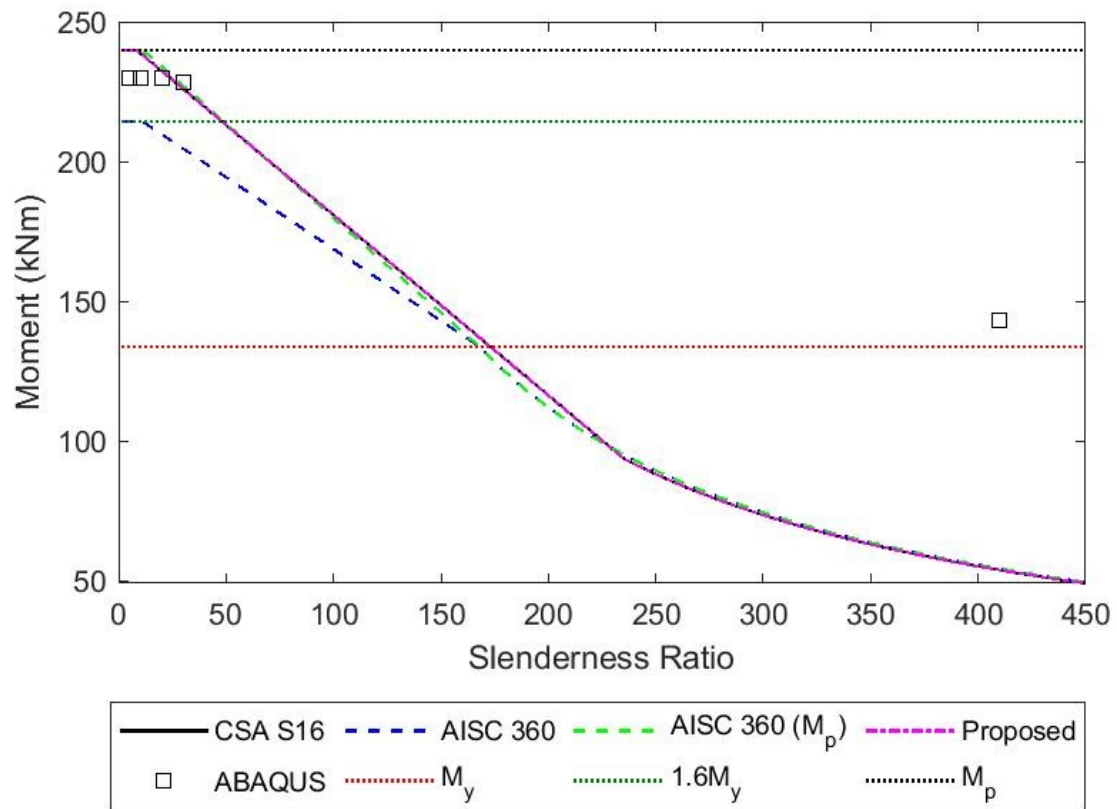


Figure B- 3: Lateral–Torsional Buckling Curve for Beams with a WT265×109 Section Subjected to a Constant Moment

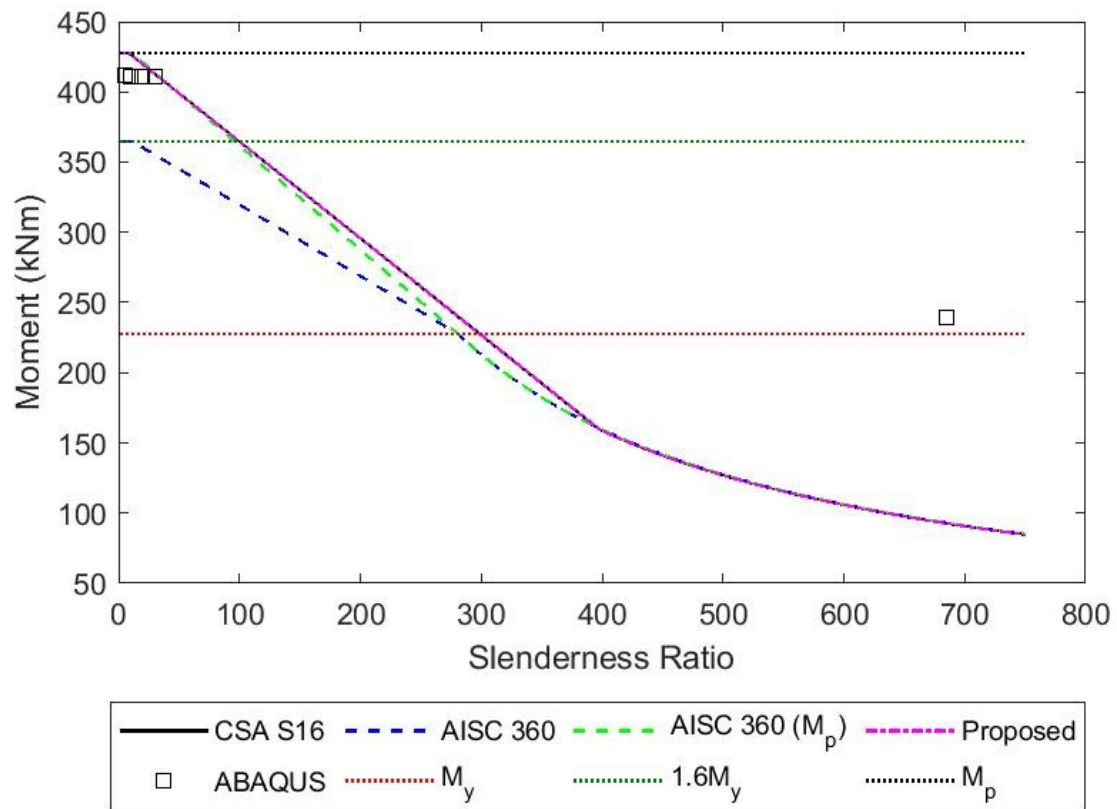


Figure B- 4: Lateral-Torsional Buckling Curve for Beams with a WT265x184 Section Subjected to a Constant Moment

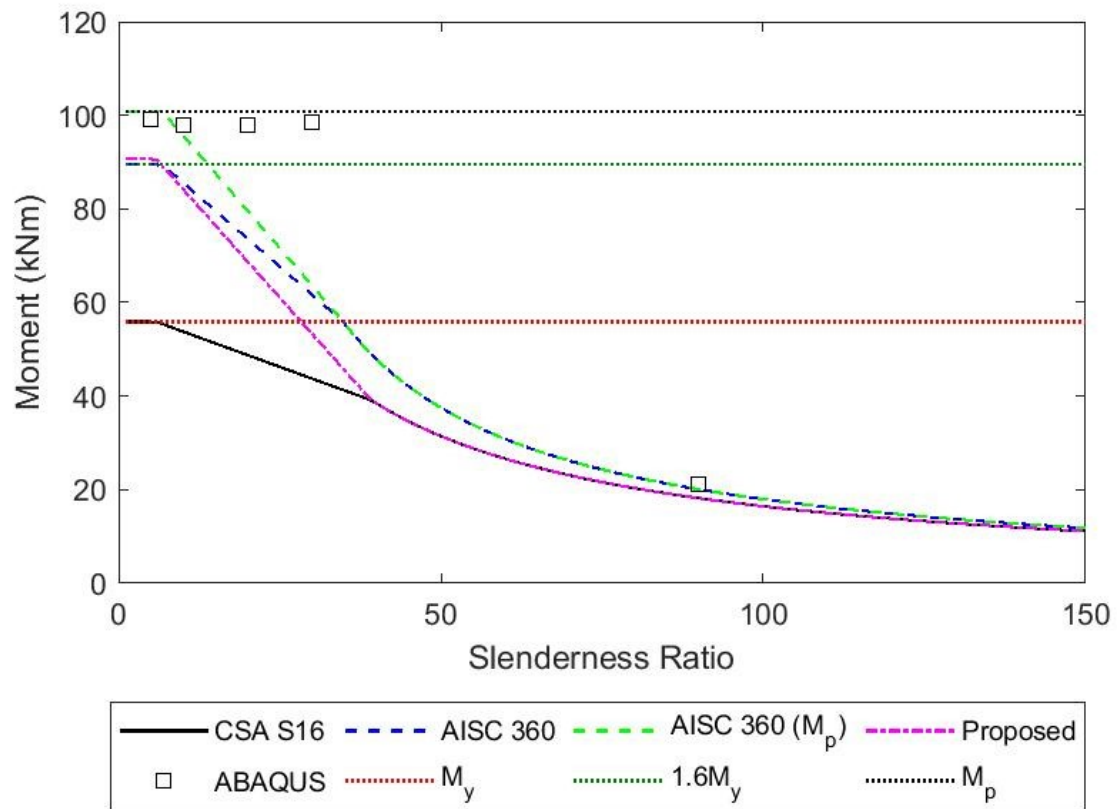


Figure B- 5: Lateral-Torsional Buckling Curve for Beams with a WT265x36 Section Subjected to a Constant Moment

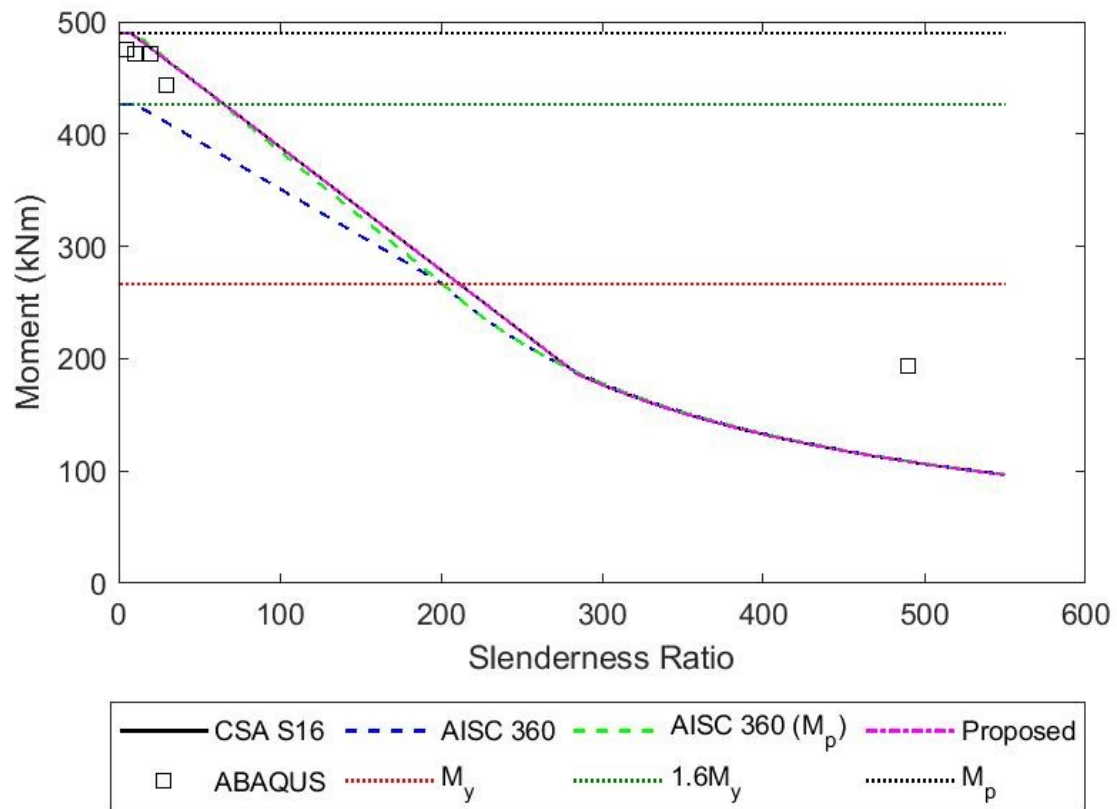


Figure B- 6: Lateral-Torsional Buckling Curve for Beams with a WT305x186 Section Subjected to a Constant Moment

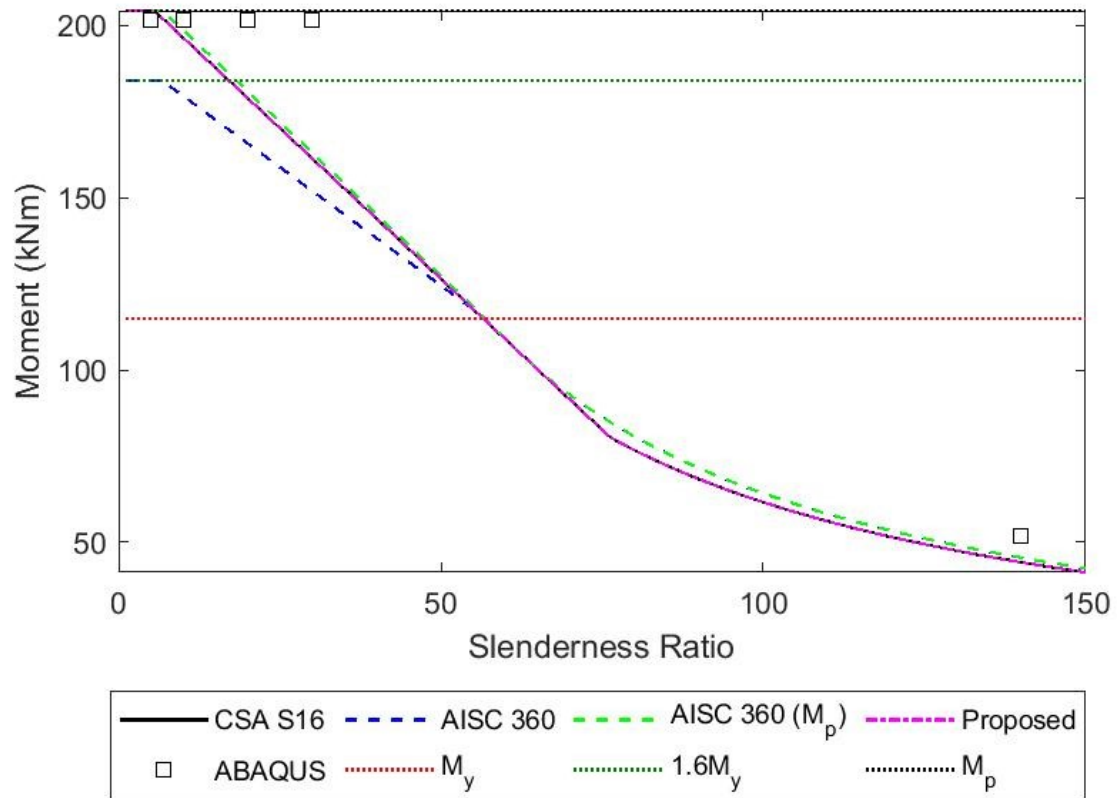


Figure B- 7: Lateral-Torsional Buckling Curve for Beams with a WT305x70 Section Subjected to a Constant Moment

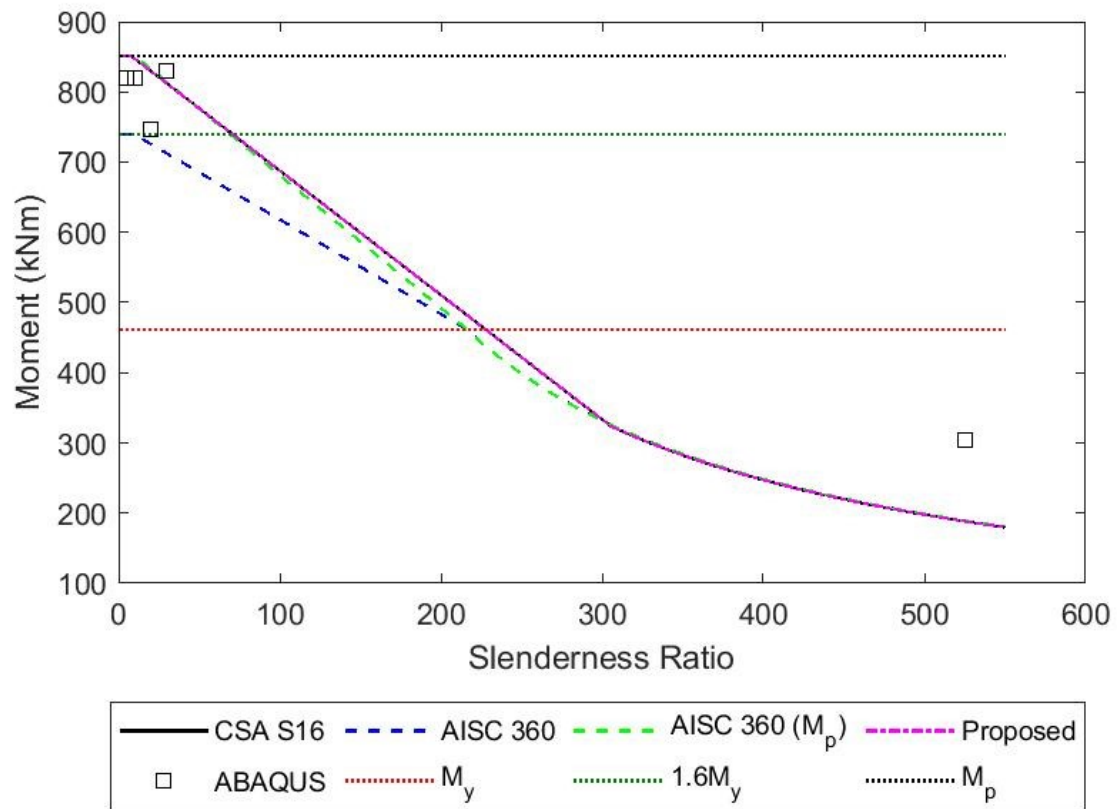


Figure B- 8: Lateral-Torsional Buckling Curve for Beams with a WT345x274 Section Subjected to a Constant Moment

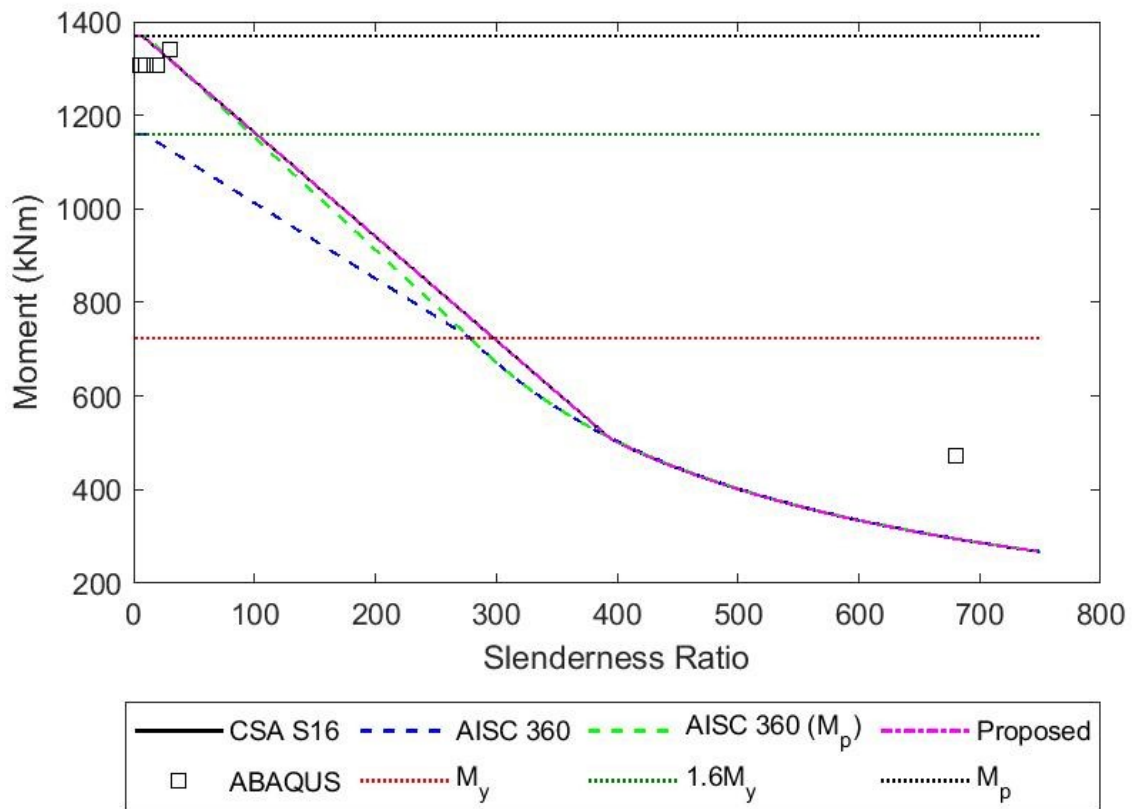


Figure B- 9: Lateral-Torsional Buckling Curve for Beams with a WT345x401 Section Subjected to a Constant Moment

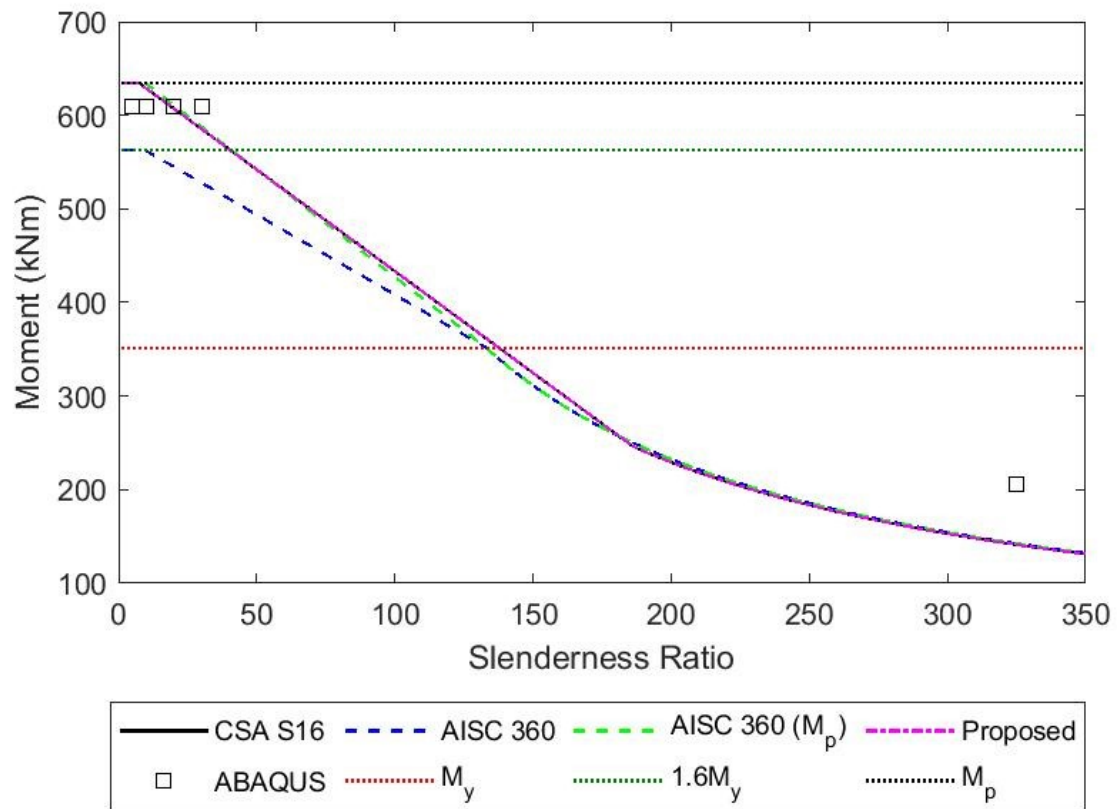


Figure B- 10: Lateral-Torsional Buckling Curve for Beams with a WT380x194 Section Subjected to a Constant Moment

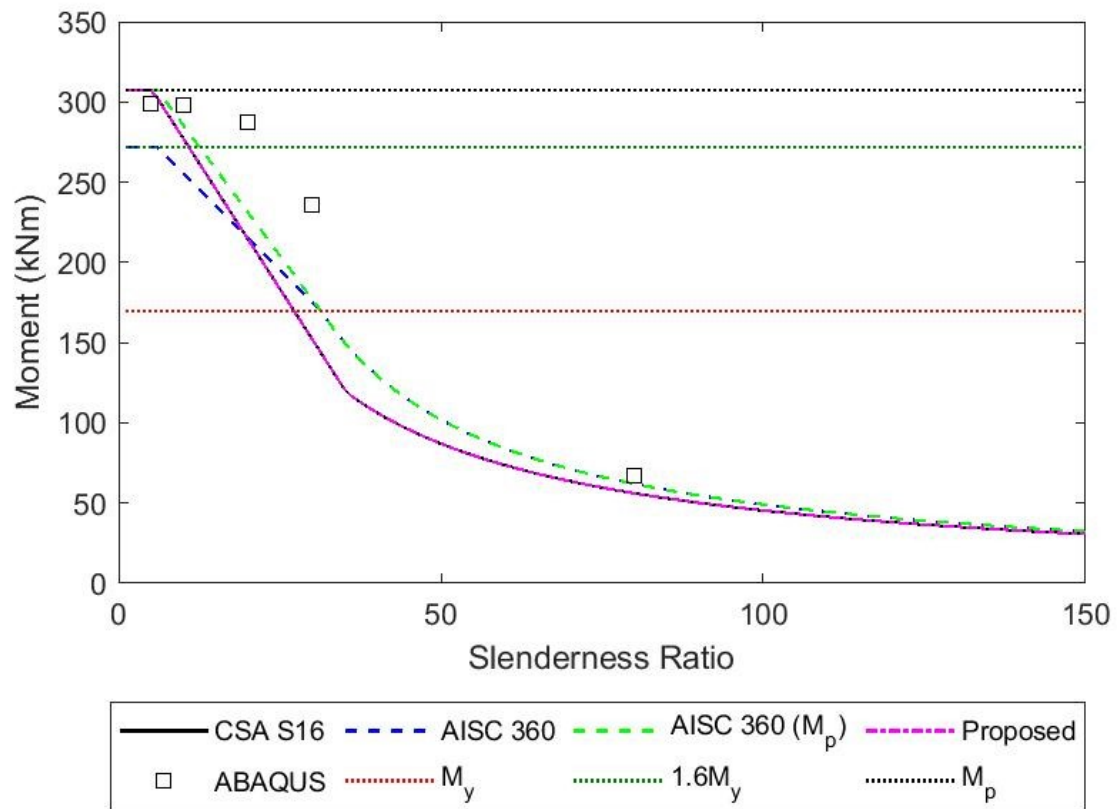


Figure B- 11: Lateral-Torsional Buckling Curve for Beams with a WT380x73 Section Subjected to a Constant Moment

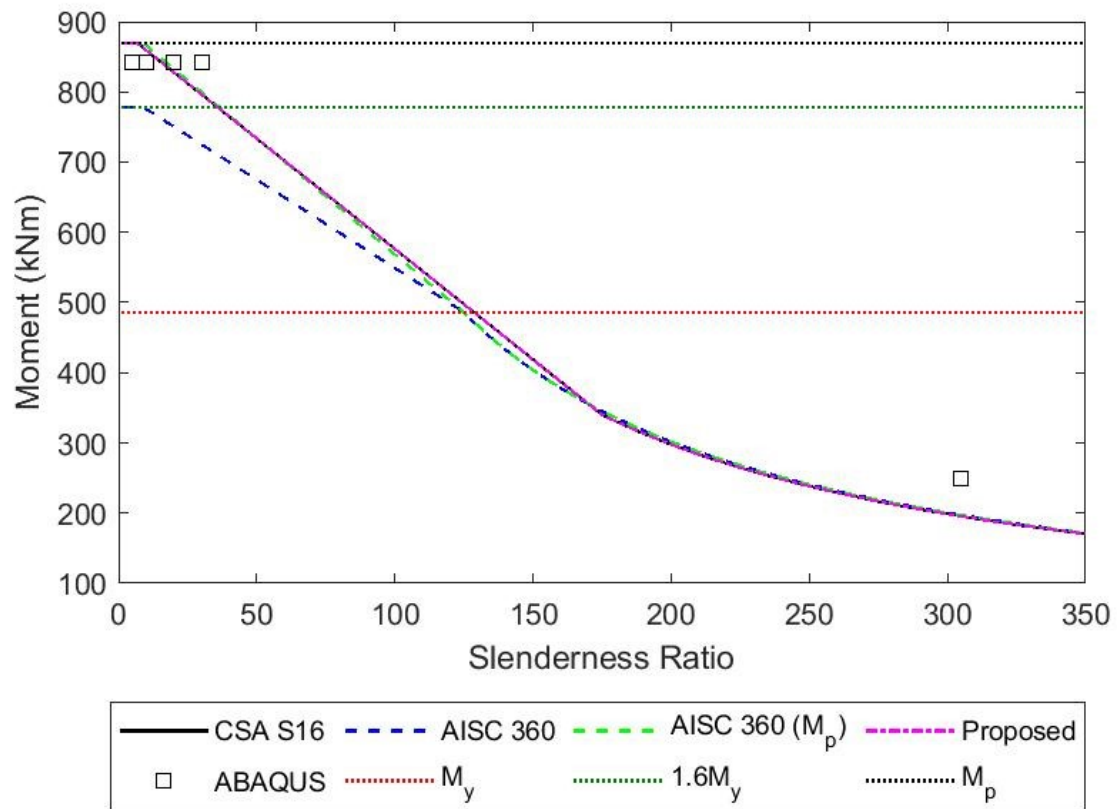


Figure B- 12: Lateral-Torsional Buckling Curve for Beams with a WT420x236 Section Subjected to a Constant Moment

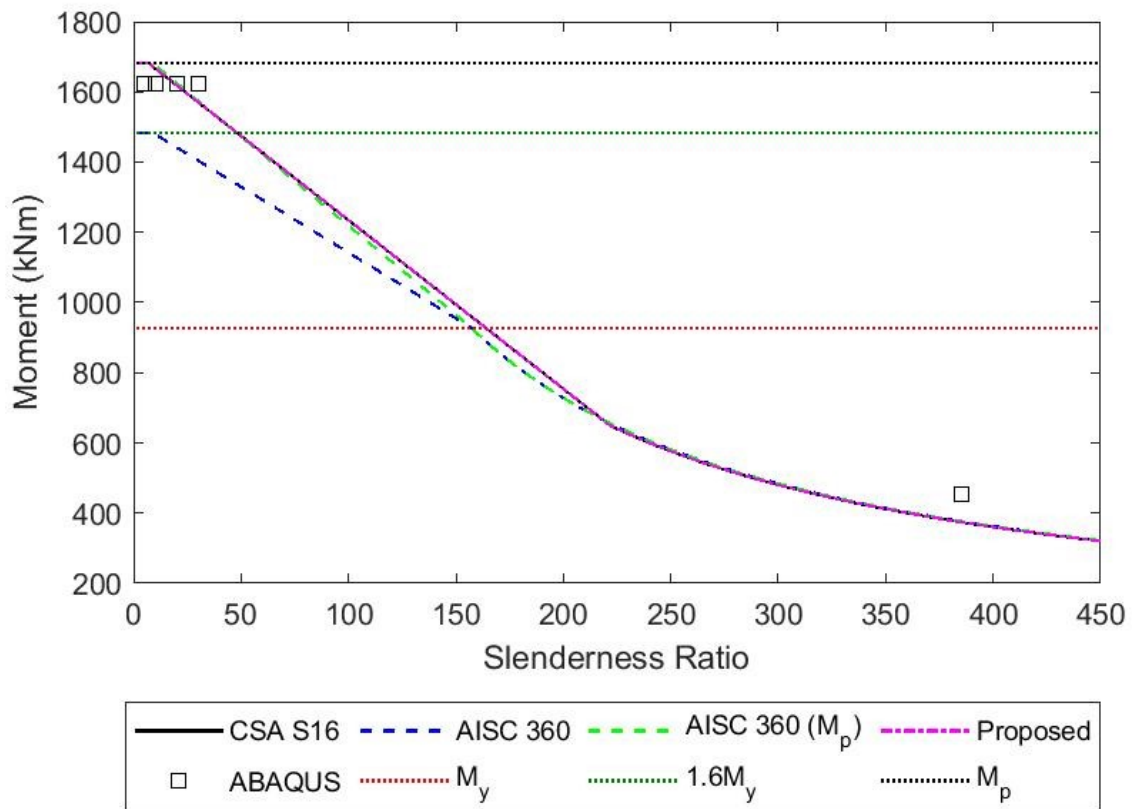


Figure B- 13: Lateral-Torsional Buckling Curve for Beams with a WT460x393 Section Subjected to a Constant Moment

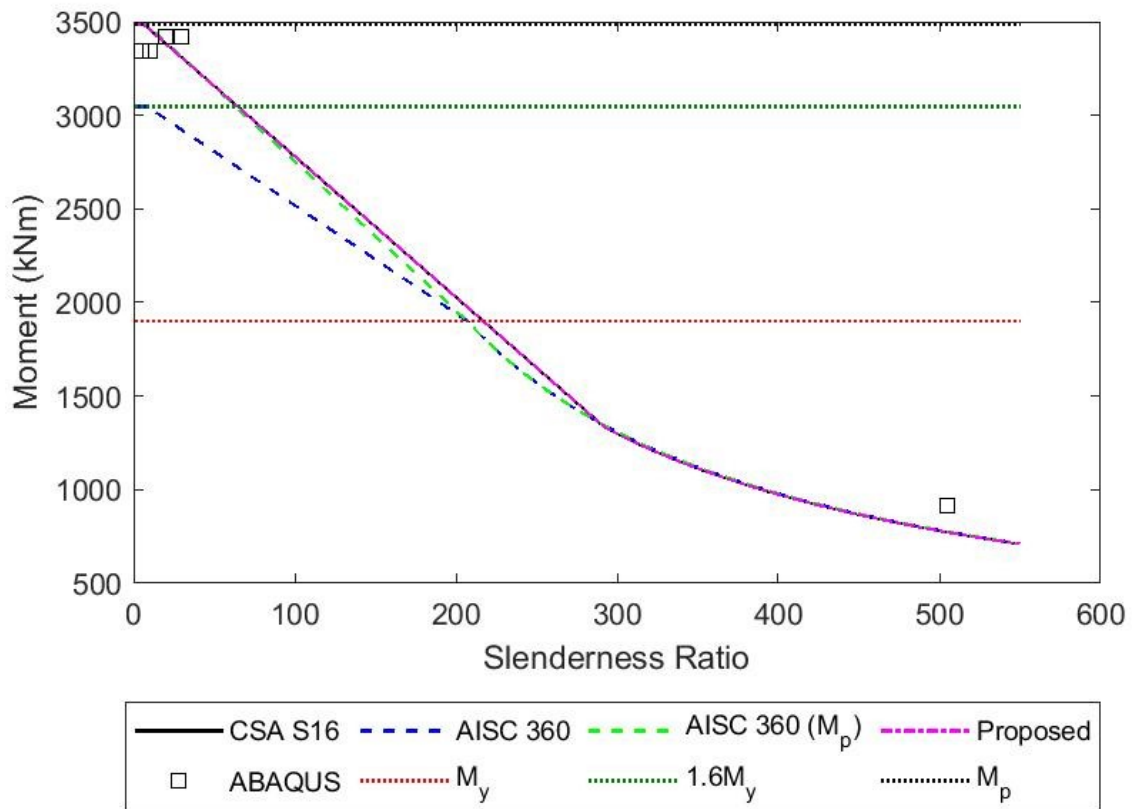


Figure B- 14: Lateral-Torsional Buckling Curve for Beams with a WT460x688 Section Subjected to a Constant Moment

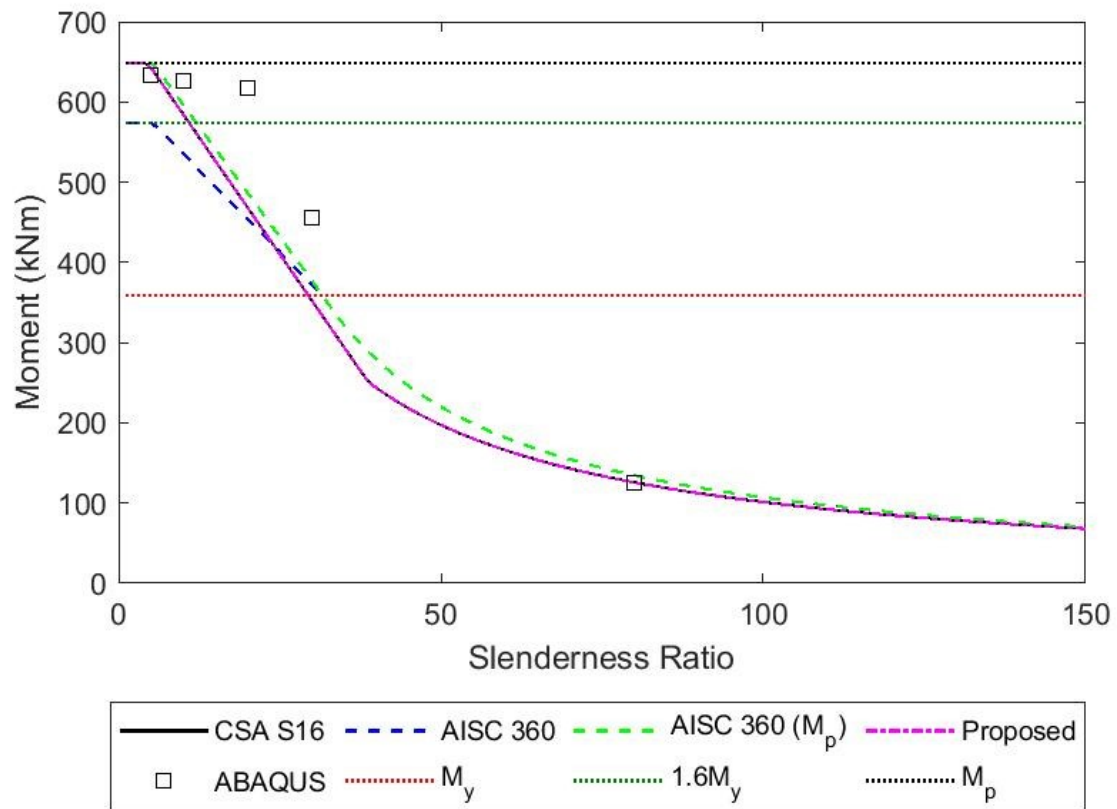


Figure B- 15: Lateral-Torsional Buckling Curve for Beams with a WT500x124 Section Subjected to a Constant Moment

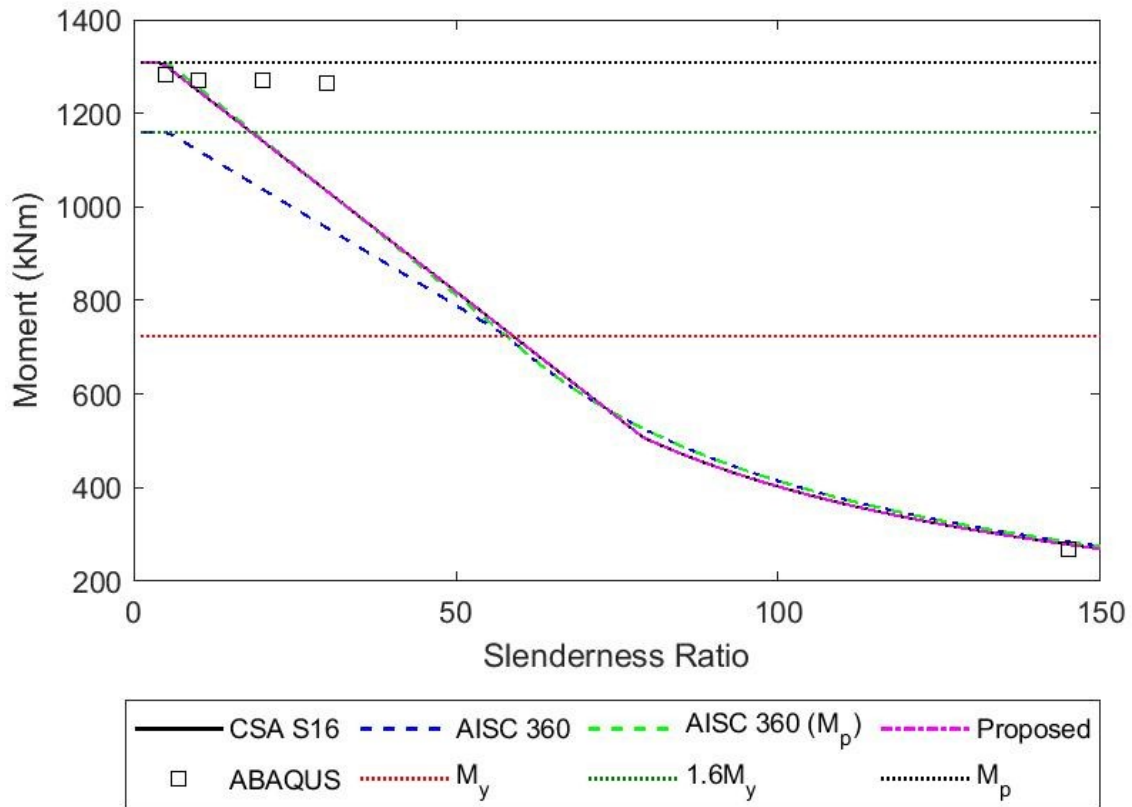


Figure B- 16: Lateral-Torsional Buckling Curve for Beams with a WT500x247 Section Subjected to a Constant Moment

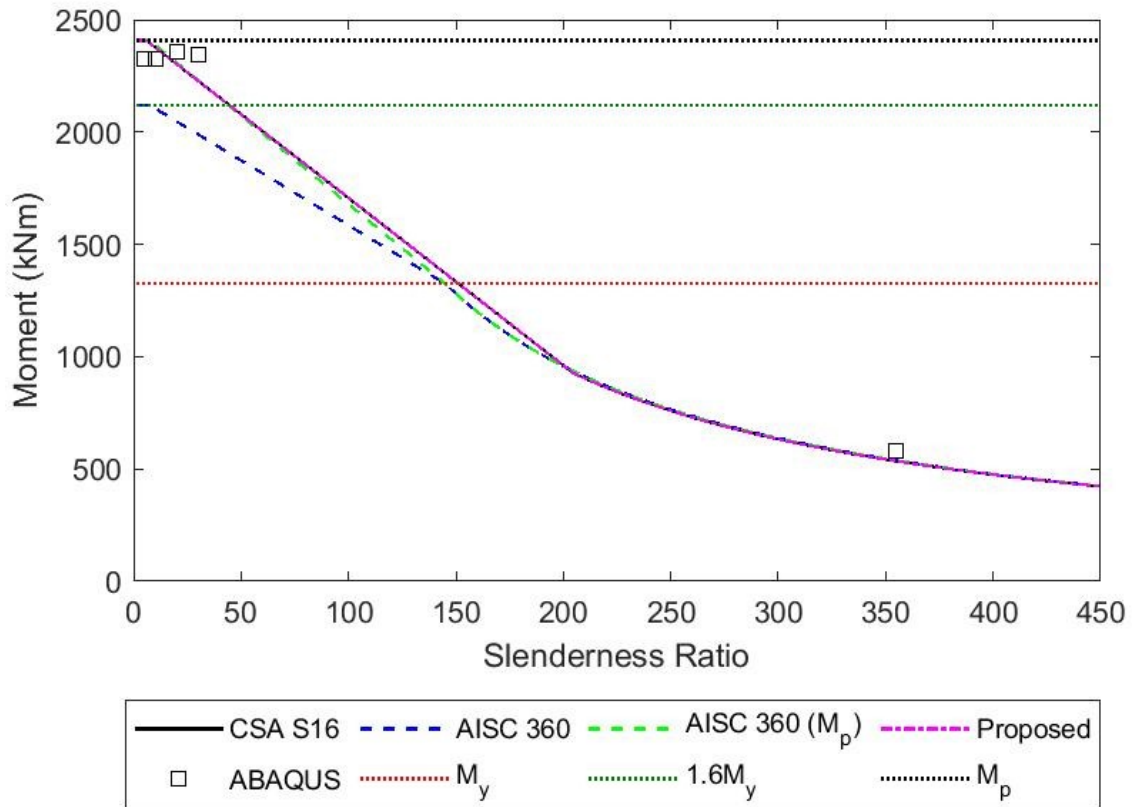


Figure B- 17: Lateral-Torsional Buckling Curve for Beams with a WT500x488 Section Subjected to a Constant Moment

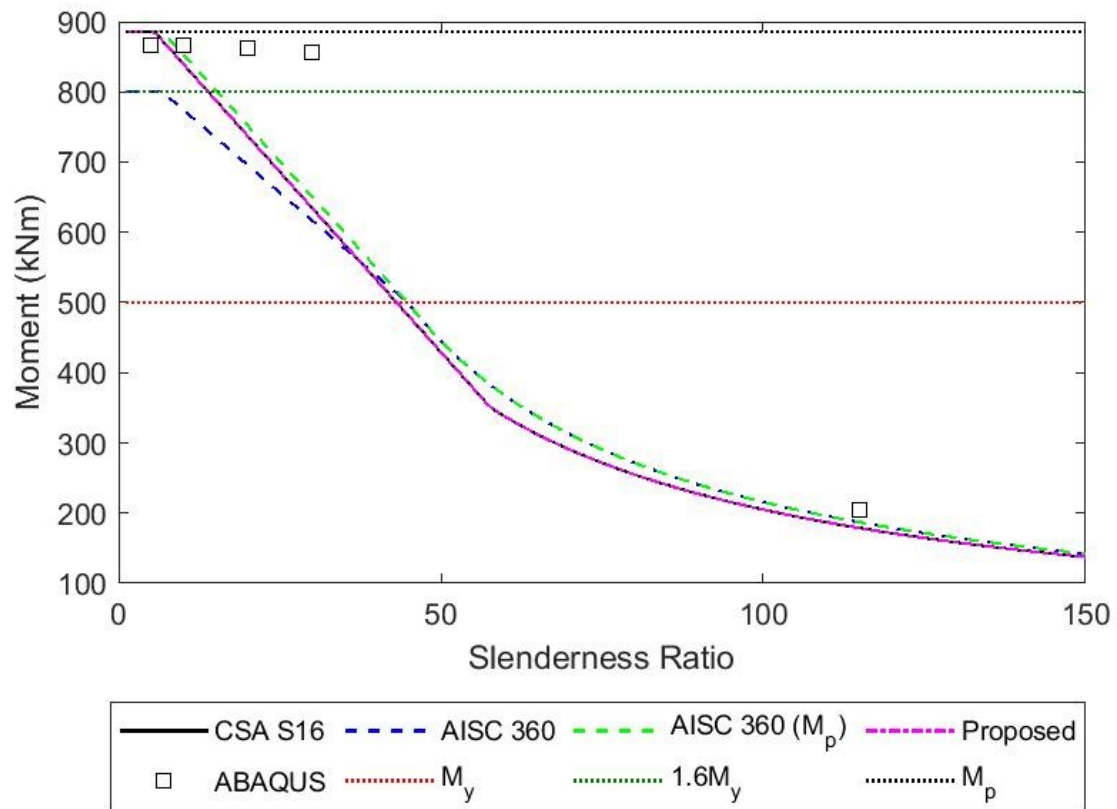


Figure B- 18: Lateral-Torsional Buckling Curve for Beams with a WT550x171 Section Subjected to a Constant Moment

B.2b: Point Load Loading Scenario

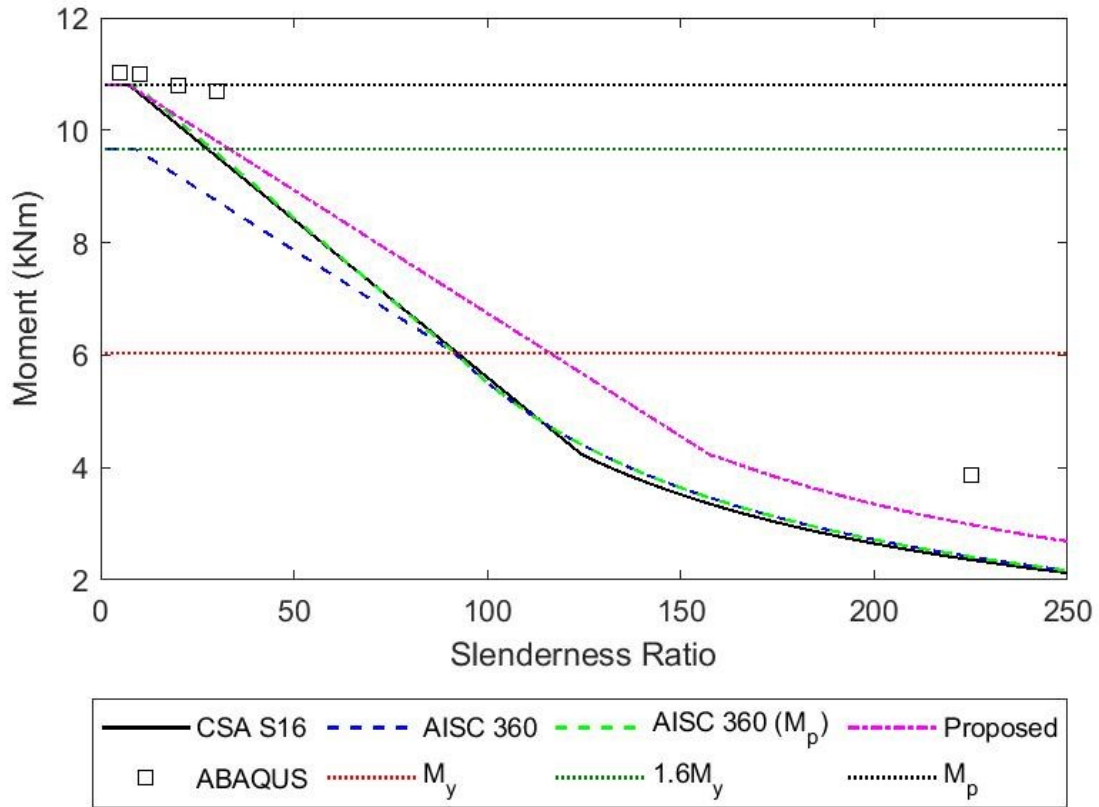


Figure B- 19: Lateral-Torsional Buckling Curve for Beams with a WT100x11 Section Subjected to a Point Load

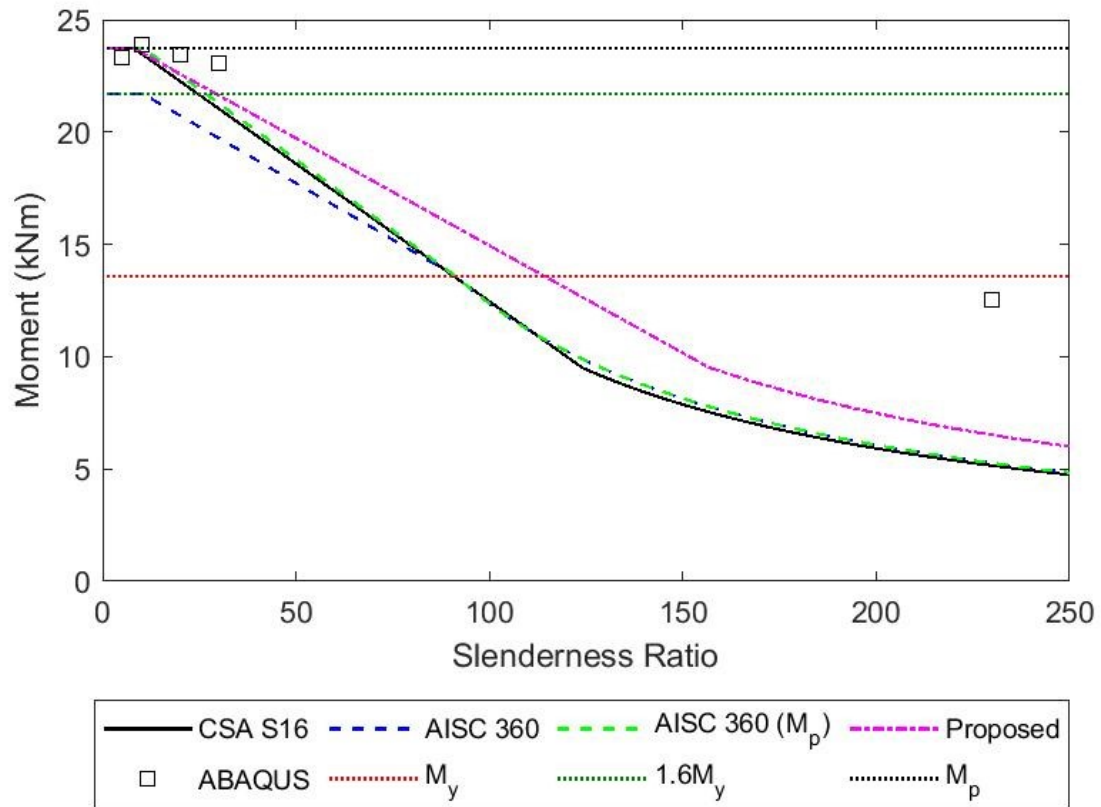


Figure B- 20: Lateral-Torsional Buckling Curve for Beams with a WT155×19 Section Subjected to a Point Load

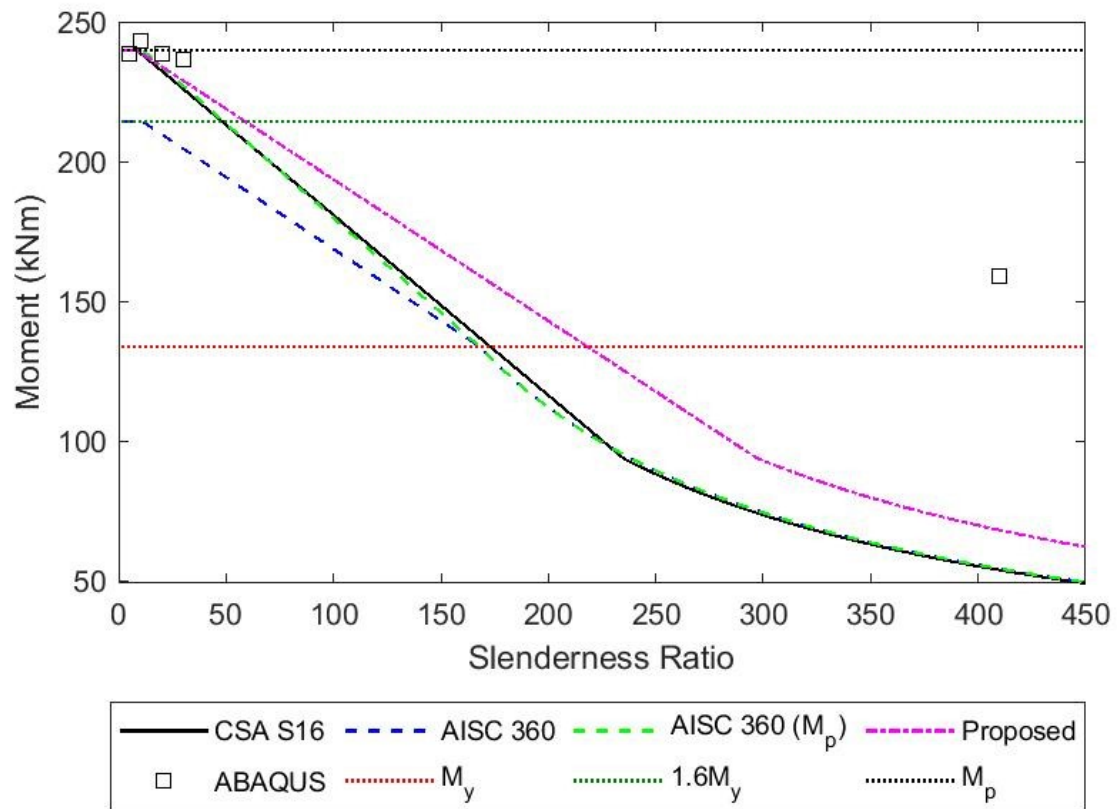


Figure B- 21: Lateral-Torsional Buckling Curve for Beams with a WT265x109 Section Subjected to a Point Load

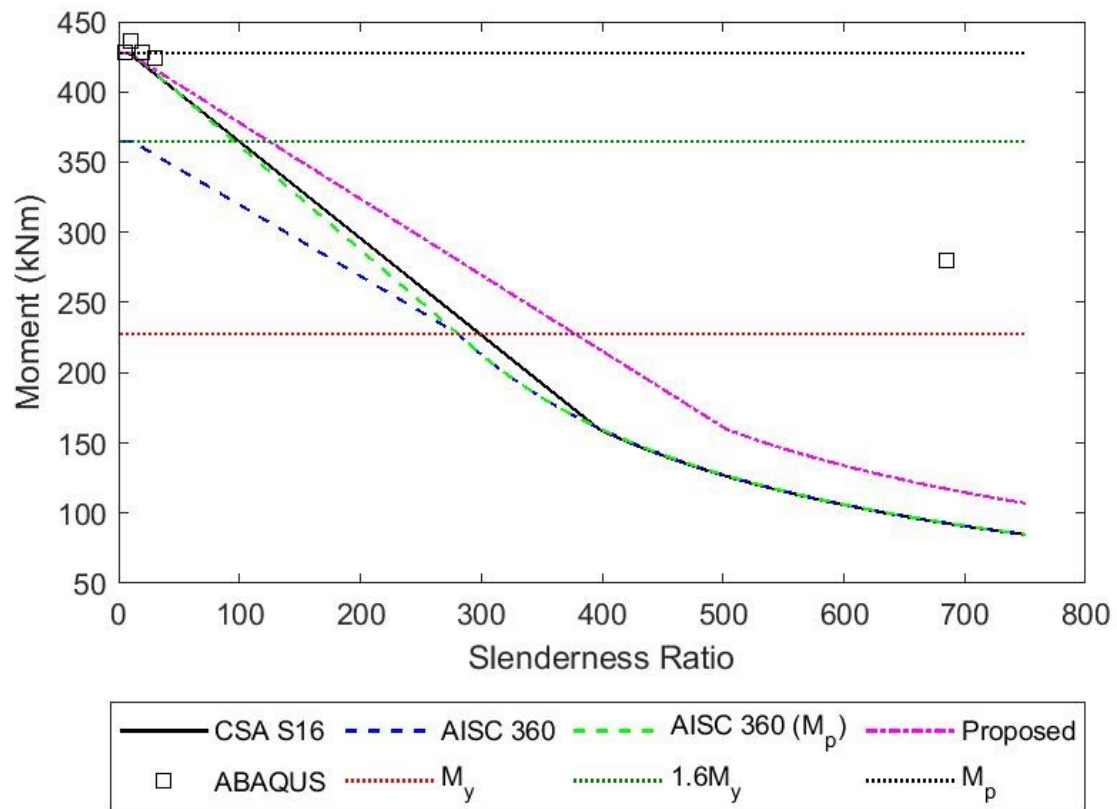


Figure B- 22: Lateral-Torsional Buckling Curve for Beams with a WT265x184 Section Subjected to a Point Load

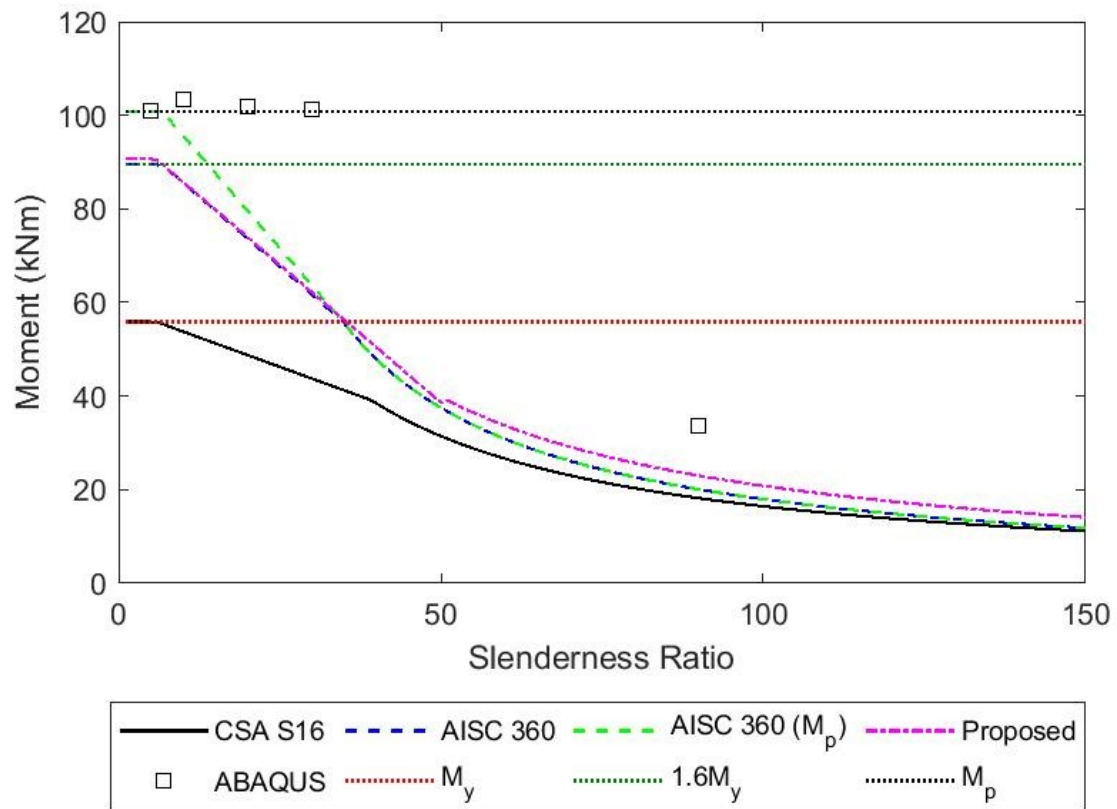


Figure B- 23: Lateral-Torsional Buckling Curve for Beams with a WT265x36 Section Subjected to a Point Load

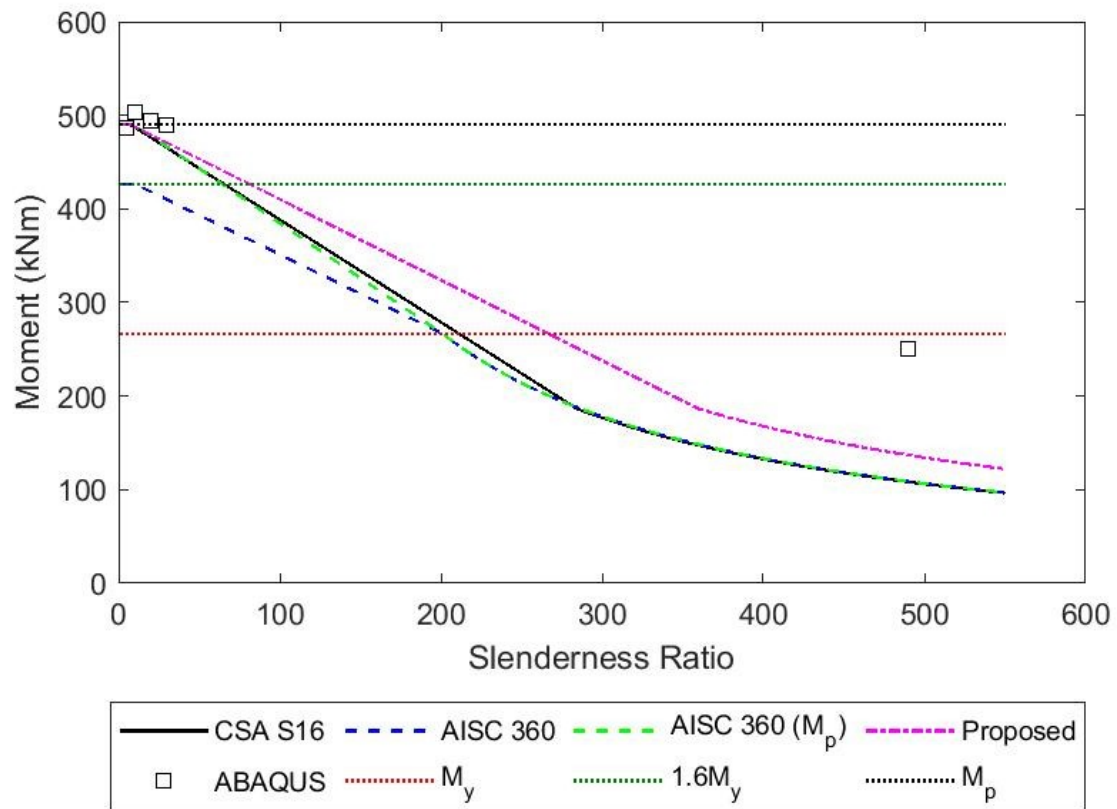


Figure B- 24: Lateral-Torsional Buckling Curve for Beams with a WT305x186 Section Subjected to a Point Load

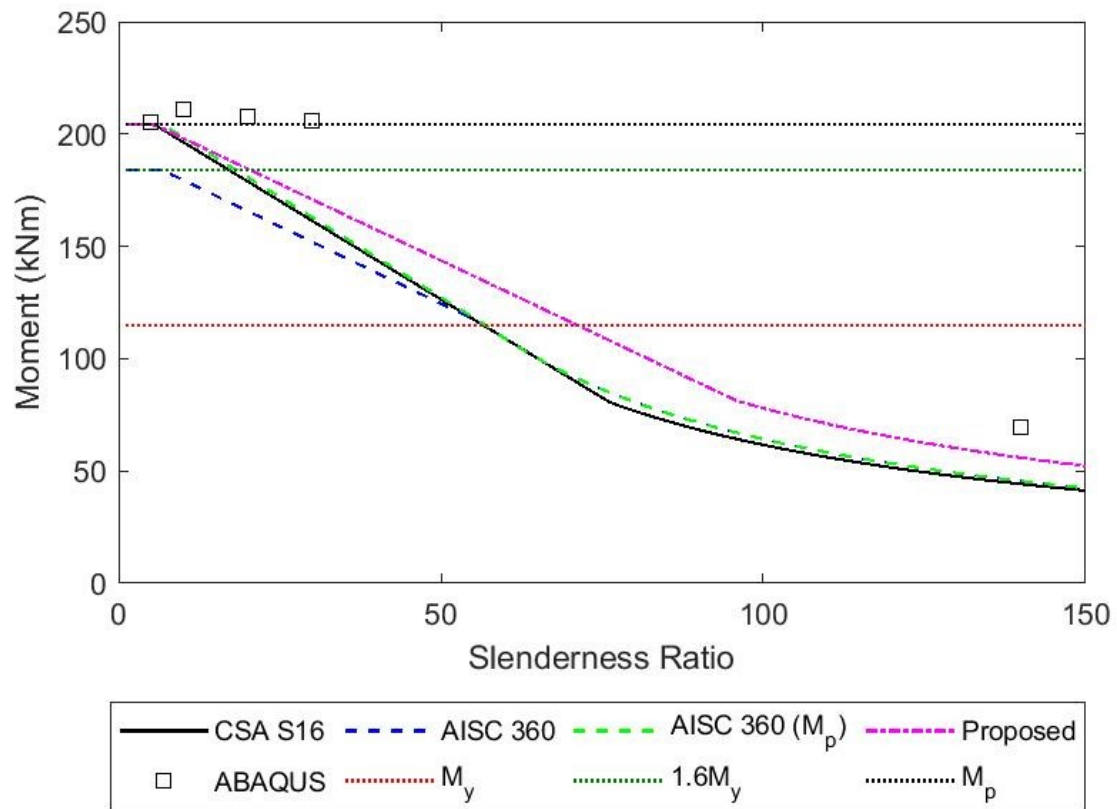


Figure B- 25: Lateral-Torsional Buckling Curve for Beams with a WT305×70 Section Subjected to a Point Load

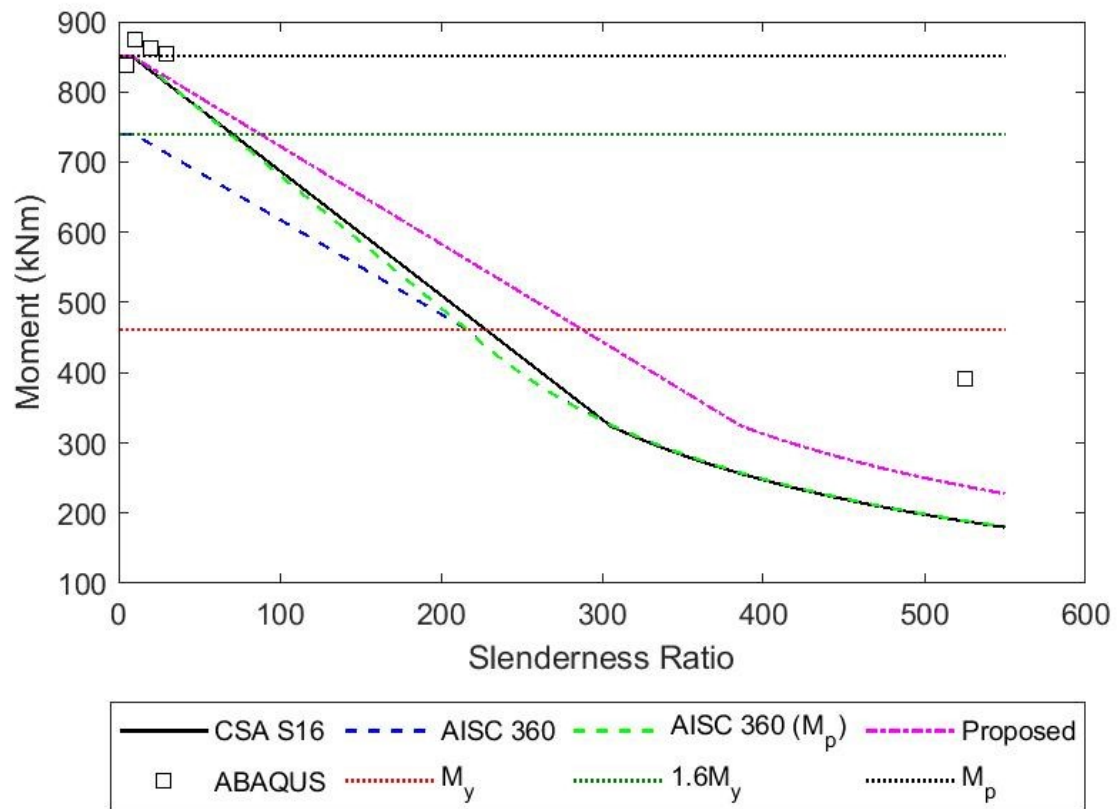


Figure B- 26: Lateral-Torsional Buckling Curve for Beams with a WT345x274 Section Subjected to a Point Load

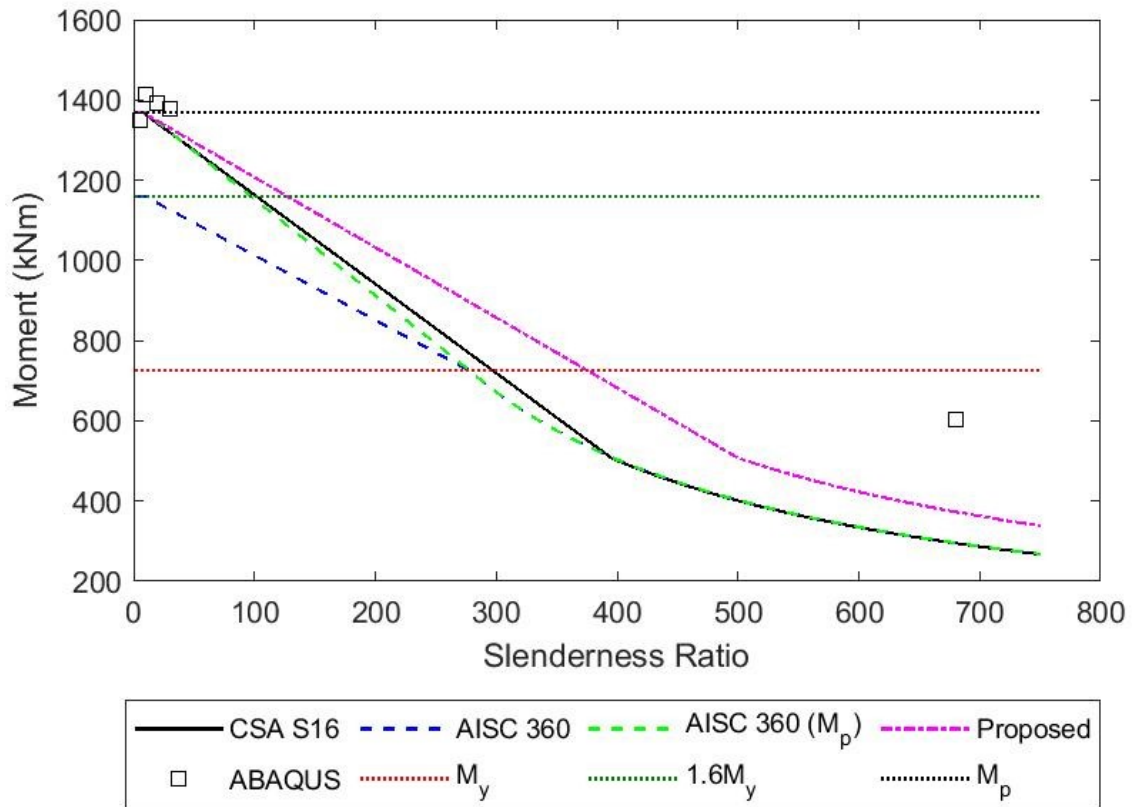


Figure B- 27: Lateral-Torsional Buckling Curve for Beams with a WT345x401 Section Subjected to a Point Load

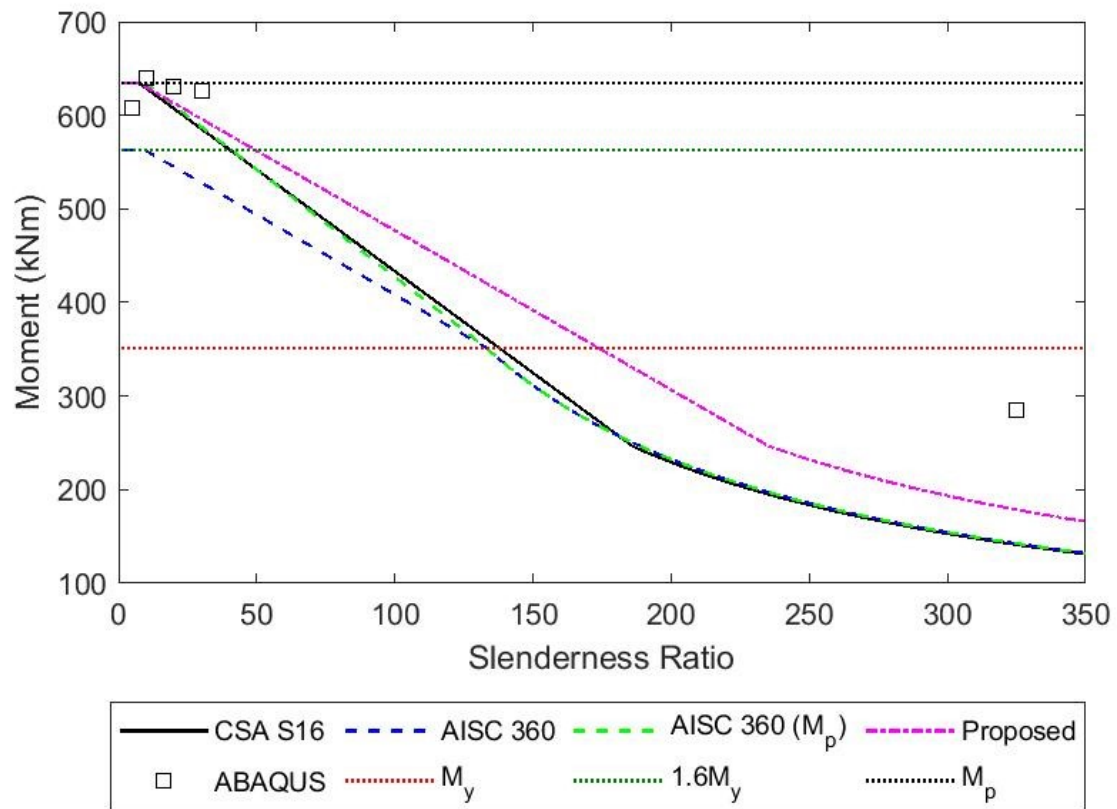


Figure B- 28: Lateral-Torsional Buckling Curve for Beams with a WT380x194 Section Subjected to a Point Load

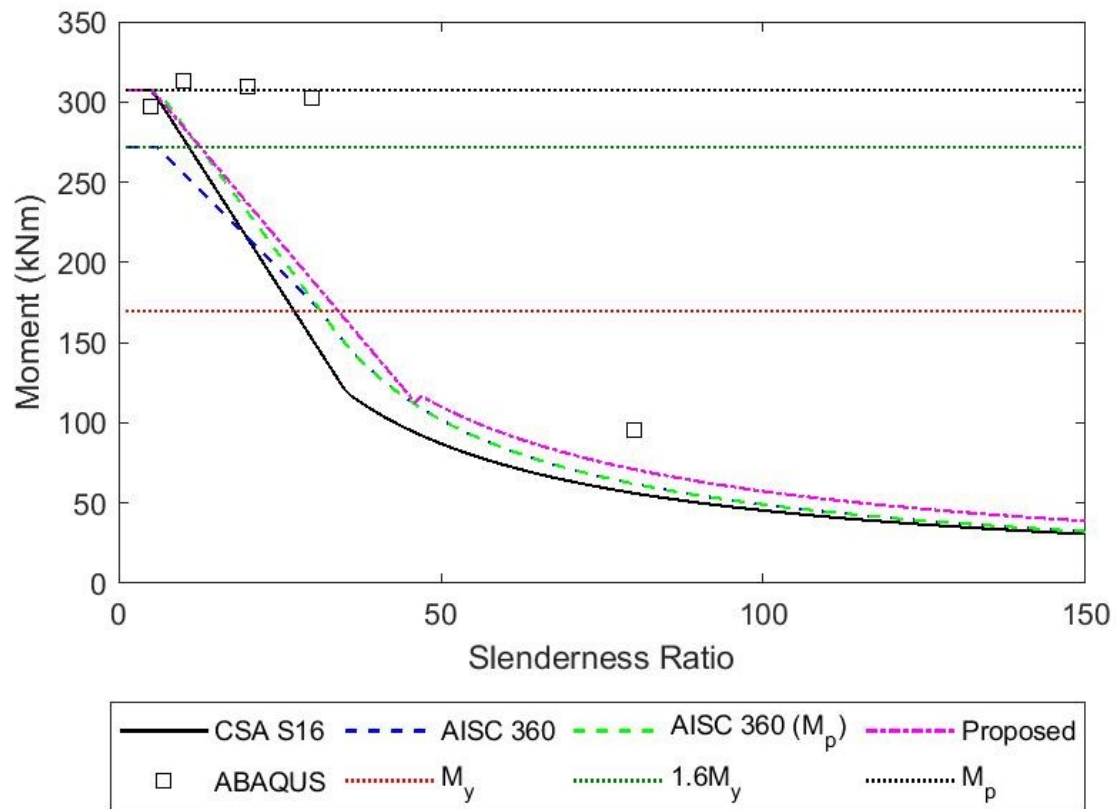


Figure B- 29: Lateral-Torsional Buckling Curve for Beams with a WT380x73 Section Subjected to a Point Load

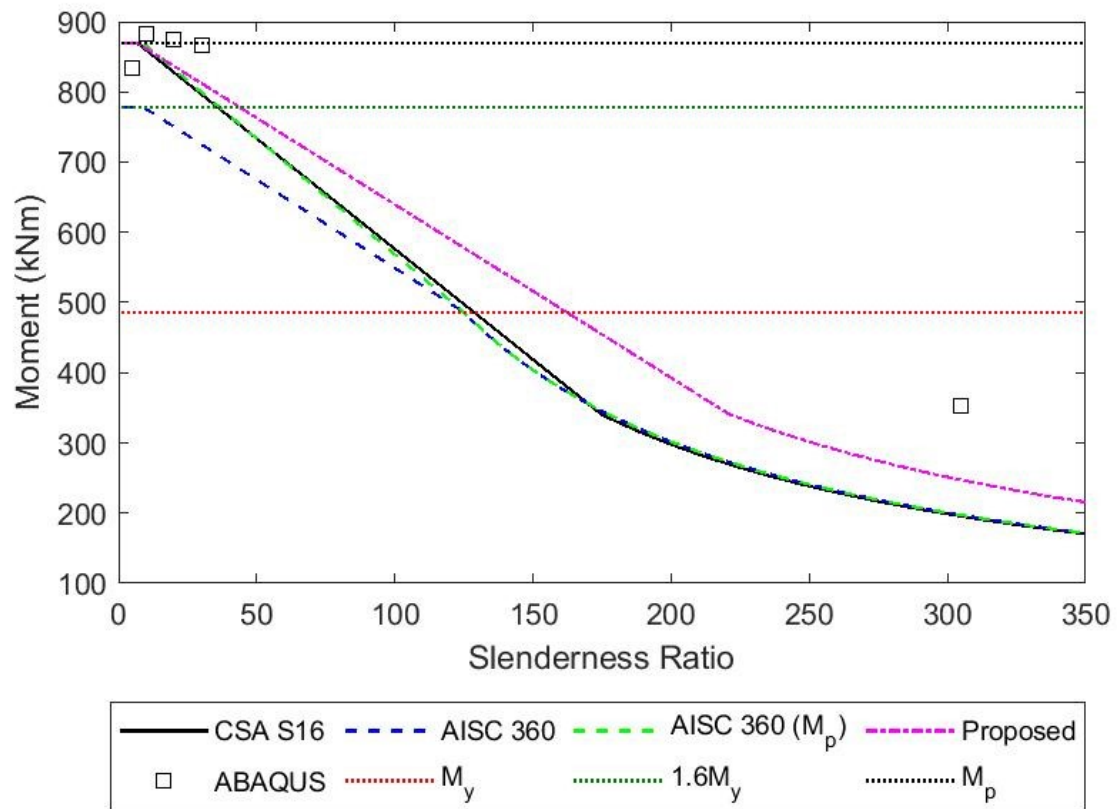


Figure B- 30: Lateral-Torsional Buckling Curve for Beams with a WT420x236 Section Subjected to a Point Load

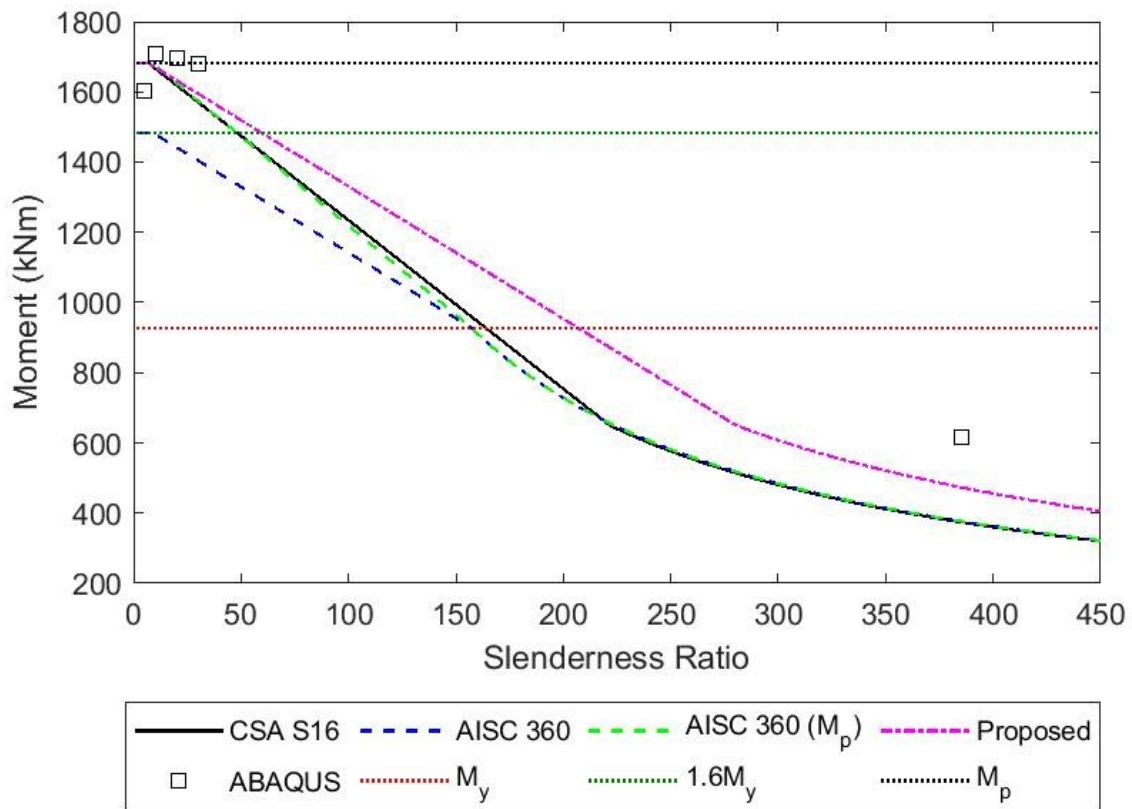


Figure B- 31: Lateral-Torsional Buckling Curve for Beams with a WT460x393 Section Subjected to a Point Load

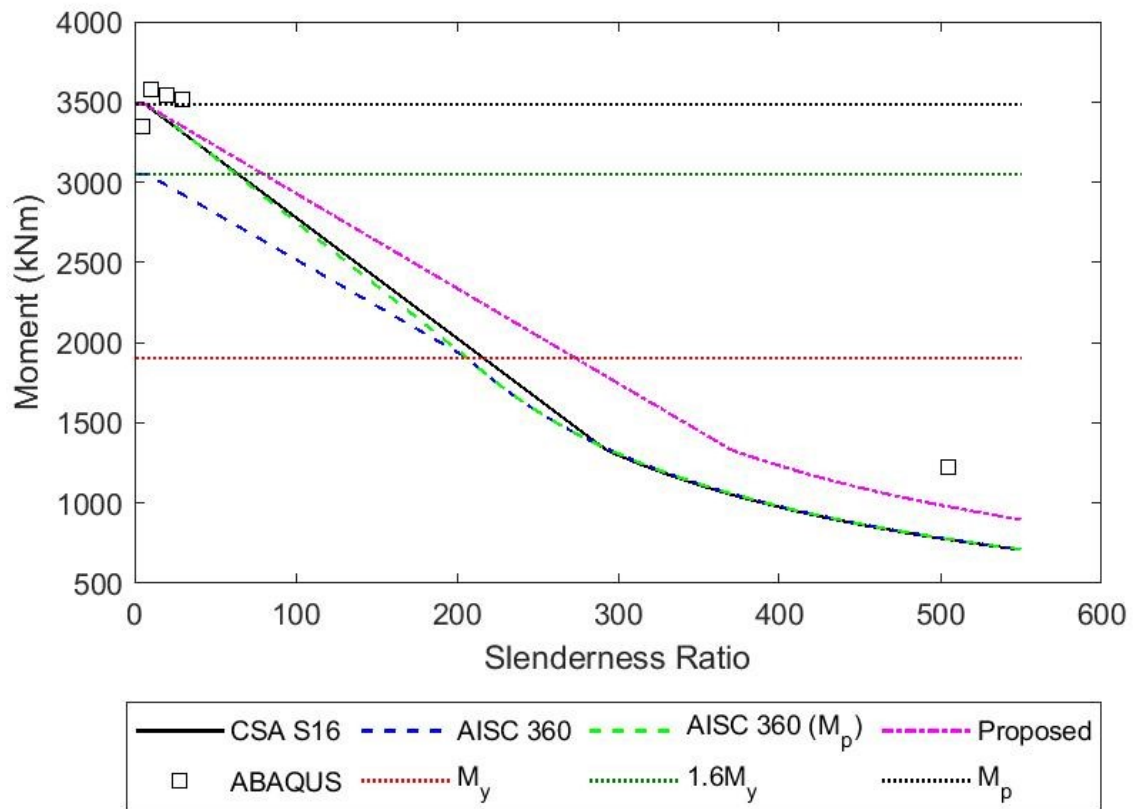


Figure B- 32: Lateral-Torsional Buckling Curve for Beams with a WT460x688 Section Subjected to a Point Load

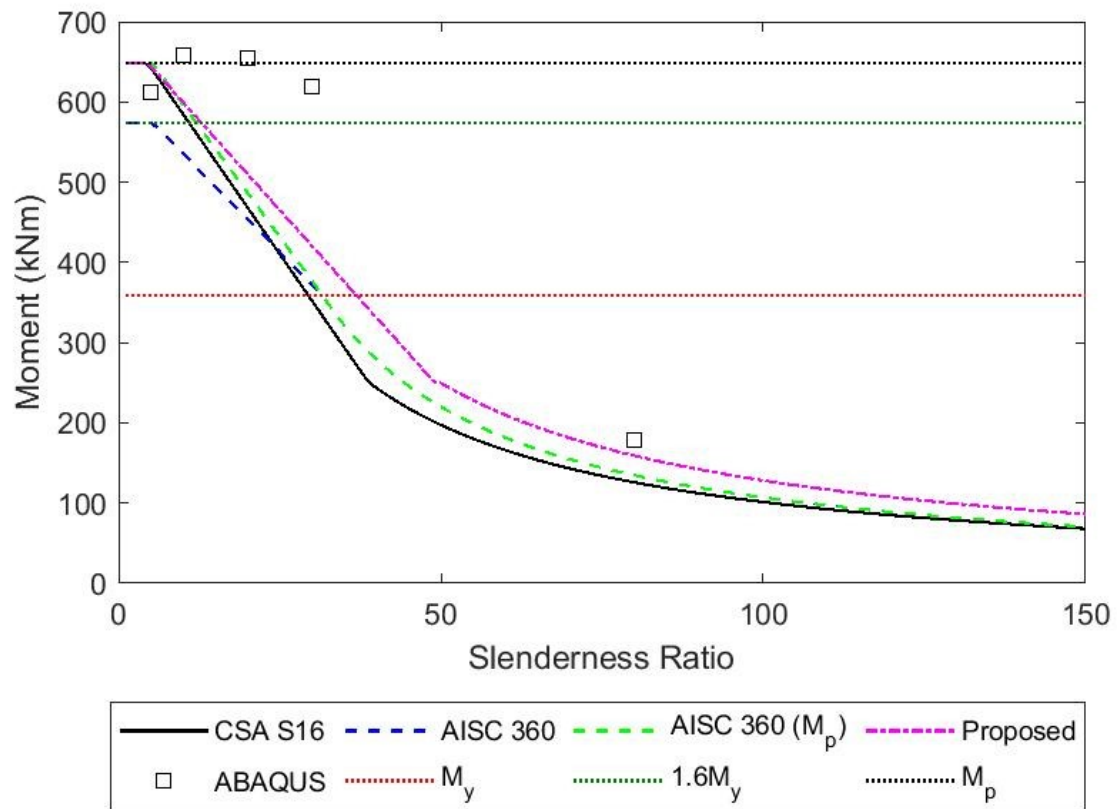


Figure B- 33: Lateral-Torsional Buckling Curve for Beams with a WT500x124 Section Subjected to a Point Load

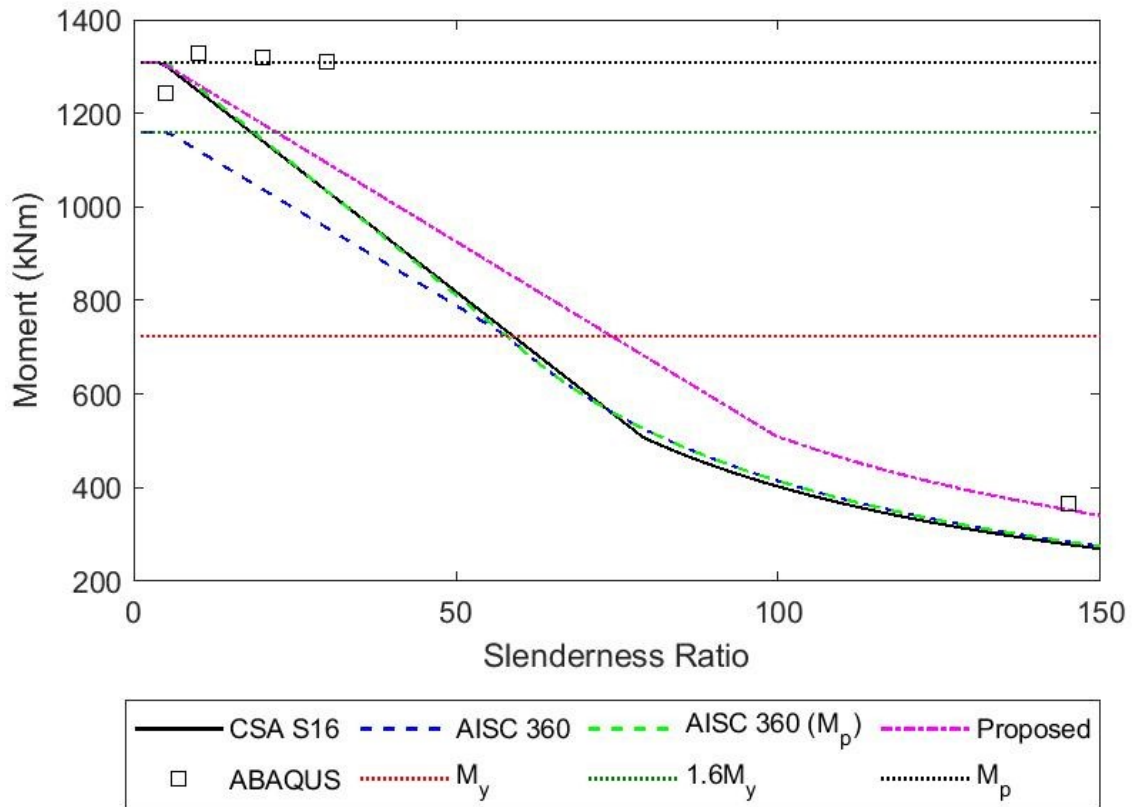


Figure B- 34: Lateral-Torsional Buckling Curve for Beams with a WT500x247 Section Subjected to a Point Load

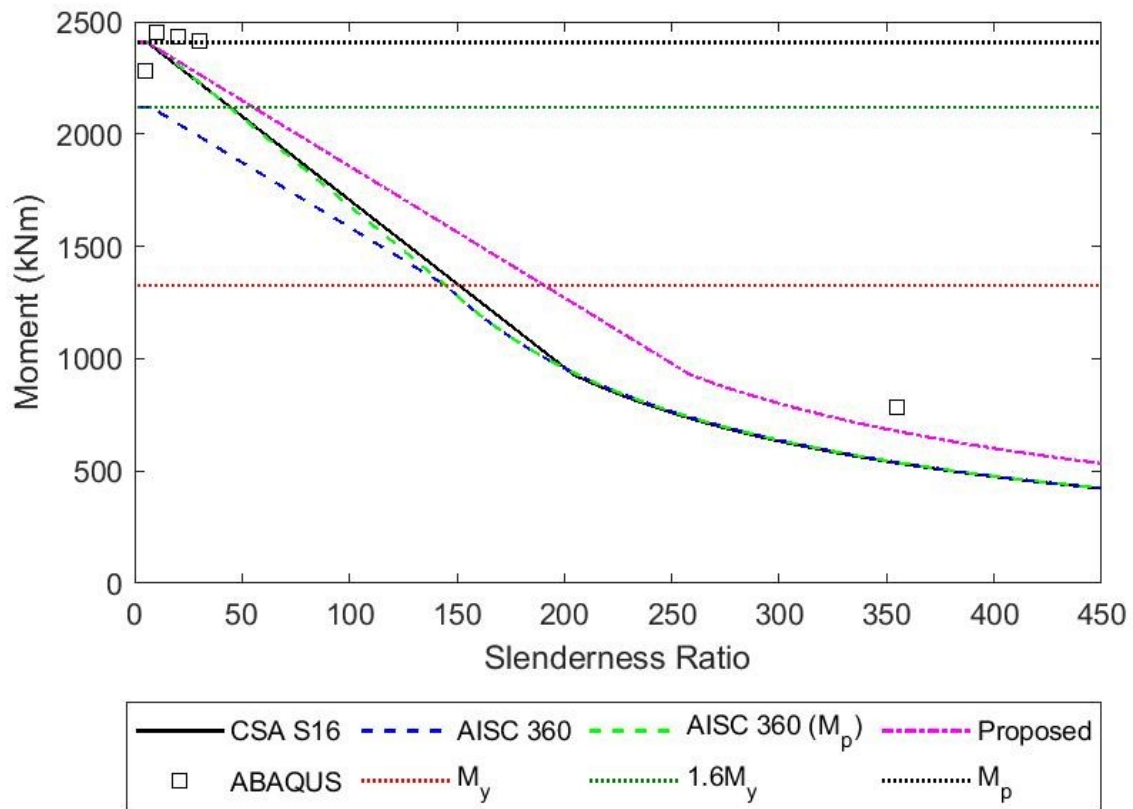


Figure B- 35: Lateral-Torsional Buckling Curve for Beams with a WT500x488 Section Subjected to a Point Load

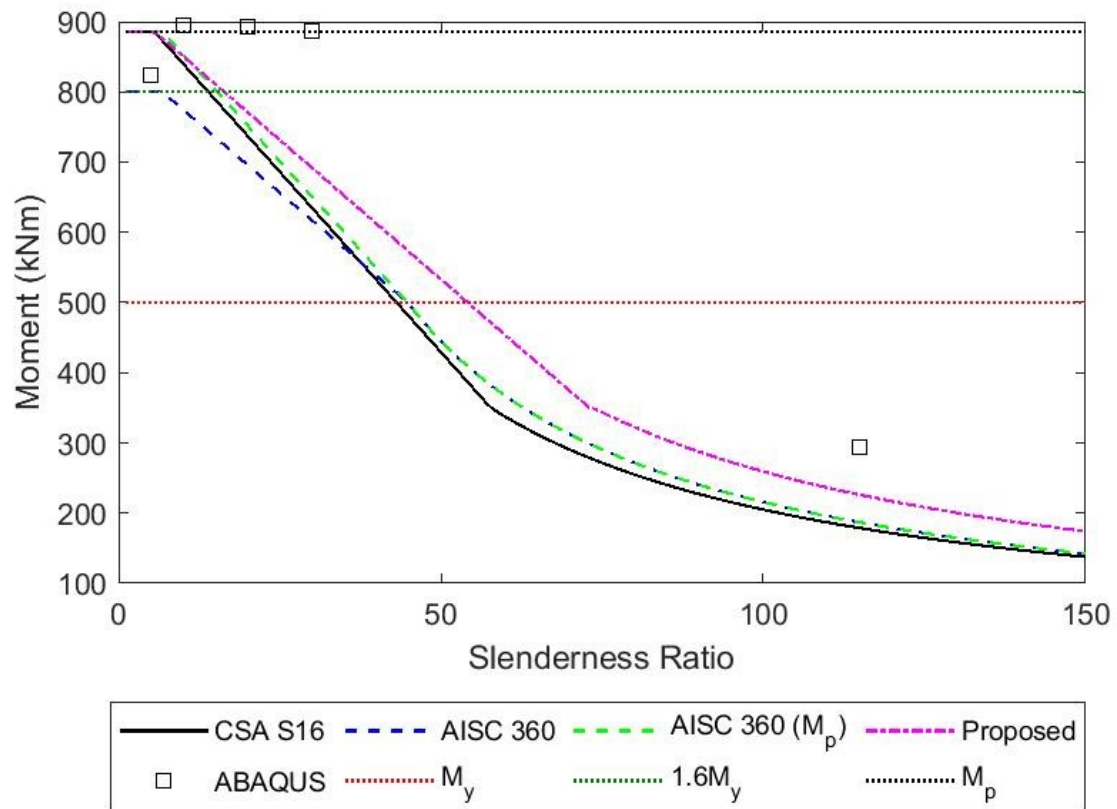


Figure B- 36: Lateral-Torsional Buckling Curve for Beams with a WT550x171 Section Subjected to a Point Load

B.2c: UDL Loading Scenario

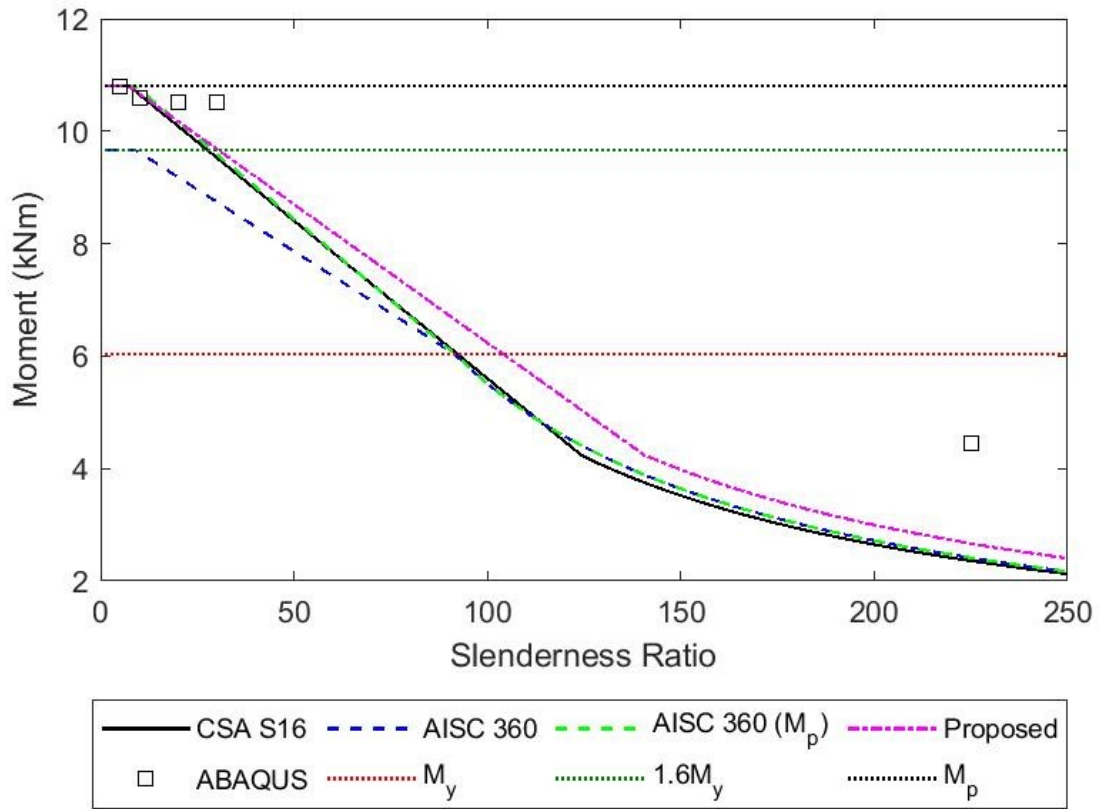


Figure B- 37: Lateral-Torsional Buckling Curve for Beams with a WT100×11 Section Subjected to a UDL

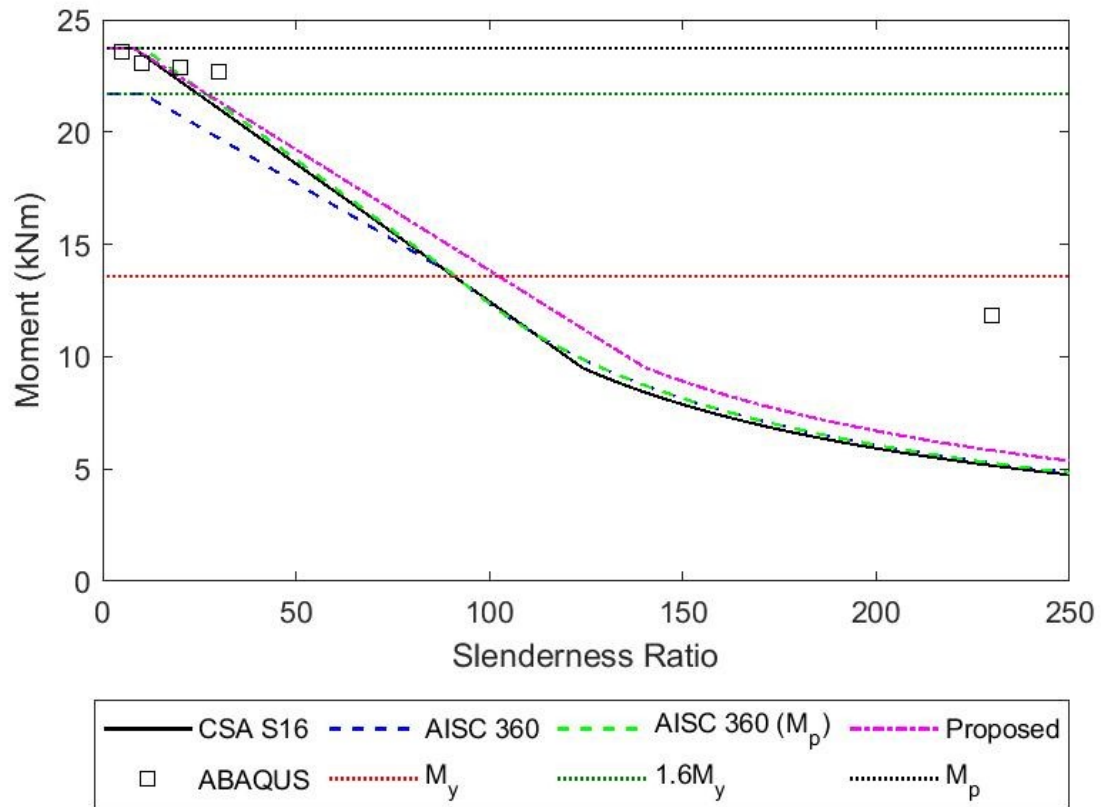


Figure B- 38: Lateral-Torsional Buckling Curve for Beams with a WT15x19 Section Subjected to a UDL

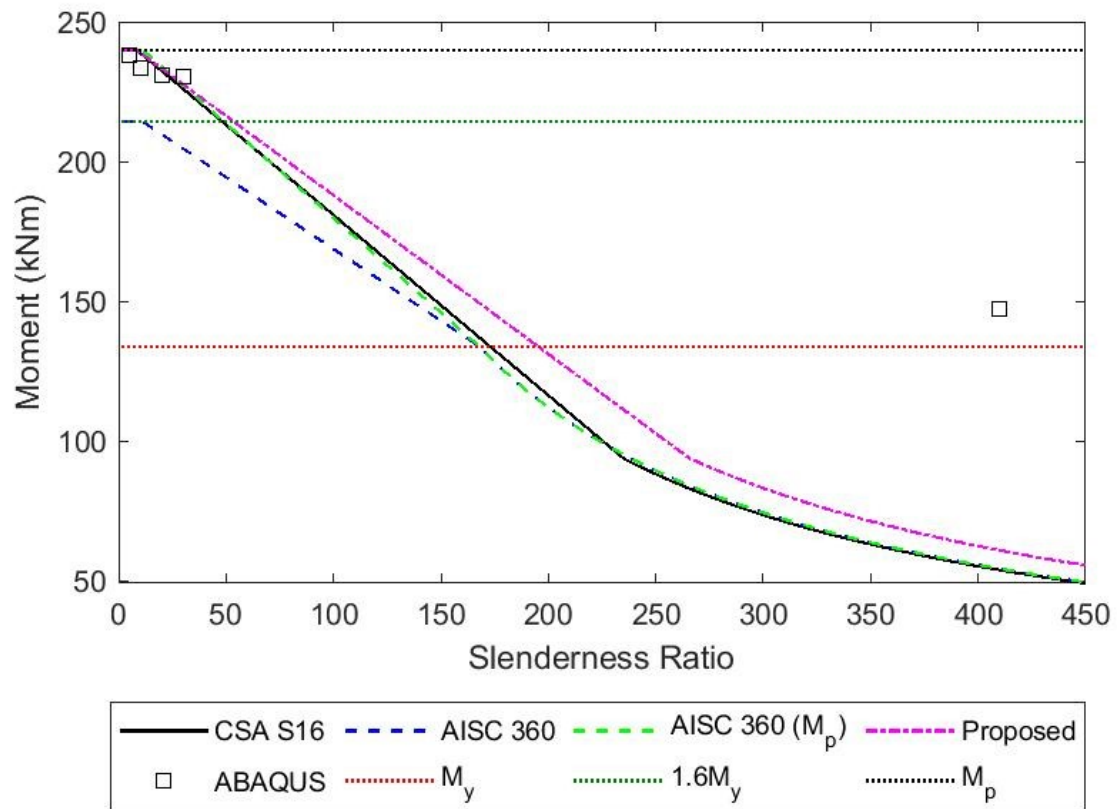


Figure B- 39: Lateral-Torsional Buckling Curve for Beams with a WT265x109 Section Subjected to a UDL

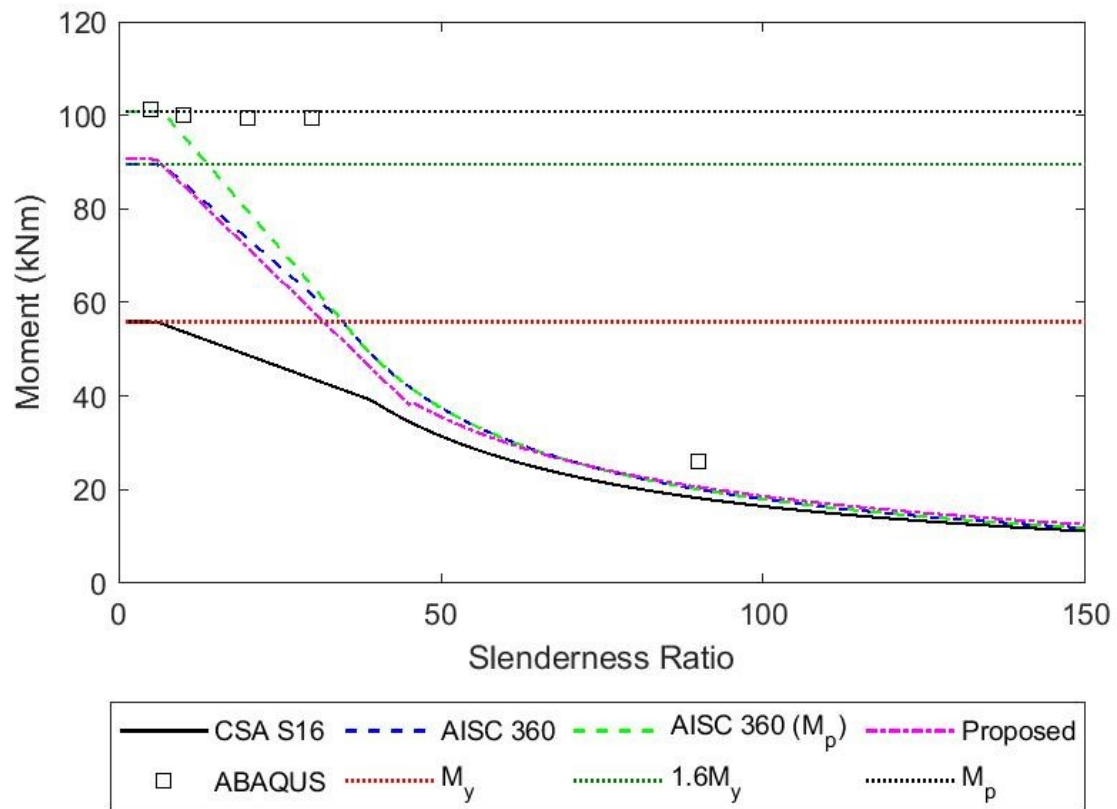


Figure B- 40: Lateral-Torsional Buckling Curve for Beams with a WT265x36 Section Subjected to a UDL

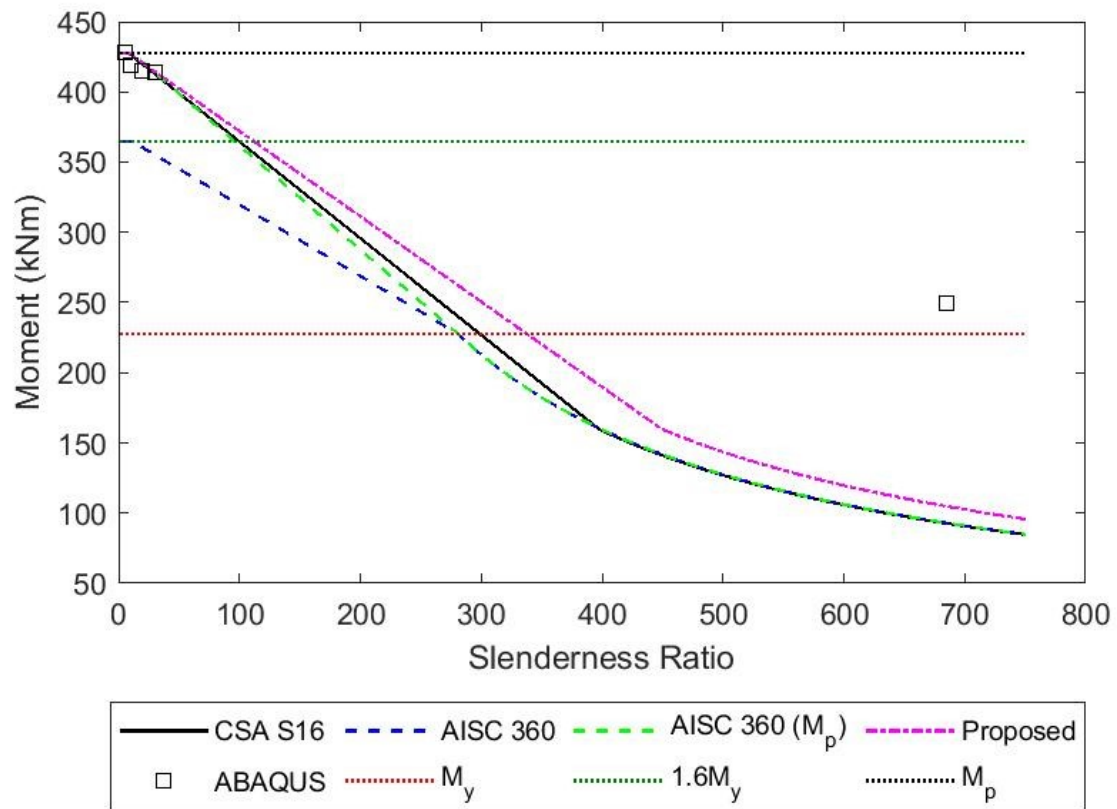


Figure B- 41: Lateral-Torsional Buckling Curve for Beams with a WT265x184 Section Subjected to a UDL

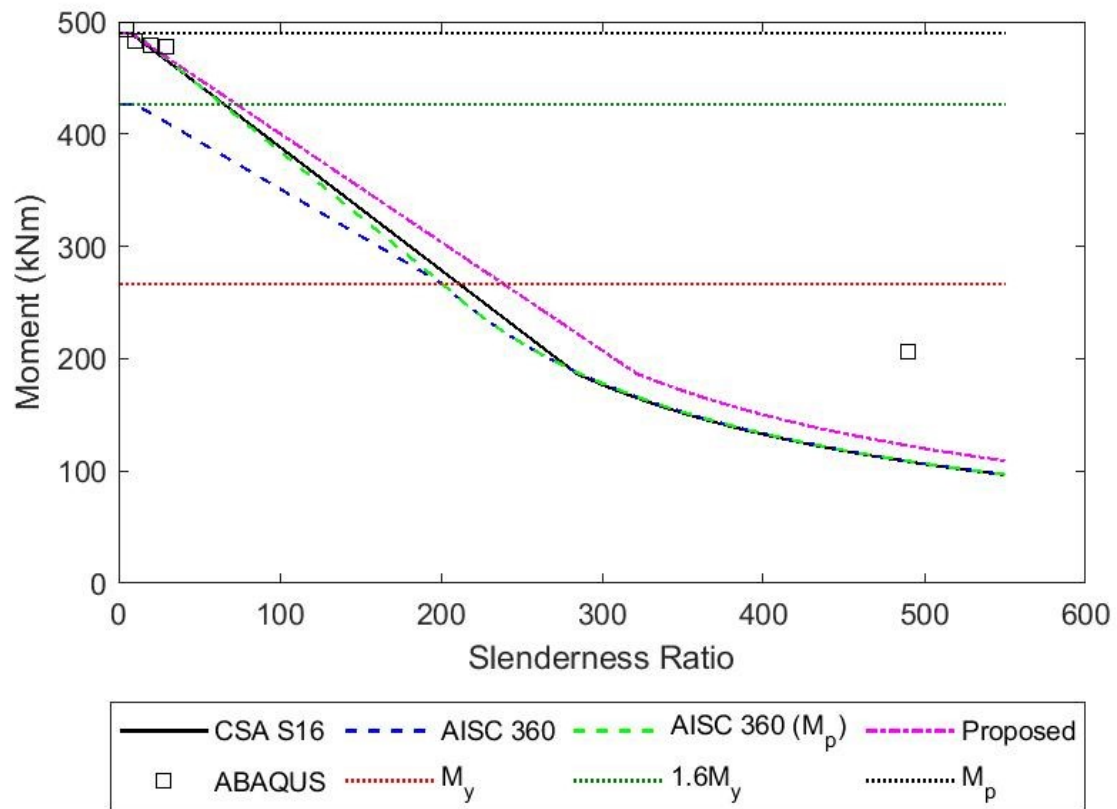


Figure B- 42: Lateral-Torsional Buckling Curve for Beams with a WT305×186 Section Subjected to a UDL

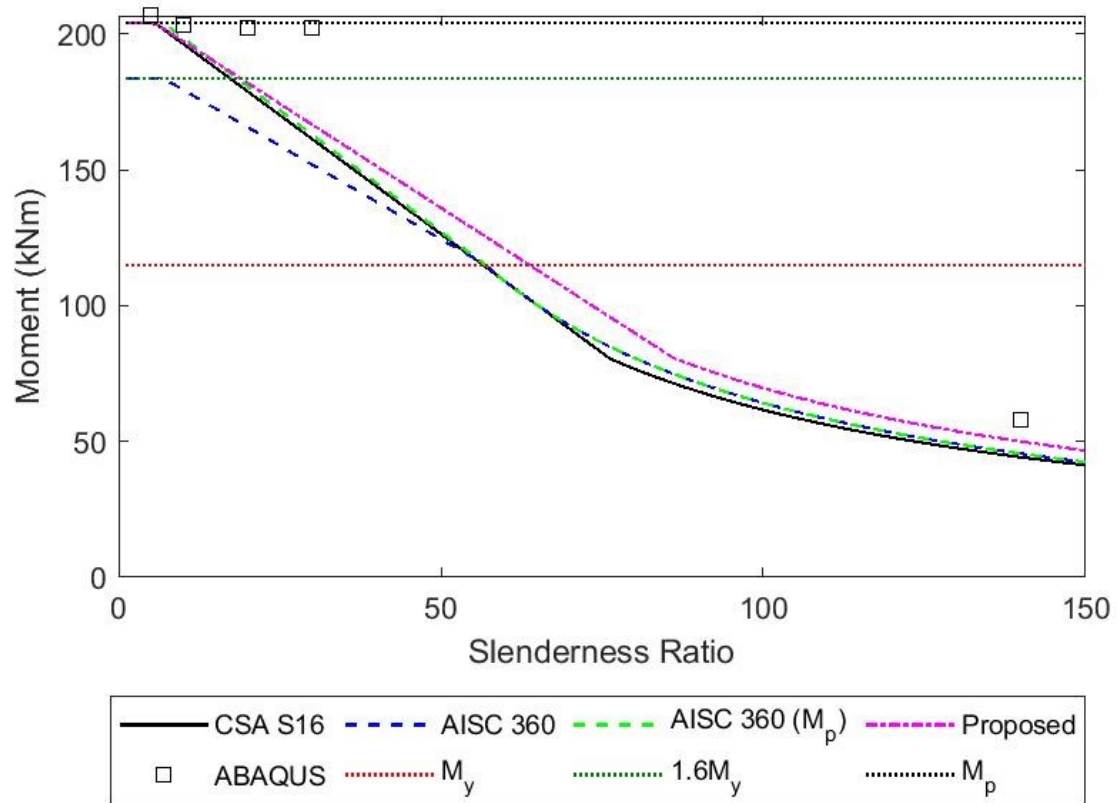


Figure B- 43: Lateral-Torsional Buckling Curve for Beams with a WT305x70 Section Subjected to a UDL

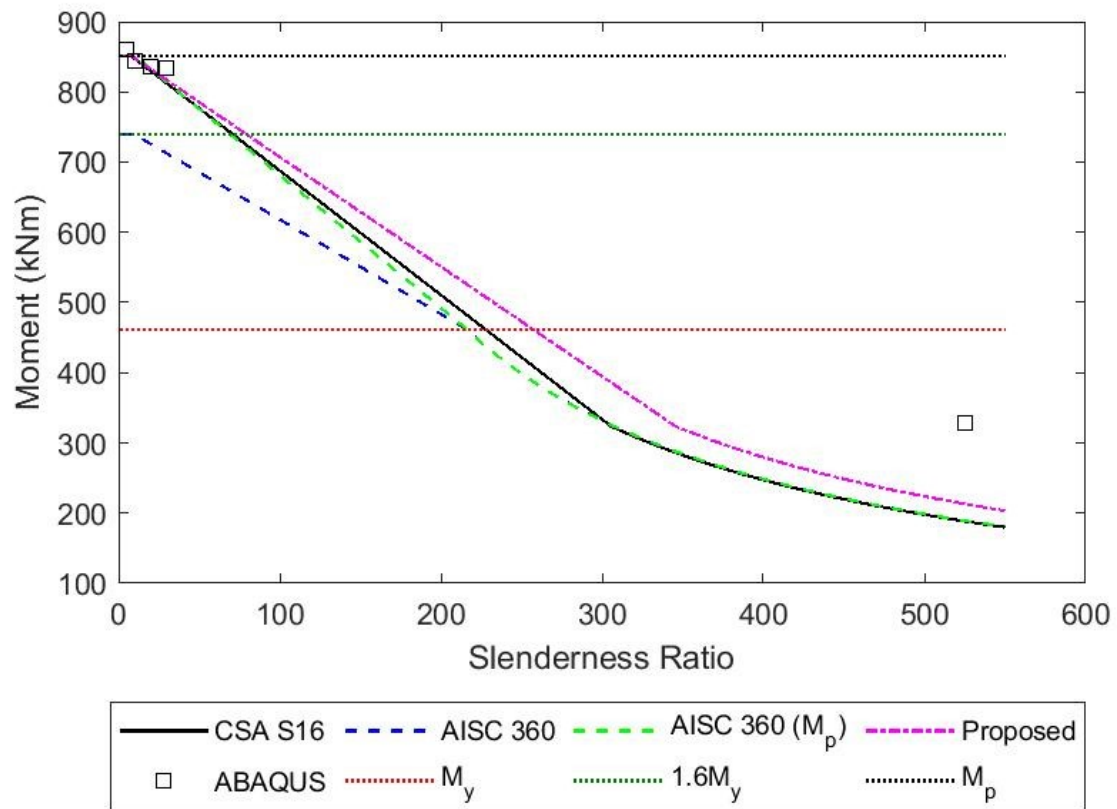


Figure B- 44: Lateral-Torsional Buckling Curve for Beams with a WT345x274 Section Subjected to a UDL

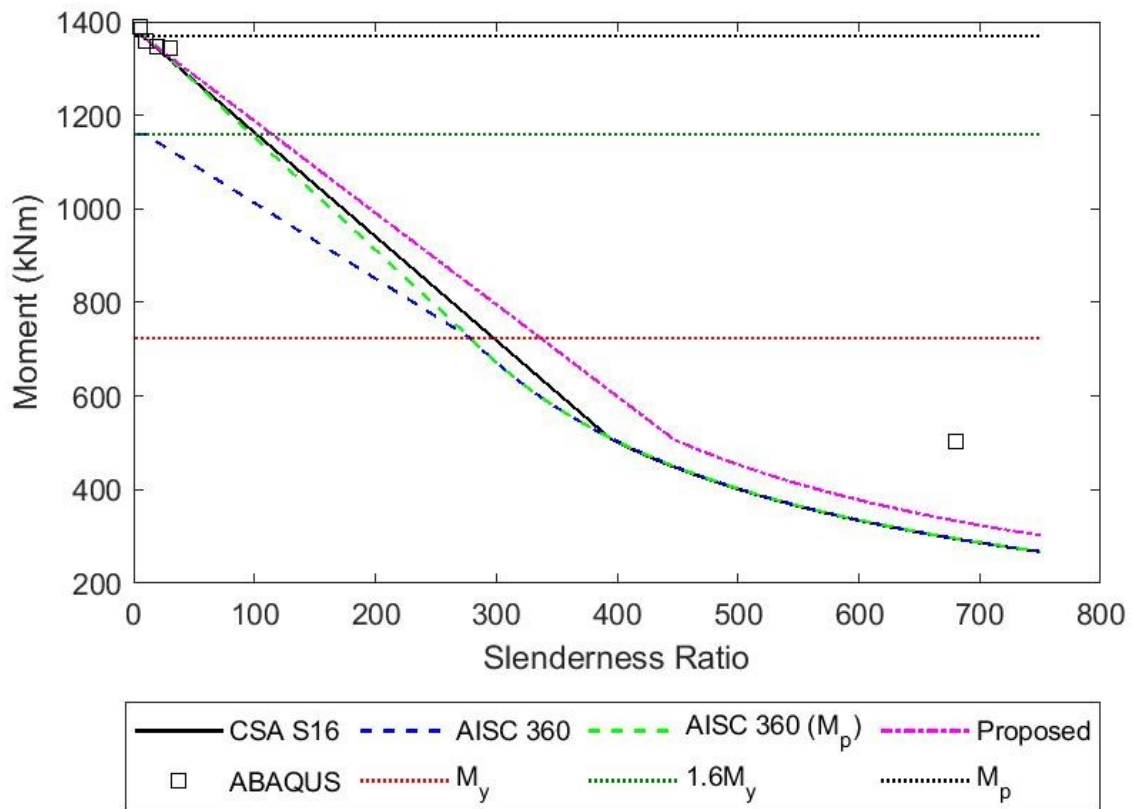


Figure B- 45: Lateral-Torsional Buckling Curve for Beams with a WT345x401 Section Subjected to a UDL

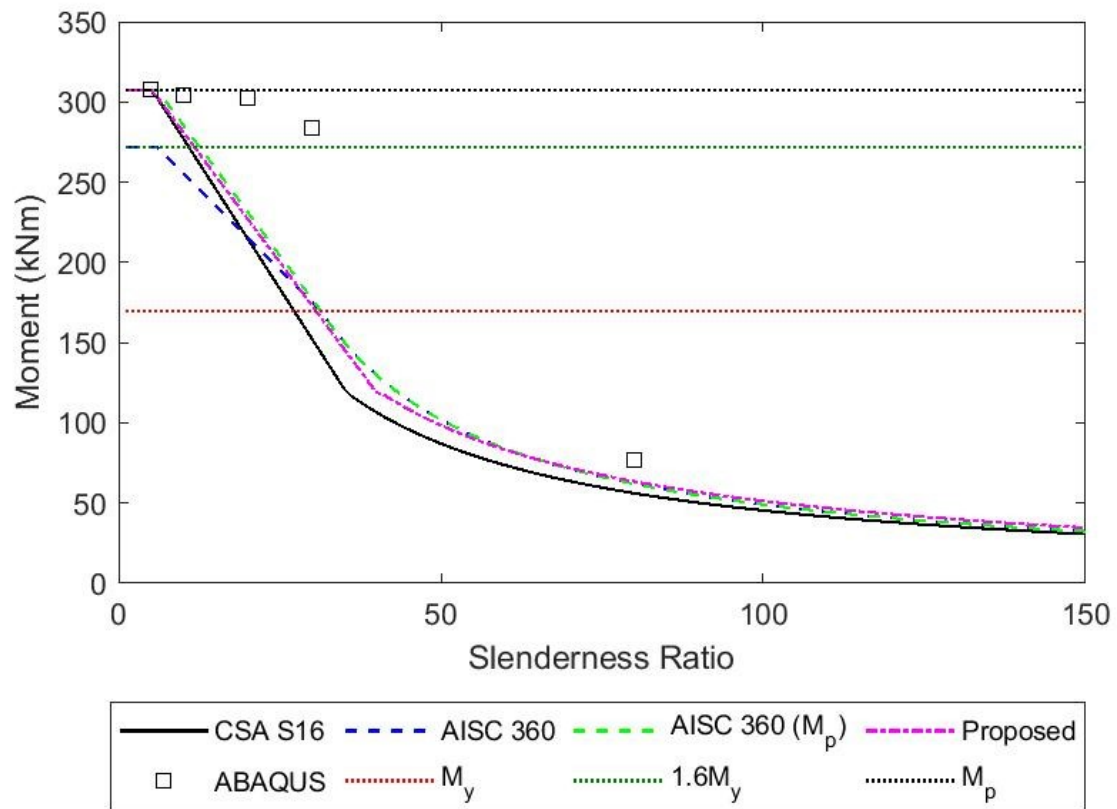


Figure B- 46: Lateral-Torsional Buckling Curve for Beams with a WT380x73 Section Subjected to a UDL

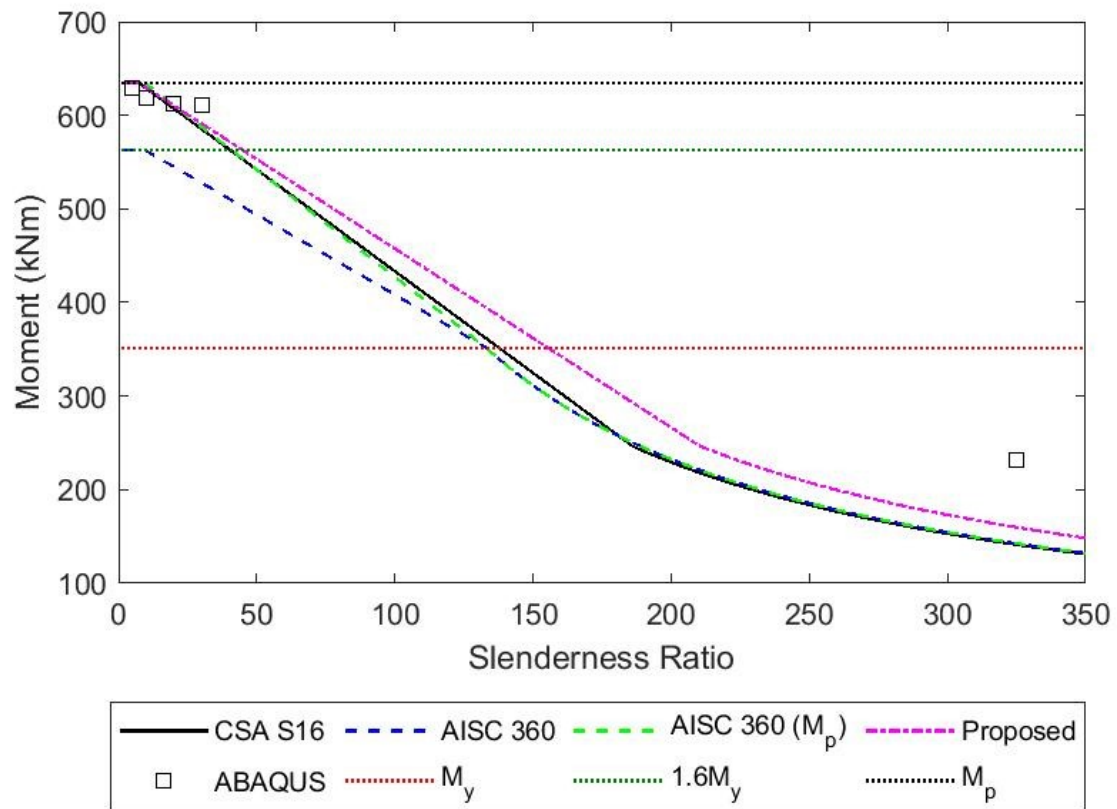


Figure B- 47: Lateral-Torsional Buckling Curve for Beams with a WT380x194 Section Subjected to a UDL

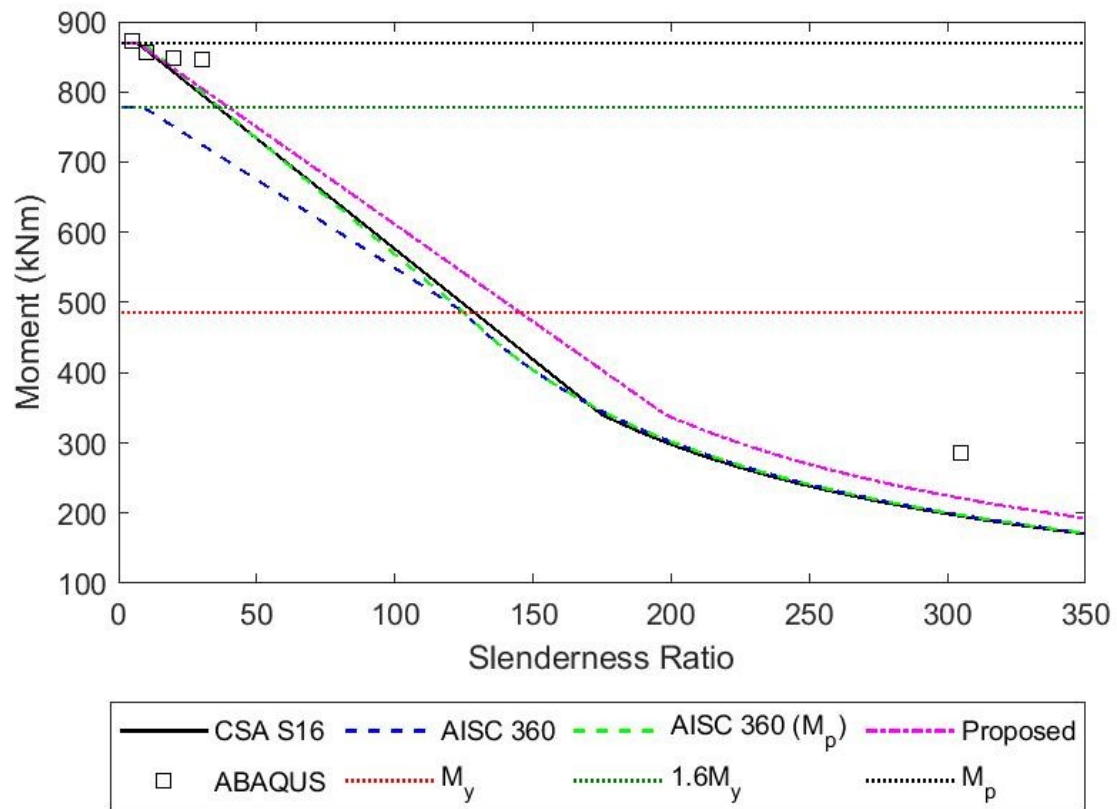


Figure B- 48: Lateral-Torsional Buckling Curve for Beams with a WT420x236 Section Subjected to a UDL

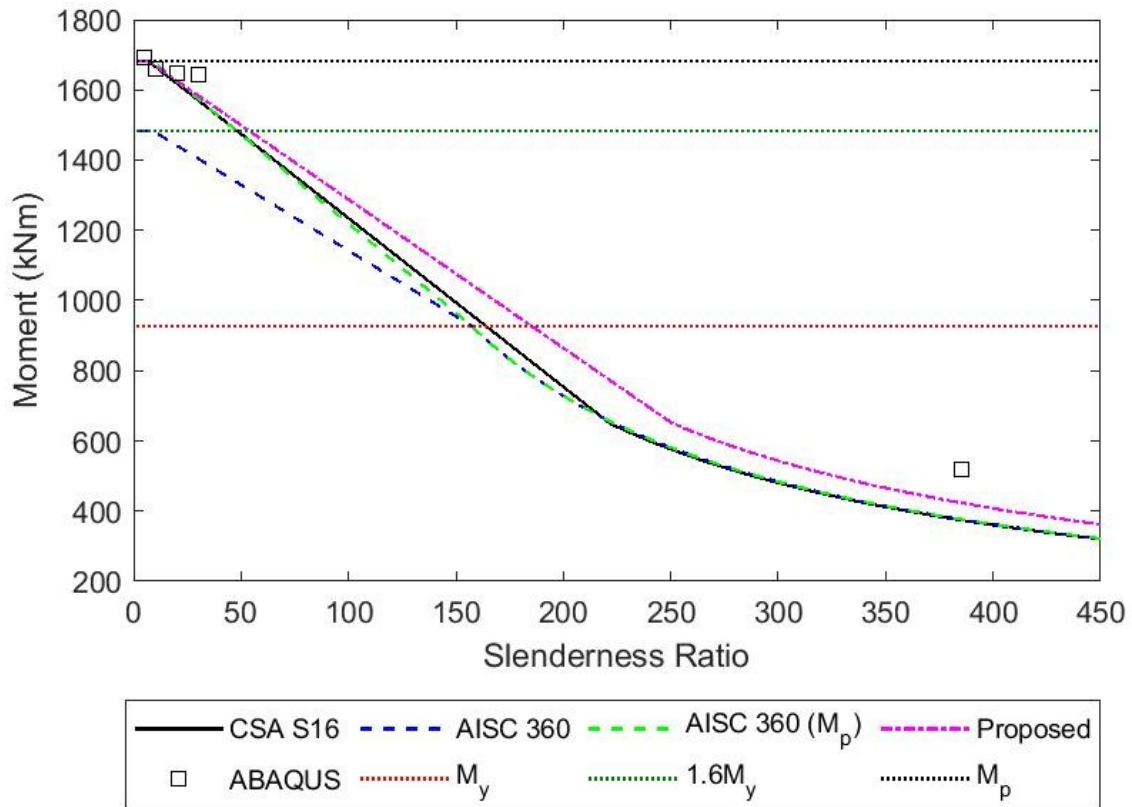


Figure B- 49: Lateral-Torsional Buckling Curve for Beams with a WT460x393 Section Subjected to a UDL

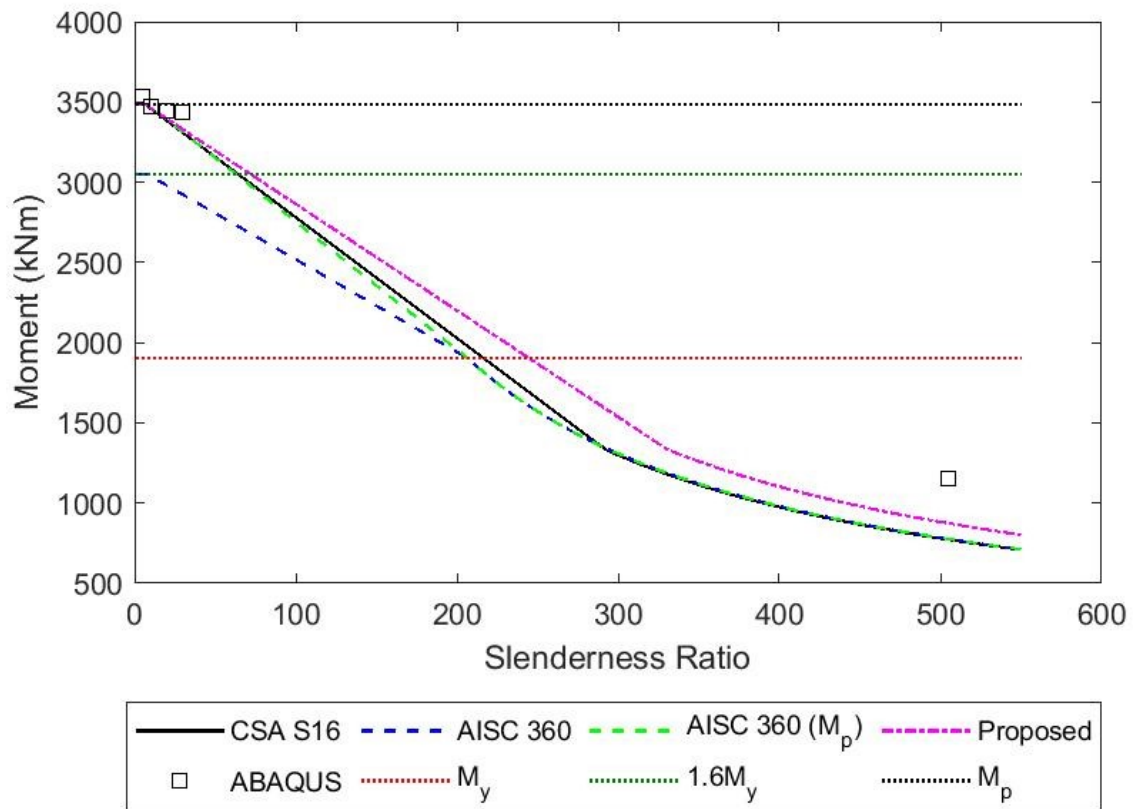


Figure B- 50: Lateral-Torsional Buckling Curve for Beams with a WT460x688 Section Subjected to a UDL

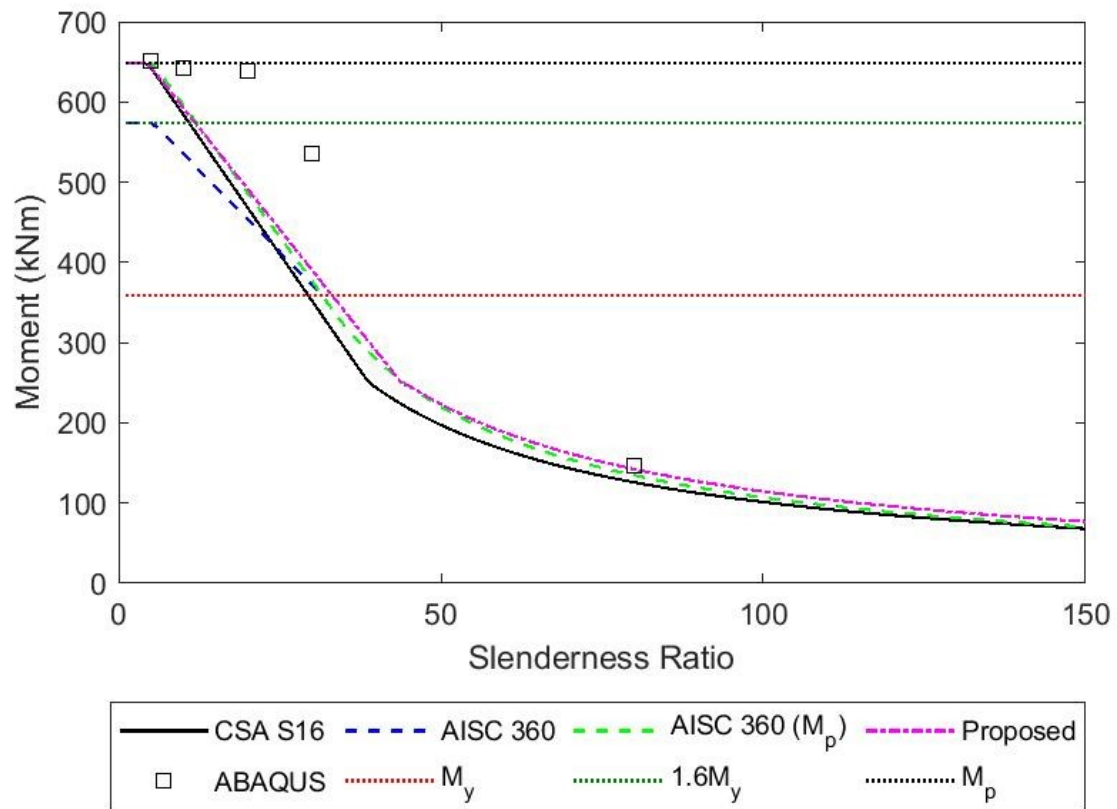


Figure B- 51: Lateral-Torsional Buckling Curve for Beams with a WT500x124 Section Subjected to a UDL

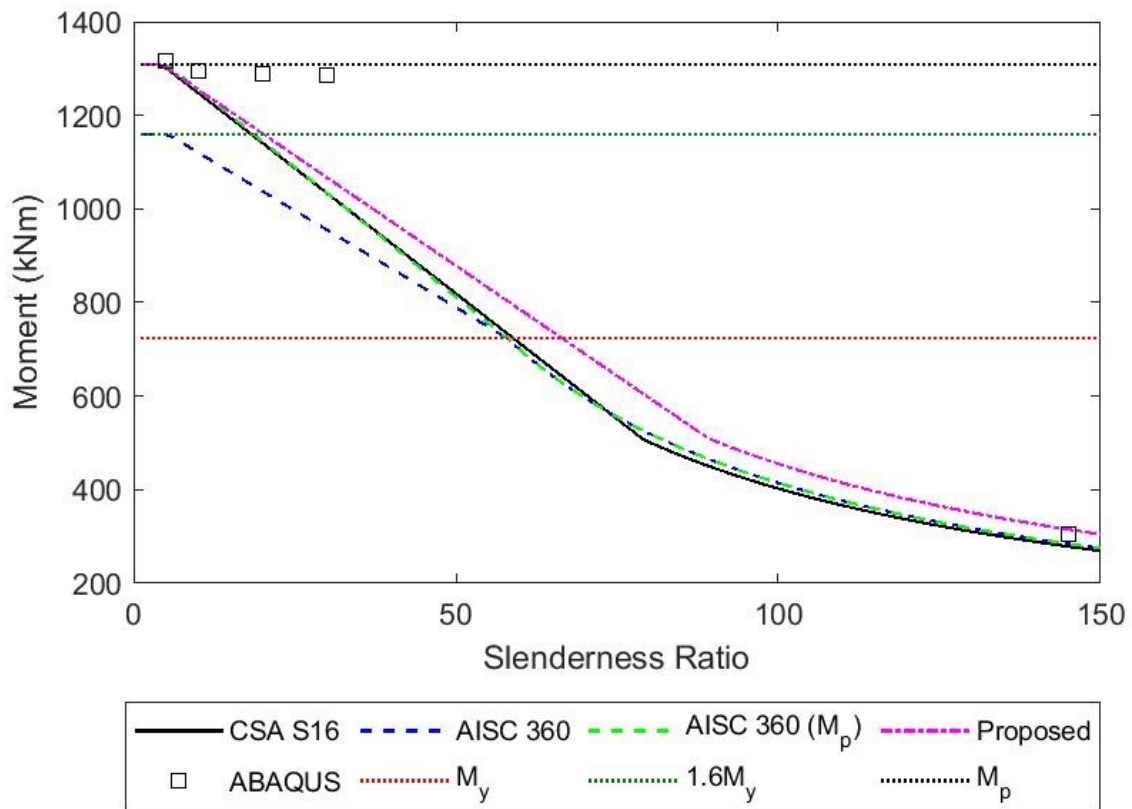


Figure B- 52: Lateral-Torsional Buckling Curve for Beams with a WT500x247 Section Subjected to a UDL

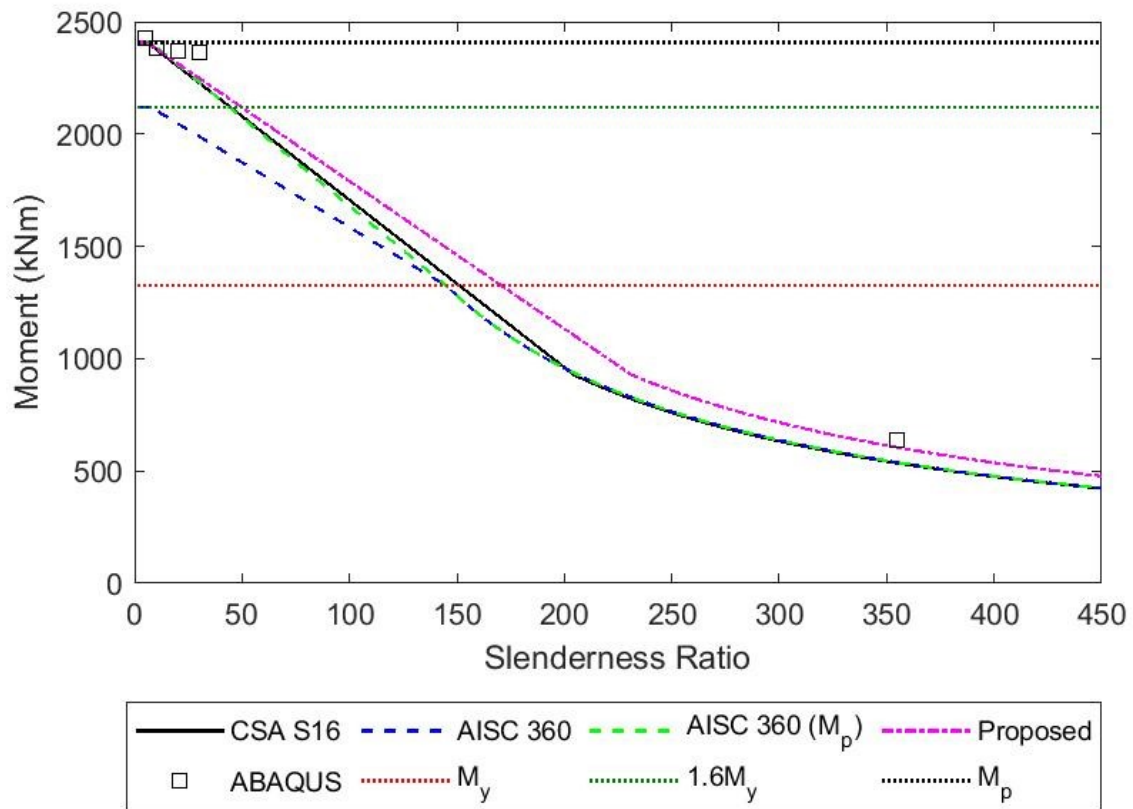


Figure B- 53: Lateral-Torsional Buckling Curve for Beams with a WT500x488 Section Subjected to a UDL

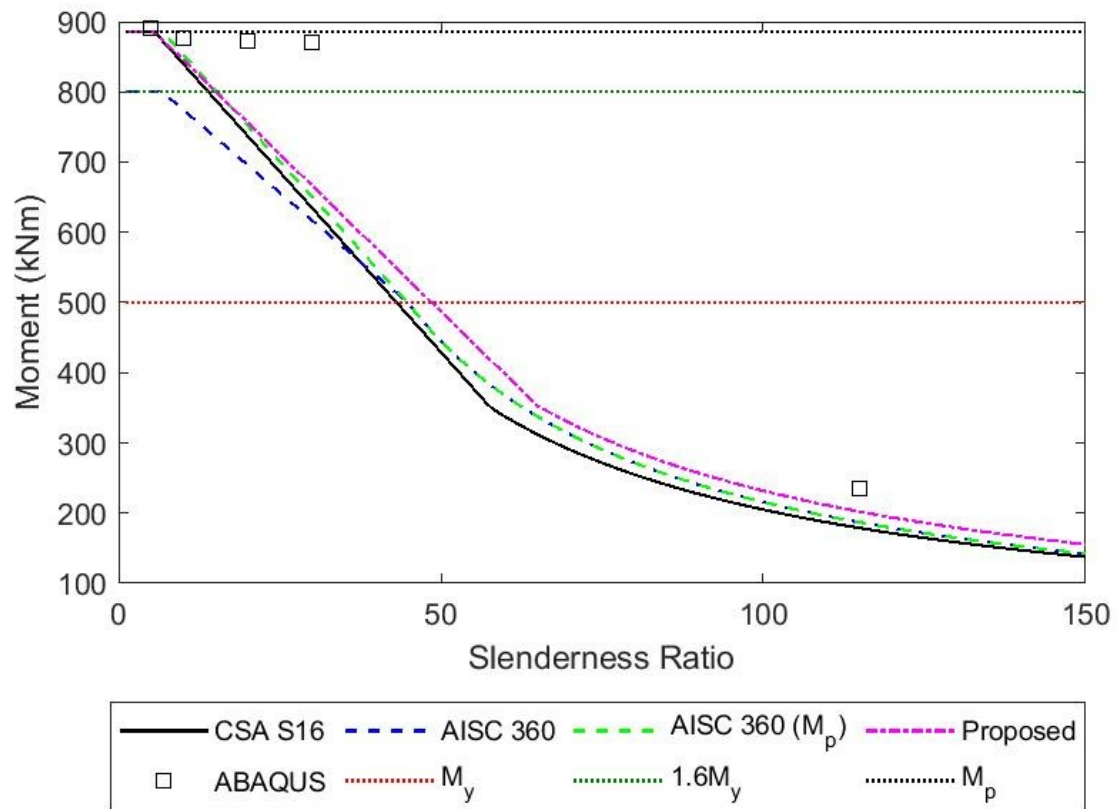


Figure B- 54: Lateral-Torsional Buckling Curve for Beams with a WT550x171 Section Subjected to a UDL